UNIVERSITY OF SOUTHAMPTON

Variability in the South Indian Ocean gyre circulation derived from Argo floats

by

Klaus Getzlaff

A thesis submitted in partial fulfillment for the
degree of Doctor of Philosophy

in the
Faculty of Engineering, Science and Mathematics
School of Ocean & Earth Sciences

June 2009

UNIVERSITY OF SOUTHAMPTON

ABSTRACT

FACULTY OF ENGINEERING, SCIENCE AND MATHEMATICS
SCHOOL OF OCEAN & EARTH SCIENCES

Doctor of Philosophy

VARIABILITY IN THE SOUTH INDIAN OCEAN GYRE CIRCULATION DERIVED FROM ARGO FLOATS

by Klaus Getzlaff

All subtropical oceans exhibit wind-driven, basin-scale gyre circulations, that carry heat poleward. Together, the gyres cover forty percent of the Earth's surface. Once thought to represent areas of steady flow, research in the last decade has shown that the subtropical gyres may exhibit substantial changes both in their strength and spatial structure.

In this study the previously unknown seasonal to interannual changes of the subtropical gyre in the South Indian Ocean are analysed between 2002 and 2006. This has only recently become possible due to the availability of hydrographic profiles acquired by Argo floats. A quality control based on historical observations is applied to the float data, giving a final accuracy of 0.04 psu in salinity for the seasonally averaged fields. Geostrophic transports are calculated using a level of no motion of 1900 dbar and 1000 dbar at 32°S and 20°S, respectively. To suppress transport contributions to the estimates of gyre strength resulting from eddies at the section end points a linear regression is applied to the vertically integrated northward transports. From this fit the gyre strength at 32°S and 20°S is then estimated as the northward transport integrated from 110°E to 45°E and from 110°E to 55°E, respectively.

The gyre strength at 32°S averaged over the 5 year period is 44.4±1.2 Sv, while displaying variations of 5.2 Sv rms on interannual and 3.0 Sv rms on seasonal time scales. It does not exhibit a significant trend between 2002 and 2006. Estimates of the gyre strength from hydrographic data from two cruises in 1987 and 2002 yield 33.6±3.4 Sv and 43.7±5.5 Sv, respectively. A maximum correlation of 0.92 between the one-year low-pass filtered gyre strength and the geostrophic contribution to the wind-stress derived Sverdrup transport is found for wind stress leading the gyre by one year.

The change in gyre strength between 1987 and 2002 as derived from the cruise data is of the same size as the largest year-to-year change inferred from Argo between 2002 and 2006. However, it is shown that the circulation in 1987 differs significantly from the gyre state in the 5 year period 2002 to 2006, both in magnitude and structure. These results suggest that care must be taken when single hydrographic sections are used to describe long-term trends or to provide an initial state or a boundary condition for numerical models.

Contents

List of Figures

List of Tables

Acronyms

AAIW	Antarctic Intermediate Water
AC	*Agulhas Current*
ACC	*Antarctic Circumpolar Current*
ADT	absolute dynamic topography
ARC	*Agulhas Return Current*
Aviso	Archiving, Validation and Interpretation of Satellite Oceanographic data
BEAGLE	Blue Earth Global Expedition
BP	Broken Plateau
CB	Crozet Basin
CD139	*Charles Darwin* 139
CD29	*Charles Darwin* 29
CEC	Cross-Equatorial Cell
CLIVAR	Climate Variability and Predictability Programme
CR	Crozet
CTD	conductivity-temperature-depth
DAC	Data Assembly Centre
DH	Dynamic Height
DMQC	delayed-mode quality control
EMC	*East Madagascar Current*
ENSO	El Niño/Southern Oscillation
GDAC	Global Data Assembly Centre
GODAE	Global Ocean Data Assimilation Experiment
IO	Indian Ocean
IOD	Indian Ocean Dipole
IOHB	Indian Ocean Hydrobase
IW	Intermediate Water
ITF	*Indonesian Throughflow*
LC	*Leeuwin Current*
LUC	*Leeuwin Undercurrent*
LCS	*Leeuwin Current System*
MADB	Madagascar Basin
MAD	Madagascar
MADR	Madagascar Ridge
MAU	Mauritius
MOZB	Mozambique Basin
MOZC	Mozambique Channel
MOZP	Mozambique Plateau
MW	Mode Water
NCAR	National Center for Atmospheric Research
NCEP	National Centers for Environmental Prediction
NER	Ninetyeast Ridge
OI	Optimal Interpolation
PB	Perth Basin
PV	potential vorticity
RMS	Root-mean-square
RE	Reunion
SAB	South Australia Basin
SAM	Southern Annular Mode
SAMW	Subantarctic Mode Water
SEC	*South Equatorial Current*
SEISAMW	Southeast Indian Subantarctic Mode Water
SICC	*South Indian Counter Current*
SIO	South Indian Ocean
SIOC	*South Indian Ocean Current*
SLA	sea level anomaly
SNR	Signal-to-noise ratio
STC	Subtropical Cell
STMW	Subtropical Mode Water
SWIR	Southwest Indian Ridge
WAC	*West Australian Current*
WOA01	World Ocean Atlas 2001
WOA05	World Ocean Atlas 2005
WOCE	World Ocean Circulation Experiment
WOD05	World Ocean Database 2005
ZV	zero-velocity

Declaration

I, Klaus Getzlaff, declare that this thesis is the result of work done wholly or mainly by myself while in canditure for a research degree at the University of Southampton.

Acknowledgements

I would like to thank my supervisors, Harry Bryden, Elaine McDonagh and Brian King for their endurance and patience with my work. Additionally, I would like to thank Heiner Dietze for a very useful birthday present, which value I only realised lately during the final stage of writing up. Further thanks for proof reading goes to John Armitage, Uta Krebs, Torsten Kanzow, Miriam Glessmer and Julia Getzlaff.

My friends and family supplied great support during the whole project. Especially, I am very thankful to Roswitha, Christa and Reinhard for supporting me and my family during the last years. Moreover, I am deeply indepted to my love Julia and our lovely daughters Leonie and Paulina, for their patience and for keeping me grounded, without them I would never have completed this work. I would also like to thank Uta, Torsten, Brita and Daniel for providing bikes, home and a social life during my frequent visits. Finally, I thank Caroline, John, Ralf, Sven and Julia for numerous coffee breaks, without which no work would ever be done.

To Paulina, Leonie and Julia

Chapter 1

Introduction

The focus of the public, politicians and scientists in recent years is more and more directed towards climate change. The growing evidence of global climate change (IPCC, 2007) makes it necessary to collect and understand changes in the climate system on many time scales. This was the main ambition of the World Climate Research Programme (WCRP) initiated in the early 1980s, while only about ten years later the field program of the first truly global ocean study, named World Ocean Circulation Experiment (WOCE), started. WOCE was predicated on international collaboration and the implementation of new satellite technology as well as global ocean models. The data collected during WOCE provided the foundations for the research into variability and predictability. With the knowledge of the need for long-term observation new research programmes such as the Global Ocean Data Assimilation Experiment (GODAE) and the Climate Variability and Predictability Programme (CLIVAR) programm have been implemented with a focus on a global system of observations, communications, modelling and assimilation. The Argo project is implemented in CLIVAR and GODAE and it contributes to the global observing system. Since it's start in early 1998, Argo aims to provide high resolution measurements of the upper ocean in space and time. Therefore, the first phase of the project was to set up a global array of more than 3000 free drifting autonomous profiling floats. This goal had been fulfilled in October 2007, while by now more than 3170 floats are in operation. Argo data can measure the "pulse" of the upper ocean, with many possible applications important for the global climate such as for example changes in heat storage (Hadfield et al., 2007), or changes in the subtropical gyre circulation (Roemmich et al., 2007). The spatial and temporal resolution of nominal $3° \times 3°$ every 10 days can be used to generate time series with a much better temporal resolution than those obtained from repeated hydrographic shipboard observations. Hence, Argo data will greatly contribute to help answering key questions about the sensitivity of the global climate system. This knowledge about low-frequency

variability on interannual or seasonal time scales is important to improve the reliability of numerical models used to predict possible trends in the global climate system. Nevertheless, the Argo data have their weaknesses too, as for example they measure solely the upper 2000 m of the world's ocean and show generally a sparse coverage in the boundary current systems. Therefore, other long-term operational systems, such as the Rapid Climate Change (RAPID) mooring array (Hirschi et al., 2003; Cunningham et al., 2007) are needed to be able to address the low-frequency characteristics of the Atlantic meridional overturning circulation by continuous measurements.

In the present work Argo float data collected between 2002 and 2006 are used to define the low-frequency variability in the South Indian Ocean (SIO) gyre circulation on interannual and seasonal time scales and to verify recently observed changes in the gyre strength between 1987 and 2002, indicating a positive decadal trend in the SIO.

1.1 Background

The global oceanic and atmospheric circulation play a crucial role in climate because they transport heat from the Equator to the Poles, with both contributing about equally in maintaining the global heat balance (Bryden and Imawaki, 2001) but in different ways. While the atmosphere does contribute to the heat balance mainly by transient eddies in mid and high latitudes, the ocean does it mainly by boundary currents, large gyres and the vertical overturning of the ocean (Grassl, 2001). This shows the two main forcing mechanisms of the global ocean circulation, the winds and buoyancy fluxes. On large scales the winds drive the ocean circulation in the upper thousand meters by transmitting momentum and vorticity to the ocean surface, forcing anticyclonic subtropical and cyclonic subpolar gyres in each ocean basin. The subtropical gyres have the crucial role in the climate system to export heat gained in the tropics to the Poles. Additionally, spatial variations in the heat and fresh water surface fluxes drive the thermohaline circulation (THC), which connects all ocean basins by the so-called "ocean conveyor" (Broecker, 1991). Although mentioned separately, both driving mechanisms are directly connected, while the concept of the global "ocean conveyor" is still somewhat a theoretical concept due to the lack of direct observational evidence.

The Indian Ocean (IO) is unique in its location and role within the world oceans. Firstly, the IO has no subpolar region in the north due to its closed northern boundary at 20°N. This affects in combination with the prevailing mean zonal wind field at the equator and the upwelling regions in the north the shallow meridional circulation

(Schott and McCreary, 2001; Schott et al., 2004; Miyama et al., 2003). While in the Atlantic and the Pacific the subduction areas in the subtropics are connected with upwelling regions at the Equator, to form what is known as shallow Subtropical Cells (STCs), in the IO that connection takes place as shallow inter-hemispheric cell known as Cross-Equatorial Cell (CEC) (Lee and Marotzke, 1998; Schott and McCreary, 2001; Schott et al., 2004). The CEC connects the *South Equatorial Current* (SEC) with the northern upwelling regions along the western boundary via a subsurface, northward flowing part of the *Somali Current*, while at the surface it is closed by southward, cross-equatorial, Sverdrup transport in the interior ocean. Therefore, the CEC implies a major contribution to the meridional exchange of mass and heat between the hemispheres (Schott et al., 2004; Miyama et al., 2003; Schoenefeldt and Schott, 2006).

Secondly and related to the first, the IO's direct connection to the Pacific Ocean via the Indonesian Passages is a pathway for warm surface waters (Gordon and Fine, 1996). As a consequence all heat gained from the *Indonesian Throughflow* (ITF) and as surface fluxes further north, has to leave the IO in the south (Fu, 1986; Lee and Marotzke, 1998), mainly with the *Agulhas Current* (AC) in the southwest corner. The net heat export from the IO to the rest of the world oceans is feeding the warm upper limb of the northward thermohaline transport in the South Atlantic (Gordon, 1986; De Ruijter et al., 1999). While model studies suggest that this exchange has a stabilising influence on the meridional overturning circulation in the North Atlantic (Weijer et al., 2002) it becomes clear that the ability to understand the dynamical mechanisms that participate in the global interocean exchanges relies on our understanding of the processes controling the variability of the IO gyres (Matano et al., 2008). In this context, Bryden and Beal (2001) stressed that the circulation in the subtropical SIO across 32°S is in fact very important since there is a substantial horizontal gyre circulation, a factor of 5 larger than their estimated overturning, with a strong southward flow of warm and salty waters in the western boundary and a basin wide northward flow of colder and fresher waters.

1.2 The South Indian Ocean

The connection between the equatorial IO and the AC, the major export path in the south, is built by the subtropical SIO (Fig. 1.1 and additionally, for a detailed description of major components of the large-scale circulation of the SIO the reader is referred to e. g. Stramma and Lutjeharms (1997); Lutjeharms and Ansorge (1997); Reid (2003); Davis (2005); Ridgway and Dunn (2007)). This connection is

provided either by permanent currents (Stramma and Lutjeharms, 1997; Schott and McCreary, 2001) or by eddy propagation (Schouten et al., 2003). The SEC transports warm ITF waters to the west, feeding the *East Madagascar Current* (EMC) and *Mozambique Current*, respectively and therewith the SEC provides major supply for the AC. While classically the AC was thought of as a straighforward extension of an upstream western boundary current comprising, the *Mozambique Current*, and from the east the EMC (Fig. 1.1). Schouten et al. (2003) showed from satellite altimetry that instead of a continuous *Mozambique Current*, a pathway of anticyclonic eddies drifting southward persists. Also a possible connection of the EMC to the AC is still under debate. De Ruijter et al. (2004) suggested that the interannual variability found in the EMC is related to the large-scale climate variability in the IO, especially the equatorial climate modes such as El Niño/Southern Oscillation (ENSO) and Indian Ocean Dipole (IOD). The westward propagation of the large-scale anomalies, associated with ENSO/IOD-cycles is suggested to take one year (Murtugudde et al., 2000). Supporting this, Palastanga et al. (2006) concluded that the ending of a positive ENSO/IOD event is ultimately responsible for high amplitude eddies and a larger southward transport through the Mozambique Channel (MOZC). A positive ENSO/IOD event correlates to a weakening of the surface flow of the SEC. As a consequence of this there is an intensification and northward extension of the subtropical gyre after a positive ENSO/IOD event.

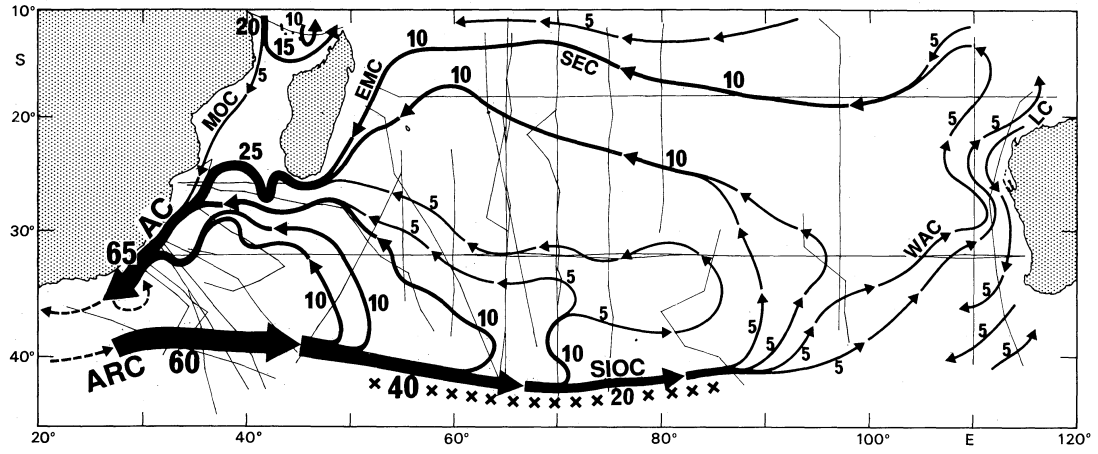

Figure 1.1: Schematic illustration of the flow field in the South Indian Ocean. The transports for the upper 1000 m in Sverdrups are given by numbers in 5-Sv steps. Thin lines indicate the sections used. Current bands for *Agulhas Return Current* (ARC), *South Indian Ocean Current* (SIOC), *West Australian Current* (WAC), *Leeuwin Current* (LC), *South Equatorial Current* (SEC), *East Madagascar Current* (EMC), *Mozambique Current* (MOC), and *Agulhas Current* (AC) are marked. Figure is taken from Stramma and Lutjeharms (1997)

Recent studies that focussed on the subtropical SIOs flow structure and variability conclude that although understanding of the variability in the SIO has been achieved, mainly from model and altimeter data, these findings need further validation by direct hydrographic observations (Palastanga et al., 2006; Matano et al., 2008). This need for direct observations is addressed in this study by utilising Argo float data to provide estimates of changes in the SIO gyre circulation over the 5 year period 2002 - 2006.

1.3 Motivation and structure of the thesis

This study is motivated by the results from recent studies analysing changes in the SIO thermocline properties (McDonagh et al., 2005), and in the gyre strength (Palmer et al., 2004), using hydrographic transects at a nominal latitude of 32°S. McDonagh et al. (2005) used 5 hydrographic section taken in 1936, 1965, 1987, 1995 and 2002. From their analysis of thermocline properties and dissolved oxygen concentrations they concluded an increase in gyre strength of up to 20% between 1987 and 2002. Additionally, Bryden et al. (2003b) stated that the 2002 upper thermocline waters were found to be saltier on isotherms than 1987. This increase reverses the reported slow-down of 20% of the gyre circulation between 1962 and 1987 (Bindoff and McDougall, 2000). Bindoff and McDougall (2000) reported a freshening of the upper thermocline waters based on property changes and changes in dissolved oxygen concentrations. Additionally, Palmer et al. (2004) found an increase of 40% in the gyre strength over the ocean interior by applying a zero-velocity (ZV) assumption to the geostrophic velocity fields at 2230 dbar derived from the hydrographic data in 1987, 1995 and 2002. They showed that most of the change happened between 1995 and 2002. Furthermore, they concluded that there has been a persistent change between the flow structure of the 1987 and 2002 sections, that can be seen by the westward shift of the maximum southward transport (in 1987 this maximum is located at 55°E, while in 1995 at 45°E and in 2002 at 40°E, respectively). Finally, Palmer et al. (2004) stated that their results are qualitively consistent with the increased gyre strength suggested by McDonagh et al. (2005) but it seems plausible that some of the transport changes between 1987 and 2002 are not related to the shallow water mass changes. In contrast, Stark et al. (2006) concluded from model simulations initialised with a range of different forcing scenarios, that the isopycnal changes observed between the 1960s and 2002 are best explained by internal variability. These findings, together with the start of the Argo project in the SIO area, are the foundations of this work. Argo float data provide a good estimate to fill the spatial and temporal gaps in the observational system of the ocean interior, so that low-frequency variability on basin wide

scales can be resolved. The Argo data in this study are used to resolve interannual and seasonal variability of the subtropical South Indian Ocean gyre circulation. In detail, the following questions are addressed:

- How large is the interannual and seasonal variability in the interior gyre circulation at 32°S over the 5 year period between 2002 and 2006 derived from Argo floats?
- Does the gyre strength exhibit a trend between 2002 and 2006?
- How well do the results derived at 32°S compare with those derived at 20°S?

Addressing these questions using Argo float data requires a careful preparation of the data, which is described in chapter 2, as well as supplementary datasets that have been used. Chapter 3 introduces and describes the OI algorithm, which is used to generate annual and seasonal averages of temperature and salinity, as well as reproductions of temperature and salinity of different cruise sections with different temporal resolution. Additionally, a simple method to derive subsurface velocities from a float's subsurface drift is described. In chapter 4 two methods are introduced to estimate the gyre strength at 32°S, and after selecting the appropriate method for this work, the low-frequency variability of the gyre strength at 32°S and 20°S is estimated from interpolated float data. In addition to the results based on the geostrophic and hydrostatic assumption

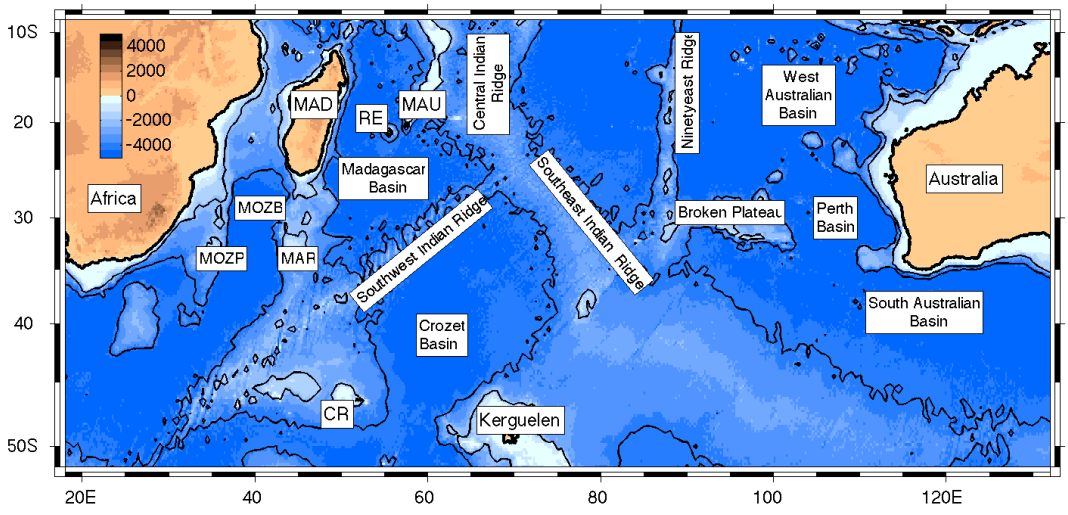

FIGURE 1.2: Map of the subtropical South Indian Ocean showing major topographic features and ocean basins. Acronyms listed are Madagascar (MAD), Reunion (RE), Mauritius (MAU), Crozet (CR), Mozambique Plateau (MOZP), Madagascar Ridge (MADR) and Mozambique Basin (MOZB). Countours indicate coastline (bold) and 2000 m and 4000 m bathymetry, respectively (thin).

using cruise data and Argo float data, the results are compared with estimates using the wind-driven circulation as well as with altimeter data. Chapter 5 contains the comparison of deep reference velocities derived from float data with those derived from an inverse calculation using the 2002 cruise data as initial fields (McDonagh et al., 2008). Additionally, seasonal and annual velocity sections at 32°S and 20°S are used to detect possible deep circulation features. In chapter 6 the interannual property changes are examined following the study of McDonagh et al. (2005). Chapter 7 contains a summary of the work with final conclusions.

The SIO has a relatively complex topography with several sub-basins, ridges and plateaus with some playing a role in the following work. Therefore, figure 1.2 gives an overview of the SIO with the location of major topographic features and their naming in this work.

Chapter 2

Data[1]

The following work is mainly based on Argo float data of the SIO (Sec 2.1). Additionally, several other datasets are used for quality control procedures of the float data (Sec. 2.1.1) and as reference and accompanyment, respectively (Sec. 2.2), to evaluate the results derived from the floats data. The following chapter describes in detail, which data are used and gives, where necessary, a detailed description of how the data are processed.

2.1 Argo float data

The Argo project is embedded in GODAE, which is a follow-on of the successful WOCE program. The goal of the Argo project is to set up and maintain a global array of active floats with a nominal resolution of $3° \times 3°$. In the first stage of the project, the objective of a global array of 3000 operational floats was set up. That goal was achieved in October 2007, while in August 2008 the number of active floats reached 3175. Now, since a continuous operational monitoring system has been established it is important to maintain the system to provide accurate data with good spatial and temporal resolution. This study gives one of many records for the important role of the Argo project in the global ocean observing system (GOOS).

Argo floats are drifting freely, typically for a period of 9 days, at a predefined pressure level in the ocean (Fig. 2.1). After that time the float descends to the predefined profiling pressure level (down to 2000 dbar) and from there ascends to the surface while

[1]Salinity in the context of this work is always given on the practical salinity scale. The practical salinity scale was defined as conductivity ratio with no units (UNESCO, 1985). Temperature in the context of this work is always used as potential temperature. The exception is section 2.1 where in-situ temperature is meant

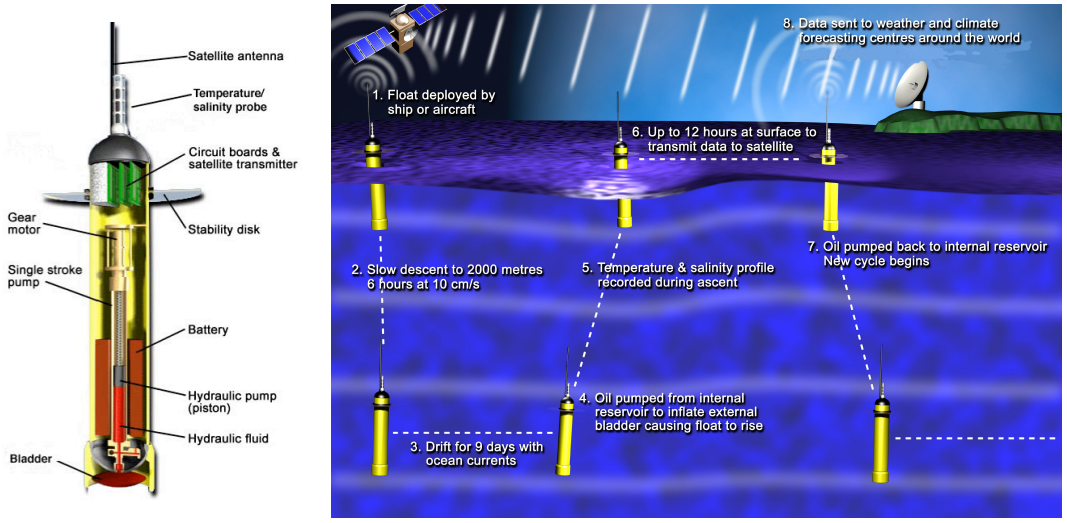

FIGURE 2.1: Schematic of an Argo float's cross-section (left) and it's operational cycle (right). Figures are taken from the Argo homepage.

the hydrographic paramters conductivity-temperature-depth (CTD) are recorded. At the surface the float transmits the previously collected data for 6 to 12 hours. After the surface period it descends again at about 10 cm s^{-1}, to the predefined parking pressure level of for example 2000 dbar. The total time used for one such cycle takes 10 days (CARVAL ET AL., 2006). The autonomous ascent (descent) of the float is accomplished by decompressing (compressing) an internal bladder (Fig. 2.1). While at the surface, nearby satellites receive data of the position of the float and the profile measurements and forward them to the operational centres. Newer technologies allow two way communication, optimising the surface period to increase battery lifetime but also to reduce surface drift and therefore errors in subsurface velocity estimates. This is possibly important for analysing export pathways in specific regions (GETZLAFF ET AL., 2006). Typically, the float data are available within 24 hours after passing a real-time quality control. More detailed information can be accessed on the Argo homepage[2] with information on new communication and sensor technologies developed within the project's framework.

The *in situ* float profile series, that have passed the standard real-time quality control checks performed by the Data Assembly Centres (DACs) were downloaded for the 5 year period 2002 to 2006 from the USGODAE Argo Global Data Assembly Centre Data Browser[3]. Note, that only a small fraction (less than 30%) of available profiles had been delayed-mode quality controlled by the DACs at the beginning of this project in

[2]http://www.argo.ucsd.edu/index.html; These data were collected and made freely available by the International Argo Project and the national programs that contribute to it. Argo is a pilot program of the Global Ocean Observing System.

[3]http://www.usgodae.org/argo/argo.html

2005, therefore a separate quality control was performed as described in section 2.1.1. The data contain the hydrographic parameters (salinity, temperature and pressure), the position and time records of the profiles and the trajectory records. The latter contains all position and time records during the surface period of the float, the predefined parking pressure level and, ideally, time stamps for each step during the floats cycle. A detailed description of the content of the freely available profile and trajectory files is given in the Argo User's manual (Carval et al., 2006).

2.1.1 Argo float delayed mode calibration

The autonomous character of the floats requires several additional steps of quality control, depending on the final purpose of the analysis. The necessity and the realisation of a thorough quality control is described in the following section. Note that besides the real-time checks which were performed by the DACs, all following quality control procedures were specifically performed for this study during the project.

Firstly, the profiles are checked for bad measurements, that are identified with the quality control flags provided by the data centre (Carval et al., 2006). Data flagged as 3, 4 or 9 are excluded. Additionally, the profiles are checked for unrealistic measurements, time and position records. In detail that means the accepted salinity range is set between 24 to 40, the in-situ temperature range is set between -2°C and 40°C and the pressure range is set below 9999 dbar. Secondly, temperature and salinity properties and salinity anomalies on isotherms of each float profile series are plotted and visually checked, to remove obvious outliers in the data. Temperature measurements from the floats that passed the Argo real-time quality control were assumed to be accurate to 0.002°C. Pressure measurements were assumed to be accurate to 2.4 dbar, though at the beginning of 2007 several SOLO[4] floats with FSI[5] CTD sensors have been identified to have incorrect pressure values. In the SIO area only one float was affected by incorrect pressure values. It was a float operated by AOML[6] with the number 3900369 and was excluded from the dataset. For the salinity measurements an additional quality control was applied, which is described in the following.

In the Argo community the DMQC algorithm described by Wong et al. (2003) is widely used and continuously improved (Böhme and Send, 2005; Owens and Wong, 2008). The software is freely available from the University of Washington's working group on Argo Floats Delayed-Mode Salinity Calibration[7]. Generally the DMQC is

[4]Sounding Oceanographic Lagrangian Observer
[5]Falmouth Scientific, Inc., MA, USA
[6]Atlantic Oceanographic and Meteorological Laboratory
[7]http://prelude.ocean.washington.edu/references.html

necessary because, due to the free drifting nature of the floats, a direct calibration of the measurements is not possible. Furthermore, only few floats can be recovered after their mission for calibration. Therefore, a system has been set up to apply a quality control to the measurements, which compares the individual float time series with a background climatology, in this work the Indian Ocean Hydrobase (IOHB) dataset (Kobayashi and Suga, 2006).

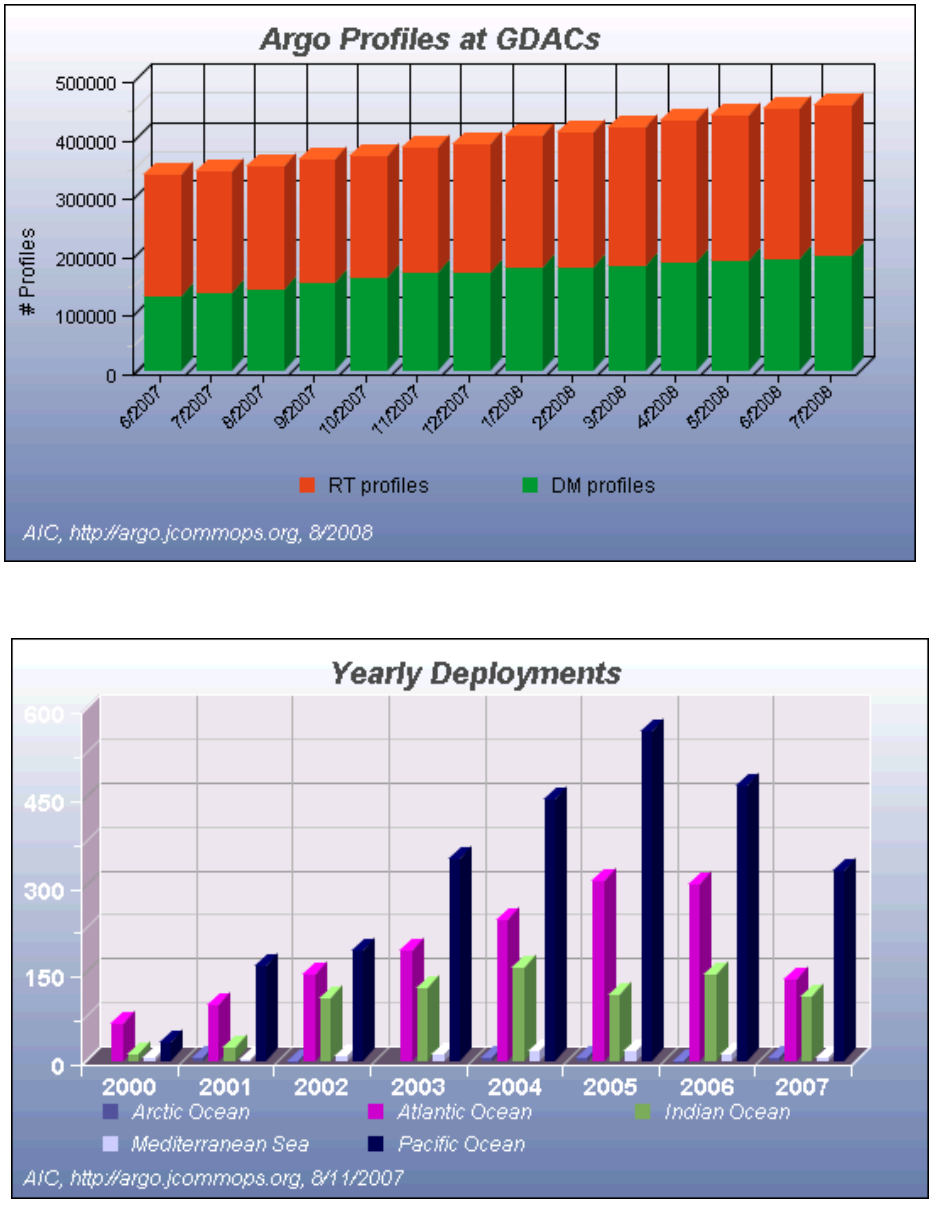

Figure 2.2: Number of total real-time (RT) and delayed-mode (DM) profiles of the Argo project available at the GDAC over the last 13 months (top). Additionally shown, is the number of yearly float deployments for the different ocean basins (bottom). Figures are taken from the monthly report from the Argo Information Centre (AIC).

The aim of the Argo project is to provide highly accurate data within 12 months including an appropriate DMQC. Especially since 2006, the Data Assembly Centres (DACs) managed to increase the number of DMQC profiles to more than 40%, while at the beginning of the project, depending on the region, only 10% to 30% of the profiles had been processed. In the SIO the Argo project started tentatively in late 1999, while at the end of 2001 only about 650 profiles were available for the 2 year period (Fig. 2.2). In early 2002 a major step towards a continuous monitoring of the ocean basins was made in the SIO, marked by the deployment of 25 floats along 32°S during the *Charles Darwin* 139 (CD139) cruise (Bryden et al., 2003a). This delay made it necessary to run a DMQC on the float data in this study by hand, to assure the high quality of the measurements and the final results.

Historical and other data used for delayed-mode quality control The quality of the historical dataset is important for an optimal DMQC. It was shown that care needs to be taken to prepare the dataset appropriately and additionally, that existing databases need modification for example because of quality reliability issues or over-sampled regions dominating the reference dataset (Kobayashi and Suga, 2006; King and Sudheer, 2006). During the 2nd Argo delayed-mode quality control workshop it was agreed to use the IOHB dataset (Kobayashi and Suga, 2006) as historical reference climatology for DMQC procedures in the Indian Ocean. Böhme and Send (2005) showed that the DMQC method relies on the availability of a dense and recent

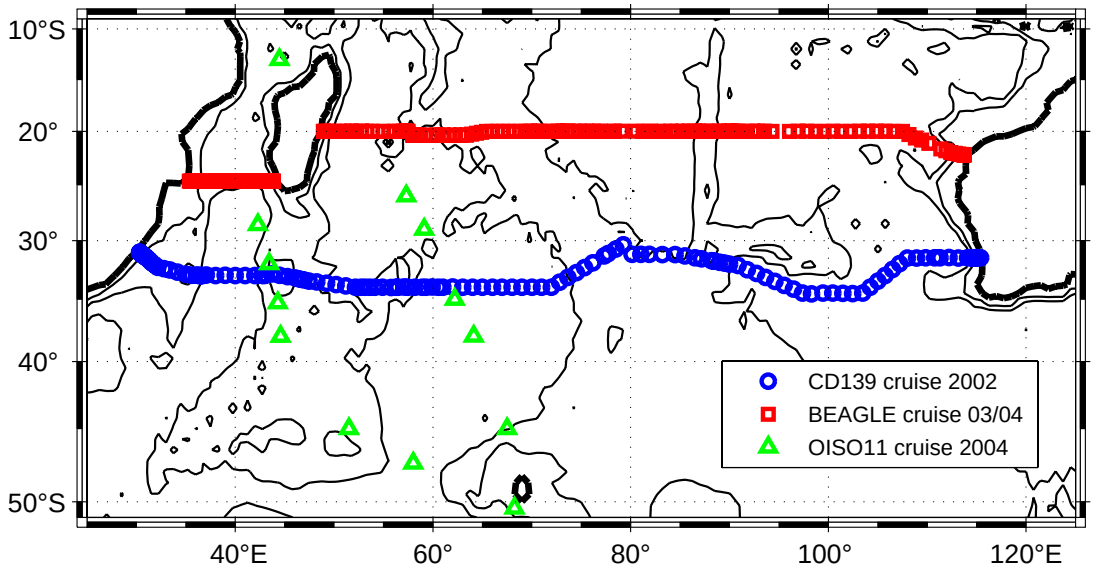

Figure 2.3: Map of the subtropical South Indian Ocean showing station positions of cruises that are added to the Indian Ocean Hydrobase, the historical dataset. Contours indicate 1900 m and 3500 m isobaths.

hydrographic dataset to provide a good representation of the temporal climate regime contemporary with the float measurements, therefore the following recent cruise data are added to the historical reference climatology (Fig. 2.3): Firstly, the data taken during R/V *Charles Darwin* 139 (CD139) cruise in early 2002 along 32°S (Bryden et al., 2003a); secondly, the data taken during the Blue Earth Global Expedition (BEAGLE) along 20°S (Uchida and Fukasawa, 2005) and finally data from a cruise in 2004 contributing to the OISO[8] project (Metz, 2008). These cruise data are processed following the instructions in a technical report (Wong, 2005a) on how to include additional data in the reference database used in the DMQC software. Therefore, the additional hydrographic data are cleaned and vertically interpolated, performing an Akima spline interpolation (Shamsundar, 1970), onto standard Θ-levels, before they are added to the reference database.

The DMQC algorithm gives weighted least squares fits and associated uncertainties of the float profiles to the background climatology. During the DMQC process a selection criterion was used to identify possible salinity sensor malfunctions. This criterion is expressed in the vertically averaged salinity additive correction term ΔS and was set to $\Delta S \geq 0.05$, representing about 3 to 4 σ (standard deviations) of the float profile salinity series compared to the historical database. This allows identification of possible sensor drift or malfunctions but also to sample the natural variability without being too much constrained by the climatology. Floats exceeding that selection criterion were subjected to further analysis, which means a visual inspection of the affected individual profiles. The selected criterion here, $\Delta S \geq 0.05$, was chosen in the beginning of the delayed-mode quality control (DMQC) procedure to be able to attribute an uncertainty to the transport estimates derived from the float profiles. The idea behind that criterion was, that with an offset of 0.05 psu in salinity, applied to the whole profile at one of the end points used to estimate the maximum transport difference between 35°E and 110°E at 32°S, for example from CD139 cruise data, the estimated transport would increase by 7.5 Sv ($1\,\mathrm{Sv} = 10^6\ \mathrm{m^3\,s^{-1}}$). The averaged error contribution, induced by the ΔS criterion, could be reduced by the number of independant profiles, which is set to 100 in the later Optimal Interpolation (OI) described in section 3.1. That would reduce the average transport error of the $\Delta S \geq 0.05$ criterion to ± 0.8 Sv, using the end point method. With a regression applied the transport uncertainties would reduce to less than ± 0.1 Sv and could then be neglected. A detailed visual inspection of the profile series during the DMQC process showed that the final set of float series, that passed the DMQC, did not differ from the weighted least squares fits (Wong et al., 2003) by more than the 2 x estimation uncertainties ($\Delta S \geq 2\sigma$).

[8] Océan Indien Service d'Observation (www.ipsl.jussieu.fr/services/Observations/fr/OISO.htm)

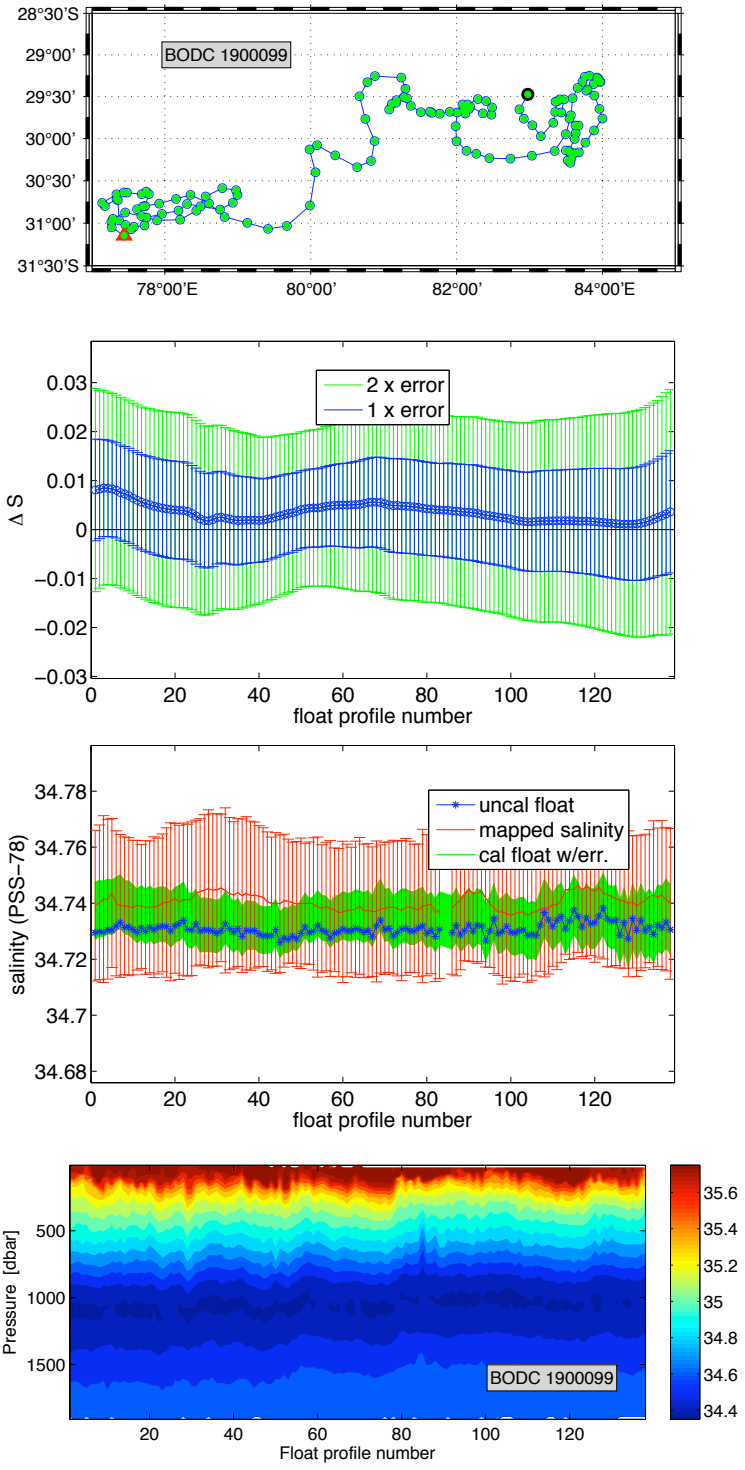

FIGURE 2.4: Plots from float 1900099 (operated by BODC) active from April 2002 to January 2006. The profile positions are shown (1st panel) with the first (red triangle) and last (black circle) profile marked but also those assumed to be good (green). From delayed-mode quality control procedure, the vertically averaged salinity additive corretion term (ΔS) is shown with errors of $1\,\sigma$ and $2\,\sigma$ from least squares fits (2nd panel) as well as the salinities with errors on θ=9.5°C, the isotherm with the smallest salinity variance (3rd panel). Finally shown, the salinity series from the float assumed to be good (4th panel).

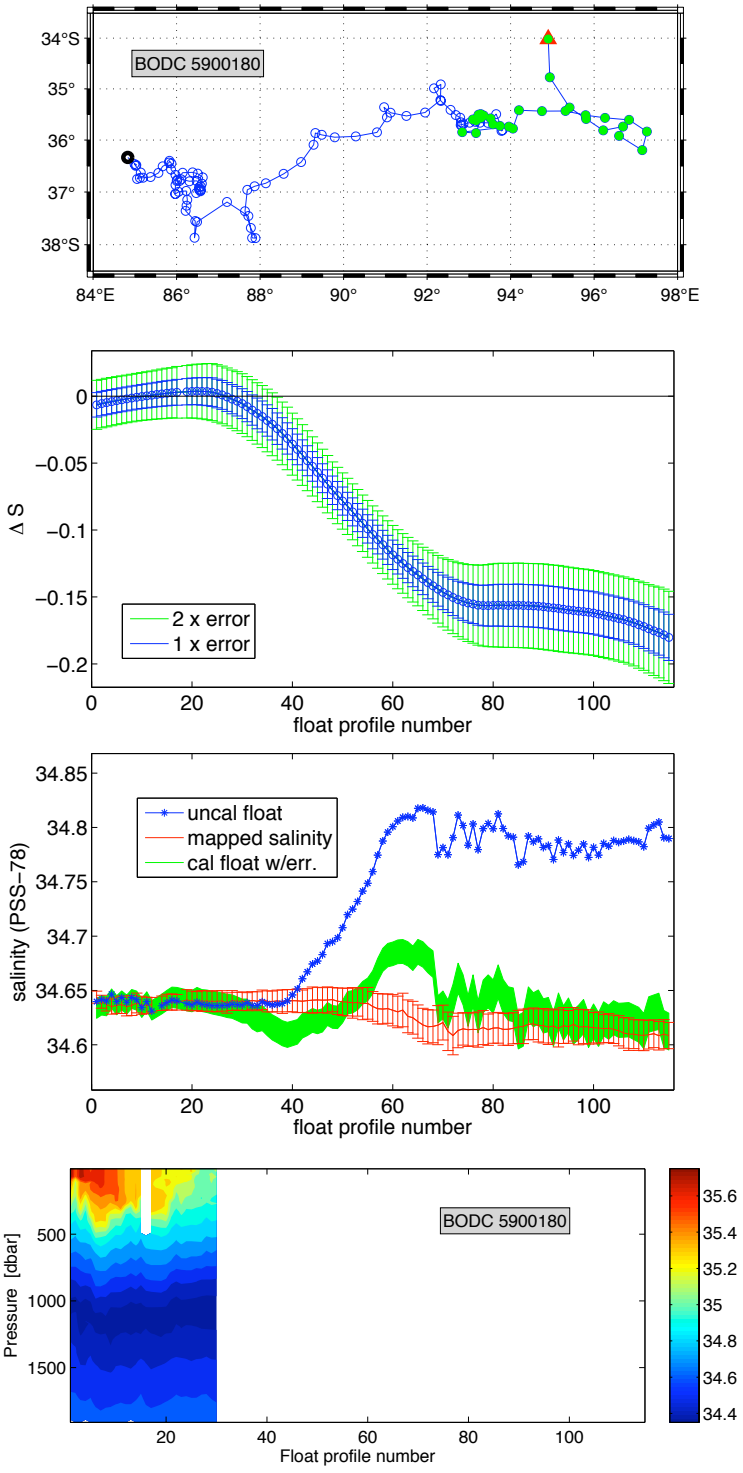

FIGURE 2.5: Plots from float 5900180 (operated by BODC) active from April 2002 to May 2005. The profile positions are shown (1st panel) with the first (red triangle) and last (black circle) profile marked but also those assumed to be good (green). From delayed-mode quality control procedure, the vertically averaged salinity additive corretion term (ΔS) is shown with errors of $1\,\sigma$ and $2\,\sigma$ from least squares fits (2nd panel) as well as, the salinities with errors on θ=2.6°C, the isotherm with the smallest mapping error (3rd panel). Finally shown, the full salinity series from the float assumed to be good (4th panel).

In the following example, two floats are presented, one without any sensor malfunction (BODC[9] 1900099) and one with profiles that needed to be rejected due to sensor malfunction (BODC 5900180). The first example (Fig. 2.4) for a float with high accuracy profiles, shows small deviations of less than 1 standard deviation (σ) in the vertically averaged salinity additive correction term ΔS derived from the least squares fits compared with the background climatology. Over the 4 year period it has collected more than 130 profiles all within an area of 10° longitude and 3° latitude in the interior of the SIO. Note that the 3 to 4 standard deviations in the vertically averaged salinity additive correction term is $\Delta S \approx 0.05$. The second example (Fig. 2.5) shows a profile series that is erroneous indicated by large deviations in the vertically averaged salinity additive correction term ΔS, which is estimated in the least squares fits. From profile number 40 the float measurements of the salinity at θ=2.6°C (at about 1900 dbar) exceeds the salinity estimated from the DMQC algorithm, which suggest a vertically averaged salinity correction of more than 0.15 for profiles at the end of the series. This jump-like increase in salinity of more than 0.15 within a period of about 200 days is a very good indication for a salinity sensor malfunction. The area covered by the float profiles is in the close vicinity of the CD139 cruise data from 2002, which are included in the historical database. The drift in the salinity sensor seems to have started in the beginning of 2003 and ended around April 2004. On the one hand, this period is too long that the change in salinity could be attributed to eddy activity. On the other hand, the difference of 2 years between the float profiles and the CD139 cruise seems to be too short to reasonably see such a large increase in salinity. Furthermore there is the fact that none of the floats nearby, within a couple of months and within 5° latitude and 10° longitude (e. g. BODC_5900178, BODC_5900179 and BODC_5900182), show any similar tendencies during the DMQC procedure. Hence only the first 30 profiles are used, while the other 84 are excluded from the analysis.

The 375 floats operating in the SIO between 2002 and 2006 have collected 23572 profiles. The above described DMQC rejected about 11% of the profiles leaving a total of 20916 profiles. As pointed out previously, only few floats operated in the SIO before 2002, while at the end of the 5 year period more than 600 profiles are available every month with still increasing tendency (Fig. 2.6). The difference in the monthly number of rejected profiles between our DMQC and the Global Data Assembly Centre (GDAC) holdings is mainly due to a delay in processing of the RT data becoming apparent at the end of 2004 (Fig. 2.6 and 2.2).

Generally, the finally selected profiles show a good spatial coverage of the SIO for the whole 5 year period (Fig. 2.7). Only between 60°E to 80°E and 31°S to 27°S, where

[9]British Oceanographic Data Centre

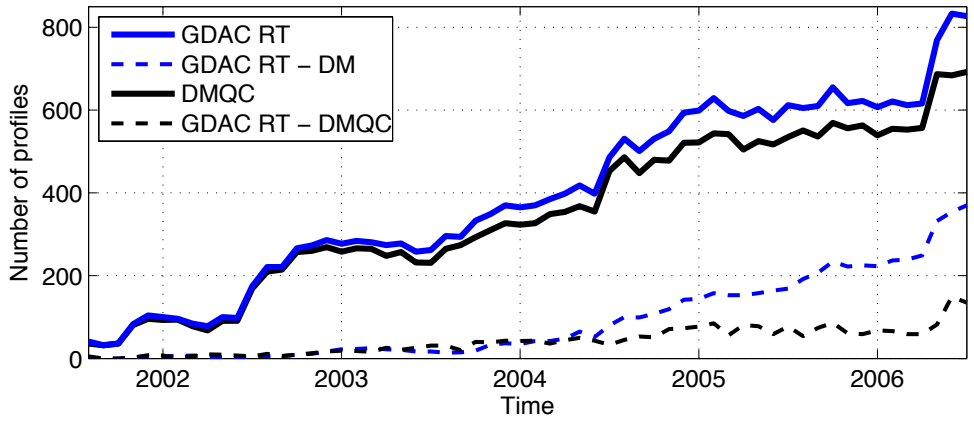

FIGURE 2.6: Time series of monthly number of Argo profiles in the subtropical South Indian Ocean (50°S to 10°S and 25°E to 125°E) from 2002 to 2006. Showing either real-time (RT) profiles available from the GDACs (bold blue) or the delayed-mode quality control profiles in this study (bold black). Additionally shown is the difference in the numbers between available RT and delayed-mode (DM) data at the GDACs (dashed blue) as well as between available RT data and the delayed-mode quality control data used in this study (dashed black).

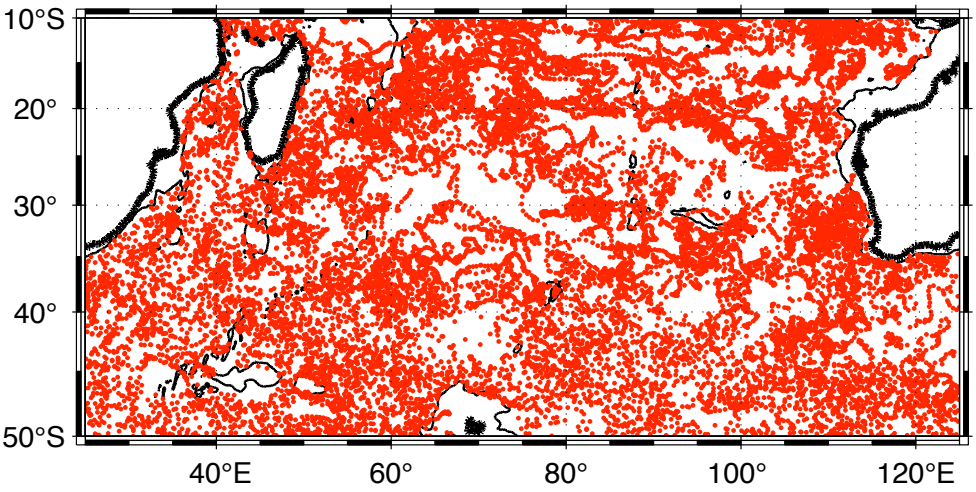

FIGURE 2.7: Map of the subtropical South Indian Ocean showing the position of the delayed-mode quality controlled Argo profiles (red), which are used in this study for the period January 2002 to December 2006. Black contours highlight coastline (bold) and 1900 m isobaths (thin).

the *Southwest Indian Ridge* and the *Southeast Indian Ridge* join, very sparse coverage exists. That gives the impression that these deep topographic features influence the general circulation of the upper waters in that area constraining a direct flow across the ridges from the separated basins (e. g. from the Crozet Basin to the Madagascar Basin or from the Crozet Basin to the *Mid-Indian Ocean Basin*).

2.1.2 Accuracy of delayed-mode quality control data

The accuracy of the quality controlled salinity measurements is estimated at 32°S following the approach used by Wong (2005b) who analysed Subantarctic Mode Water (SAMW) and Antarctic Intermediate Water (AAIW) properties and their distribution from Argo float measurements in the subtropical SIO (30°E - 120°E; 55°S - 15°S) averaged over the period 2000 and 2004. The estimates for the present study are based on time series of optimally interpolated float data using a moving 12 month period every 6 months at 32°S. The OI groups the profiles according to the length scales applied. The scales as well as the mapping itself are later used for the analysis of the data. This approach also gives an appropriate noise estimate. The OI scheme and the procedure to select appropriate decorrelation length scales are described in detail in chapter 3.

The estimated noise level in salinity is generally smaller than 0.04 for the time series at 32°S (compared to 0.008 reported by Wong (2005b). The noise level is estimated from the minimum noise variance on 4 isotherms (Θ = 11.7°C, 10°C, 9.5°C and 9°C). These four isotherms are selected because the tightest part of the Θ-S relationship in the SIO is between 9°C and 12°C (Wong, 2005b). Since the Argo float data used

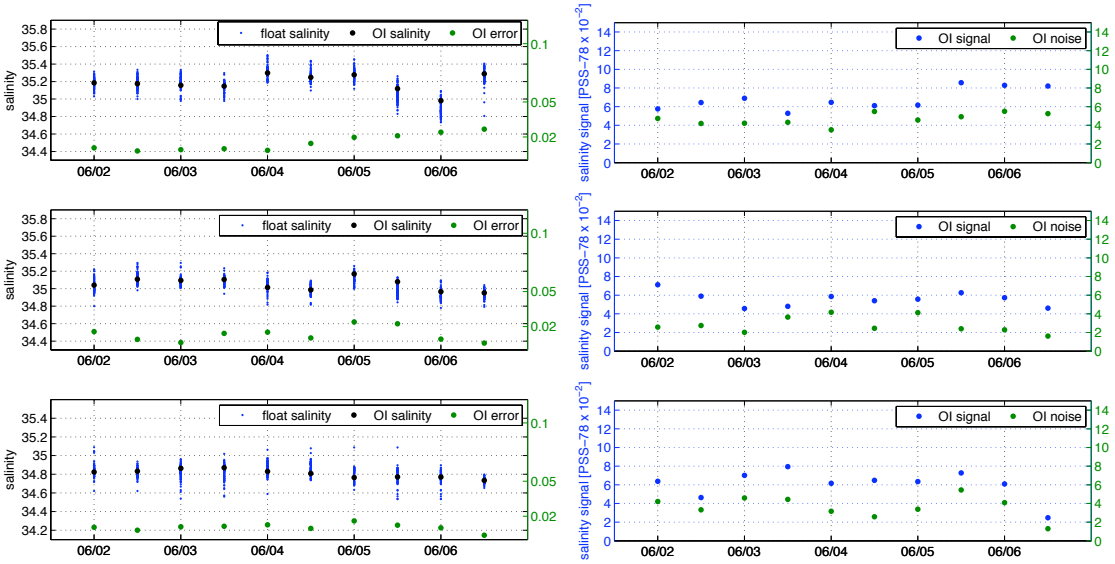

Figure 2.8: Left column: Time series of the final salinity estimate (black) and the associated error (green) given by the Optimal Interpolation, as well as the salinity from individual float profiles (blue) that are taken into account. Right column: Signal ($s = \sqrt{1/N \sum_i (S_i - \bar{S})^2}$; blue) and noise ($\eta = \sqrt{1/2N \sum_i (S_i - S_k)^2}$; green) estimated from the OI on the isotherm with smallest noise level, as described by Wong (2005b). Shown are time series at 32°S taken at three different longitudes, at 50°E (top), 75°E (middle) and 95° (bottom). For details of the Optimal Interpolation including the signal and noise estimates, please refer to chapter 3.1

in this study are interpolated onto 20 dbar levels, the nearest pressure level to these isotherms is selected. The large noise estimate mainly results from interpolation and averaging on isobars and from the averaging period of 12 months. In contrast, (Wong, 2005b) estimated the noise level from profiles grouped together within 10° x 5° boxes by averaging on isotherms for the 4 year period 2000 to 2004. Testing with a larger mapping period of 24 months gives smaller salinity noise estimates but still of the order of O(0.02). It is concluded that the final accuracy of the salinity measurements here is about 0.04, which is mainly attributed to the here described large noise estimate.

2.2 Additional datasets used for evaluation

In addition to the previously mentioned float dataset and the accompanying historical dataset to be used for the DMQC, several other data are used for evaluation and comparison. These are listed and described briefly in the following.

Hydrographic data: It was mentioned previously that recent hydrographic data are added to the historical database. These are then also partly used for comparison with results from the analysis of the float data (Chapter 4.1.3 and 4.2.3) but also to estimate decorrelation length scales (Tab. 2.1, Chapter 3.1.1). In the following it is described how the data are processed for our purposes. Parts of the WOCE I08S/I09S (McCartney, 1998) and WOCE I09N (Gordon, 1997) sections occupied in late 1994 and early 1995 are used to estimate meridional decorrelation length scales. Therefore, the appropriate stations along 95°E between 50°S and 10°S are selected and bin-averaged into 20 dbar bins. The high resolution 32°S Indian Ocean transect hydrographic data taken during CD29 in November and December 1987 (Toole and Warren, 1993) and during CD139 in March and April 2002 (Bryden et al., 2003a) are used to estimate decorrelation length scales but also for direct comparison with

Table 2.1: List of additional hydrographic datasets used to estimate decorrelation length scales but also for direct comparison with float realisations.

Dataset	Region	Date
WOA01	globally 1° x 1°	climatology up to 2001
WOCE I08S/I09S	95°E meridional section	12/1994 to 01/2005
WOCE I09N	95°E meridional section	01/1995 to 03/1995
CD29	32°S zonal section	11/1987 to 12/1987
CD139	32°S zonal section	03/2002 to 04/2002
BEAGLE	20°S zonal section	12/2003 to 01/2004

the float realisations. The temperature and salinity data are bin-averaged into 20 dbar bins to remove high-wavenumber noise and to produce a uniform grid in accordance to the float data. These data have been recently analysed and discussed in the context of decadal changes in ocean water mass properties and gyre circulation in the South Indian Ocean (Bryden et al., 2003b; Palmer et al., 2004; McDonagh et al., 2005, 2008). Additionally the 20°S Indian Ocean transect hydrographic data taken during the BEAGLE cruise in December 2003 and January 2004 (Uchida and Fukasawa, 2005) are used and processed in a similar way as the 32°S data.

Essential for the later analysis is the fact that a climatology is used as reference field during the Optimal Interpolation (Chapter 3.1). Here we used the WOA01 dataset, which we interpolated onto a vertical 20 dbar grid by linear interpolation. In the early stage of this study an updated version, the World Ocean Atlas 2005 (WOA05) was published. Nevertheless, for our analysis the new version would not be helpful because some of the recent cruise data have been included. Furthermore, the main source of profiling float data included was the Argo project (Johnson et al., 2006; Locarnini et al., 2006). Since the historical data coverage in the study area is generally relatively spare such inclusions would have caused a bias towards the recent cruise and float data.

Wind stress data: Monthly means of zonal (τ_x) and meridional momentum flux (τ_y) for the 59 year period 1948-2007 were obtained from the NCEP-NCAR Reanalysis Project CDAS-I[10] (Kalnay et al., 1996; Kistler et al., 2001) available from the Data Library maintained by the International Research Institute for Climate and Society[11]. These data are given on a Gaussian grid, with 1.875° x 1° horizontal resolution. Time series of Sverdrup transport across 20°S and 32°S were computed using the vertical component of the wind-stress curl ($curl_z(\tau_\eta)$, see equation 4.6) averaged over a 6° latitudinal band centred around 20°S and 32°S, respectively. Following the decomposition of the total mass transport in the wind-driven layer into Ekman (M_{yE}) and geostrophic (M_{yg}) component (Eq. 4.7) we derive geostrophic Sverdrup transport across 20°S and 32°S, respectively. The data are low-pass filtered with a 1-year second-order Butterworth filter (Butterworth, 1930) to reduce the high-frequency noise in the data.

[10] Climate Data Assimilation System I from NCEP-NCAR Reanalysis Project
[11] http://ingrid.ldeo.columbia.edu/SOURCES/.NOAA/.NCEP-NCAR/.CDAS-1

Satellite altimetric data: Merged altimetric data from Ssalto[12]/Duacs[13] multimission altimeter products are used, which are freely available from Aviso[14]. The multimission products use Topex[15]/Poseidon, Jason-1[16], ERS-1[17] and Envisat[18] data with the same ground track. Gridded high-resolution ($1/3° \times 1/3°$, Mercator grid) weekly averaged sea level anomalies are downloaded. The anomalies are computed with respect to the 1993-1999 seven-year mean (Dibarboure et al., 2008). Additionally, absolute dynamic topography (ADT) was downloaded with the same spatial and temporal resolution. Dynamic topography is sea surface height above the geoid and is here expressed as the sum of the sea level anomaly (SLA) and the mean dynamic topography, determined from 7 years of altimetric data (TOPEX and ERS1,2), taken from the Rio05[19] dataset (Rio and Hernandez, 2005; Rio et al., 2005; Dibarboure et al., 2008). The global weekly averages were used to generate monthly, seasonal and annual means for the SIO area by appropriate averaging. Additionally, time series of SLA and ADT are generated, averaged over a 5° latitudinal band centred around 20°S and 32°S, respectively, and filtered with a 3 months and 5° longitude moving average.

[12] Segment Sol multimissions d'ALTimétrie, d'Orbitographie et de localisation précise
[13] Data Unification and Altimeter Combination System
[14] Archiving, Validation and Interpretation of Satellite Oceanographic data
[15] Ocean TOPography Experiment
[16] Jason-1 was launched on December 7, 2001 as follow-on of Topex/Poseidon
[17] European Remote Sensing satellite
[18] ENVIronmental SATellite
[19] http://www.aviso.oceanobs.com/en/data/products/auxiliary-products/mdt/description-rio05/index.html

Chapter 3

Method

Argo floats are passively advected, at any given time after their deployment their distribution is determined only by the existing velocity and eddy field. For the later analysis of geostrophic velocity and transport fields, derived from the float data, an interpolation on regular grids or exact station positions is needed. It is beyond the scope of this work to evaluate all the possible techniques to generate regularly gridded fields from Argo data (e. g. averaging on isopycnal surfaces (Ridgway and Dunn, 2007), objective analysis (Gille, 2003) or local regression (Thacker, 2008)). The Optimal Interpolation (OI) method used in this study was selected because it finds successful appliance in the DMQC procedure (Wong et al., 2003; Böhme and Send, 2005; Owens and Wong, 2008) and it has been used in several studies analysing Argo float data (e. g. Guinehut et al. (2002); Wong (2005b); Hadfield et al. (2007); Roemmich et al. (2007)).

This chapter firstly contains a description of the applied OI, including a description of the estimation of the decorrelation length scales of the subtropical SIO, which are necessary for the OI. Secondly, the accuracy of the method is then tested by comparing float realisations interpolated onto CTD station positions with CTD profiles from existing cruise tracks that have been taken within the period 2002 to 2006. Finally, at the end of the chapter, a simple method to estimate reference velocities from the subsurface drift of the floats at their parking pressure level is described.

3.1 The optimal interpolation Algorithm

The selected OI algorithm first introduced by Gandin (1963), based on the *Gauss-Markov* theorem, gives an unbiased pointwise estimate. It is optimal in the least squares

sense and additionally provides an estimate of the error variance by taking the distribution of the used data into account. It is described in detail in several publications (Bretherton et al., 1976; McIntosh, 1990; Wong et al., 2003; Böhme and Send, 2005).

This method requires knowledge about the structure of the mean field, therefore, the WOA01 (Stephens et al., 2002; Boyer et al., 2002) has been used as first-guess background climatology representing the mean field. Furthermore, knowledge about the correlation structure of the field is required to successfully apply the OI. The spatial decorrelation length scales are used to define a weighting factor for the individual data points taken into account. In the following subsections a detailed explanation is given of how the decorrelation length scales have been estimated and which data have been used, while the description of the OI continues in section 3.1.2.

3.1.1 Estimating decorrelation length scales

The OI uses a background climatology and therefore the decorrelation length scales are calculated from variance analysis of temperature and salinity residuals either between cruise data (Fig. 3.1) and the WOA01 climatology or between delayed-mode quality controlled Argo float data (Fig. 3.6) and the WOA01 climatology. In both cases the

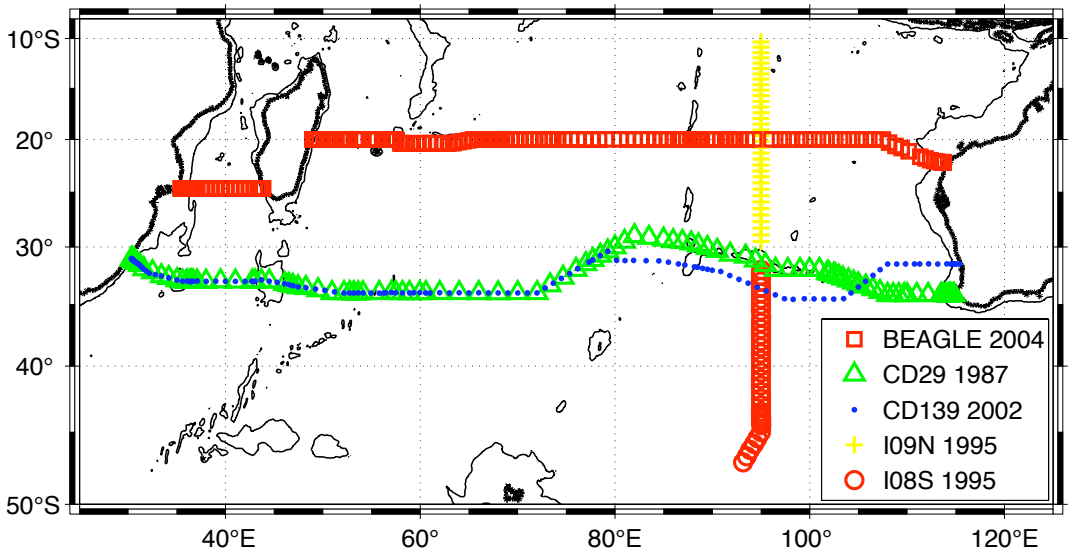

Figure 3.1: Tracks from different cruises in the subtropical South Indian Ocean. The longitudinal transects are the BEAGLE cruise along 20°S taken in 2003/2004 (red squares), the *Charles Darwin* CD29 cruise in 1987 along 32°S (green triangles) and the *Charles Darwin* CD139 cruise in 2002 along 32°S (blue dots). The meridional sections are part of the cruise track from WOCE section I09N taken in early 1995 (yellow crosses) and part of the cruise track from WOCE I08S section taken in 1994/1995 (red circles). Contours indicate coastline (bold) and 2000 m isobath (thin).

datasets are resampled by using the nearest grid point of the WOA01 climatology to the CTD-station or float profile position as estimate for temperature and salinity. The so derived "climatological" sections or datasets are then subtracted from the original cruise data and the float dataset to get the final residual fields. These datasets of residuals are then used for the further analysis of the decorrelation length scales. The scales estimated here provide the first order large-scale spatial decorrelation scales on time scales of one to 5 years.

It was shown by (Haines et al., 2006) that decorrelation length scales, estimated over large regions of the globe, mainly in the midlatitudes and lower latitudes, are often larger if they are estimated for salinity on isotherms $S(T)$ than at a particular depth $S(z)$. Haines et al. (2006) point out, that this is because the $S(T)$ relationship is less influenced by mesoscale eddies as well as gravity and inertial oscillations. Additionally they showed that the dominant temporal variability in $S(T)$ occurs on a longer time scale than the dominant variability in $S(z)$. However, in this work spatial decorrelation length scales are estimated on pressure surfaces, to be used in the OI algorithm to interpolate float profile data on pressure surfaces on a regular one-degree spacing grid, which is similar to some of the analysis of the gyre circulation in the subtropical South Pacific by Roemmich et al. (2007). These gridded salinity and temperature fields are then used to calculate geostrophic velocities, transports and dynamic height, therefore the final gridded fields are on pressure surfaces. Although for the assesment of property changes mapping on isotherms would prevent property changes being diluted by the mapping.

Decorrelation length scales estimated from cruise data: The zonal cruise tracks are divided in two subsections. A western subsection from the African coast (30°E) to the *Madagascar Ridge* and to *Madagascar* respectively (45°E), the eastern subsection from 45°E to the Australian coast. The decision to split the whole zonal section into 2 subsections follows the given separation provided by *Madagascar* that forms a natural barrier from 15°S to 25°S between the interior of the ocean and the boundary region. Further south, this separation can be thought to be continued by several topographic features like the *Mozambique Ridge* (35°E, 34°S, 1800 m depth), the *Madagascar Ridge* (45°E, 34°S, 800 m depth), the *Crozet Plateau* (50°E, 46°S) and the *Western Indian Ridge* extending from south west at 35°E, 45°S to north east at 43°E, 40°S up to 1900 m depth.

For each of the subsections the distance between the CTD-stations is calculated. Then the whole length of the subsection evenly divided into 200 stations gives the horizontal grid used for the following analysis of the decorrelation length scales. The

grid gives a station spacing of about 8 km on the western and about 35 km on the eastern subsection respectively. This is 2 to 4 times smaller than the average spacing of the original stations, which is about 35 km on the western subsection and about 75 km on the eastern subsection. The salinity and temperature anomalies are linearly interpolated onto the new horizontal grid for each pressure level. Finally, the autocorrelation R is calculated for salinity and temperature simply as the correlation of the signal against a space shifted version of itself, following the formulation in Eq. 3.1 and Eq. 3.2,

$$R_{xx} = \frac{K_{xx}}{\sigma^2} \tag{3.1}$$

$$K(x_1, x_2) = \sum (x_1 - \mu_1)(x_2 - \mu_2) \tag{3.2}$$

where K is the autocovariance and σ^2 the variance of the signal x. While x_1, μ_1 and x_2, μ_2 indicate different space shifted versions of the signal with the associated mean. The decorrelation length scales are operationally defined as the distance of the point with $R \leq e^{-3}$, fulfilled for the first time in the auto-correlation function. The estimated decorrelation length scale for temperature and salinity on each pressure level is then shown as a vertical profile for each subsection, together with their temperature and salinity anomaly section, to find a few uniform length scales to use in the OI (Fig. 3.2 , 3.3 , 3.4 , 3.5 , 3.8 , 3.9 and 3.10).

Zonal decorrelation length scales estimated from cruise data: There exist large variations in these derived zonal decorrelation length scales (Lx_W, Lx_E), especially in the eastern subsection, between the BEAGLE cruise along 20°S taken in 2003/2004 and the CD29 and CD139 cruises along 32°S taken in 1987 and 2002, respectively (Fig. 3.2 , 3.3 and 3.4).

First, at 20°S there exists less vertical structure in the zonal scales (Lx_W, Lx_E) compared to 32°S, especially in the eastern subsection between 45°E and 115°E. This becomes apparent not only in the vertical profiles of the spatial decorrelation length scales for salinity and temperature but also in their anomalies sections (right panels of Fig. 3.2, Fig. 3.3 and Fig. 3.4). At 20°S the largest scales ($Lx_E \geq 1200$ km) can be found for salinity between 400 dbar and 500 dbar and between 800 dbar and 1000 dbar (Fig. 3.2 bottom right). These horizons are occupied by the high-salinity layer of Subtropical Surface Waters (Wyrtki, 1973) between 100 m and 400 m (Warren, 1981) and on depth between 500 m and 1200 m characterised by the salinity minimum of the AAIW (Warren, 1981). Shallower at about 700 dbar a minimum in the length

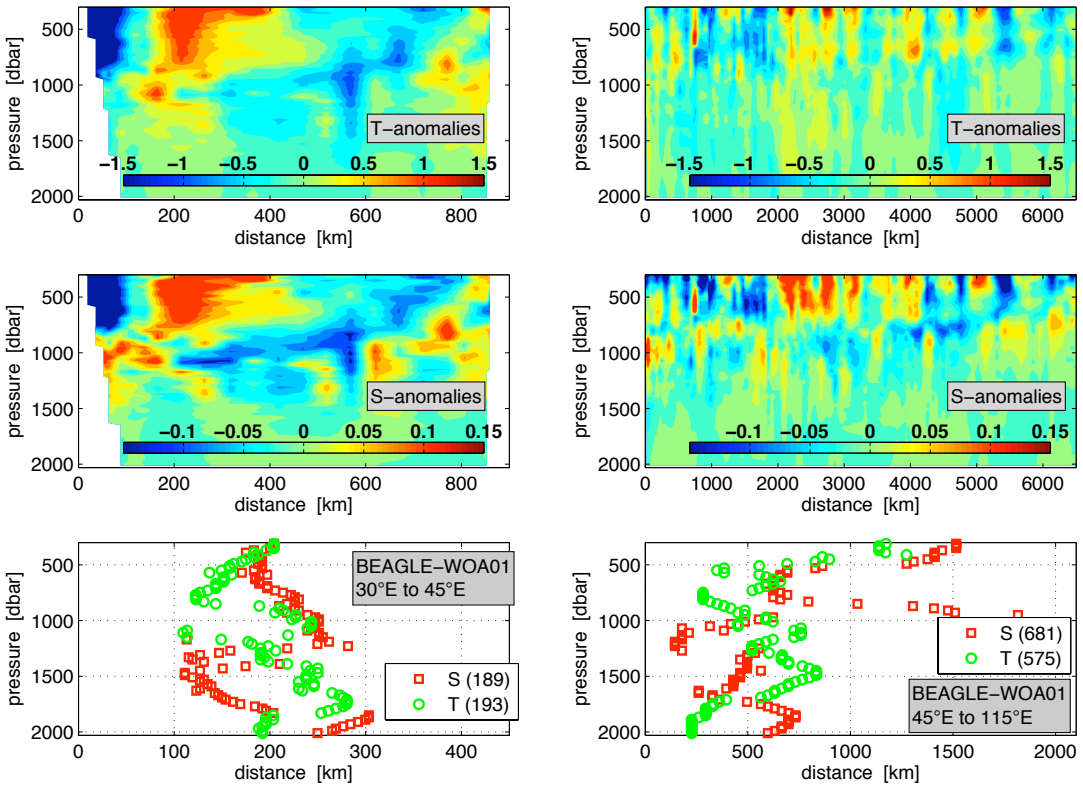

FIGURE 3.2: *Top and middel:* Sections of anomalies (BEAGLE cruise minus WOA01) of temperature (top) and salinity (middle) on pressure levels along the BEAGLE cruise track taken in 2003/2004 at 20°S with the western subsection from 30°E to 45°E (left) and the eastern subsection from 45°E to 115°E (right). *Bottom:* Vertical profiles of zonal decorrelation length scales for salinity (red) and potential temperature (green) estimated on pressure levels along the BEAGLE cruise track taken in 2003/2004 at 20°S with the western subsection (left) and the eastern subsection (right).

scales for temperature and salinity can be found associated with the transition between SAMW and AAIW. Additionally, the westward deepening of isopycnals and also the location of the core of the SAMW can bias the estimate on pressure levels. In the western subsection at 20°S two large patches of negative and positive anomalies in temperature and salinity exist at the western end of the subsection (Fig. 3.2 left column, 1st and 2nd panel). These patches could result from a mesoscale eddy or recirculation at the southern exit of the *Mozambique Channel* that was crossed during the BEAGLE cruise (Fig. 3.1). The scales for temperature and salinity are centred around 200 km but varying by up to ±100 km at around 750 dbar and below 1500 dbar. The scales for salinity show an increase to almost 250 km from the surface to about 1200 dbar. There exists a drop in the length scales to about $Lx_W = 120$ km but finally increasing to $Lx_W = 250$ km at 2000 dbar. For temperature, the estimated scales decrease in the beginning from 200 km to 120 km at 800 dbar. At 1150 dbar a second minimum exists with $Lx_W = 120$ km, while for the rest of the vertical below 1000 dbar

the scales range between 180 km and 280 km.

At 32°S the estimated length scales show much more vertical coherence than at 20°S (Fig. 3.3 and Fig. 3.4). In the western subsection the majority of the length scales estimated for salinity and temperature range between 100 km and 200 km. In the CD29 data from 1987 at 32°S (Fig. 3.3, left column) some local maxima can be found around 970 dbar, around 1350 dbar and around 1850 dbar but with different magnitudes for salinity and temperature. In the CD139 data from 2002 (Fig. 3.4, left column), the bandwidth of the majority of length scales is even more narrowed but still exhibits local maxima around 970 dbar, 1400 dbar and 1700 dbar, respectively. In the eastern subsection at 32°S (Fig. 3.4, right column), the analysis of the CD139 data taken in 2002 shows again a very tight vertical structure, for both temperature and salinity, with minima of about 180 km between 450 dbar and 950 dbar. This minimum might result from the distribution of two different modes of SAMW between 45°E and 115°E (McDonagh et al., 2005; Bryden et al., 2003b), which comes along with

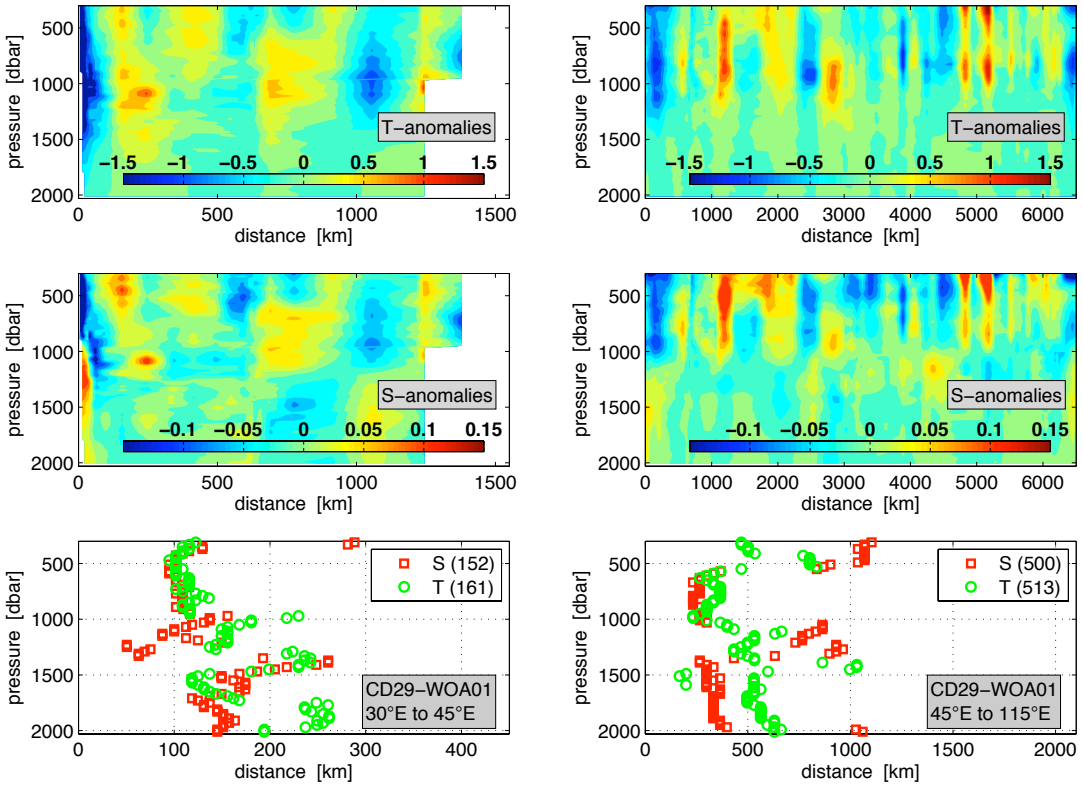

Figure 3.3: *Top and middel:* Sections of anomalies (CD29 cruise minus WOA01) of temperature (top) and salinity (middle) on pressure levels along the CD29 cruise track at 32°S taken in 1987 with the western subsection from 30°E to 45°E (left) and the eastern subsection from 45°E to 115°E (right). *Bottom:* Vertical profiles of zonal decorrelation length scales for salinity (red) and potential temperature (green) estimated on pressure levels along the CD29 cruise track at 32°S taken in 1987 with the western subsection (left) and the eastern subsection (right).

a large east-west gradient in salinity. The local maximum of $Lx_E = 500$ km in the scales of salinity and temperature at 1000 dbar might result from the distribution of the AAIW along that pressure horizon. At 2000 dbar a similar maximum exists in the length scales estimated from salinity. Below 1000 dbar the majority of the scales ranges between 250 km and 500 km. The analysis of the data from the eastern subsection of the CD29 cruise at 32°S (Fig. 3.3, right column) taken in 1987 show broadly the same vertical structure of the length scales but with a tendency to larger values at pressure levels of the maxima. The minimum associated with the SAMW is identifiable between 600 dbar and 950 dbar with a length scale of $Lx_E = 350$ km. The maximum at 1000 dbar is deepened and broadened between 1050 dbar and 1350 dbar with values of $Lx_E \geq 750$ km. The fact that the scales estimated from the 2002 data tend to be smaller might be due to at least two strong small scale features at 75°E and 104°E, with a vertical displacement of the isopycnals below 300 dbar by more than 150 dbar in the 2002 section (Palmer et al., 2004). Additionally, significant differences have

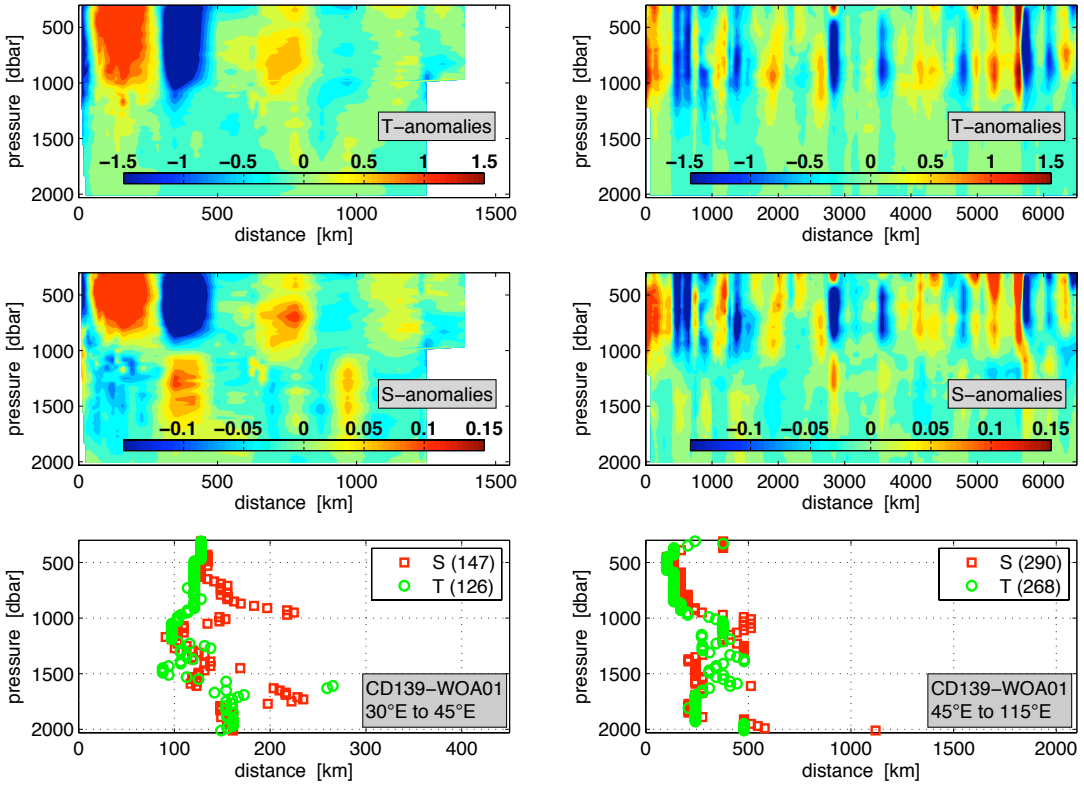

Figure 3.4: *Top and middel:* Sections of anomalies (CD139 cruise minus WOA01) of temperature (top) and salinity (middle) on pressure levels along the CD139 cruise track at 32°S taken in 2002 with the western subsection from 30°E to 45°E (left) and the eastern subsection from 45°E to 115°E (right). *Bottom:* Vertical profiles of zonal decorrelation length scales for salinity (red) and potential temperature (green) estimated on pressure levels along the CD139 cruise track at 32°S taken in 2002 with the western subsection (left) and the eastern subsection (right).

been found in the thermocline properties comparing those two sections along 32°S (McDonagh et al., 2005). Furthermore, the different sampling periods, CD29 in 1987 during austral spring and CD139 in 2002 during autumn, could have an affect on the estimates of length scales at least in the near-surface layers.

Meridional decorrelation length scales estimated from cruise data: For the meridional cruise sections along 90°E the estimation of the decorrelation length scales (Ly) follows the description as given in the beginning of section 3.1.1 including equation 3.1 and 3.2. The meridional cruise sections along 90°E have been taken during two different cruises in 1994/1995 but within a total time period of 4 months. Therefore, the meridional decorrelation length scale (Ly) has been estimated for the whole section as well as for the separate cruise sections, also shown are the temperature and salinity anomalies (Fig. 3.5).

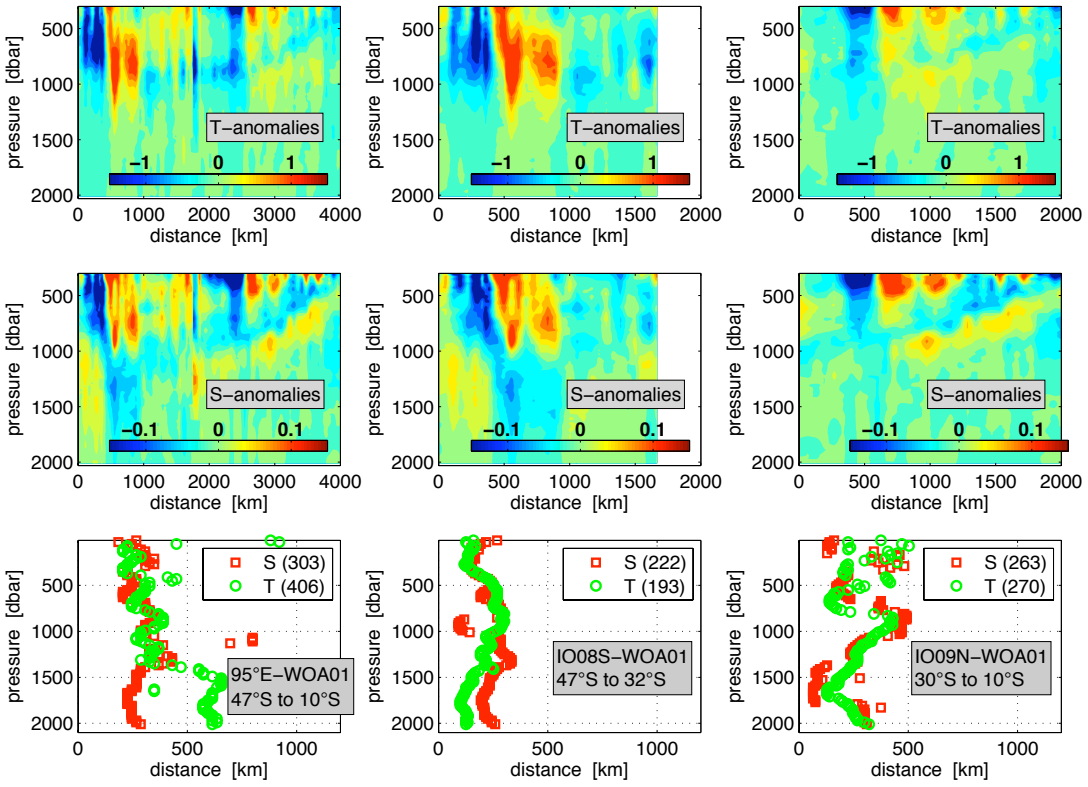

Figure 3.5: *Top and middel:* Sections of anomalies (Cruise minus WOA01) of temperature (top) and salinity (middle) on pressure levels along 95°E between 47°S and 10°S (left) and parts of the I08S cruise track between 47°S and 32°S (middle) and the I09N cruise track between 32°S and 10°S (right). *Bottom:* Vertical profiles of meridional decorrelation length scales for salinity (red) and potential temperature (green) estimated on pressure levels along 95°E (left) and parts of the I08S (middle) and I09N (right) cruise tracks.

The scales (Ly) estimated from salinity residuals for the whole section (Fig. 3.5 left) seem to be similar, both in magnitude and structure with the salinity scales estimated only from the southern part of the section between 47°S and 32°S (Fig. 3.5 middle). Only the maximum of $Ly = 800$ km around 1000 dbar does not exist in the later one. On the contrary there exists a minimum in the salinity scales between 900 dbar and 1000 dbar ($Ly \leq 180$ km). This is due to the property distribution in that frontal region, where south of 43°S the isohalines are almost vertically orientated from the surface to about 800 dbar depth. The maximum in the salinity scales is more present in the estimate from the northern part of the section between 30°S and 10°S. Here this maximum is spread over a wide depth range, between 850 dbar and 1050 dbar and represents the horizon of the AAIW with the characteristic salinity minimum, which is spreading equatorwards and sloping upwards slightly. The estimated length scales for temperature for the whole meridional section are similar to the salinity scales except for a local maximum around 450 dbar ($Ly = 450$ km) associated with the horizon of Southeast Indian Subantarctic Mode Water (SEISAMW), the dense variation of the SAMW characterized by a minimum in potential vorticity (McCartney, 1977). Furthermore deeper than 1500 dbar the temperature length scales are about two times larger than the length scales of salinity.

The different hydrographic cruise data have on the one hand the advantage to provide information on the spatial scales not constrained by the Argo dataset but on the other hand they have a short temporal coverage ($\leq$4 months) and can include strong small scale variability not necessarily representative on annual time scales or longer. Therefore, the Argo dataset itself has been used additionally, to estimate decorrelation length scales. The Argo data also include small scale variability but they have the advantage to cover the 5 year period of the analysis and therefore they can provide a better reference for the actual time period 2002 to 2005. The Argo data are interpolated linearly onto appropriate meridional or zonal sections (Fig. 3.6) reducing the influence of possible strong small scale features as seen for example in the CD139 cruise data (Palmer et al., 2004).

Decorrelation length scales estimated from Argo data: Here the Argo data within different longitudinal (for meridional length scales) or latitudinal (for zonal length scales) bands are interpolated linearly to generate sections along 20°S, 32°S, 55°E and 95°E, respectively (Fig. 3.6). For example at 32°S three realisations are calculated including all profiles within a ±0.5°, ±1° and ±2° latitudinal envelope, respectively. Within the area of 32°S±0.5° latitude only 544 profiles exist and within ±2° latitude 2167 profiles exist. It is quite obvious that since the number of profiles is not equally distributed in time over the 5 year period (Fig. 3.7) it is important to

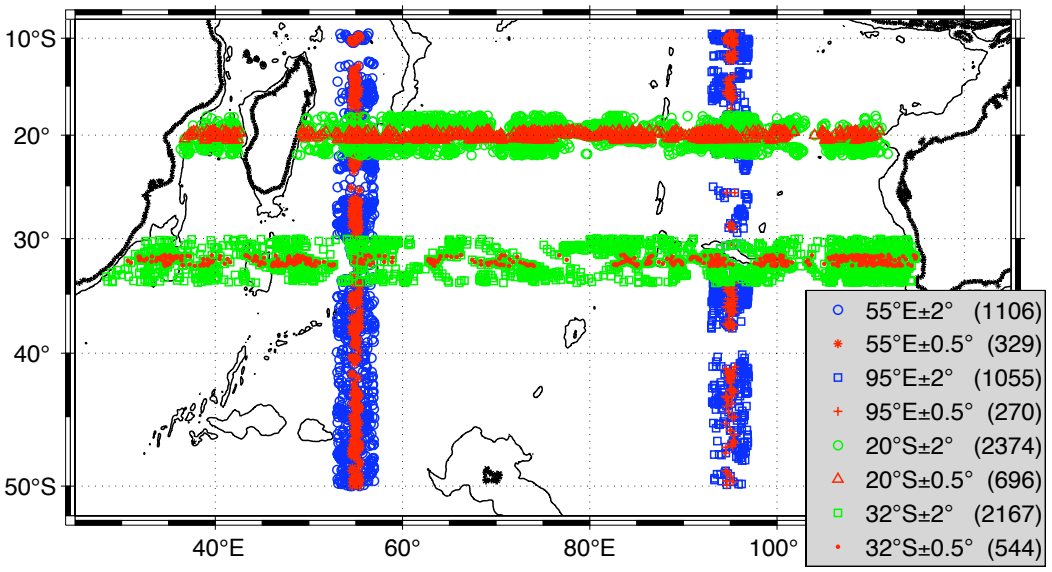

FIGURE 3.6: Positions of Argo profiles (from January 2002 to December 2006) along different sections in the subtropical South Indian Ocean, with zonal sections at 32°S (green circle: ±2° latitude; red dots: ±0.5° latitude) and 20°S (green circle: ±2° latitude; red triangle: ±0.5° latitude) and with meridional sections along 55°E (blue circle: ±2° longitude; red stars: ±0.5° longitude) and 95°E (blue circle: ±2° longitude; red cross: ±0.5° longitude). Total number of available data points within the selected area are given in brackets. Contours indicate coastline (bold) and 2000 m isobath.

use a wider range including more profiles to provide a representative estimate of the length scales. Therefore, the final plots shown here use a ±2° latitudinal/longitudinal band to select profile data to get a better spatial and temporal coverage.

The analysis of the decorrelation length scales (Lx_W, Lx_E and Ly) then follows again the previously described steps (Sec. 3.1.1 with Eq. 3.1 and 3.2). The selected profiles are sorted along their longitudinal position and the salinity and temperature anomalies (Argo data minus "climatological" dataset) are linearly interpolated onto the new generated grid of the spatial distance of the subsection evenly spaced into 200 stations. Then the decorrelation length scales are estimated again as the distance of the point with $R \leq e^{-3}$, fulfilled for the first time in the auto-correlation function (Eq. 3.1 and 3.2).

Zonal decorrelation length scales estimated from Argo data: The zonal decorrelation scales (Lx_W) for the western subsection along 20°S and 32°S (Fig. 3.8 and 3.9 left column) show a strong vertical structure with slowly increasing scales to $Lx_W = 220$ km at depth with small variations (Fig. 3.8 lower panel left) or with larger variations (Fig. 3.9 lower panel left) centred around $Lx_W = 300$ km.

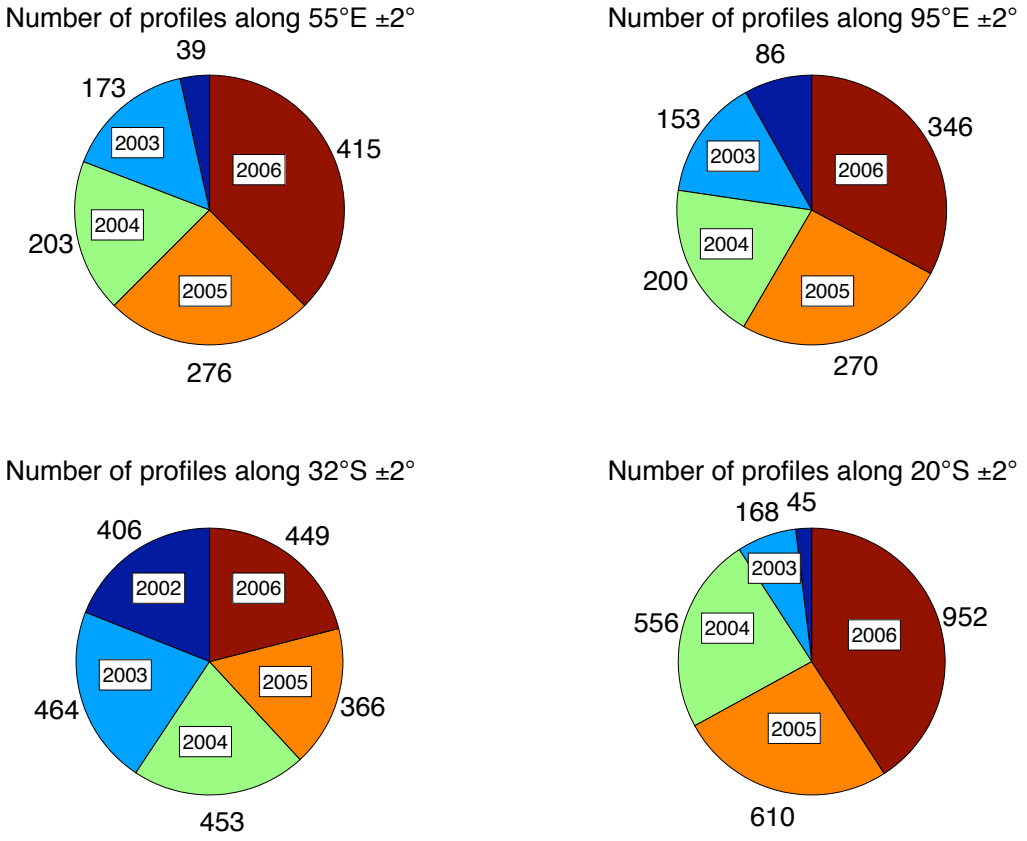

FIGURE 3.7: Annual number of profiles contributing within a range of ±2° longitude to the meridional sections 55°E (top left) and 95°E (top right) and within a range of ±2° latitude to the zonal sections 32°S (bottom left) and 20° (bottom right).

Aside from the top 300 dbar and the level between 1200 dbar and 1700 dbar at 32°S the scales for salinity and temperature are very similar. In the eastern subsection along 20°S there exists less vertical structure, especially in the scale estimates (Lx_E) for temperature (Fig. 3.8 bottom right) but generally the vertical profiles of temperature and salinity scales agree well with those estimated from the BEAGLE cruise (Fig. 3.2 bottom right). The length scale for salinity increase with depth to $Lx_E = 700$ km around 950 dbar, which is the horizon of the AAIW characterized by a salinity minimum. Below 1000 dbar the scales decrease to about $Lx_E = 500$ km at 2000 dbar with a local maximum in between of $Lx_E = 1200$ km at 1500 dbar. Here it is appropriate to mention, that a large number of profiles near 20°S result from floats adjusted to drift at 1000 dbar taking only every 3rd cycle or less frequently a deep profile from 2000 dbar, that means that about 40% of the profiles cover only the upper 1000 dbar range of the water column. The length scale for temperature shows similar characteristics with stronger pronounced maxima and an additional local maximum of $Lx_E = 1100$ km around 500 dbar (Fig. 3.2 bottom right). Along 32°S in the eastern section the scales

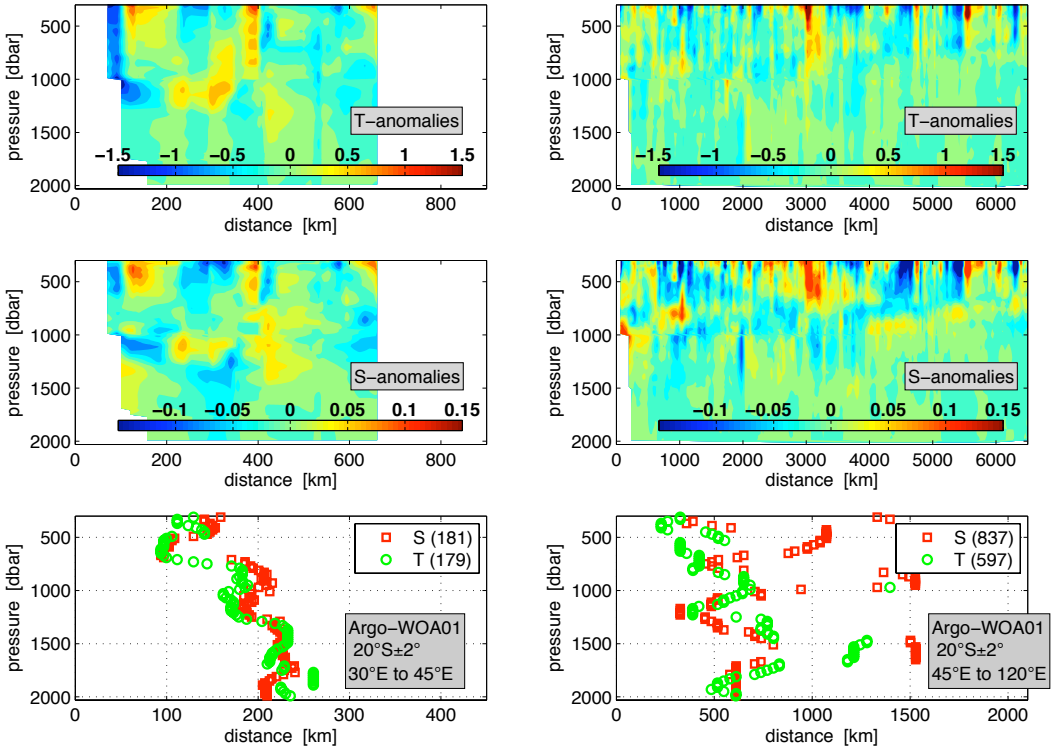

FIGURE 3.8: *Top and middel:* Sections of anomalies (Argo minus WOA01) of potential temperature (top) and salinity (middle) on pressure levels along 20°S. *Bottom:* Vertical profiles of zonal decorrelation length scales for salinity (red) and potential temperature (green) estimated on pressure levels along 20°S.

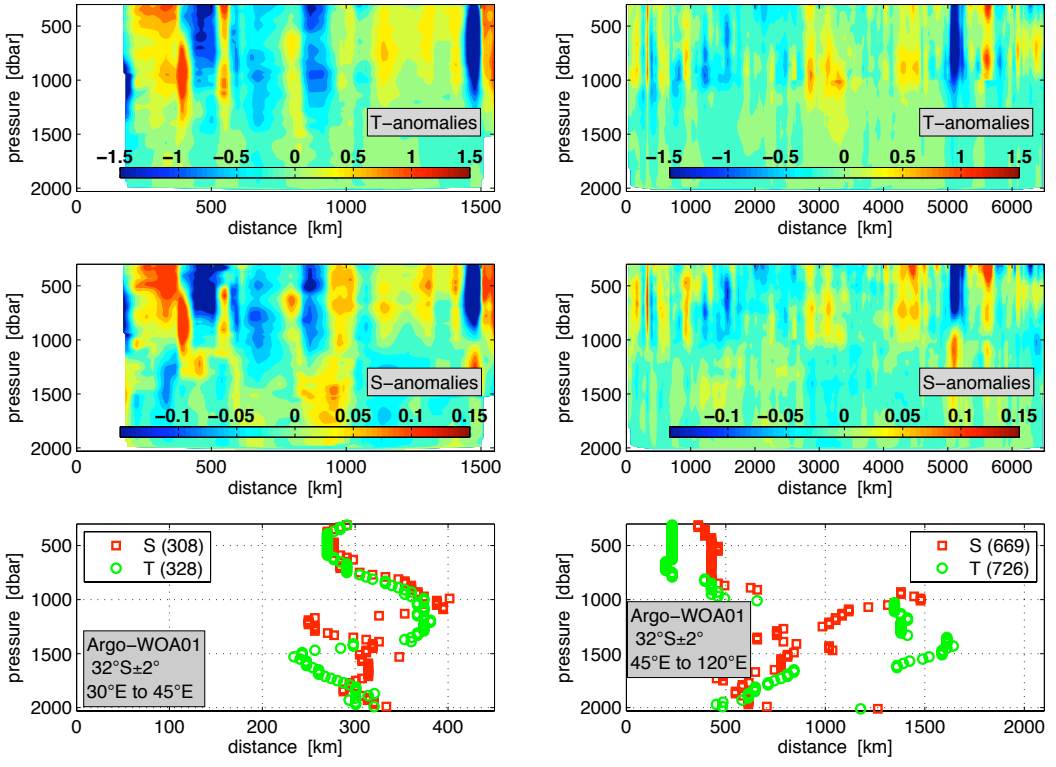

FIGURE 3.9: As figure 3.8 but along 32°S.

for temperature and salinity between the surface and 950 dbar are $Lx_E = 300$ km and $Lx_E = 500$ km, respectively (Fig. 3.9 bottom right). Around 1000 dbar, which is the horizon of the AAIW, both scales are large, $Lx \geq 1400$ km, decreasing to about $Lx = 600$ km at 2000 dbar. Here nearly all profiles cover the whole water column since a large number of the floats adjusted to drift at 2000 dbar have been deployed along 32°S in early 2002.

Meridional decorrelation length scales estimated from Argo data: The meridional length scales (Ly) at 55°E (Fig. 3.10 left column) are between $Ly = 250$ km and $Ly = 300$ km down to 1000 dbar. Below 1000 dbar, the scales for temperature increase to about $Ly = 400$ km, while the salinity scales show a maximum of $Ly \geq 750$ km at about 1100 dbar, which is at the horizon of the AAIW between 41°S and 23°S. Below 1100 dbar the scales for salinity decrease to about $Ly = 200$ km. Again it is appropriate to mention that about 40% of the profiles included here do not reach deeper than 1000 dbar, therefore one would expect smaller variations along the section

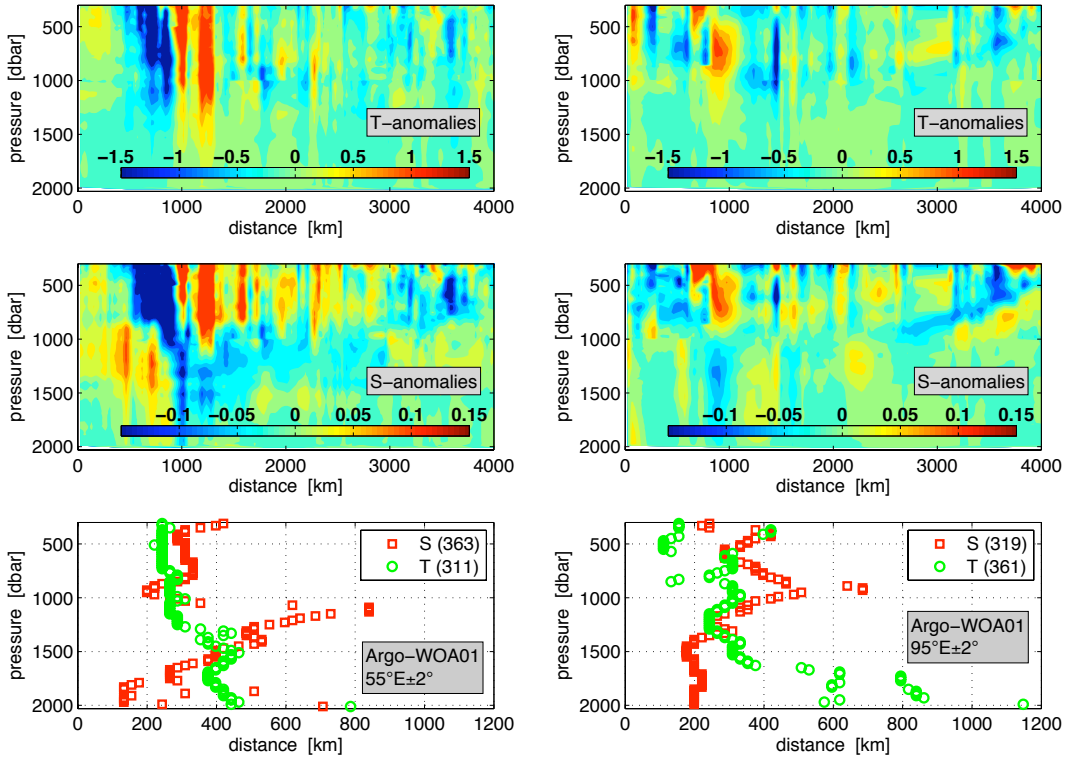

FIGURE 3.10: *Top and middel:* Sections of anomalies (Argo minus WOA01) of temperature (top) and salinity (middle) on pressure levels along 55°E (left) and 95°E (right). *Bottom:* Vertical profiles of zonal decorrelation length scales for salinity (red) and potential temperature (green) estimated on pressure levels along 55°E (left) and 95°E (right).

due to fewer data points used for the interpolation. At 95°E (Fig. 3.10 right column), the estimated length scales are $Ly = 300$ km for temperature above 1400 dbar with local minima of $Ly = 150$ km at 500 dbar and 900 dbar. Below 1500 dbar the temperature scales increase to about $Ly = 600$ km. The salinity scales decrease from $Ly = 400$ km to $Ly = 200$ km at 1400 dbar with a local maximum of $Ly \geq 600$ km at 950 dbar. Below 1400 dbar the salinity scales are $Ly = 200$ km.

Final selection of decorrelation length scales The aim of the previously described procedure is to define appropriate decorrelation length scales to be used in the OI. Therefore, temperature and salinity measurements from zonal and meridional cruise tracks as well as from DMQC Argo float data, have been utilised. The scales estimated from cruise data are of the same order as those estimated from the Argo float data, while different temporal time periods are covered, a few weeks in the cruise data and a year or longer in the Argo data. The scales will finally be used to generate annual and seasons averages, respectively, over the 5 year period 2002 - 2006. Knowing that the results leave a variety of possible length scales to select, three single scales have been chosen, more or less subjectively: A mean zonal length scale for the western boundary region west of 45°E (Lx_W), a mean zonal length scale for the interior east of 45°E (Lx_E) and a meridional length scale for the whole SIO area (Ly). The meridional length scale is chosen to be $Ly = 400$ km, which is about the average or slightly larger than the scales estimated from the cruise data and Argo float data as previously discussed. This is also about the latitudinal scale discussed by King and McDonagh (2005). They analysed float data collected up to May 2003 along 32°S and found that a latitudinal variation of about 5° latitude (550 km) in the position of the profile data reflects small changes compared to changes between the 1987 and 2002 cruise sections. The zonal length scales are chosen to be $Lx_W = 200$ km, for the western subsection west of 45°E, connected to the boundary region and $Lx_E = 600$ km for the eastern subsection between 45°E and 120°E. These final length scales are about the average smaller than the estimated scales from the previous analysis using cruise data and float data. With these defined decorrelation length scales we now proceed with the description of the major elements of the OI.

3.1.2 Distance weighting and the final objective estimate

In the following, salinity is used exemplarily as a parameter that is supposed to be interpolated on a regular grid. The final objective estimate S^{obj} given by the OI at each mapping grid point for each 20 dbar surface is composed from

$$S^{obj} = S_{WOA} + w \bullet (S - S_{WOA}) \tag{3.3}$$

where S_{WOA} denotes the salinity taken from the nearest WOA01 climatology grid point, w is the coefficient weighting matrix using the decorrelation scales, $S = [S_1, ..., S_N]$ is the set of salinity measurements from the selected float profiles on each grid point. In other words the a priori estimate is the nearest climatological value S_{WOA}. This first-guess background climatology is not essential but in the light of the early stage of the Argo project in the SIO and the distribution of its contributing float profiles, it was used.

The full OI algorithm applied in this work consists of two steps, a preselection of the data (1st step) and the actual mapping of the selected data (2nd step). Depending on the application of the OI, it might be necessary to apply a further step with a "small-scale" mapping including temporal separation. Wong et al. (2003); Böhme and Send (2005) showed that this is essential during the delayed-mode quality control process, where the float profiles are compared with historical observations to reduce sensor drift or off-sets, since the multi-step mapping realistically gives increased error estimates where recent historical data are not available. In the present study the small scale mapping is omitted since the data fall within a relative tight time range of a few days for the realisations of the cruise sections and the spatial density is not enough to gain advantages from the small-scale mapping step. Due to the focus of this work to analyse seasonally and annually averaged fields (compared for example to Hadfield et al. (2007)), no temporal separation is included in the OI procedure (Eq. 3.4 , 3.8 and 3.9) in compliance with the focus of this work to analyse seasonally and annually averaged fields (compared for example to Hadfield et al. (2007)). Therefore, for consistency, the results of the original cruise tracks, being resampled from Argo float data (Sec. 3.2), are also generated without temporal separation in order to validate the accuracy of the finally applied OI to the seasonal and annual averages. The so called 'generalized' distance weighting, that accounts for the cross-isobath separation in the OI (Davis, 1998; Böhme and Send, 2005) was omitted as well, because no adequate scale for the fractional distance F could be determined. But the separation into two subsections with different longitudinal scales, the western accounting for the western boundary region ($Lx_W = 200\,\mathrm{km}$), and the eastern accounting for the basin interior ($Lx_E = 600\,\mathrm{km}$), compensates partly the missing fractional distance weighting in the boundary region.

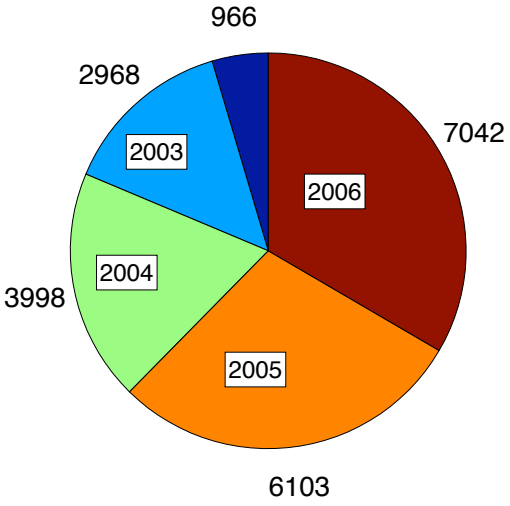

FIGURE 3.11: Annual number of delayed-mode quality control profiles in the subtropical South Indian Ocean between 50°S and 10°S and 25°E and 125°E. The dark blue unlabelled section represents year 2002.

First step of the OI In this step the profiles contributing to the actual mapping grid point are "preselected". This is mainly important to speed up the calculations if the OI is applied to generate 3-dimensional fields of the whole subtropical SIO, because more than 20 000 profiles exist between 50°S and 10°S between the beginning of 2002 and the end of 2006 (Fig. 3.11). This selection process includes a routine that eliminates data points which are separated by topography from the mapping point. Here the TerrainBase 5′ elevation database [http://dss.ucar.edu] is used and interpolated onto a 0.5° x 0.5° grid. Now if there exists intercepting topography between the mapping grid point and data point, the data point is excluded. Additionally, a simple distance weighting scheme is applied to the remaining data points assuming a Gaussian distribution of the data in space. Only those data points are used with a weighting factor $wd_{i,g} \geq e^{-3}$ following the equation

$$wd_{i,g} = \exp\left\{-\left[\frac{Dx_{i,g}^2}{Lx^2} + \frac{Dy_{i,g}^2}{Ly^2}\right]\right\} \qquad \text{for } i = 1:N \tag{3.4}$$

where $Dx_{i,g}$ and $Dy_{i,g}$ are the meridional and longitudinal distances in km between the i-th data point and the mapping grid point with index g. Lx is the decorrelation length scale as estimated in Section 3.1.1, with $Lx = Lx_W$ west of 45°E and $Lx = Lx_E$ between 45°E and 120°E. Note that in the following the subscripts i and j refer to Argo profile locations with N the number of selected profiles, while the subscript g refers to the mapping grid point. No temporal separation is used because the OI is used to generate seasonal and annual averages. Only in section 3.2 the original cruises tracks are resampled using the OI from Argo float data but for consistency and to validate

the accuracy of the mapping finally applied to the seasonal and annual averages no temporal separation is included (compared to HADFIELD ET AL. (2007) for example).

Second step of the OI Now the actual mapping is done and the objective estimate is calculated. According to WONG ET AL. (2003), each salinity measurement S_i can be separated into a true signal (s_i) and into a random noise (η_i), including measurement errors, unpredictable processes and the natural variability in the ocean that cause deviations from the mean state. FUKUMORI AND WUNSCH (1991) showed that the signal and noise variance of the data can be approximated from the relationship $S_i = s_i + \eta_i$ assuming that the noise is uncorrelated over distance, that it has uniform variance and that the signal has a longer correlation distance than the data separation. The signal variance s^2 is then approximated by

$$s^2 \;=\; \frac{1}{N} \sum_i (S_i - \mathbf{S}_{WOA_i})^2 \tag{3.5}$$

and the noise variance η^2 is approximated from the difference of S from neighbouring measurements given by

$$\eta^2 \;=\; \frac{1}{2N} \sum_i (S_i - S_k)^2 \tag{3.6}$$

where S_k is the salinity measurment that has the shortest distance from S_i on each isobath. The signal and noise variance are then joined into the coefficient weighting matrix w, given by

$$w \;=\; \mathbf{Cdg} \bullet [\mathbf{Cdd} \;+\; I \bullet \langle \eta^2 \rangle]^{-1} \tag{3.7}$$

where I denotes the identity matrix and **Cdg** and **Cdd** being the data-grid and data-data covariance matrices given by

$$\mathbf{Cdg} \;=\; \langle s^2 \rangle \bullet \exp \left\{ - \left[\frac{Dx_{i,g}^2}{Lx^2} + \frac{Dy_{i,g}^2}{Ly^2} \right] \right\} \tag{3.8}$$

$$\mathbf{Cdd} \;=\; \langle s^2 \rangle \;\bullet\; \exp\left\{ -\left[\frac{Dx_{i,j}^2}{Lx^2} + \frac{Dy_{i,j}^2}{Ly^2} \right] \right\} \tag{3.9}$$

with $Dx_{i,j}$ and $Dy_{i,j}$ as the meridional and longitudinal distance between the two data points with indices i and j. The final error variance of the OI is then given by

$$\sigma_{OI}^2(S^{obj}) \;=\; s^2 \;-\; \mathbf{Cdg} \;\bullet\; \mathbf{Cdd}^{-1} \;\bullet\; \mathbf{Cdg}^T \tag{3.10}$$

and it takes into account the number of profiles as degrees of freedom with which to scale the standard deviation.

Advantages of the Optimal Interpolation This paragraph illustrates and explains the effect of the non-isotropic distance weighting with the aid of the western boundary and the interior region, respectively but also the effect of the unbiased pointwise estimate given by the *Gauss-Markov* theorem (Fig. 3.12). The upper two panels show the influence of the different zonal decorrelation length scales applied in the "pure" distance weighting step (Eg. 3.4), but also the final selection of the profiles after the "full" optimal interpolation algorithm is applied (coloured dots). It can be seen that for the western subsection with $Lx_W < Ly$ ($Lx_W = 200\,\mathrm{km}$, $Ly = 400\,\mathrm{km}$) the area with a pure distance weighting is compressed in the longitudinal direction forming an ellipse (Fig. 3.12 top). Along the eastern subsection, here in the *Crozet Basin* (Fig. 3.12 middle) the orientation of the ellipse is reversed, since the zonal scale is now larger than the meridional scale ($Lx_E = 600\,\mathrm{km}$, $Ly = 400\,\mathrm{km}$). The lower panel in Figure 3.12 illustrates the effect based on the *Gauss-Markov* theorem, which is used in this method, to get unbiased pointwise estimates. Here for this schematic isotropic length scales are used ($Lx = Ly$). Assume the case of three perfect observations on a circle as shown in Figure 3.12 with observation P1, P2 and P3 being equidistant from the estimation point C and therefore having the same distance weighting value. By putting reasonable correlation values into the equations for the weights, one finds that the weight for P1 is larger than for P2 or P3. This occurs because P1 carries more independent information than either P2 or P3, which are closer together. As the angle α increases towards 60°, the three weights approach equality.

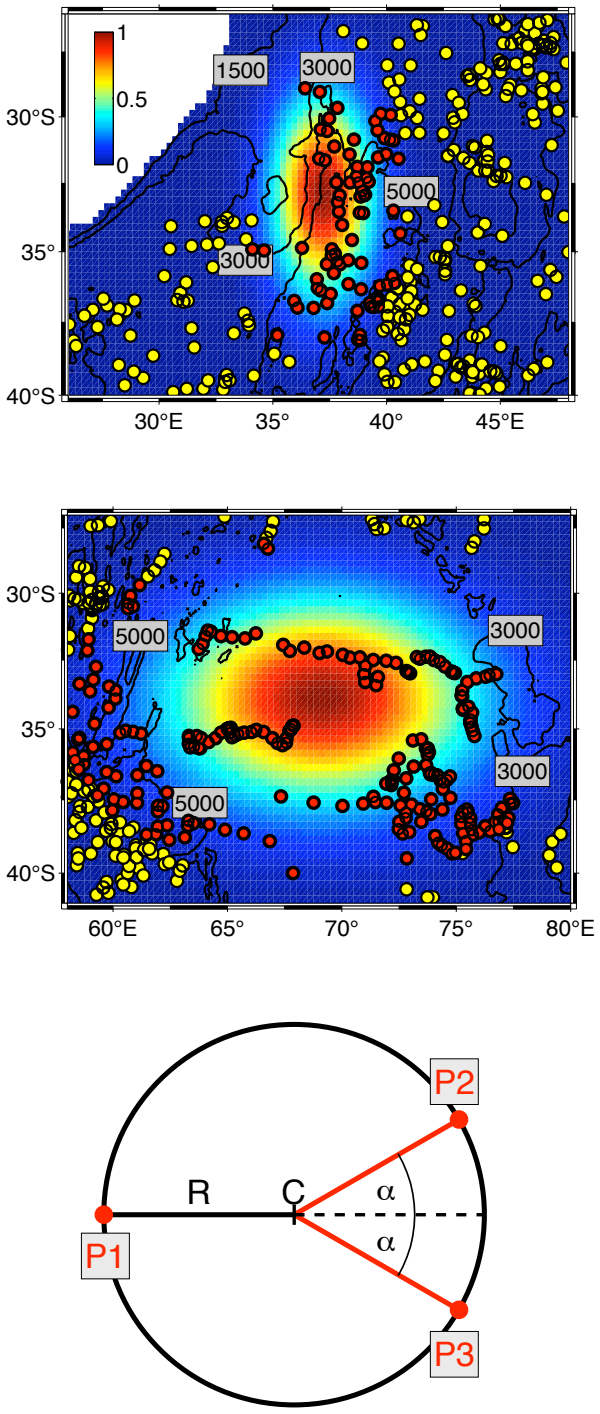

FIGURE 3.12: Color shading of the distance weighting (wd) used in the Optimal Interpolation with anisotropic length scales computed on a 0.25° x 0.25° grid. In the top panel near the western boundary region at 37°E / 33°S the patch from the distance weighting has a meridional orientated eliptic shape due to the smaller zonal scales (Lx_W = 200 km; Ly = 400 km). In the middle panel here in the *Crozet Basin*, at 69°E / 34°S the patch from the distance weighting has a longitudinally orientated, elliptic shape due to the larger zonal scales in the interior (Lx_E = 600 km; Ly = 400 km). The dots indicate the position of all available float profiles (yellow) and those with a distance weighting (wd) of $wd \geq e^{-3}$ (red). Bottom panel: Illustration of the "unbiased pointwise estimate" used in the *Gauss-Markov* theorem. Shown are three perfect observations (P1, P2 and P3) on a circle (assuming isotropic decorrelation length scales) with radius R and gridpoint C at the centre. Observations P2 and P3 are at angular distance α from the latitude of gridpoint C. Whereas P1 has a larger angular distance to P2 and P3.

With this OI algorithm it is now possible to reproduce or create sections and maps from the float data with appropriate error estimates too. The next section gives an overview of the float realisations used in this study.

3.1.3 Realisations generated from Argo floats and cruise datasets

For ease of reading the following analysis (Chapter 4), a short overview of the realisations is given, which are used later in this work. The float realisations (Tab. 3.1 and 3.2) have been produced by collecting the float data from the DMQC dataset within the desired time frame and generating mean estimates of salinity and temperature with the Optimal Interpolation. Whereas the cruise realisations (Tab. 3.3) have been produced by running the OI on the cruise data. First, for the comparison of the accuracy of float realisations, the estimates along the cruise tracks have been used. Different temporal coverages have been realised, ranging from ±0 months to ±2 months along CD139 and BEAGLE, respectively. Second, for the analysis of changes in the gyre strength and its variability the float realisations on the 1° x 1° grid given by the background climatology WOA01, along the fixed latitude of 32°S and 20°S respectively, have been used. Annual averages and 5 year mean seasonal averages have been generated for the whole subtropical SIO. All realisations used in this study use anisotropic decorrelation length scales Lx_W =200 km, Lx_E = 600 km and Ly = 400 km derived from combined hydrographic cruise data, float measurements and climatological data as described in detail in the previous section (Chapter 3.1.1).

TABLE 3.1: Float realisations generated from Argo float dataset with different temporal resolutions using the Optimal Interpolation to reproduce the recent cruise sections CD139 and BEAGLE.

Name	temporal coverage	region/latitude
$\text{Argo}_{\text{CD139}\pm\text{0mon}}$	04.03.2002 - 14.04.2002	CD139 cruise track
$\text{Argo}_{\text{CD139}\pm\text{1mon}}$	04.02.2002 - 14.05.2002	CD139 cruise track
$\text{Argo}_{\text{CD139}\pm\text{2mon}}$	04.01.2002 - 14.06.2002	CD139 cruise track
$\text{Argo}_{\text{BEAGLE}\pm\text{0mon}}$	09.12.2003 - 24.01.2004	BEAGLE cruise track
$\text{Argo}_{\text{BEAGLE}\pm\text{1mon}}$	09.11.2003 - 24.02.2004	BEAGLE cruise track
$\text{Argo}_{\text{BEAGLE}\pm\text{2mon}}$	09.10.2003 - 24.03.2004	BEAGLE cruise track

TABLE 3.2: Float realisations generated from Argo float dataset with different temporal resolutions (annual mean, 5 year seasonal mean) using the Optimal Interpolation to estimate temperature and salinity fields for the subtropical South Indian Ocean on a regular 1° x 1° grid.

Name	temporal coverage	region/latitude
SIO_02	year 2002	25°E - 125°E; 45°S - 18°S
SIO_03	year 2003	25°E - 125°E; 45°S - 18°S
SIO_04	year 2004	25°E - 125°E; 45°S - 18°S
SIO_05	year 2005	25°E - 125°E; 45°S - 18°S
SIO_06	year 2006	25°E - 125°E; 45°S - 18°S
SIO_SPR	spring (SON)	25°E - 125°E; 45°S - 18°S
SIO_SUM	summer (DJF)	25°E - 125°E; 45°S - 18°S
SIO_AUT	autumn (MAM)	25°E - 125°E; 45°S - 18°S
SIO_DEC	winter (JJA)	25°E - 125°E; 45°S - 18°S

TABLE 3.3: Cruise realisations generated from cruise datasets using the Optimal Interpolation either to smooth the cruise data to investigate the effect from the mapping, or to project onto the closest WOA01 latitudinal grid.

Name	data	region/latitude
selfCD29	CD29	CD29 track
selfCD139	CD139	CD139 track
selfBEAGLE	BEAGLE	BEAGLE track
20SBEAGLE	BEAGLE	20°S

3.2 Accuracy of the Optimal Interpolation tested with resampled cruise tracks using Argo float data

In the previous section the OI was introduced and described. Now, the hydrographic cruise data along 32°S taken in 2002 and 20°S taken in 2004, respectively, are compared with Argo float data interpolated onto the same cruise tracks. No temporal decorrelation scale has been included in the OI, because the focus is directed to annual and seasonal averages. Therefore, the estimates from the float realisations are finally compared with smoothed versions of the cruise data with a 5-point moving average applied. The 5-point moving average is of the order of the zonal decorrelation length scales (Lx_W and Lx_E) applied in the OI (CD139ma5pt and BEAGLEma5pt).

3.2.1 Comparison of the 2002's cruise data along 32°S with optimal interpolated Argo float data

In this section the CD139 hydrographic section along 32°S, sampled from the 4th of March to the 14th of April 2002 (Bryden et al., 2003a), is reproduced using optimal interpolated Argo float data in the subtropical South Indian Ocean between 10°S and 50°S. The float data are interpolated to the cruise CTD stations to obtain salinity and temperature sections.

Initially three float datasets are used with a different temporal coverage to get an idea which sampling period might be appropriate to reproduce a hydrographic section (Tab. 3.1). The first dataset covers only the time period of the cruise ($\text{Argo}_{\text{CD139}\pm 0\text{mon}}$) with 43 profiles used in the OI out of 66 available. The second one covers 1 month before and after the cruise, in total a period of 14 weeks covered by 129 out of 190 profiles ($\text{Argo}_{\text{CD139}\pm 1\text{mon}}$). The third dataset expands the time period by ± 2 months ($\text{Argo}_{\text{CD139}\pm 2\text{mon}}$). It covers 22 weeks in total with 213 profiles used out of 320 available. At this stage from the distribution of the profiles for each realisation (Fig. 3.13) it becomes clear that the realisation using only profiles from within the cruise period ($\text{Argo}_{\text{CD139}\pm 0\text{mon}}$) cannot provide any estimates other than the climatological values east of 105°E. Therefore, for the comparison of the accuracy of the OI the realisations $\text{Argo}_{\text{CD139}\pm 1\text{mon}}$ and $\text{Argo}_{\text{CD139}\pm 2\text{mon}}$ have been used, since they provide a full section without relying only on climatological values. There exist only few profiles earlier than the cruise date, because during the 2002 cruise 25 floats were launched (Bryden et al., 2003a). That marked the starting point of the Argo project in the subtropical SIO. Before the CD139 cruise only 5 floats were sampling the area of the subtropical

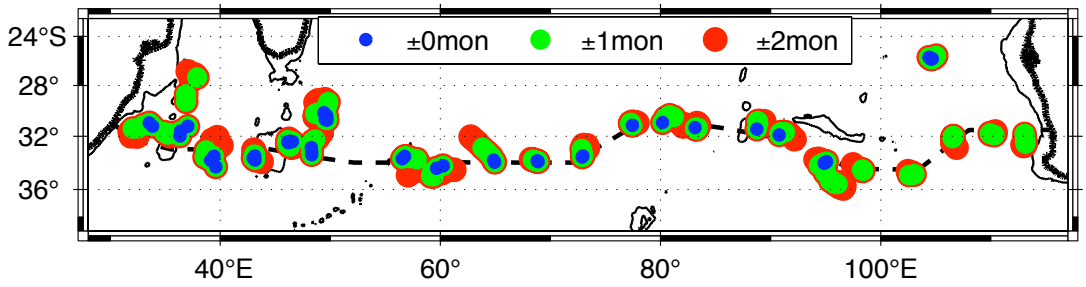

FIGURE 3.13: Positions of Argo float profiles used for interpolation onto CD139 cruise stations (track shown as black dashed line), within the cruise period only (blue dots) and within ±1 month (green dots) and within ±2 months (red dots) of the cruise date respectively. Contour lines highlight coastline (black bold) and 1900 m isobath (black thin).

TABLE 3.4: Number of Argo profiles available in the subtropical South Indian Ocean (between 45°S and 20°S and 25°E and 120°E) for different periods of 2 and 6 months. Numbers of DMQC profiles shown in brackets.

6 months period	Profiles	2 months period	Profiles
01.01.2007 - 30.06.2007	3076 (1266)	01.01.2007 - 28.02.2007	1002 (479)
01.02.2007 - 31.07.2007	3065 (1181)	01.02.2007 - 31.03.2007	1008 (436)
01.03.2007 - 31.08.2007	3117 (1123)	01.03.2007 - 30.04.2007	1040 (419)
01.04.2007 - 30.09.2007	3073 (1026)	01.04.2007 - 31.05.2007	1040 (393)
01.05.2007 - 31.10.2007	3087 (925)	01.05.2007 - 30.06.2007	1034 (368)
01.06.2007 - 30.11.2007	3061 (777)	01.06.2007 - 31.07.2007	1017 (352)
01.07.2007 - 31.12.2007	3067 (646)	01.07.2007 - 31.08.2007	1043 (336)
01.08.2007 - 31.01.2008	3069 (504)	01.08.2007 - 30.09.2007	1016 (281)
01.09.2007 - 29.02.2008	3076 (368)	01.09.2007 - 31.10.2007	1010 (221)

SIO. Just for comparison, from the beginning of 2007 onwards more than 1000 profiles are available for a 2 month period while for a 6 month period more than 3000 profiles are available which is up to 10 x more than in the beginning of 2002 (Tab. 3.4; taken from USGODAE Argo GDAC Data Browser[1]).

The CD139 cruise dataset itself does contain large variability on scales of about 100 km to 200 km in the interior with displacements of the isohalines and the isopycnals, as shown by PALMER ET AL. (2004), of 200 dbar or more, for example around 52°E, at 75°E and 104°E (Fig. 3.14 top). This small-scale variability cannot be fully resolved in the Argo section due to the coarse coverage of data. Although some of the float deployments were close to CTD stations, where the large shift/displacement in isohalines can be found, the characteristics of the floats to sample the profile during ascent from parking depth to the surface after almost 10 days of drift at parking

[1] http://www.usgodae.org/cgi-bin/argo_select.pl

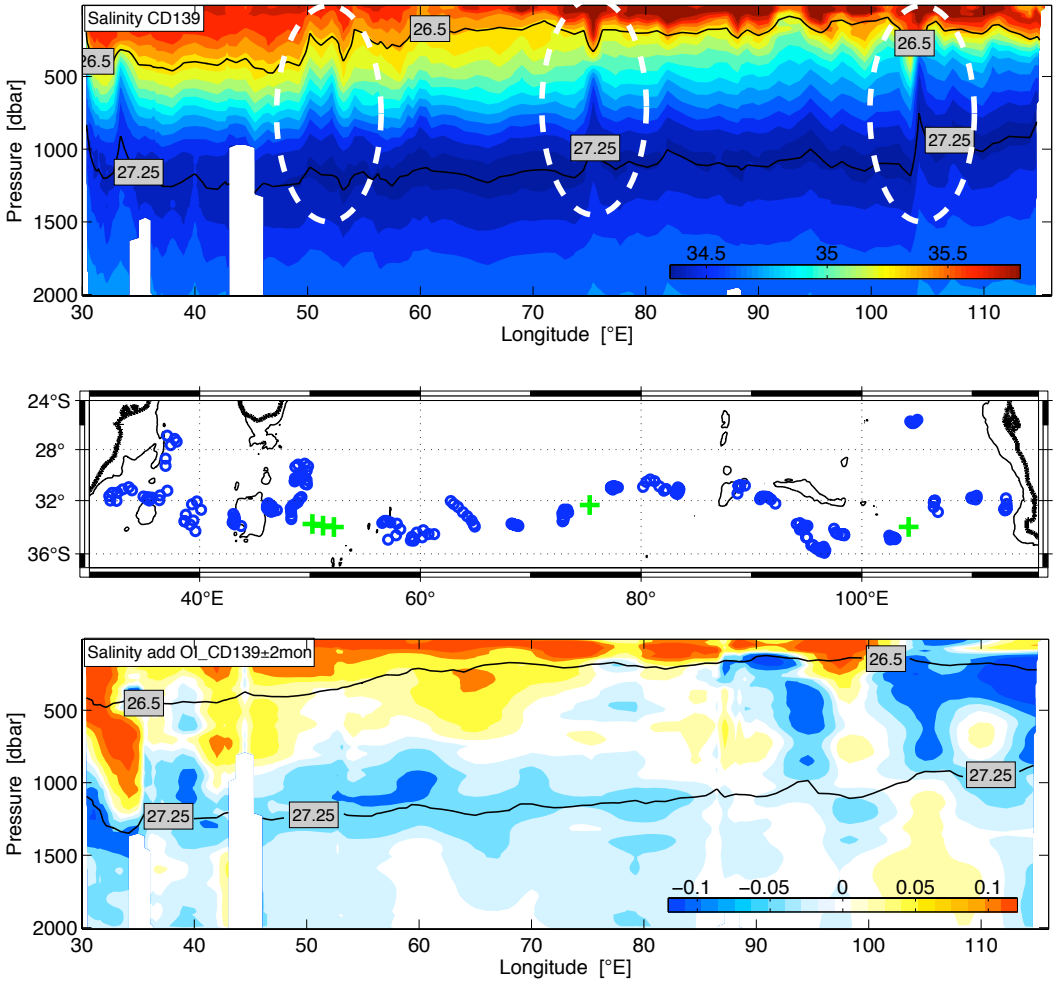

FIGURE 3.14: *Top:* Vertical salinity section of CD139 cruise data. White dashed ellipses mark location of high amplitude small spatial scale features. *Middle:* Position of Argo float profiles in the vicinity of the cruise track ± 2 months of the cruise date (blue circles) and location of large shift/displacement in the isohalines and isopycnals of the cruise section (green crosses). Contours indicate 1900 m isobath (black) and coastline (black bold). *Bottom:* Vertical section along CD139 cruise track of additive salinity term estimated in the Optimal Interpolation for float realisation $\text{Argo}_{\text{CD139}\pm\text{2mon}}$.

pressure delays the possibility to sample the displacement. Nevertheless in the additive salinity term estimated during the OI, clear signals appear in the east at 95°E and 104°E (Fig. 3.14, bottom) between 200 dbar and 1000 dbar, as well as between 50°E and 60°E between 800 dbar and 1200 dbar. It is surprising that the strong signal in salinity around 104°E is better represented in the float realisation $\text{Argo}_{\text{CD139}\pm\text{2mon}}$ (Fig. 3.14 bottom) than in $\text{Argo}_{\text{CD139}\pm\text{1mon}}$ (not shown separately). This could be an indicator that the signal at 104°E has a lifetime of longer than 30 days.

The main interest is the large scale field, therefore it seems appropriate to use a dataset without the large small-scale variability (Fig. 3.14 top), to compare with the

original cruise data. Therefore, the small-scale variability from the original CD139 cruise data has been removed. Since the average station separation during the CD139 cruise west of Madagascar Ridge (MADR) (at 45°E) is about 35 km and along the rest of the section about 80 km respectively, a 5-point moving average filter has been applied to the data. This is of the order of the decorrelation length scales ($Lx_W = 200$ km and $Lx_E = 600$ km) applied during the OI. The filtered dataset (CD139ma5pt) will be the reference dataset for the following comparison.

The two different float realisations ($Argo_{CD139\pm1mon}$ and $Argo_{CD139\pm2mon}$) are used to obtain an idea of the errors associated with the temporal coverage of profiles in the area of the cruise track since no temporal separation is included in the OI. Additionally, the original cruise data are referenced to the filtered cruise data (CD139ma5pt) to give a measure of the small-scale variability. For the purpose of clarity a look at vertically averaged properties should be sufficient to select a preferred float realisation for a more detailed comparison. The Root-mean-square (RMS) of salinity or temperature difference at all depths down to 1900 dbar (Argo minus cruise) gives a good measure of the differences in the realisations. Generally the RMS of both float realisations shows the same structure and magnitude as the RMS from the cruise dataset. The RMS in salinity differences is generally smaller than 0.07 for both float realisations (Fig. 3.15), only at the western boundary around MOZP at 35°E the RMS is larger than 0.15, which is due to the high variability in the boundary current. The RMS in salinity difference between the original and smoothed cruise data shows very much the same structure and magnitude at 35°E. In this area the first floats were deployed therefore a larger number of profiles exist close to the cruise track with additional profiles from older floats further north around 29°S, that means a smoother estimate is achieved there. The two spikes at 75° and 104°E in the RMS of the salinity difference between

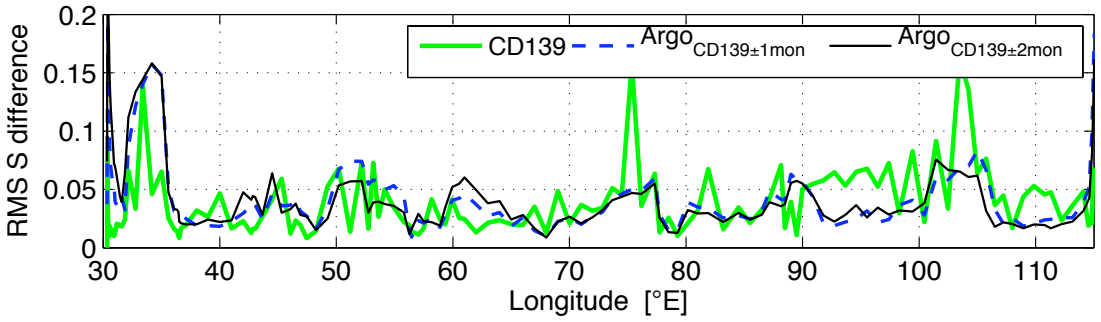

FIGURE 3.15: Root-mean-square of salinity difference between original and smoothed cruise data (green) and between float realisations and smoothed cruise data ($Argo_{CD139\pm1mon}$: blue dashed; $Argo_{CD139\pm2mon}$: black).

CD139 and CD139ma5pt data result from the small-scale variability present in the cruise data (PALMER, 2005) and described in the previous paragraph (Fig. 3.14). The largest deviations between the two float realisations exist east of 50°E and around 60°E. The mean RMS of salinity difference for the whole section is 0.05 for both float realisations and for the section east of MADR at 45°E it reduces to only 0.04. The vertical averaged salinity error estimate provided by the OI has for both realisations the same structure again with very little differences (Fig. 3.16 top). The mean salinity error estimate is about 0.026 and for the part of the section east of 45°E it decreases to about 0.015. Both realisations have a vertical averaged Signal-to-noise ratio (SNR) greater than two throughout the section (Fig. 3.16 bottom). According to (SCHILLER ET AL., 2004) a SNR of one or more should provide statistically significant information about the Argo data. Outside the upper 500 dbar and the western boundary area large values in the true signal exist at depths between 700 dbar and 1200 dbar, which is the level between SAMW and AAIW. Here in contrast to the first two areas the noise is relatively small. The differences in temperature for the previously described parameters gives very analogous results, with a very similar structure. The section wide averaged RMS is 0.6°C for the float realisations and 0.7°C for the climatology, therefore the plots are not shown separately.

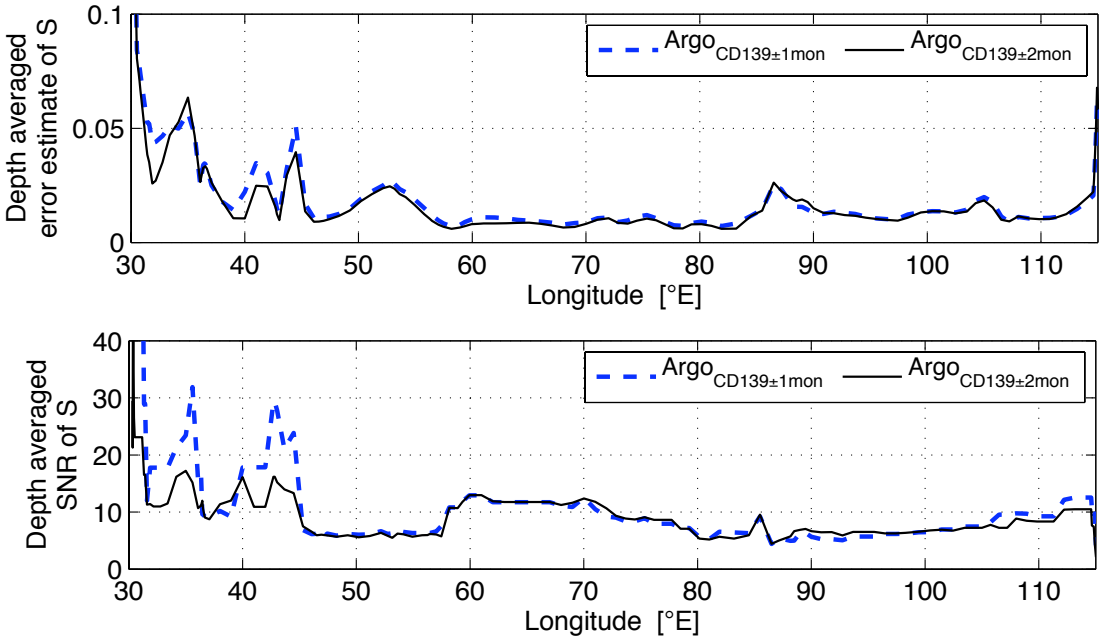

FIGURE 3.16: Different vertical averaged parameters along CD139 cruise track using float realisations with different temporal coverage ($\text{Argo}_{\text{CD139}\pm1\text{mon}}$: blue dashed; $\text{Argo}_{\text{CD139}\pm2\text{mon}}$: black). *Top:* Error estimate for salinity from OI. *Bottom:* Signal-to-noise ratio for salinity given by the OI.

Finally the differences between the two float realisations are very small if vertically averaged properties are used. Taking into account the larger number of profiles in total and also at each station grid point (not shown), but also the better representation of the small scale signals in the east, float realisation $\text{Argo}_{\text{CD139}\pm\text{2mon}}$ has been chosen for a detailed comparison. Compared to the climatological values the float realisation show better accuracy than the WOA01 climatology on average better than 0.01 in salinity (Fig. 3.17) and 0.1°C in temperature (figure not shown separately) for the whole section. Generally the RMS of the salinity difference from $\text{Argo}_{\text{CD139}\pm\text{2mon}}$ is smaller compared to that one from WOA01. The averaged RMS of salinity difference along the whole section is 0.051 for the float realisation, 0.063 for the WOA01 and 0.056 for the WOA05 climatological section respectively. It is not surprising that the averaged RMS of salinity difference is smaller for WOA05 since this dataset contains hydrographic data available until 2004, including cruise and float measurements. Near Mozambique Plateau (MOZP) the RMS of the float realisation is much larger than for the climatological sections. Here the averaged salinity difference shows a positive bias in the float realisations, especially west of 45°E, where contributing profiles come from as far north as 27°S (Fig. 3.17 and 3.13). In the basin interior there remains a small positive bias possibly resulting from the broad northward position of the floats, for example between 60°E and 90°E all profiles are taken a bit further north than the original cruise CTD stations (Fig. 3.13).

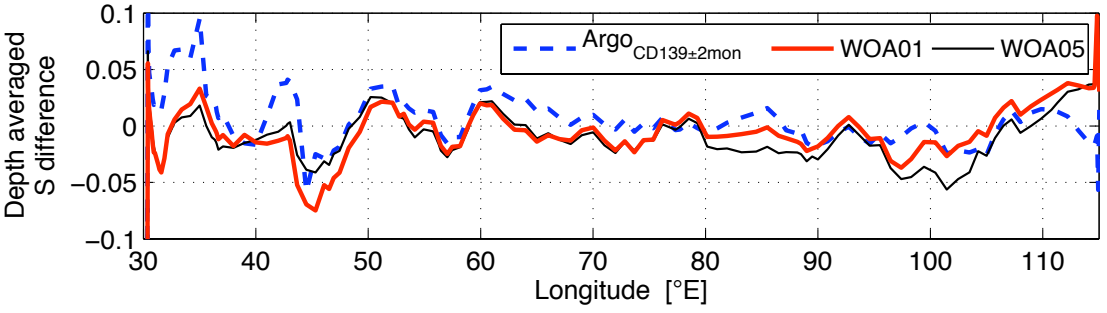

FIGURE 3.17: Vertical averaged salinity difference (referenced to CD139ma5pt) along CD139 cruise track comparing different datasets ($\text{Argo}_{\text{CD139}\pm\text{2mon}}$: blue dashed; WOA01: red thick; WOA05: black).

Generally an agreement within 0.05 in salinity and 0.6°C in temperature was achieved along 32°S, keeping in mind that almost no float profiles existed in that region before the cruise took place. This comparison confirms that Argo data have the capability to reproduce hydrographic sections as shown recently for the North Atlantic (HADFIELD ET AL., 2007). Even a global operation system such as Argo cannot

replacement for single/repeated hydrographic shipboard measurements or mooring arrays nor extensive numerical modelling. It is clear that the Argo data need a high quality reference dataset for the DMQC procedure, but, in regions where hydrographic shipboard measurements are sparse (due to less sampling or ice coverage for example), the Argo float data provide a good estimate to fill the spatial and temporal gaps in the observational system so that low-frequency variability on basin wide scales can be resolved. The Argo data in this study are used to resolve interannual and seasonal variability within the 5 year period 2002-2006, when repeated hydrographic shipboard observations are sparse.

Property sections along CD139 cruise track at 32°S: The floats deployed during CD139 cruise have been adjusted to drift at parking pressure for almost 10 days (the standard cycle time for Argo floats). Hence, during that 60 days time period there are generally less profiles available from the floats deployed the further east (Fig. 3.18), as the cruise direction was from West to East. Only between 88°E and 106°E does a better spatial coverage exist where 6 floats provided 63 profiles compared to the part of the section between 58°E and 88°E where 7 floats provided only 54 profiles. Therefore, between 88°E and 106°E a large number of profiles is used in the OI although it is at the eastern end of the section. The largest number of profiles occurs near 55°E, where the larger zonal decorrelation length scale Lx_E of 600 km applies and only half of the time of the cruise has past.

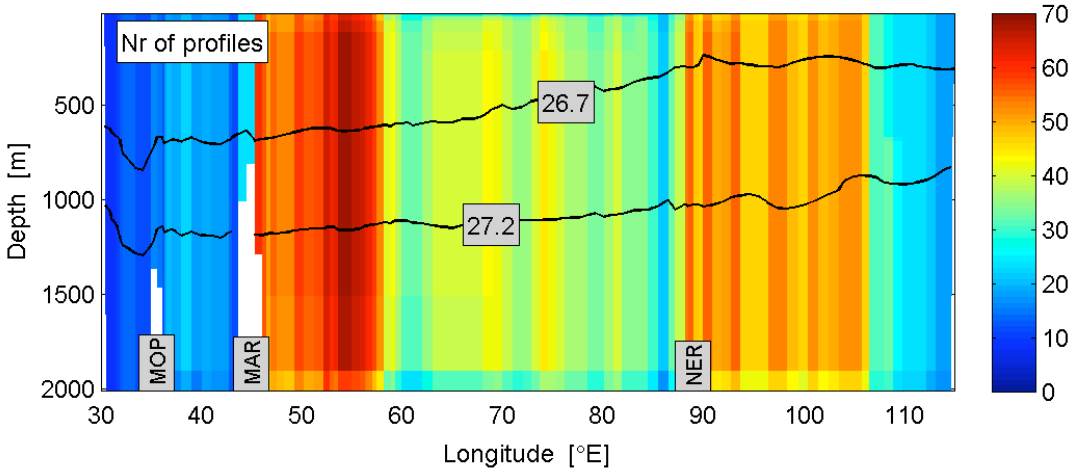

FIGURE 3.18: Section along CD139 cruise track showing number of profiles taken into account during the OI for realisation $\text{Argo}_{\text{CD139}\pm 2\text{mon}}$ at each grid point and on each 20 dbar pressure surface to estimate salinity and temperature.

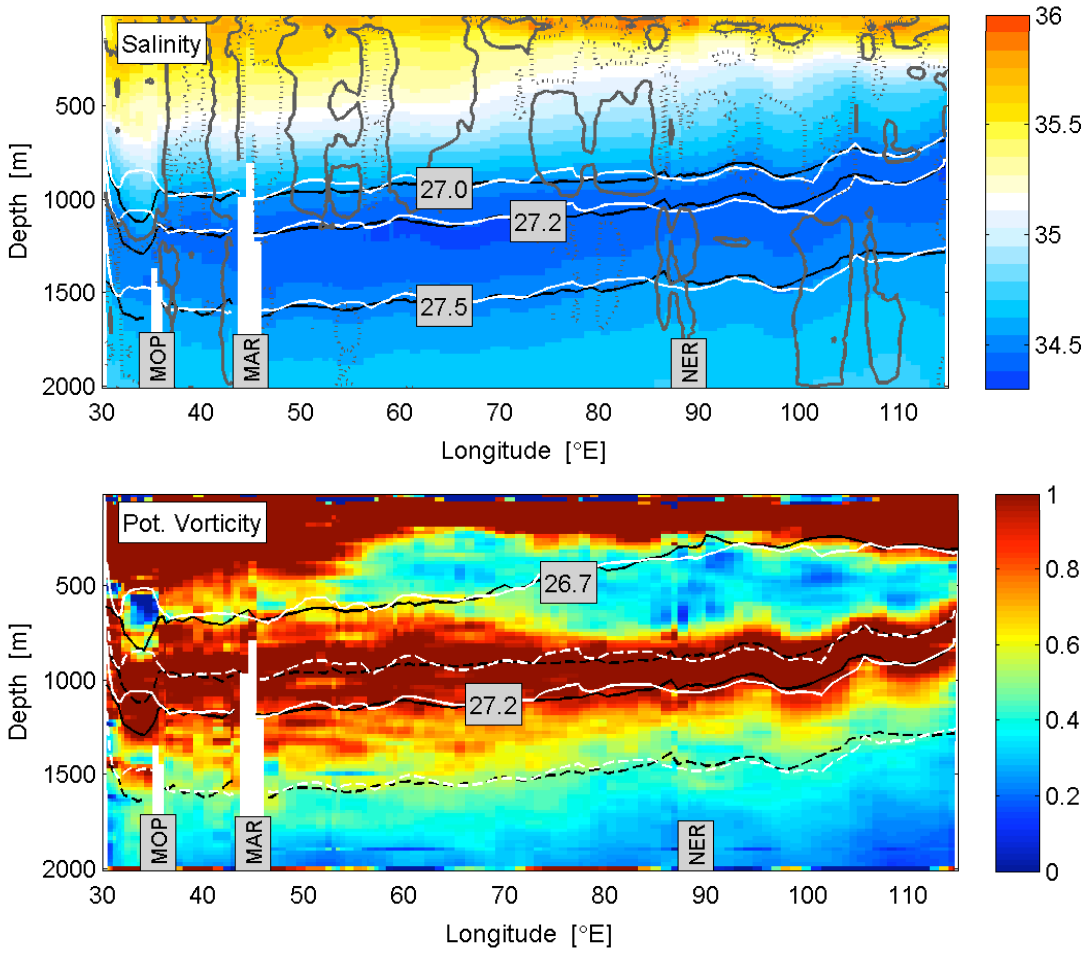

FIGURE 3.19: Section along CD139 cruise track for salinity (top) showing as grey contours the 0.02 (solid) and -0.02 (dotted) salinity difference $\text{Argo}_{\text{CD139}\pm\text{2mon}}$ - CD139ma5pt; also shown potential vorticity (bottom). Contour lines show potential density for $\text{Argo}_{\text{CD139}\pm\text{2mon}}$ float realisation (black) and CD139ma5pt smoothed cruise data (white). The $\sigma_\Theta = 26.7$ indicates the SAMW level while $\sigma_\Theta = 27.2$ indicates the AAIW horizon respectively. Additional contours shown are $\sigma_\Theta = 27.0$ and $\sigma_\Theta = 27.5$ (dashed white). Major topographic features like Mozambique Plateau (MOZP), Madagascar Ridge (MADR) and Ninetyeast Ridge (NER) are included.

The general characteristics of the CD139 section are well reproduced from the OI of Argo profiles. For example, the core of the AAIW, which is characterised by the minimum in salinity, decreases in depth from 1200 dbar at 39°E to 850 dbar at 114°. The major differences in salinity between $\text{Argo}_{\text{CD139}\pm\text{2mon}}$ and CD139ma5pt exist above 1000 dbar and in the western boundary region (Fig. 3.19 top). Between 45°E and 85°E mainly positive anomalies exist of up to 0.02, while east of 90°E anomalies are mainly negative. Between 100°E and 110°E two deep patches exist showing a increase in salinity of 0.02 compared to the smoothed cruise data. This agrees partially with findings from KING AND MCDONAGH (2005). They found float salinity being fresher on an

isotherm at the core of SAMW compared to CD139 cruise data. For the temperature differences a very similar distribution exists, with positive anomalies of up to 0.2°C between 45°E and 85°E whereas between 90°E and 106°E above 500 dbar the float estimate is up to -0.2°C cooler. From the density field, derived from the interpolated salinity and temperature fields, potential vorticity (PV) can be calculated ($PV = |f|/\rho \cdot d\rho/dz$, where f is the Coriolis parameter, ρ the density and z is the depth). Then the core of SAMW can be identified by the minimum in PV along the section (Fig. 3.19 bottom). In the far east a stronger minimum exists in PV characteristic for the SEISAMW centred between 85°E and 100°E below 400 dbar. In contrast the AAIW has larger PV indicating a less homogenised water mass. Generally, if density is needed for the final calculations, it is also possible to map density directly, instead of temperature and salinity separately. The advantage of mapping density directly is that possible artificial cabbeling is avoided. The cabbeling results from the non-linear contributions of temperature and salinity in the density equation. In this study, temperature and salinity are mapped separately and contributions of possible cabbeling are included in the error estimates, at least partly, for the later transport calculations, as discussed in Chapter 4.1.1.1.

With a better spatial and temporal coverage it is expected to get even better results. Next the section along 20°S taken in 2003/2004 is compared with interpolated float data, here more profiles are available before the cruise which could improve the accuracy.

3.2.2 Comparison of the 2004's cruise data along 20°S with optimal interpolated Argo float data

The approach described in the previous section (Section 3.2.1) is now used, with the aim to reproduce the BEAGLE hydrographic transect along 20°S taken between the 9th of December 2003 and the 24th of January 2004. During that cruise, 13 Argo floats have been deployed between 55°E and 95°E (Uchida and Fukasawa, 2005), again a region that was only sparsely covered with profiles up to this date.

Three different temporal coverages of float data have been used to interpolate onto the cruise CTD stations. The first dataset covers only the 55 day period of the cruise ($Argo_{BEAGLE\pm0mon}$) with 78 profiles used out of 308 available ones for the whole subtropical gyre region. The second dataset covers 1 month before and after the cruise dates, in total about 100 days covered by 222 profiles out of 826 ($Argo_{BEAGLE\pm1mon}$). The third dataset expands the time period by 2 months before and after the cruise ($Argo_{BEAGLE\pm2mon}$). This dataset takes into account 359 profiles out of 1348 available

ones (Fig. 3.20). Here again the dataset using only the time period of the cruise is rejected because of an insufficient number of deep profiles. In this area a large number of floats are adjusted to drift at 1000 dbar parking pressure and only every 7th profile is taken from 2000 dbar depth to the surface. So in total only about 50% of the profiles reach to 2000 dbar. As previously, the comparison is focussed on the two realisations extending the cruise period by 1 months ($\text{Argo}_{\text{BEAGLE}\pm1\text{mon}}$) and 2 months ($\text{Argo}_{\text{BEAGLE}\pm2\text{mon}}$), respectively, to avoid stations being filled with first guess climatological values from WOA01.

Again a 5-point moving average is applied to the original cruise data to analyse the depth averaged difference in salinity and temperature to the smoothed cruise data (BEAGLEma5pt). The RMS of the salinity differences derived from the float realisations referenced to BEAGLEma5pt shows less agreement with the RMS taken from the salinity difference of the original and the smoothed cruise data. Especially in the western boundary region and on both sides of Madagascar the values differ by a factor of two (Fig. 3.21). For the whole section the mean RMS of the salinity differences is about 0.05 for both float realisations, which is 0.01 smaller than the values calculated for the cimatological section derived from WOA01. The averaged salinity difference is slightly positive with 0.003 for $\text{Argo}_{\text{BEAGLE}\pm1\text{mon}}$ and 0.004 for $\text{Argo}_{\text{BEAGLE}\pm2\text{mon}}$ respectively. Here these values do not further reduce if only the part of the section east of 45°E is used. The vertically averaged error in salinity estimated by the OI is 0.035 for both float realisations averaged for the whole section with little difference in the structure. Also the vertical averaged SNR is quite similar for both realisations with values of more than two for the whole section. Nevertheless the number of profiles contributing at each station grid point differs greatly with $\text{Argo}_{\text{BEAGLE}\pm2\text{mon}}$ including

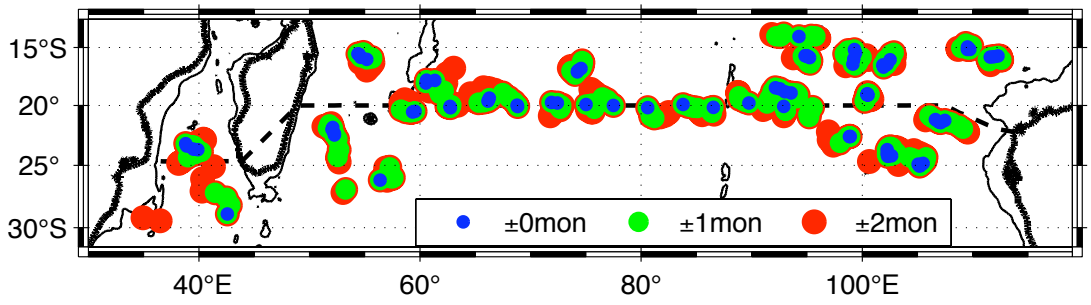

FIGURE 3.20: Positions of Argo float profiles used for interpolation onto BEAGLE cruise stations (track shown as black dashed line), within the cruise period only (blue dots) and within ±1 month (green dots) and within ±2 months (red dots) of the cruise date respectively. Contour lines highlight coastline (bold) and 1900 m isobath (thin).

between 30% to 50% more profiles at most of the stations. Therefore, the float realisation $\text{Argo}_{\text{BEAGLE}\pm 2\text{mon}}$ is chosen which extends the cruise period by ± 2 months for a more detailed comparison of the properties.

Property sections along BEAGLE cruise track at 20°S Although the BEAGLE cruise was taken in 2003/2004, about 18 months after the CD139 cruise, the spatial coverage is still very sparse due to the fact that only 13 Argo floats had been deployed during that cruise along 20°S. Additionally, the majority of the floats in that region are adjusted to a parking pressure of 1000 dbar which reduces the number of deep profiles and also produces areas without any profiles at the eastern flank of Madagascar between 49°E and 54°E (Fig. 3.22). Additionally, at depth the estimates depend heavily on profiles from one or two floats only which could include a possible bias by malfunctions not detected during the delayed-mode quality control.

The characteristic properties at 20°S are well reproduced by the $\text{Argo}_{\text{BEAGLE}\pm 2\text{mon}}$ estimate. Along the whole transect a salinity maximum exists above the $\sigma_\Theta = 26.4$ isopycnal with its core at 250 dbar. Near the surface lower salinities between 34.85 and 35.1 exist (Fig. 3.23). At depth between 1000 dbar and 700 dbar, decreasing to the

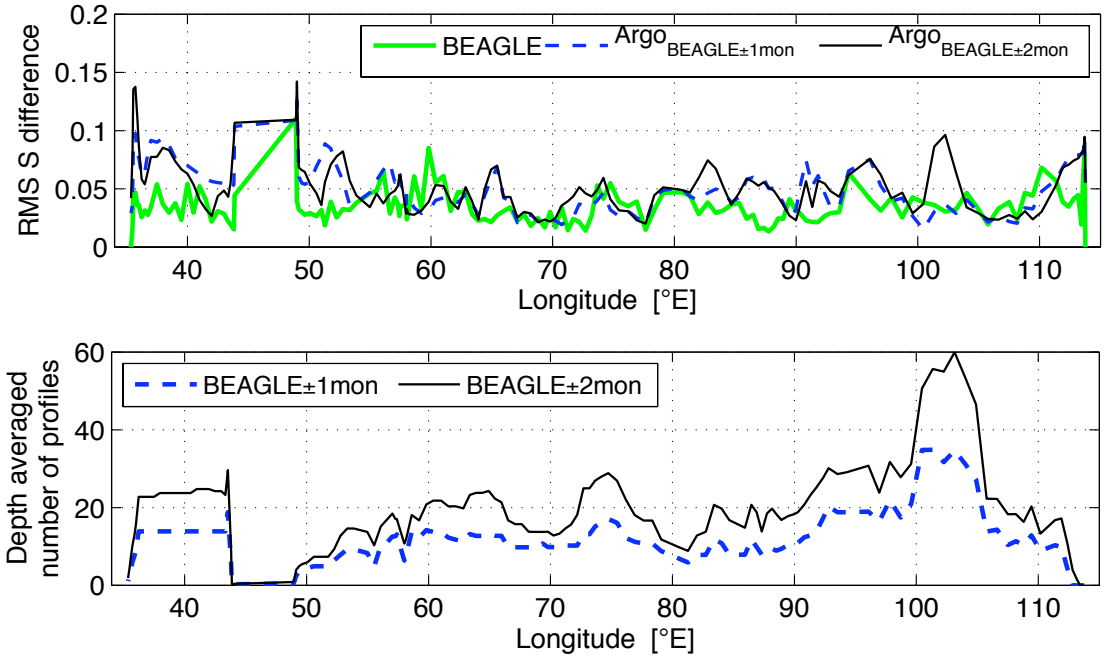

FIGURE 3.21: Top: Root-mean-square of salinity difference between original and smoothed cruise data (green) and between float realisations and smoothed cruise data ($\text{Argo}_{\text{BEAGLE}\pm 1\text{mon}}$: blue dashed; $\text{Argo}_{\text{BEAGLE}\pm 2\text{mon}}$: black). Bottom: Vertical averaged number of profiles along BEAGLE cruise track taken into account for the OI.

east, the minimum in salinity related to the AAIW appears. A freshening of 0.02 exist between 65°E and 90°E in the core of the SAMW and upper thermocline waters up to the maximum salinity zone above the $\sigma_\Theta = 26.4$ isopycnal. Simultaneously that part of the section appears to be cooler too in the $\text{Argo}_{\text{BEAGLE}\pm 2\text{mon}}$ realisation. The water mass with the minimum in PV containing the SAMW and SEISAMW, has decreased in its vertical extent, has deepened and is less homogeneous compared to the CD139 section at 32°S as the SAMW spreads northward away from its formation region south of 45°S. The floats provide useful and good data to reproduce the BEAGLE cruise section but caution is needed because of the small number of contributing profiles at each station. Although the cruise took place much later in the Argo project period very few floats and profiles could be used because many profiles did not go to 2000 dbar. With a better spatial and temporal resolution the results could be improved further with reduced differences in properties but also reduced error estimates.

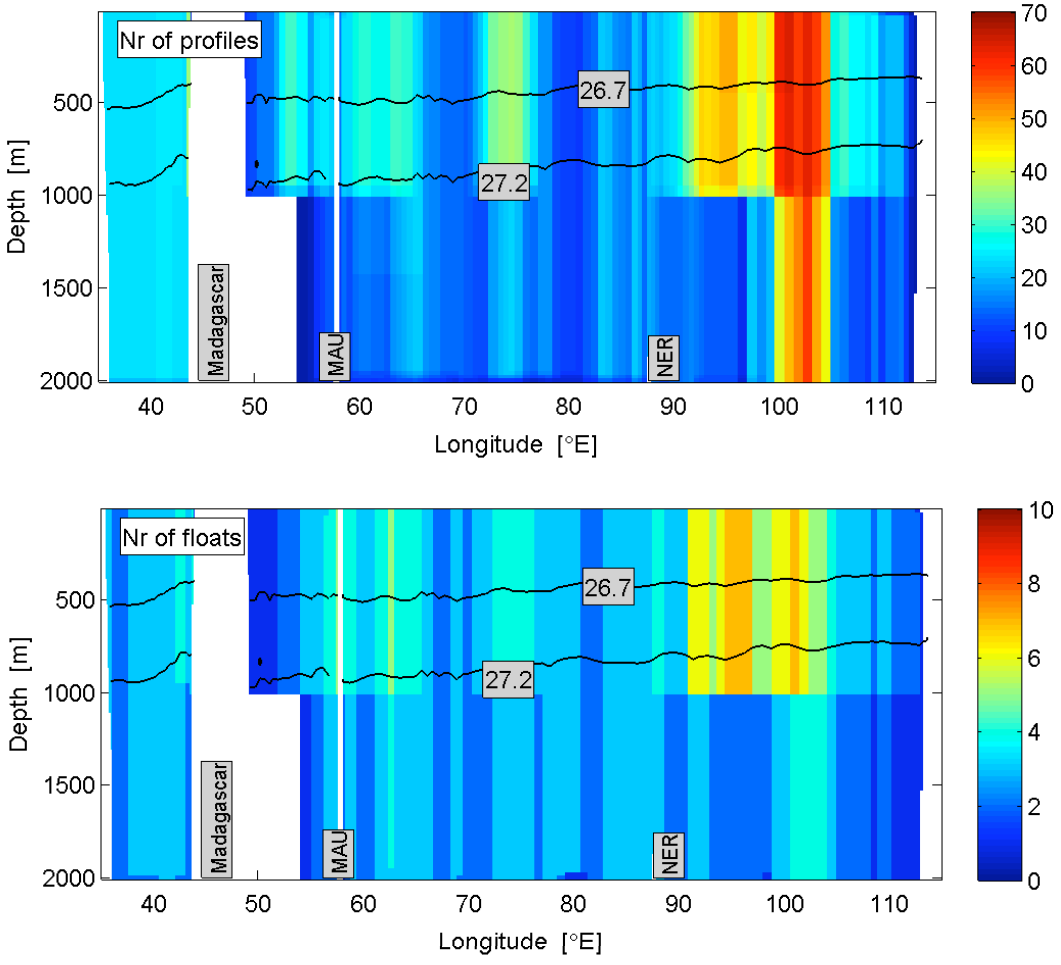

FIGURE 3.22: Number of profiles (top) and number of individual floats (bottom) taken into account by the OI to estimate salinity and temperature at each grid point and on each 20 dbar pressure surface for $\text{Argo}_{\text{BEAGLE}\pm 2\text{mon}}$ realisation.

Finally, it is concluded that at the present time, for the upper ocean (≤ 2000 dbar) the floats could reproduce hydrographic sections even without a temporal weighting in the OI and therefore, they could be used to generate sections when no shipbased observations are available to fill spatial and temporal gaps in hydrographic datasets. Compared to the WOA05 climatology the OI float profiles provide better accuracy in reproducing the CD139 and BEAGLE section, although the majority of the cruise and float data have been included into the dataset World Ocean Database 2005 (WOD05) to generate the climatology. The good quality and spatial and temporal density of the DMQC Argo float data could make it possible to generate a global float climatology as well as annual and seasonal hydrographic fields.

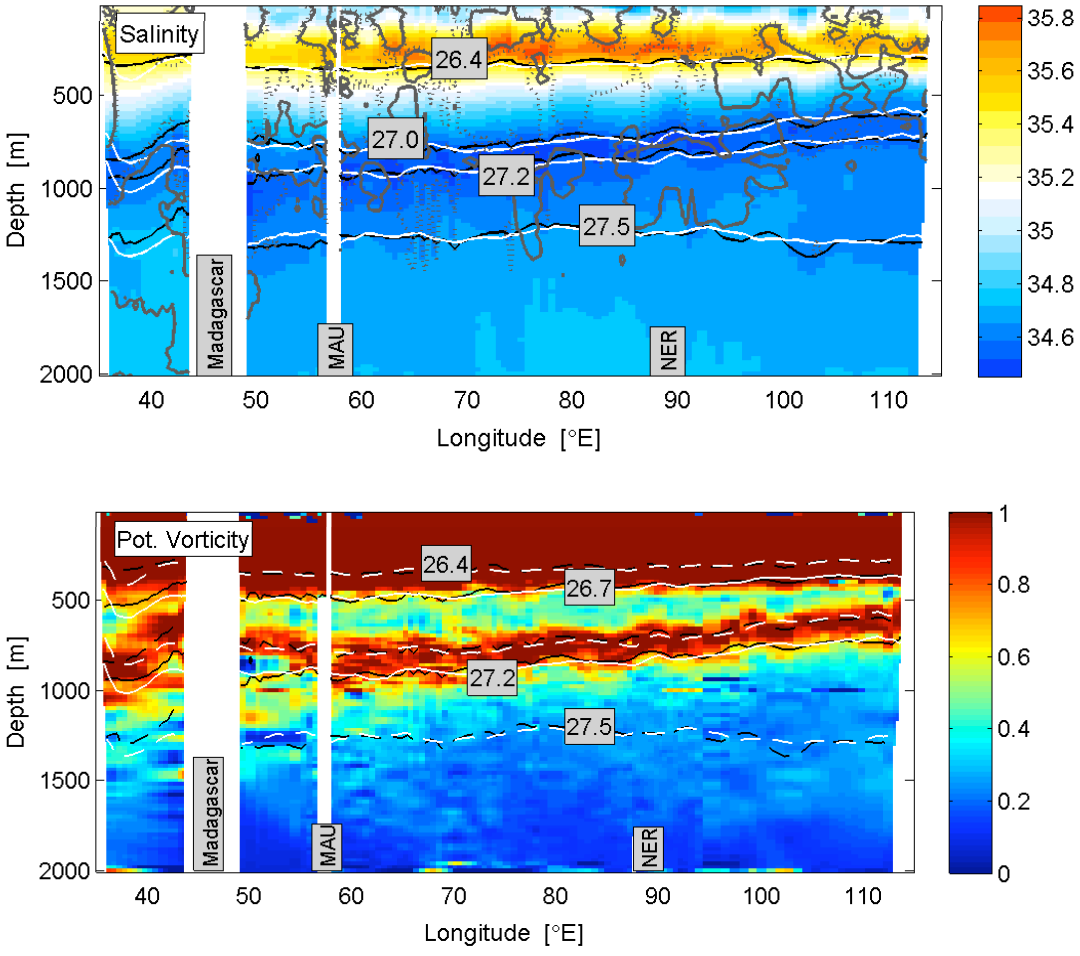

FIGURE 3.23: Salinity estimated by the Optimal Interpolation using Argo profiles from the time period of the BEAGLE cruise extended by ± 2 months ($\text{Argo}_{\text{BEAGLE}\pm 2\text{mon}}$) objectively mapped onto cruise CTD stations (top) and derived potential vorticity times 10^{-10} (bottom). Contour lines show potential density. The $\sigma_\Theta = 27.0$ and $\sigma_\Theta = 27.2$ line indicate the Antarctic Intermediate Water level. Major topographic features like Madagascar, Mauritius (MAU) and Ninetyeast Ridge (NER) are included.

3.3 Mean velocities from float's subsurface drift

In this section a simple method to estimate reference velocities from floats subsurface drift is described, followed by an overview of the float realisations used in this context.

The floats are programmed to drift on a predefined parking pressure level during their subsurface drift (Chapter 2.1). In the subtropical SIO the most common parking pressure values are 1000 dbar, 1900 dbar and 2000 dbar with a share of 48%, 13% and 30% respectively of the total trajectories. These are used here for further calculations, although at 32°S the 1000 dbar surface is at the AAIW level and will have larger errorbars than the deeper level. In contrast at 20°S this level at mid-depth might be useful as a reference due to small vertical shear between 1000 dbar and 2000 dbar (Warren, 1981) promising smaller error estimates in the reference velocities. Furthermore 6% of the floats are adjusted to drift at 1500 dbar and 3% at 350 dbar, respectively.

The parking pressure velocities were calculated by using the time and position reported in the trajectory data of each float (Carval et al., 2006). Here all time and position transmissions during the surface drift are recorded, so the last valid reported time and position can be used as the initial point of the following subsurface drift. And the earliest reported time and position in the following surface period can be used as the endpoint. This is a more simplified solution to derive the parking pressure velocities than described by Park et al. (2005), but at least it is realisable with more than 200 floats using different recording formats. Soon there will be a product available which allows the application of the method from Park et al. (2005) to all available floats in the region of interest (B. King; pers. comm).

This method largely reduces one of the major source of uncertainties, i.e. the displacement during the surface drift which has been shown to be highly important in analysing deep western boundary current export pathways in the North Atlantic (Getzlaff et al., 2006). Uncertainties from the reported position accuracy by the positioning system are estimated as about 1000 m using a weighted mean. That gives an error in the estimated velocities of $\epsilon_{pos} = 0.12\,\mathrm{cm/s}$. Park et al. (2005) estimated a typical drifting distance of 1300 m as a result of velocity shear for the subtropical South Indian Ocean using data from WOD98 (Levitus et al., 1998), assuming uniform ascent and descent velocities of about 8 cm/s. So ϵ_{asc_desc} gives the error for the velocities as a result of this displacement by the velocity shear during ascent and descent and is estimated to be $\epsilon_{asc\_desc} = 0.45\,\mathrm{cm/s}$. The error indicated by ϵ_{nosat} includes the unknown distance a float drifts at the surface before its position is determined by an Argos satellite and the estimation of this error contribution is somewhat difficult. A good approximation as upper error margin is $\epsilon_{nosat} = \epsilon_{asc\_desc}/3$ since the error

associated with the ascent and descent occurs within 14 hours while a drift of less than 6 hours without satellite contact is assumed. This is the same order as Davis (2005) reports for random errors associated with untracked surface motion. These errors are assumed to be independent, then the total error of the velocities at parking pressure can be estimated by

$$\epsilon = \sqrt{\epsilon_{pos}^2 + \epsilon_{asc\_desc}^2 + \epsilon_{nosat}^2} \tag{3.11}$$

and with the previously estimated values this gives an upper error estimate of $\epsilon = 0.49\,\mathrm{cm/s}$.

In the late stage of this work an updated product of surface and subsurface velocity datasets estimated from float trajectories became available (Lebedev et al., 2007). Although this new product was not used in this study a comparison of the results from the interpolated float data along CD139 cruise track or 32°S showed only marginal differences, while this new product provides a more detailed error estimate.

3.3.1 Adjustments made in the Optimal Interpolation algorithm to be used to estimate subsurface velocities

For the estimates of reference velocities the previously described OI is utilised. But small adjustments to the OI method need to be applied, because no background climatology of subsurface velocities is available yet. That means equation 3.3 can be written as

$$V^{obj} = \langle V \rangle + w \bullet (V - \langle V \rangle) \tag{3.12}$$

where V^{obj} denotes the final objective meridional velocity estimate, $\langle V \rangle$ denotes the mean of the meridional velocities from the float velocity data, w is the coefficient weighting matrix using the decorrelation scales, $V = [V_1, ..., V_N]$ is the set of meridional velocity estimates from the selected float profiles on each grid point. The use of $\langle V \rangle$ instead of a background velocity field means that V itself is mapped rather than deviations from a background

There exist a variety of different pressure levels used to adjust the Argo float data (350 dbar, 500 dbar, 1000 dbar, 1500 dbar, 1750 dbar, 1900 dbar and 2000 dbar), with the largest contribution coming from floats drifting at 1000 dbar, 1900 dbar or

2000 dbar, respectively. For the deep velocity estimate, floats drifting at the 1900 dbar are used, together with floats drifting at 2000 dbar. The final velocity estimate is labelled with 1900 dbar. For the intermediate-depth velocity estimate solely data from floats that drift at 1000 dbar are used, since no additional parking pressure level exists within ±100 dbar.

3.3.2 Float realisations to estimate reference velocities

Several realisations have been generated to use for the comparison with the reference velocities derived from the inverse calculations from McDonagh et al. (2008) along the CD139 cruise track (Chapter 5), but also to evaluate the estimates of a zero-velocity (ZV) assumption for later transport calculations (Chapter 4.1 and 4.2), an overview is given in table 3.5.

Table 3.5: Float realisations generated from Argo float subsurface velocity dataset with different temporal and spatial resolutions either along CD139 cruise track or on a regular 1° x 1° grid for the subtropical South Indian Ocean.

Name	temporal coverage	region/latitude
$\text{Argo}_{\text{CD139}\pm1\text{mon}}$	04.02.2002 - 14.05.2002	CD139 cruise track
$\text{Argo}_{\text{CD139}\pm2\text{mon}}$	04.01.2002 - 14.06.2002	CD139 cruise track
CD139_2002	year 2002	CD139 cruise track
CD139_AUT	autumn	CD139 cruise track
SIO_02	year 2002	25°E - 125°E; 45°S - 18°S
SIO_03	year 2003	25°E - 125°E; 45°S - 18°S
SIO_04	year 2004	25°E - 125°E; 45°S - 18°S
SIO_05	year 2005	25°E - 125°E; 45°S - 18°S
SIO_06	year 2006	25°E - 125°E; 45°S - 18°S
SIO_SPR	spring (SON)	25°E - 125°E; 45°S - 18°S
SIO_SUM	summer (DJF)	25°E - 125°E; 45°S - 18°S
SIO_AUT	autumn (MAM)	25°E - 125°E; 45°S - 18°S
SIO_DEC	winter (JJA)	25°E - 125°E; 45°S - 18°S

3.4 Summary

This chapter introduced and described the different methods used to prepare regularly gridded data for the analysis, with a major focus on the OI but also on the simple method to derive reference velocities from floats subsurface drift.

It is beyond the scope of this work to evaluate the possible techniques to generate a regularly gridded field from the Argo data (e. g. averaging on isopycnal surfaces (Ridgway and Dunn, 2007) or objective analysis (Gille, 2003)). The described OI is chosen because it finds successful appliance in the DMQC procedure (Wong et al., 2003; Böhme and Send, 2005; Owens and Wong, 2008) and it is used in several studies analysing Argo float data (e. g. Guinehut et al. (2002); Wong (2005b); Hadfield et al. (2007); Roemmich et al. (2007)). The final application of the optimal interpolated data is to derive geostrophic velocity and transport fields to estimate the gyre transport, therefore the OI is applied on pressure levels.

The OI is presented in two parts, with the first step allowing a pre-selection of data, mainly to speed up the routine and the second step including the actual distance weighting according to the spatial data-grid and data-data covariance matrices. This technique assumes knowledge of the spatial correlation structure of temperature and salinity (Wong et al., 2003). Therefore, a method to estimate spatial decorrelation length scales is presented, using the WOA01 climatology together with recent hydrographic cruise sections at 20°S, 32°S and 95°E but also together with the DMQC Argo float data along these sections. From the vertical profiles of decorrelation length scales representative scales for the meridional and zonal directions are estimated. The zonal scales are $\mathrm{Lx}_W = 200\,\mathrm{km}$ for the greater western boundary region west of 45°E, $\mathrm{Lx}_E = 600\,\mathrm{km}$ for the area east of 45°E and $\mathrm{Ly} = 400\,\mathrm{km}$ as meridional scale. The main focus of this work is the assessment of annual and seasonal averages from the float data. Therefore, a temporal separation (in the sense of a separate temporal decay scale (ΔT)) is neglected in the configuration of the OI (Sec. 3.1.2).

The accuracy of the OI is tested by resampling cruise tracks along 32°S and 20°S. These are then compared with 5 point box averaged smoothed data from the CD139 cruise in 2002 and from the BEAGLE cruise in 2003/2004, respectively. Float realisations extending the cruise periods by ± 1 month and ± 2 months, respectively, are compared. The results indicate only marginal differences in both realisations. At 32°S, the mean RMS difference between the salinity of the float realisations and the smoothed cruise data was about 0.05 for both sections, which was still 0.01 smaller than the mean RMS of salinity differences from WOA01 with the smoothed cruise data (CD139ma5pt). The mean RMS of temperature differences showed similar results with 0.5°C for the float realisations and 0.6°C for the WOA01 climatology. At 20°S similar results are achieved for the mean RMS of salinity and temperature differences, respectively. The accuracy of the method is good and comparable with recent results at 36°N in the North Atlantic (Hadfield et al., 2007), keeping in mind that for the float realisation a maximum of 213 profiles near 32°S and 359 profiles near 20°S

were available within the ± 2 months period with most of these sampled after the cruise period and additionally, that no temporal separation is included in the OI.

Lastly, a simple method is described to derive reference velocities at depth from floats subsurface drift. This method bears relatively large errors from unknown drift during ascent/descent of the floats and from the surface time without contact to a satellite. These errors are estimated based on earlier estimates from Park et al. (2005) and an upper error of $\epsilon = 0.49\,\mathrm{cm/s}$ is given. The subsurface velocities are used later to generate reference velocities at 32°S and 20°S for comparison.

Chapter 4

Changes in the South Indian Ocean gyre circulation

On large scales the winds drive the ocean circulation in the upper thousand meters by transmitting momentum and vorticity to the ocean surface, forcing anticyclonic subtropical and cyclonic subpolar gyres in each ocean basin. The subtropical gyres have the crucial role in the climate system to export heat gained in the tropics to the Poles. In the IO the situation is different, due to it's closed northern boundary and the lack of a subpolar region in the north and due to the IO's direct connection to the Pacific Ocean via the Indonesian Passages which is a pathway for warm surface waters (Gordon and Fine, 1996). Consequently all heat gained through the ITF and further north, has to leave the Indian Ocean in the south (Fu, 1986; Lee and Marotzke, 1998), mainly with the AC in the southwest corner, feeding the upper limp of the northward thermohaline transport in the South Atlantic (Gordon, 1986). The subtropical SIO is of major interest, because it connects the equatorial Indian Ocean and its major export path in the south west, the *Agulhas Current* (AC). This connection is largely accomplished by narrow currents or eddy propagations in the Mozambique Channel (MOZC) and the east of Madagascar (MAD), respectively (De Ruijter et al., 2004; Schouten et al., 2002; Quartly and Srokosz, 2004). While the boundary regions and its low-frequency variability have been in the focus of recent studies (Schouten et al., 2002; Palastanga et al., 2006; Matano et al., 2008; Birol and Morrow, 2001, 2003), only little is known on the variability of the interior subtropical gyre, in strength and structure. Recent studies that focussed on the subtropical SIO's flow structure and variability conclude that although understanding of the variability in the SIO has been achieved, mainly from model and altimeter data,

these findings need further validation by direct hydrographic observations (Palastanga et al., 2006; Matano et al., 2008).

Recent analyses reported decadal changes in the gyre circulation of the SIO at 32°S over the past 50 years (Bindoff and McDougall, 2000; Palmer et al., 2004; McDonagh et al., 2005) as well as for the South Pacific (Roemmich et al., 2007), indicating an increase in gyre strength. Palmer et al. (2004) reported an increase in the gyre strength of up to 40% estimated from three hydrographic transects along 32°S in the SIO taken in 1987, 1995 and 2002. They showed that most of the change happened between 1995 and 2002. Furthermore, they concluded that there has been a persistent change between the flow structure of the 1987 and 2002 sections, that can be seen by the westward shift of the maximum southward transport (in 1987 this maximum is located at 55°E, while in 1995 at 45°E and in 2002 at 40°E, respectively). This increase between 1987 and 2002 reverses the reported slow-down of 20% of the gyre circulation between 1962 and 1987 (Bindoff and McDougall, 2000). Their results are based on property changes and changes in dissolved oxygen concentrations and they show a freshening of the upper thermocline waters. In contrast the 2002 upper thermocline waters were found to be saltier on isotherms than the 1987 estimates (Bryden et al., 2003b; McDonagh et al., 2005), their results are based on five hydrographic transects taken in 1936, 1965, 1987, 1995 and 2002. Note, that the 1995 cruise data are not used in this study, due to the sparse coverage in the interior resulting from the different cruise tracks compared to 1987 and 2002. In this context, Argo float data are used to provide estimates of changes in the SIO gyre circulation over the 5 year period 2002 to 2006. Using the dynamic method (Sec. 4.1 and 4.2) based on geostrophic and hydrostatic balance (Pond and Pickard, 1983) the results are compared with estimates using the wind-driven circulation (Sec. 4.3) as well as with altimeter data (Sec. 4.4).

4.1 Estimates of the gyre strength at 32°S

We use results from the annual realisations of the OI applied to Argo profile data to estimate the annual gyre strength and to identify possible trends in changes in the gyre circulation. In the analysis the 1° x 1° grid from the WOA01 climatology is used to avoid further interpolation of the background climatology, therefore the nominal 32°S section is at 32.5° latitude. The distribution of profiles along the 32°S section shows variations in spatial coverage (Fig. 4.1). As expected, the spatial distribution in 2002 is good with no gaps larger than 200 km, since most of the floats were deployed in the beginning of 2002 during the CD139 cruise (Bryden et al., 2003a). In 2003 there

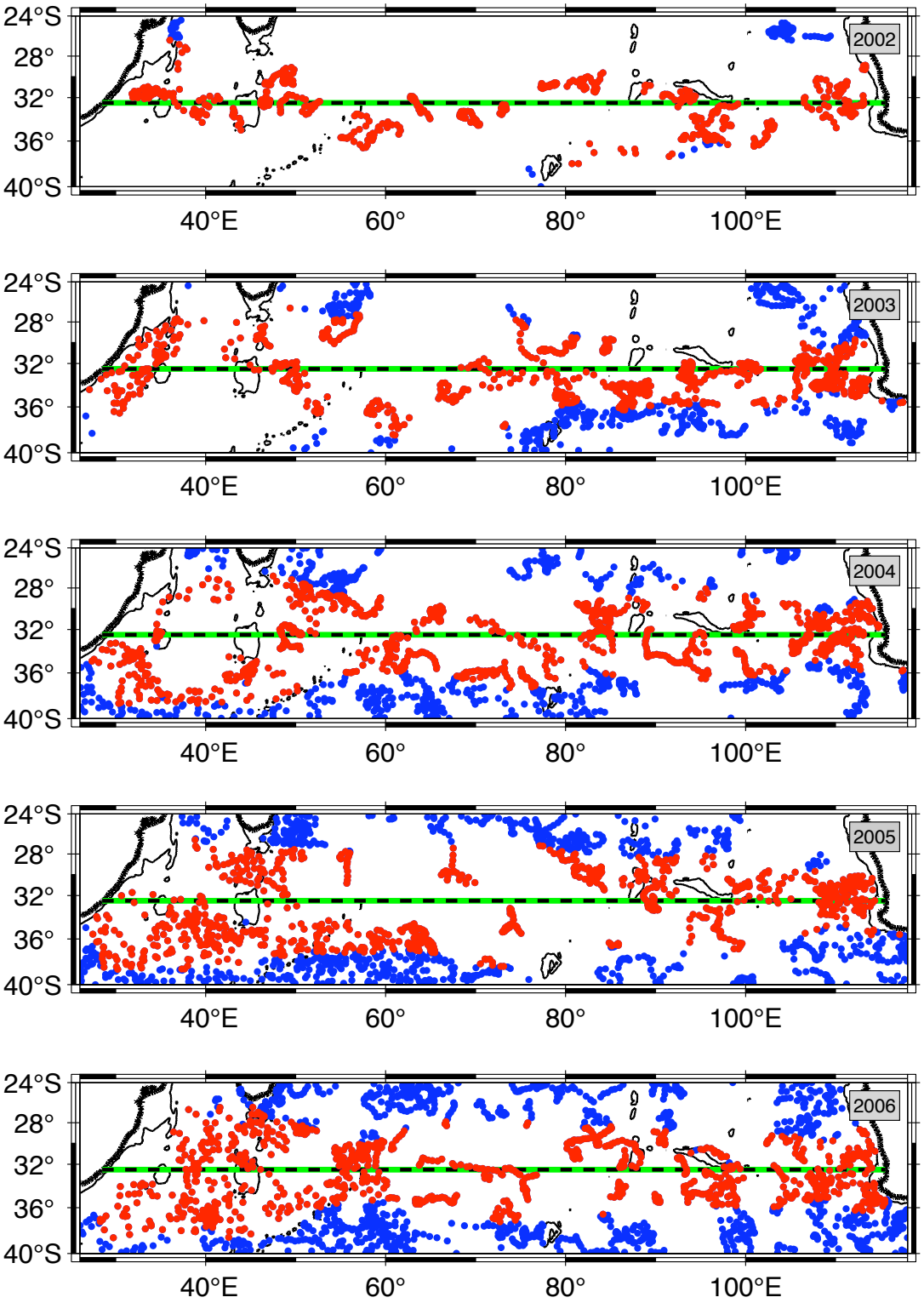

FIGURE 4.1: Maps showing annual distribution of all delayed-mode quality controlled Argo float profiles in the subtropical South Indian Ocean (blue dots) and those finally taken into account for the annual estimate of temperature and salinity from the optimal interpolation scheme (red dots) along 32°S (green and black dashed). Contours highlight 1900 m isobath (thin solid black) and coastline (bold).

exists a gap in spatial coverage of 200 km in the Madagascar Basin (MADB) which is of the order of the decorrelation length scales estimated in that region (Chapter 3.1.1). Additionally the region between 53°E and 65°E has no profiles next to the section and the gaps here are also of the order of the decorrelation length scales. The 2004 distribution map also shows a gap of profiles in the MADB between 37°E and 45°E ($\approx$ 800 km). This gap is filled by interpolated data taken into account from north of 30°S as well as from south as far as 38°S. In 2005 in the interior between 50°E and 85°E there are few profiles close by the section (closer than 200 km) with larger gaps in between ($\approx$ 800 km). The spatial coverage in 2006 is good, but here only few profiles exist west of 35°E close to the western boundary. The limitations in the spatial coverage are important for the later analysis and are also represented in the error estimate given by the OI, as shown later. Not represented in the error estimate of the OI is a possible bias of the final estimate to larger or smaller values respectively in the case when data only exist towards one side of the section. There is only one region where this might apply to, namely in 2003 around 40°E.

From the annual realisations we can now calculate geostrophic velocity fields and geostrophic transport relative to, and above 1910 dbar, using the practical form of

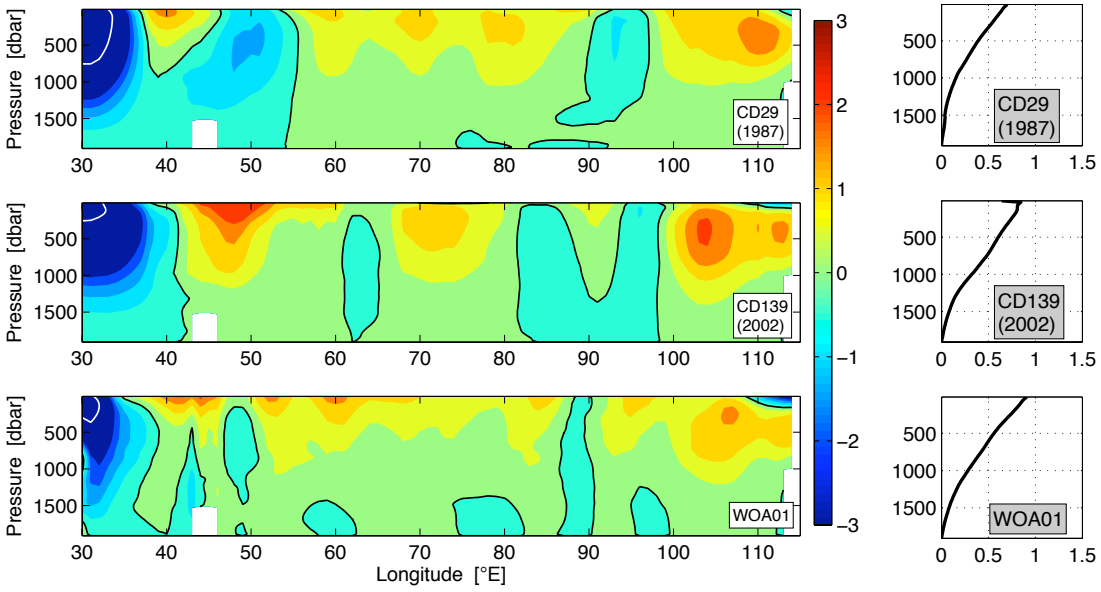

FIGURE 4.2: Left: Geostrophic velocities [in cm s^{-1}; positive values indicate northward velocities] referenced to and above 1900 dbar across 32°S, calculated from the CD29 (top) and CD139 (middle) cruise data interpolated onto 32°S and filtered with an 8°-longitude Gaussian filter (PALMER ET AL., 2004) as well as from the WOA01 climatology (bottom). Black contours indicate zero velocity and white contours indicate $\pm$5 cm s^{-1}). Right: Mean geostrophic velocity profiles [in cm s^{-1}] referenced to 1900 dbar averaged between 45°E and 110°E for the cruises CD29 (top) and CD139(middle) and the WOA01 climatology (bottom).

the geostrophic equation (Pond and Pickard, 1983). In the following we label the zero-velocity (ZV) level with 1900 dbar for ease of reading although the actual pressure level is 1910 dbar. Before the velocity sections of the float data are discussed, first a quick look at the velocity sections derived from the filtered CD29 and CD139 cruise data from 1987 and 2002 (both datasets are filtered with an 8°-longitude Gaussian filter to remove the high wavenumbers, as described by Palmer et al. (2004)) as well as from the WOA01 climatology (Fig. 4.2). The most striking feature of the changes in geostrophic velocities referenced to and above 1900 dbar between the CD29 and the CD139 cruise data is the apparent westward shift of the area of southward flow, centred at about 50°E in 1987 (Fig. 4.2 left column, 1st and 2nd panel). The main areas of change in the geostrophic velocities are just east of MADR and around Broken Plateau (BP). The greatest difference between the 1987 and 2002 sections occurs at about 50°E, where southward flow ($\leq -1\,\mathrm{cm\,s^{-1}}$) in 1987 is replaced by northward flow ($\geq 2\,\mathrm{cm\,s^{-1}}$) in 2002. Additionally, On the western side of BP (80E to 90E) a change from predominantly northward flow in 1987 to southward flow in 2002 occurs. Furthermore, there exists a strong signal of northward flow at 104°E in 2002. Palmer et al. (2004) showed that these changes are consistent with a change from downward sloping isopycnals in the west-east direction in 1987 to upward sloping isopycnals in 2002 east of MADR and vice versa around BP.

Palmer et al. (2004) showed that the zonal structure of the velocities and consequently the integrated (from west to east) geostrophic transports, referenced to and above 2230 dbar, has changed significantly. In 1987 the maximum southward transport was located around 55°E, while in 2002 the maximum southward transport was located around 35°E. This change in the structure of the gyre is important for the later analysis, since different longitudinal ranges are applied for the 1987 cruise data (55°E to 110°E) and the 2002 cruise data and Argo float data, respectively (45°E to 110°E). The strengthening of the gyre, over the period 1987 to 2002, can be seen in the northward velocities penetrating to greater depth in 2002 than 1987 (Fig. 4.2 right column, 1st and 2nd panel). The geostrophic velocity section derived from the WOA01 climatology shows strong southward velocities mainly in the western boundary region, while around MADR and BP only at the surface northward velocities of more than $1\,\mathrm{cm\,s^{-1}}$ exist. The mean velocity profile shows the same structure in depth as the one from 2002, while near the surface the velocities derived from the climatology are about $0.1\,\mathrm{cm\,s^{-1}}$ larger (Fig. 4.2 lower panel).

In contrast to the smooth velocity sections from the filtered cruise data and the climatology, the geostrophic velocities referenced to and above 1900 dbar from the annual float realisations show narrow and strong bands of alternating southward and

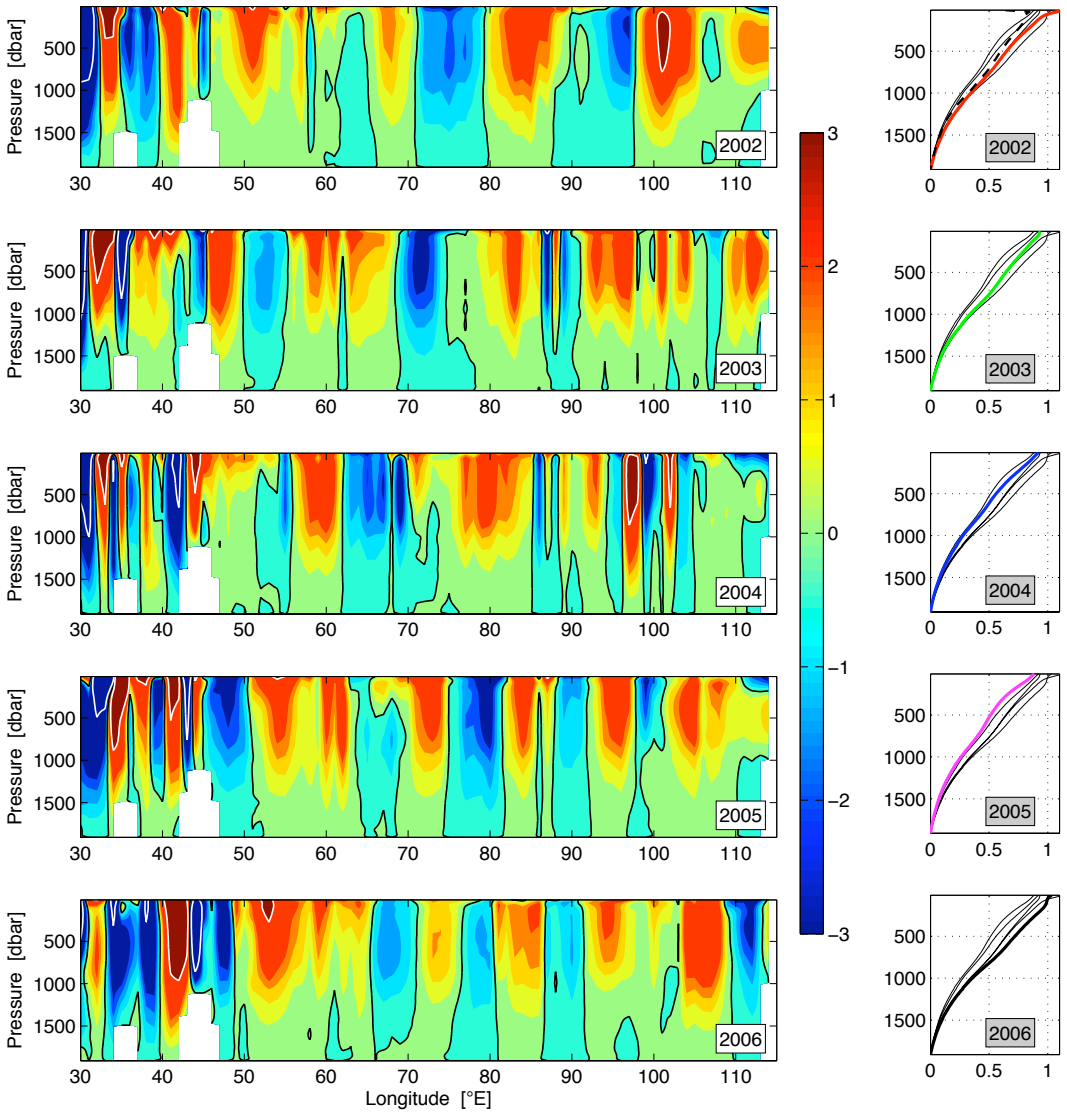

FIGURE 4.3: Left: Geostrophic velocities [in $\mathrm{cm\,s^{-1}}$; positive values indicate northward velocities] referenced to and above 1900 dbar across 32°S, calculated from annual realisations using optimally interpolated Argo profiles (black contours indicate zero velocity and white contours indicate $\pm 5\,\mathrm{cm\,s^{-1}}$). Right: Mean annual geostrophic velocity profiles [in $\mathrm{cm\,s^{-1}}$] referenced to 1900 dbar averaged between 45°E and 110°E. Each year the actual profile is shown in colour whereas the other years are shown as black lines only. In 2002 additionally the mean profile estimated from the geostrophic velocity field from the CD139cruise data interpolated onto 32°S and filtered with an 8°-longitude Gaussian filter (PALMER ET AL., 2004) is shown for comparison (black dashed).

northward flow in the western boundary region (Fig. 4.3). This results from the different spatial scales applied in the OI and with the 8°-Gaussian filter. The alternation of northward and southward flow can be attributed to mesoscale eddy activity and the recirculation signature of the AC and its retroflection in the MOZB and MADB west of 45°E. The vertical structure reaches deep to 1000 dbar or more associated with

absolute velocities of more than 5 cm s^{-1} at 1000 dbar. There exist annual differences in the location of the patch of strongest southward flow in the boundary current system. In 2002 and 2005 a large patch of southward velocities exists right at the western boundary, while in 2003 and 2004 this patch is split into two or more focused and strong bands of southward velocities. In 2006 it seems that the major part of the southward flow occurs between 33°E and 40°E indicated by a broad patch of southward velocities, and not directly at the western boundary. This could be a result of the lack of data in 2006 west of 33°E.

At the far eastern end of the section east of 110°E, the southward velocities in the upper 300 dbar can be attributed to mesoscale eddies connected to interactions of the southward flowing *Leeuwin Current* (LC) with the northward flowing *Leeuwin Undercurrent* (LUC) right below (Waite et al., 2007). Especially the large southward velocities at 110°E in 2006 may result from a large mesoscale eddy associated with the *Leeuwin Current System* (LCS) (Feng et al., 2007). Around 105°E northward velocities can be associated with the *West Australian Current* (WAC) flowing at the eastern flank of the *Subtropical Gyre* (Domingues et al., 2007; You and Tomczak, 1993) continuing the far end of the *South Indian Ocean Current* (SIOC) to the north east (Stramma and Lutjeharms, 1997).

The structure in the ocean interior between 45°E and 100°E is dominated by northward velocities split up into several patches associated with recirculations from the SIOC possibly connected to the local bottom topography (Stramma and Lutjeharms, 1997). These patches are not stationary over time, they are shifted laterally or split up in smaller parts over the five year period with core velocities of 3 cm s^{-1} or more. Additionally there exist large deep reaching patches with southward velocities of up to 3 cm s^{-1} located between 70°E and 80°E and between 90°E and 100°E respectively in 2002. In 2003 these two patches are narrowed and focused but also shifted westward by 5° longitude, while at 50°E a broad relatively weak southward velocity patch also exists. In 2004 this patch at 50°E is much smaller again, while the interior patch is shifted further west between 60°E and 70°E, whereas the eastern patch is split up into several small narrow bands between 85°E and 105°E. In 2005 four southward flowing patches exist with a lateral scale of 3° to 5° longitude and different intensities. The patch around 80°E shows the largest and most intense southward velocities of up to -3 cm s^{-1} in the upper 1000 dbar. In the realisation for 2006 the strength of the southward flowing patch at 80°E has decreased again, leaving three relatively weak southward flowing patches in the interior between 50°E and 105°E with core velocities of about 1 cm s^{-1}. Along the whole section these velocity patches have a barotropic vertical structure, at least in the upper 2000 dbar, and we will return to that in the

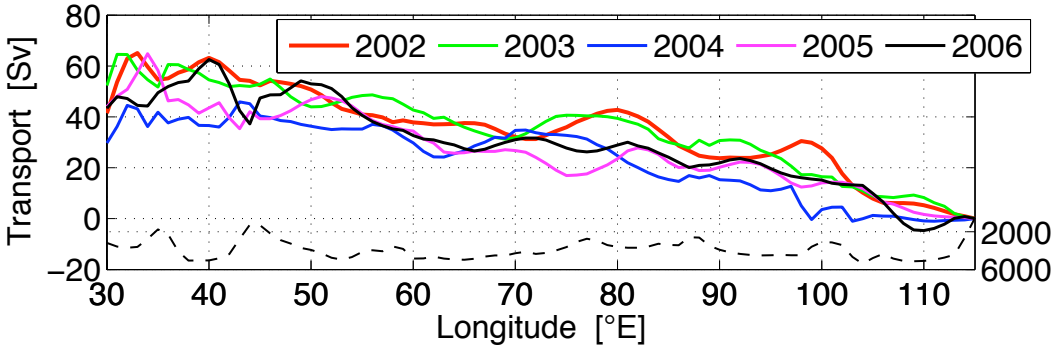

FIGURE 4.4: Annual meridional transport relative to and above 1900 dbar at 32°S cumulative integrated from East to West (started at 115°E); dashed line indicates the 32°S bathymetry with depth given on the right y-axis.

later analysis of sub-surface velocities estimated from the float's sub-surface drift at parking pressure.

The mean geostrophic velocity profiles, referenced to and above 1900 dbar, averaged over the longitude band between 45°E and 100°E indicate the largest velocities in the year 2006 and the smallest in 2005 (Fig. 4.3). This result is not surprising at least for the year 2006 since there exist only weak southward velocity patches in the interior. For the estimate in 2002 we have also added the profile calculated from the CD139 cruise data, interpolated onto 32°S with an 8°-longitude Gaussian filter applied. Here, both profiles indicate a strong increase in the velocities between 1500 dbar and 800 dbar and weaker ones above, compared to the CD29 cruise data (Fig. 4.11). This signature can be found in the years 2002, 2003 and 2006 respectively, while for 2004 and 2005 this structure in the deeper mean velocity field is less pronounced. The reason for this is, that in the years 2002, 2003 and 2006 either more deep reaching patches of northward velocities exist or fewer deep reaching patches of southward velocities, compared to the CD29 cruise data and 2004 and 2005.

As a next step, we derive cumulated geostrophic transports integrated from east to west (starting at 115°E) from the velocity fields discussed above. Since we operate at a fixed latitude, we then directly estimate meridional transports referenced to and above 1900 dbar (Fig. 4.4). The pressure level of 1900 dbar was chosen to achieve a deep reference level with a good coverage in depth by the profiles. Additionally PALMER ET AL. (2004) showed that changing the ZV level by up to 800 dbar from 2230 dbar would affect the final estimates by less than 3%.

In all the meridional transport curves the southward western boundary transport is missing, due to sampling characteristics of the Argo floats in this area which are mainly adjusted to drift at 2000 dbar parking pressure. Therefore the floats generally cannot

sample the strong southward currents further onshore than the 2000 dbar isobath, leading to the missing transport of up to 45 Sv that would provide the balance along the section. Eye catching in this plot is that in the year 2004 there exists only a very weak northward interior transport between 115°E and 100°E. In the other years a gyre strength of 10 Sv or more exist at 100°E attributed to the northward extension of the SIOC changing over into the WAC at this latitude (Domingues et al., 2007; You and Tomczak, 1993). From the previously described patches of northward or southward velocities in the interior, the patch with the southward transport between 60°E and 80°E is the most pronounced in all years, with transports of up to 12 Sv.

Furthermore the cumulated geostrophic transport estimates show a good linear relation between 110°E and the MADR at 45°E. Therefore, we will compare these results later with estimates using the Sverdrup relation of the wind-stress curl over the region from 110°E to 45°E (Chapter 4.3, Eq. 4.6). Beforehand we will first derive estimates of the annual gyre strength from float realisations.

4.1.1 Annual estimates of the gyre strength at 32°S

There exist several methods to estimate the gyre strength. Here we focus on two, the first, in the following called *MaxTrp* estimates the gyre strength according to the method used by Palmer et al. (2004) and the second, here called *LinReg* applies a linear regression to the data. Both methods are restricted to the region between 45°E and 110°E at 32°S.

4.1.1.1 *MaxTrp* method to estimate the gyre strength

The *MaxTrp* method calculates the gyre strength as the maximum difference in the cumulated transport between 45°E and 110°E, that means the western end point may vary from year to year but the eastern end point is fixed to 110°E. This method was used by Palmer et al. (2004) applied to the ocean interior defined between 35°E and 110°E, whereas we restrict the method to a smaller longitudinal band, namely between 45°E and 110°E. This decision is based on the fact that the data coverage in the western boundary region west of MADR is highly variable, with good coverage only in 2002 and 2006. This is also associated with the large variability present in the geostrophic transport field (Palmer et al., 2004) and finally as a consequence the errors given by the OI increase steadily towards the western boundary (Fig. 4.5). Additionally, at 45°E the annual variaitions in the error variance estimated during the OI procedure are small. So the aim is to give a best estimate of the gyre strength covering the

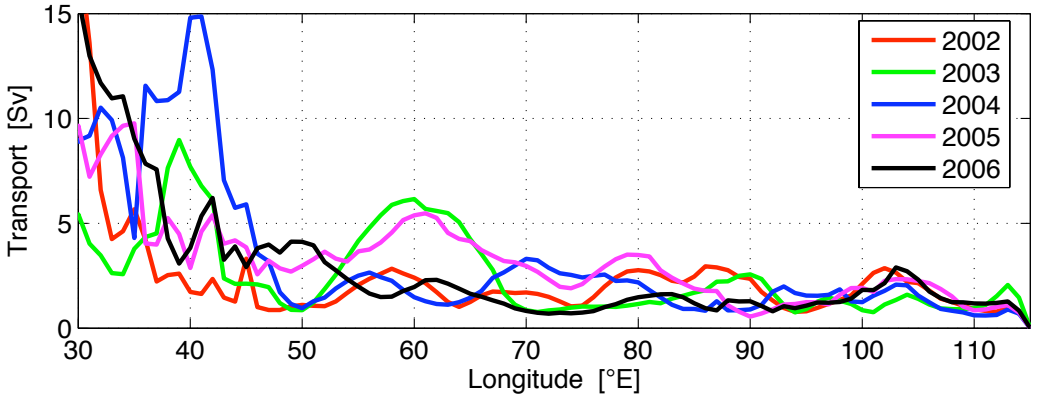

FIGURE 4.5: Error estimate for transport [Sv] given by the optimal interpolation scheme for the annual float realisations at 32°S applied as maximum error to each density profile between station pairs.

largest longitudinal band possible but still with a reasonable error estimate. Please note that variable eastern end points would not change the results, since the minimum in cumulated transport is generally in the east of the section at 110°E, if cumulated from East to West. Only in year 2004 the minimum would be at 103°E, but with a difference of only 0.1 Sv to the value at 110°E. This is due to the lack of northward transport in 2004 east of 100°E.

Note that the change in gyre strength estimated from the cruise data between 1987 and 2002 is about 32% (estimated between 35°E and 110°E for comparison) (Tab. 4.1), which is smaller than the change reported by (PALMER ET AL., 2004). This might be due to differences in the interpolation onto 32°S. With the *MaxTrp* method we then get a decrease in gyre strength from 2002 to 2004 followed by an increase afterwards (Tab. 4.1). If we exclude the surface layer and use the thermocline layer between 200 dbar and 1000 dbar mainly occupied by Mode Water (MW) and Intermediate Water (IW) the changes in the estimated gyre strength show the same directions (Tab. 4.2) and similarly for the deeper levels between 1000 dbar and 1900 dbar (Tab. 4.3).

The errors given for the float realisations (Tab. 4.1 , 4.2 and 4.3) are calculated from different independent error contributions, namely the error estimate given by the OI at the end points, applied as maximum error to the density profiles (Fig. 4.5), the errors contributing from the eddy field and for the years 2002 and 2004 errors from sub-annual variations, because the data coverage was not equally distributed at both end points in those years (Fig. 4.6). The error contribution from the eddy field (ϵ_{EDDY}) over the full depth 0 dbar to 1900 dbar varies from year to year but is of the order of 1 Sv, calculated from the standard deviation of the residuals by applying a linear fit to the transport estimates. The error estimate given by the OI at the end points, applied as maximum error to the density profiles (Fig. 4.5). In addition to the

geostrophic velocity calculation at each level between station pairs a maximum error in velocity is calculated too, resulting from the estimate of error variance during the OI procedure for temperature and salinity. That means, the estimated error variance for salinity and temperature is added to the objectively estimated temperature and salinity values and then the geostrophic velocity is calculated. This geostrophic velocity, containing the mapping error estimates, is then converted into an geostrophic transport on each pressure level between station pairs, using the practical form of the geostrophic equations (Pond and Pickard, 1983). Finally, by subtracting the annual transport estimate from the vertically integrated transport, that contains the mapping error estimates, gives a maximum error for each station pair along the section. At the western end point, we get larger error estimates (ϵ_{OI_W}) because the data coverage is sparse at least in the years 2003, 2004 and 2005. Additionally, a larger variability exist there on monthly to seasonal time scales. At the eastern end point the estimated error (ϵ_{OI_E}) is much smaller which is partially due to the good coverage with profiles. The final error contribution of the OI (ϵ_{OI}), derived from the independent errors at each end point, is then calculated as the square root of the sum of the squares of the errors at the end points. The sub-annual error contribution (ϵ_{SUB}); only taken into account for 2002 and 2004) over the full depth 0 dbar to 1900 dbar, is estimated as standard deviation of the seasonal estimates which is of the order of 3 Sv. The final error estimate for the gyre strength (ϵ_{MaxTrp}) is then calculated as the square root of the sum of the squares of the contributing errors (Eq.. 4.1 and Tab. 4.1). The errors given for the cruise data are estimated following the analysis of Palmer et al. (2004) and include the uncertainty associated with the eddy and internal wave fields, the sampling induced uncertainty of

Table 4.1: Maximum annual meridional transport above 1900 dbar across 32°S derived from the 1987 (CD29) and 2002 (CD139) cruise data (interpolated onto 32°S and with an 8°-longitude Gaussian filter applied) and from cumulated geostrophic transports of the annual float realisations using the *MaxTrp* method applied between 45°E and 110°E. Also listed are the end points, the associated errors there (ϵ_{OI_W} and ϵ_{OI_E}) and the cumulated transport at 110°E ($\mathrm{Trp}_{110\mathrm{E}}$). Errors shown including contributions from eddy field, sampling and sub-annual variations (for 2002 and 2004 only), computed as the square root of the sum of the squares.

Year	MaxTrp	End points	ϵ_{OI_W}	ϵ_{OI_E}	ϵ_{OI}	ϵ_{EDDY}	ϵ_{SUB}	$\mathrm{Trp}_{110\mathrm{E}}$
CD29	35.8 ±4.7	56°E 110°E	-	-	±2.2	±3.8	±1.7	4.3
CD139	42.3 ±5.9	45°E 110°E	-	-	±2.2	±5.2	±1.7	7.2
2002	48.9 ±3.7	46°E 110°E	±1.0	±0.9	±1.3	±1.7	±3.0	5.3
2003	46.6 ±2.8	46°E 110°E	±2.1	±1.0	±2.3	±1.6	0	8.2
2004	41.3 ±6.9	45°E 110°E	±5.9	±0.6	±5.9	±1.9	±3.0	-0.9
2005	46.3 ±3.8	51°E 110°E	±3.3	±0.8	±3.4	±1.6	0	1.7
2006	58.9 ±4.6	49°E 110°E	±4.1	±1.2	±4.3	±1.5	0	-4.7

TABLE 4.2: As Tab. 4.1 but between 200 dbar and 1000 dbar.

Year	MaxTrp	End points	ϵ_{OI_W}	ϵ_{OI_E}	Trp_{110E}
CD29	22.3 ±3.7	56°E 110°E	-	-	4.2
CD139	26.8 ±4.4	45°E 110°E	-	-	6.5
2002	30.4 ±0.8	46°E 110°E	±0.6	±0.5	4.9
2003	29.5 ±1.4	46°E 110°E	±1.3	±0.6	6.2
2004	25.4 ±4.0	45°E 110°E	±3.9	±0.4	0.3
2005	28.9 ±1.9	51°E 110°E	±1.9	±0.5	2.4
2006	37.8 ±2.6	49°E 110°E	±2.5	±0.7	-2.7

±2.2 Sv and a further uncertainty of ±1.7 Sv was associated with sub-annual variations in the geostrophic flow field (Tab. 4.1).

$$\epsilon_{MaxTrp} = \sqrt{\epsilon_{OI}^2 + \epsilon_{EDDY}^2 + \epsilon_{SUB}^2} \tag{4.1}$$

We get larger error estimates if only a few profiles are close to the actual mapping grid point as can be seen for example in the year 2003 and 2004 in the MADB around 40°E and in year 2003 and 2005 in the interior around 60°E respectively (Fig. 4.5 and 4.1). In 2004 there are only 15 profiles contributing to the OI estimate at the western end point station pair at 44.5°E and 45.5°E (Fig. 4.6) being at least 260 km away from the mapping grid point (the OI is configured to use up to a maximum of 100 profiles for the mapping at each grid point). Generally the larger seasonal variation in the number of contributing profiles takes place at the western end points (Fig. 4.6). Later in this work we will examine a possible contribution from seasonal variations in the transport fields too, then we might be able to put the large variation in the number of monthly contributing profiles in context with changes in the transport.

TABLE 4.3: As Tab. 4.1 but between 1000 dbar and 1900 dbar.

Year	MaxTrp	End points	ϵ_{OI_W}	ϵ_{OI_E}	Trp_{110E}
CD29	5.5 ±1.5	56°E 110°E	-	-	-0.1
CD139	6.3 ±1.7	45°E 110°E	-	-	0.3
2002	7.4 ±0.1	46°E 110°E	±0.1	±0.1	-0.1
2003	6.8 ±0.2	46°E 110°E	±0.2	±0.1	0.9
2004	6.0 ±0.3	46°E 110°E	±0.3	±0.1	-0.1
2005	6.9 ±0.6	51°E 110°E	±0.6	±0.1	-0.3
2006	8.2 ±0.6	49°E 110°E	±0.6	±0.1	-0.9

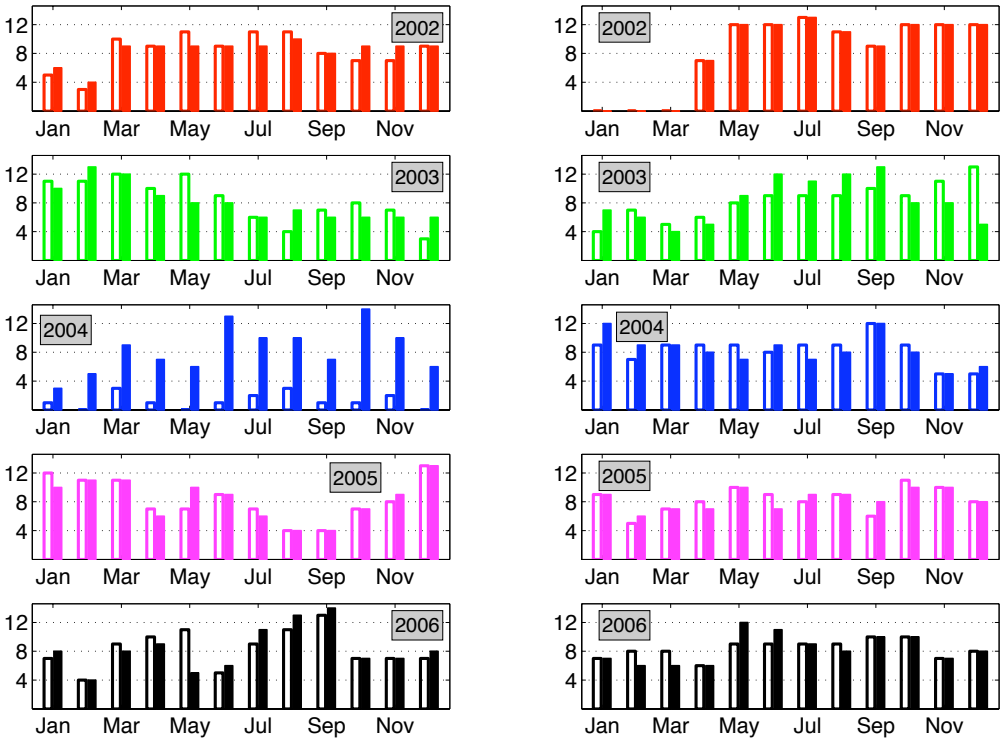

FIGURE 4.6: Monthly number of contributing profiles at the variable end points (Tab. 4.1) for each year. Left panels for western end points, right panels for eastern end points. In each panel the non-filled bars give the number of profiles contributing to the western station of the station pair used to calculate the transport and the filled bars give the number at the eastern station respectively.

The *MaxTrp* method used here is clearly sensitive to the choice of end points, here it is necessary to mention again that the western end points vary from year to year, depending on the position of the maximum northward transport east of 45°E (Fig. 4.4), whereas the eastern end point is fixed at 110°E. Hence, we would like to examine possible sensitivity of the results to variability at the eastern end points at 110°E, since there the cumulated transport, integrated from 115°E to the West, varies by up to 15 Sv (Fig. 4.4). Here we compare the total estimated gyre strength using the *MaxTrp* method with the interannual variability of the cumulated transport (integration started at 115°E) seen at the eastern end point (110°E). We also include the estimated gyre strength using the *MaxTrp* method but with the climatological value from the WOA01 estimate at 110°E called $MaxTrp_{WOA}$ in the following (Fig. 4.7).

This comparison shows two things. First, the estimated gyre strength using the *MaxTrp* method is sensitive to the variability at the eastern end point at least for the years 2002, 2003 and 2006. This is what we would expect, with a decrease in transport at the eastern end point, at 110°E, the total difference in the transport over

the longitude band increases. But it does not hold for all years, in 2004 and 2005 the change in the cumulated transport at 110°E and the change in total gyre strength have the same sign. Here either the estimate of the gyre strength is erroneous as probably in 2004 indicated by the large error at the western end point, or an additional overlaying process exists. Secondly, if we now use the $MaxTrp_{WOA}$ method and make the gyre strength estimate independent to the eastern end point we see a very good agreement in the structure of the change in gyre strength and change in transport at 110°E between 2002 and 2005. Only the estimate in year 2006 is not decreasing as the cumulated transport at 110°E does, instead it increased hugely.

This comparison shows that care needs to be taken at the eastern end point at 110°E, because of the large seasonal and interannual variations possibly remotely forced from the ITF (Potemra, 2001; Birol and Morrow, 2001), and additionally because of the variations of the coastal boundary current, the LC. The LC is a density-driven current with a strong seasonal cycle with maximum in May/June (Smith et al., 1991) that carries warm, low-salinity waters southward against the prevailing northward winds. There off the coast, mesoscale eddies form from mixed baroclinic and barotropic instability of the LC (Feng et al., 2005; Waite et al., 2007). Between 20°S and 35°S an energetic Rossby wave band exists (Morrow and Birol, 1998) that carries both the eastern boundary variations associated with the ITF and signals associated with the energetic eddy field from the LC into the ocean interior. The eddies, that may penetrate up to a depth of 2500 m (Morrow et al., 2003), are present in the latitudinal band between 20°S and 35°S (Cresswell and Golding, 1980; Griffiths and Pearce, 1985; Morrow et al., 2003) and can be tracked to

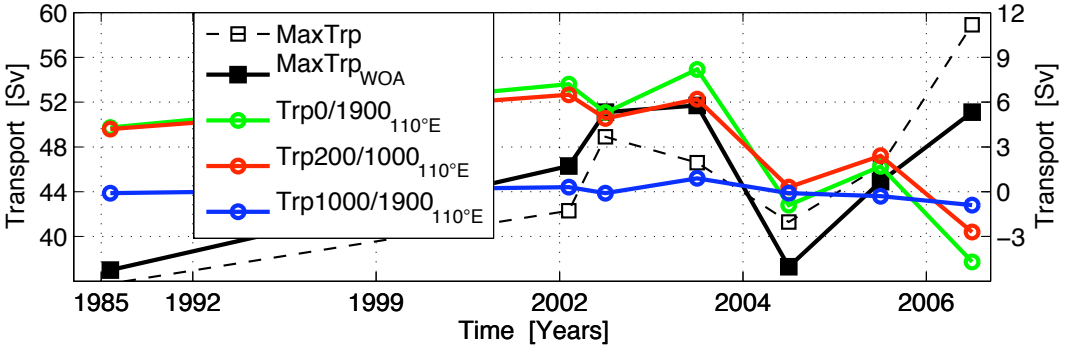

Figure 4.7: Comparison of estimated gyre strength using the *MaxTrp* method (filled black square) and the $MaxTrp_{WOA}$ (contoured black square) with the interannual variability of the cumulated transport (referenced to 115°E) seen at the eastern end point at 110°E (green: surface to 1900 dbar; red: 200 dbar to 1000 dbar and blue: 1000 dbar to 1900 dbar). note that the green and black lines use the right y-axis.

95°E using altimeter data, with maxima in SLA between 105°E and the Australian coast (Morrow et al., 2003). Therefore we use the $MaxTrp_{WOA}$ method as best estimate in this section and obtain a final set of gyre strength values (Tab. 4.4 and Fig. 4.7) that still show the same direction of interannual change.

4.1.1.2 *LinReg* method to estimate the gyre strength

The *LinReg* method uses the whole longitudinal band between 45°E and 110°E to get an estimate for the gyre strength that is independent of the choice of the end points and therefore we expect to get better results without the reference to the climatological value in the east at 110°E. A linear regression is applied to the vertically integrated geostrophic transport profiles. This method eliminates a possible bias from intense meso-scale eddies seen in the geostrophic velocity sections (Fig. 4.3) compared to the linear regression applied to the already zonally cumulated transports. The final meridional transport is calculated by integrating the regression result from east to west between 45°E and 110°E (Fig. 4.8). The maximum gyre strength is then just the difference in the cumulated transport between the western end at 45°E and the eastern end at 110°E (Tab. 4.5). Note that the end points used here are fixed and do not vary from year to year in contrast to the previously described *MaxTrp* method (An exception is the 1987 cruise estimate, where the *LinReg* method is confined to the longitudinal range between 55°E and 110°E, because west of 55°E the assumed linearity does not hold due to the extension of the southward flowing western boundary current regime

Table 4.4: Maximum annual meridional transport above 1900 dbar across 32°S derived from the 1987 (CD29) and 2002 (CD139) cruise data (interpolated onto 32°S and with an 8°-longitude Gaussian filter applied) and from cumulated geostrophic transports of the annual float realisations using the $MaxTrp_{WOA}$ method applied between 45°E and 110°E. Also listed are the end points, the associated errors there (ϵ_{OI_W} and ϵ_{OI_E}). Errors shown including contributions from eddy field (ϵ_{EDDY}), sampling (ϵ_{OI}) and sub-annual variations (ϵ_{SUB}), computed as the square root of the sum of the squares.

Year	MaxTrp$_{WOA}$	End points	ϵ_{OI_W}	ϵ_{OI_E}	ϵ_{EDDY}	ϵ_{SUB}
CD29	37.0 ±4.7	56°E 110°E	-	±2.2	±3.8	±1.7
CD139	46.3 ±5.9	45°E 110°E	-	±2.2	±5.2	±1.7
2002	51.1 ±3.6	46°E 110°E	±1.0	±1.0	±1.7	±3.0
2003	51.7 ±2.6	46°E 110°E	±2.1	±2.1	±1.6	±0
2004	37.3 ±6.9	45°E 110°E	±5.9	±5.9	±1.9	±3.0
2005	44.9 ±3.7	51°E 110°E	±3.3	±3.3	±1.6	±0
2006	51.1 ±4.4	49°E 110°E	±4.1	±4.1	±1.5	±0

into the ocean interior (PALMER ET AL., 2004).) Just for completeness, if we use the cimatological value of the cumulated transport at 110°E, integrated from 115°E to the west, the estimate of the gyre strength is less than 3% different to the values shown in Table 4.5 for all years. This confirms that the variability at the eastern end point has small influence to the final estimate of the gyre strength if we use the *LinReg* method.

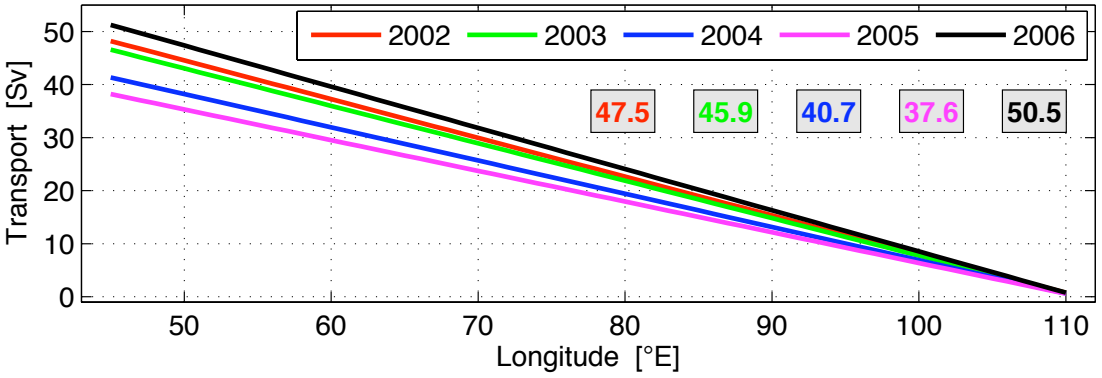

FIGURE 4.8: Linear regression applied to the annual vertical integrated transports profiles across 32°S between 45°E and 110°E shown in Figure 4.3. This solution is then zonally cumulated from East to West. Numbers give the estimated gyre strength with text colours matching legend entry.

TABLE 4.5: Maximum annual meridional transport across 32°S derived from the geostrophic transport profiles from 1987 (CD29) and 2002 (CD139) cruise data (interpolated onto 32°S and with an 8°-longitude Gaussian filter applied) and from the annual float realisations with the *LinReg* method applied to the vertical integrated geostrophic transport profiles between 45°E and 110°E (Fig. 4.8). Listed are the estimates for the full profile depth (up to 1900 dbar) and two separate layers, the thermocline layer mainly occupied by the MW and IW between 200 dbar and 1000 dbar and the deeper layer below 1000 dbar reaching to the maximum depth of 1900 dbar of the float realisations. Additionally shown the upper layer between 0 dbar and 1000 dbar for later comparison with geostrophic Sverdrup transport. The percentage in brackets indicates increase/decrease relative to the CD29 and 2002 estimates, respectively. Given errors include contributions from eddy field and sampling.

Year	LinReg $_{0/1900}$	LinReg $_{200/1000}$	LinReg $_{1000/1900}$	LinReg $_{0/1000}$
CD29	33.6 ±3.4	20.4 ±3.1	5.3 ±1.5	28.9 ±3.0
CD139	43.7 ±5.5 (+30%)	27.3 ±4.1 (+34%)	6.6 ±1.7 (+25%)	38.9 ±4.9
2002	47.5 ±2.5	29.4 ±1.5	7.4 ±0.3	40.5 ±2.1
2003	45.9 ±2.6 (-3%)	29.0 ±1.6 (-1%)	7.0 ±0.4 (-5%)	39.2 ±2.2
2004	40.7 ±2.6 (-14%)	25.3 ±1.7 (-14%)	5.9 ±0.4 (-21%)	35.1 ±2.2
2005	37.6 ±3.1 (-21%)	23.3 ±1.9 (-21%)	5.4 ±0.5 (-27%)	32.5 ±2.6
2006	50.5 ±2.3 (+3%)	32.1 ±1.5(+9%)	7.4 ±0.4 (±0%)	43.5 ±1.9

The associated errors of the method include the meso-scale variability from the eddy field along the section, as well as the mean error given by the OI resulting from sampling. The errors are independent, therefore the final error is given as square-root of the sum of the squares of the contributing errors. Note that the *LinReg* method is not influenced by sub-annual variations, since the method uses all available grid points between 45° and 110°E and it is assumed that over this longitudinal range no sub-annual bias is included in the Argo float data.

The gyre strength estimated with the *LinReg* method shows a continuous decrease from 47.5 Sv in 2002 to 37.5 Sv in 2005 followed by a large increase to 50.5 Sv in 2006, which gives the strongest gyre for the Argo float period but also compared to the cruise data. The large increase in 2006 cannot be explained just by the error estimate given with the *LinReg* method since they are relatively similar for all years with the smallest error estimate of 2.3 Sv in 2006 (Tab. 4.5). The estimates from the cruise data show an increase in the gyre strength of 30% from 1987 to 2002 over the water column down to 1900 dbar. In the thermocline layer between 200 dbar and 1000 dbar the change is a 34% increase in strength, while in the deep layer between 1000 dbar and 1900 dbar only a change of 25% in gyre strength occurred. Whereas the estimates of the annual float realisations show the contrary, at least between 2002 and 2005, where the decrease in gyre strength is proportionally larger in the deep layer than in the thermocline. Only in 2006 the proportionally largest changes occurred in the thermocline (Tab. 4.5). For the 5 year period 2002 to 2006 we calculate an interannual variability, defined as standard deviation of the annual estimates, of 5.2 Sv with a maximum amplitude of 13 Sv between 2005 and 2006.

4.1.2 Seasonal estimates of the gyre strength at 32°S

The motivation of this work is based on the analysis of the cruise data in 1987 and 2002. In this section, we will now examine a possible seasonal contribution in the signal, since during CD29 in 1987 the profiles were collected in October and November, which is the spring season in the southern hemisphere, while during CD139 in 2002 profiles were taken in the period March and April, which is the autumn season. We use the seasonal float realisations (Sec. 3.1.3, Tab. 3.2) to examine a possible seasonality in the gyre strength.

The seasonal float realisations show a very good coverage of data points with no gaps larger than about 200 km (Fig. 4.9). This is also expressed in the much smaller error estimates calculated from the given OI error applied as maximum error to the station pairs (Fig. 4.10). Nevertheless, temporal coverage of each season might have a larger

weighted contribution from the years 2004 onwards because of the small numbers of profiles in 2002 and 2003 in the region (Chapter 3.1.1).

The geostrophic velocity section referenced to and above 1900 dbar show fewer

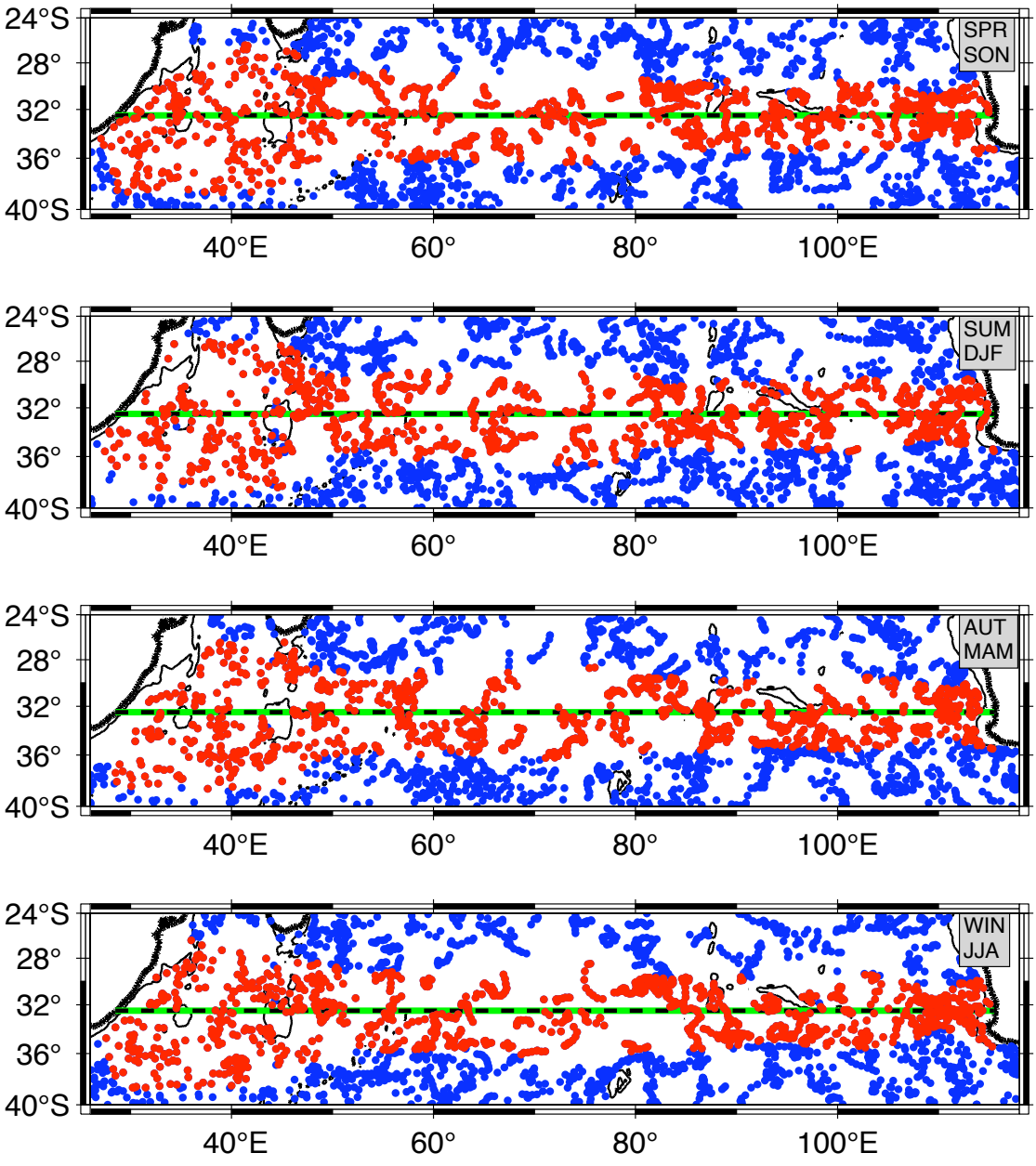

FIGURE 4.9: Maps showing seasonal distribution of all delayed-mode quality controlled Argo float profiles in the subtropical South Indian Ocean (blue dots) and those finally taken into account for the seasonal estimate of temperature and salinity from the optimal interpolation scheme (red dots) along 32°S (green and black dashed). Contours highlight 1900 m isobath (thin solid black) and coastline (bold). Seasons are set as followed: Spring contains September, October and November; Summer contains December, January and February; Autumn contains March, April and May; Winter contains June, July and August

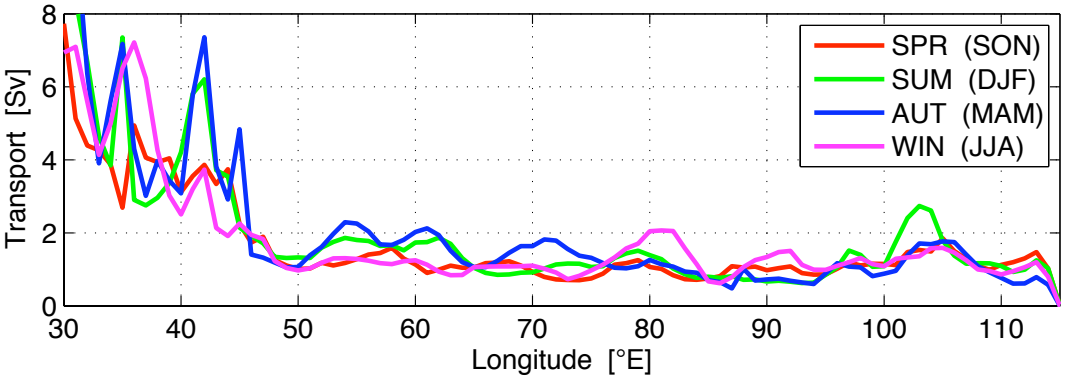

FIGURE 4.10: Error estimates for transport [Sv] given by the optimal interplation scheme for the seasonal float realisations at 32°S applied as maximum error to each density station pair.

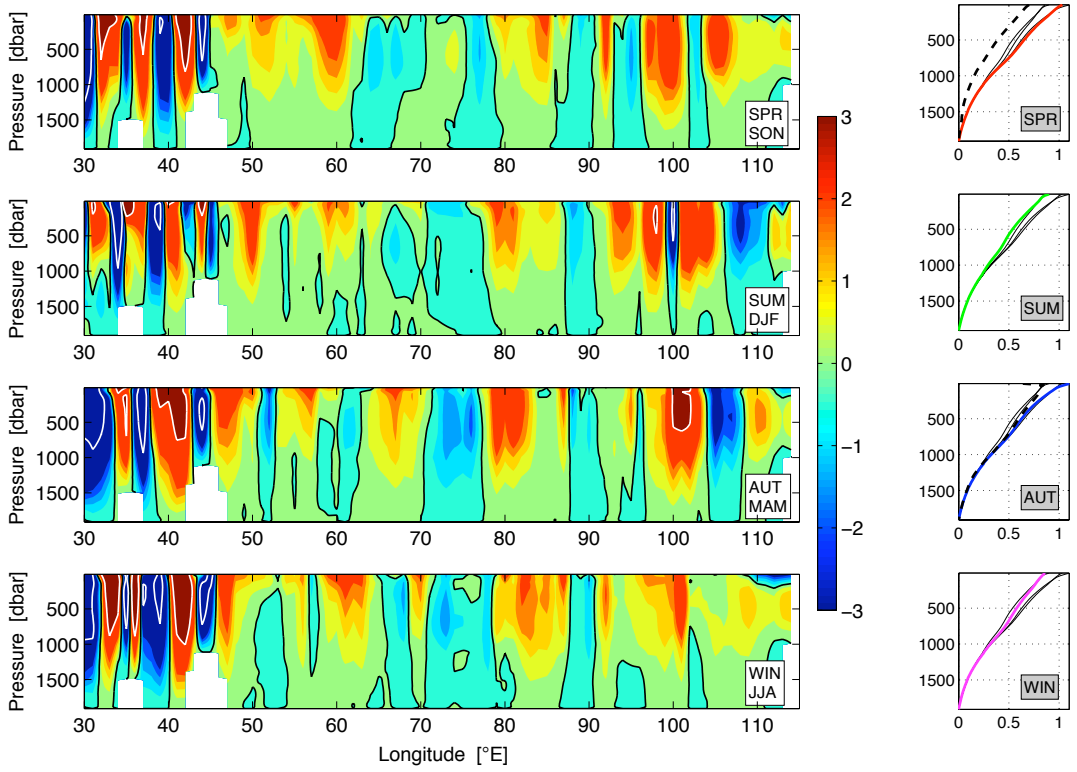

FIGURE 4.11: Left: Geostrophic velocities [in $\mathrm{cm\,s^{-1}}$] referenced to and above 1900 dbar across 32°S, calculated from seasonal realisations using optimally interpolated Argo profiles (black contours indicate zero velocity and white contours indicate absolute velocities larger than $\pm 5\,\mathrm{cm\,s^{-1}}$). Right: Mean seasonal geostrophic velocity profiles [in $\mathrm{cm\,s^{-1}}$] referenced to 1900 dbar averaged between 45°E and 110°E. Each season the actual profile is shown in colour whereas the other years are shown as black lines only. For spring and autumn the CD29 (October/November 1987) and CD139 (March/April 2002) cruise data are shown for comparison (black dashed), interpolated onto 32°S with an 8°-longitude Gaussian filter applied (PALMER ET AL., 2004).

patches of alternating flow direction in the interior compared to the annual realisations (Fig. 4.11) with the region between 60°E and 80°E mainly occupied by patches of southward flow with different intensities from 0.5 cm s^{-1} to 1.5 cm s^{-1}. Between 80°E and 88°E a stationary patch of northward flow exists over all seasons with different intensities ranging from 0.5 cm s^{-1} to 2 cm s^{-1}. Then centred at 90°E a weak but stationary patch of southward flow exists for all seasons. Around 100°E and further east the patch of intense northward velocity can be attributed to the northward flowing WAC. Only in the summer and autumn seasons intense southward velocities exist in a patch of about 5° width with velocities between 0.5 cm s^{-1} and 2.5 cm s^{-1}. The offshore parts of the southward flowing LC and the northward flowing LUC are represented in all seasons with the maximum intensity of the LC in winter as reported by Smith et al. (1991) and Feng et al. (2003).

In the western boundary region southward flow exists over the MADR at 45°E, to the west and the east of MOZP at 35°E and directly at the western boundary at 30°E. Only in the autumn season the patch of southward flow occupies the whole width of the MOZB from the western boundary to MOZP. The southward flow is focused and intense with velocities between 1 cm s^{-1} up to 1500 dbar and more than 3 cm s^{-1} in the top 1000 dbar. In between these patches of southward flow, northward flow exist with similar intensity and structure resulting from recirculations.

The geostrophic velocities averaged zonally between 45°E and 110°E (Fig. 4.11, right panel) highlight two modes in the vertical structure above 800 dbar. In spring and autumn we see a stronger increase in the averaged velocities in the pressure horizon between 700 dbar and 800 dbar as well as above 400 dbar. At the surface in both seasons a maximum mean velocity of 1.0 cm s^{-1} is reached, while for summer and winter the averaged velocities are smaller between 800 dbar and the surface with maximum velocities at the surface of about 0.8 cm s^{-1}. The estimate from the WOA01 climatology (not shown) shows the same characteristics as the summer and winter seasons. That means the seasons spring and autumn are characterised by exceptionally large northward mean velocities in the top 800 dbar.

The interpolated and filtered cruise data deviate from the averaged geostrophic velocity profiles from the float realisations. The CD29 profile from spring 1987 lacks a deep northward mean velocity below 1500 dbar. The CD139 profile from autumn 2002 follows the autumn profile from the float realisation but deviates in the upper 500 dbar with a smaller velocity (up to 0.2 cm s^{-1}) and an additional large decrease in the top 20 dbar of about 0.2 cm s^{-1}, resulting in a final mean velocity at the surface of 0.6 cm s^{-1}.

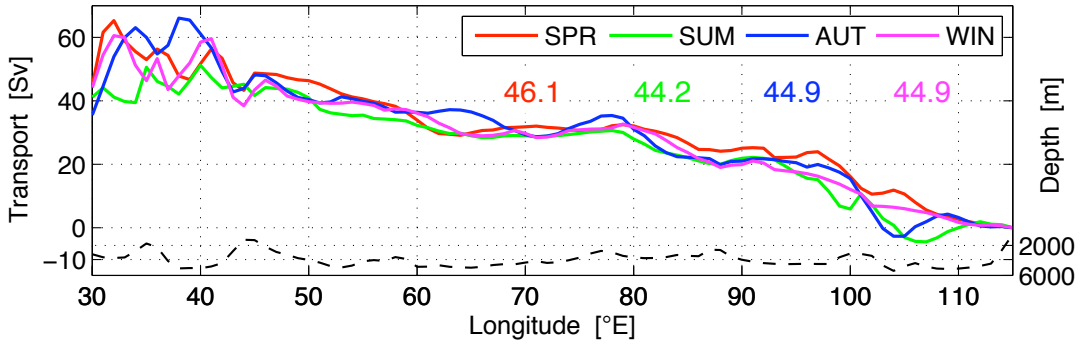

FIGURE 4.12: Seasonal meridional transports relative to and above 1900 dbar at 32°S cumulated from East to West estimated from float realisations. The numbers are seasonal estimates of gyre strength using the *MaxTrp* method with a fixed eastern end point at 110°E. Note that without the climatological reference end point in the east at 110°E no seasonality becomes apparent. The dashed line indicates the section bathymetry.

From the geostrophic velocities we now calculate cumulated geostrophic transports referenced to and above 1900 dbar and integrate them again from east to west (Fig. 4.12). We get very coherent transport curves in the interior between 95°E and 45°E and larger variations in the boundary regions, in the west between 30°E and 40°E and in the east between 95°E and 110°E. For the calculation of the gyre strength we exclude the western boundary region, while the variations in the east mainly take place in the interior west of 110°E. We show the estimates of the gyre strength using the $MaxTrp_{WOA}$ method with the fixed eastern end point at 110°E given from climatological properties (Tab. 4.6) and also the estimates using the *LinReg* method (Tab. 4.7).

TABLE 4.6: Maximum seasonal meridional transport above 1900 dbar across 32°S derived from the 1987 (CD29 in October and November) and 2002 (CD139 in March and April) cruise data (interpolated onto 32°S and with an 8°-longitude Gaussian filter applied) and from cumulated geostrophic transports of the seasonal float realisations using the $MaxTrp_{WOA}$ method applied between 45°E and 110°E. Also listed are the end points, the associated errors there (ϵ_{OI_W} and ϵ_{OI_E}) and the cumulated transport at 110°E (Trp_{110E}). The percentage in brackets indicates increase/decrease of the cruise estimate relative to the spring (SPR) and autumn (AUT) estimates, respectively.

Season	$MaxTrp_{WOA}$	End points	ϵ_{OI_W}	ϵ_{OI_E}	Trp_{110E}
SPR (SON)	45.7 ±2.5	45°E 110°E	±2.2	±1.1	2.7
CD29 (ON)	37.0 ±4.7 (-19%)	56°E 110°E	-	-	4.3
SUM (DJF)	41.1 ±2.2	46°E 110°E	±1.9	±1.1	0.0
AUT (MAM)	45.0 ±4.9	45°E 110°E	±4.8	±0.8	3.2
CD139 (MA)	42.3 ±5.9 (-6%)	45°E 110°E	-	-	7.2
WIN (JJA)	43.5 ±2.1	46°E 110°E	±1.9	±0.9	1.7

TABLE 4.7: Seasonal estimates of gyre strength across 32°S derived from the geostrophic transport profiles from 1987 (CD29 in October and November) and 2002 (CD139 in March and April) cruise data (interpolated onto 32°S and with an 8°-longitude Gaussian filter applied) and from the seasonal float realisations with the *LinReg* method applied to the vertical integrated geostrophic transport profiles between 45°E and 110°E. Listed are the estimates for the full profile depth (up to 1900 dbar) and two separate layers, the thermocline layer mainly occupied by the MW and IW between 200 dbar and 1000 dbar and the deeper layer below 1000 dbar reaching to the maximum depth of 1900 dbar of the float realisations. The percentage in brackets indicates increase/decrease of the cruise estimates relative to the spring (SPR) and autumn (AUT) estimates, respectively.

Season	LinReg $_{0/1900}$	LinReg $_{200/1000}$	LinReg $_{1000/1900}$
SPR (SON)	46.2 ±1.6	29.1 ±1.0	6.6 ±0.3
CD29 (ON)	33.6 ±3.4 (-28%)	20.4 ±3.1 (-30%)	5.3 ±1.5 (-20%)
SUM (DJF)	39.9 ±2.0	24.6 ±1.3	6.4 ±0.3
AUT (MAM)	45.7 ±2.1	28.4 ±1.3	6.7 ±0.4
CD139 (MA)	43.7 ±5.5 (-4%)	27.3 ±4.1 (-4%)	6.6 ±1.7 (-1%)
WIN (JJA)	41.7 ±1.6	26.3 ±1.0	6.6 ±0.3

Please note that the numbers given in figure 4.12 give the gyre strength using the *MaxTrp* method without the climatological reference end point at 110°E.

Both methods show the same tendency in the data, namely that the seasons spring and autumn give a 5% - 10% larger gyre strength than the summer and winter estimates, with the *LinReg* method showing the larger seasonality of the two methods. The seasonality can be found in the upper 1000 dbar whereas the gyre strength in the deeper layer between 1000 dbar to 1900 dbar indicates no seasonality. Nevertheless, the seasonal cycle found in the upper layer does not agree with the seasonal cycle estimated from geostrophic Sverdrup transport derived from wind-stress curl, which indicates maximum in winter and minimum in summer. The seasonal cycle estimated from the density field seems to be delayed by about 3 months. The Ekman transport component, derived from wind-stress curl for the 5 year period 2002 to 2006, indicates maxima in February and June of 2.8 Sv and 4.2 Sv, respectively and minima in April and December of 1.6 Sv and 1.1 Sv, respectively.

These results (Tab. 4.7 and 4.6) show clearly that the CD29 section from 1987 has an exceptionally low gyre strength compared to the spring estimate which is the appropriate season. Assuming the individual errors given in Table 4.7 to be independent, then the 1987 estimate is lower than the spring estimate by 3 times of the combined error. Whereas the CD139 section estimate from 2002 is in good agreement with the autumn estimate calculated from the float realisations.

Finally, we use the analysis of seasonal changes to adjust the error estimates for the annual gyre strength derived from the float realisations using the *MaxTrp* method, at least for the years 2002 and 2004, where no equal distribution of profiles over the year exists at the end oints. The seasonal variability, and therefore the error associated with sub-annual changes, is calculated as the standard deviation of the seasonal estimates. Then the seasonal variability (sub-annual error) is 3.0 Sv for the full profile depth up to 1900 dbar and 2.0 Sv for the thermocline layer between 200 dbar to 1000 dbar, respectively. While for the deep layer no seasonal variability is detected. Note that the sub-annual error is already only added for the years 2002 and 2004 and only using the *MaxTrp* method (Tab. 4.4).

4.1.3 Variability of the gyre strength at 32°S

We estimate a mean gyre strength over the 5 year period 2002 to 2006 of 44.4±1.2 Sv using the *LinReg* and 47.2±1.9 Sv using the $MaxTrp_{WOA}$ method, respectively (Tab. 4.5 and 4.4). Here, it is assumed that the annual error estimates (Tab. 4.5 and 4.4) are independent and any bias of the distribution of the data is already included in there. Therefore, the annual errors can be seen as randomly distributed for the 5 year period and it can be assumed that the error for the 5 year mean is smaller and more representative than the errors for the annual estimates. Using the average of the annual errors as a representation of the 5 year period seems admissible, because the annual errors show little variance. Therefore, the final errors given here are calculated as some kind of "standard error", by taking the average of the annual error estimates divided by the square-root of the number of years taken, into account (here 5 years). The interannual variability, defined as standard deviation of the annual estimates, is 5.2 Sv using the *LinReg* and 6.2 Sv using the $MaxTrp_{WOA}$ method. The overall trend of the time series of the gyre strength over the 19 year period between 1987 and 2006, taking the cruise data as well as the annual float realisations into account, estimated with a least-square linear fit is positive, no matter which method ($MaxTrp_{WOA}$ or *LinReg*) is used (Fig. 4.13). However, if we use only the estimates from the Argo float realisation over the 5 year period 2002 to 2006, a potential positive trend over the period 1987 to 2002, estimated from 2 hydrographic sections only, changes to a negative one thereafter, again no matter which method is used. It appears that the 5 year trend of the Argo period is sensitive to the method and shows a different magnitude in the slope of the trend. Therefore, we now calculate the correlation coefficient (R) for the time series of the gyre strength ($ts_{GyreStr}$) and the according time vector (ts_{time}) following the formulation in Eq. 4.2 and Eq. 4.3 and their associated confidence levels.

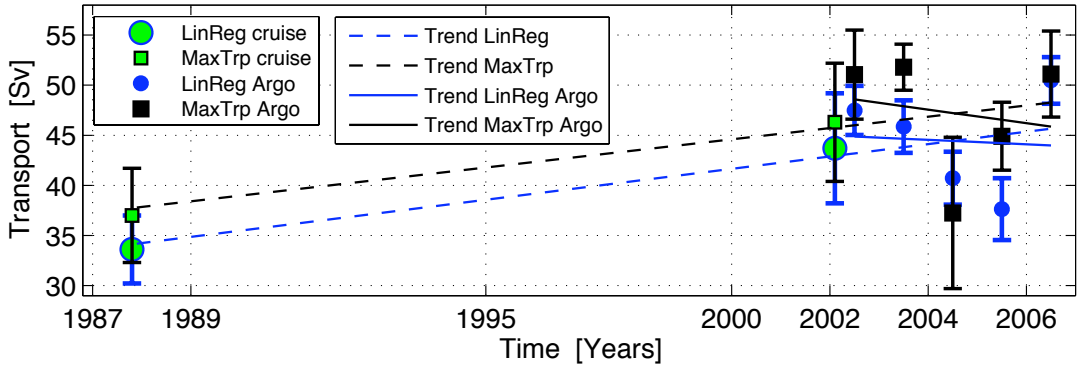

FIGURE 4.13: Comparison of the gyre strength estimated from the different methods (*LinReg* in blue; $MaxTrp_{WOA}$ in black) with associated errors for the annual float realisations (blue and black filled) and the estimates from the interpolated cruise data (green filled). Data taken from Table 4.5 and Table 4.4. Also shown is the trend estimated for each method for the period between 1987 and 2006 (dashed) and only for the Argo period between 2002 and 2006 (solid).

$$R\left(\mathrm{ts}_{\mathrm{GyreStr}}, ts_{Time}\right) = \frac{K\left(\mathrm{ts}_{\mathrm{GyreStr}}, ts_{Time}\right)}{\sqrt{K\left(\mathrm{ts}_{\mathrm{Time}}, \mathrm{ts}_{\mathrm{Time}}\right) K\left(\mathrm{ts}_{\mathrm{GyreStr}}, \mathrm{ts}_{\mathrm{GyreStr}}\right)}} \tag{4.2}$$

with the covariance K calculated from

$$K\left(\mathrm{ts}_{\mathrm{GyreStr}}, ts_{Time}\right) = \frac{1}{N} \sum_{i=1}^{N} \left(\mathrm{ts}_{\mathrm{GyreStr}} - \mu\right) \left(\mathrm{ts}_{\mathrm{Time}} - \nu\right) \tag{4.3}$$

where μ and ν are the mean of the vectors $\mathrm{ts}_{\mathrm{GyreStr}}$ and $\mathrm{ts}_{\mathrm{Time}}$ respectively. Ideally a set of observations showing a perfect linear trend would show a correlation coefficient of $R = 1$ and a p-value $p = 0$ with a significance level of 100%. For the 19 years time period 1987 to 2006 we get a statistically significant positive trend on a 80% and 90% significance level, respectively, depending which method is used (Tab. 4.8). The large significance results from the long temporal separation of the cruise data. If, additionally, the 1995 cruise data would be included (assuming that the 1995 cruise data give still similar results as the 1987 cruise data (PALMER ET AL., 2004) applying the *LinReg* or *MaxTrp* method) probably no significant trend would be detected. However, for the 5 year period 2002 to 2006 where we used only the estimates derived from Argo float realisations we find no statistically significant trend, again no matter which method is used (Tab. 4.8). This is due to the large changes in the annual gyre strength estimates. For a better confidence a longer time series

TABLE 4.8: Comparison of the time series of estimated gyre strength split into the full time period 1987 to 2006 and only the Argo era 2002 to 2006. Trends of change in the gyre strength are given with associated correlation coefficient, the p-value and the significance level for both methods (*LinReg* and $MaxTrp_{WOA}$).

Period	Trend [Sv/year]	R	p-value	Significance level
1987 - 2006 *LinReg*	0.61	0.67	0.10	90%
1987 - 2006 $MaxTrp_{WOA}$	0.56	0.56	0.19	81%
2002 - 2006 *LinReg*	-0.22	-0.07	0.91	not significant
2002 - 2006 $MaxTrp_{WOA}$	-0.67	-0.17	0.78	not significant

would be necessary providing more independent estimates. The maximum amplitude of interannual change in the estimated gyre strength over the 5 year period 2002 to 2006 is 13 Sv without and 18 Sv including the errors, respectively (Tab. 4.5).

Considering the results estimated with the *LinReg* method, the gyre strength estimate from the CD29 cruise in 1987 exceeds $2\,\sigma$ (standard deviations) of the variability in the annual estimates between 2002 and 2006. Additionally, the gyre strength using CD29 data exceeds $3\,\sigma$ of the seasonal variability of the gyre strength derived from the Argo data. Directly compared to the appropriate season, the gyre strength estimated from CD29 is about 30% smaller than the estimate for the mean spring season between 2002 and 2006 (Tab. 4.7). Considering the $MaxTrp_{WOA}$ method, the gyre strength estimate using CD29 data exceeds $3\,\sigma$ of the seasonal variability to the spring season. Compared to the 5 year mean it exceeds the gyre strength estimate by $2\,\sigma$ of interannual variability (Tab. 4.4 and 4.6).

The cumulated geostrophic transport estimated from the CD29 section in 1987 across 32°S referenced to and above 2230 dbar showed a broad regime of southward transport connected to the western boundary region up to 55°E (PALMER ET AL., 2004). In contrast, none of the annual or seasonal estimates between 2002 and 2006 showed such a structure in the large scale velocity or transport field across 32°S (Fig. 4.4 and 4.12). PALMER ET AL. (2004) showed that most of the change between 1987 and 2002 happened between 1995 and 2002. Additionally, the 1995 cruise data (not used in this study) give the impression that there has been a persistent change between the flow structure of the 1987 and 2002 sections, that can be seen by the westward shift of the maximum of southward transport (in 1987 the maximum is located at 55°E, in 1995 at 45°E and in 2002 at 40°E; Figure 3 from PALMER ET AL. (2004)). No such structural change in the gyre transport was detected from the argo float data between 2002 and 2006. In contrast to the 1987 estimates the gyre strength calculation using the recent CD139 cruise data is within $1\,\sigma$ of the interannual and seasonal variability

of the 5 year period, as well as within the given errors to the 2002 estimate, no matter which method is used. Nevertheless, that does not imply that a single hydrographic section is representative to describe the mean state of the gyre circulation, because of the large amplitude in the interannual changes.

Furthermore it is notable, that the annual float realisations indicate a proportionally larger change in the deep layer (1000 dbar to 1900 dbar) compared to the thermocline layer (200 dbar to 1000 dbar) between 2002 and 2005, while from 2005 to 2006 the increase in gyre strength is proportionally equally distributed between both layers. The proportional change in gyre strength between 1987 and 2002 takes place rather equally distributed too (Tab. 4.5), indicating a possible contribution from changes in the wind field to the interannual variability. Nevertheless, the seasonal cycle is not in agreement with the seasonal cycle estimated from geostrophic Sverdrup transport derived from wind-stress curl, which indicates maximum in winter and minimum in summer. The seasonal cycle estimated from the density field seems to be delayed by about 3 months.

In conclusion the gyre strength estimate from the CD29 cruise data in 1987 is significantly different to the mean gyre strength estimated between 2002 and 2006 from float data. This is further emphasised by looking at the seasonal variability. The results suggest that the structure as well as the strength of the gyre circulation in 1987 was significantly different to the mean state of the circulation in the very early 21st century.

4.2 Estimates of the gyre strength at 20°S

Further north at 20°S the meridional component of the gyre is smaller because that latitude is closer to the northern edge of the gyre bordered by the SEC. A larger variability is expected due to the vicinity of the ITF, which is known to show large variability on short and long time scales (Sprintall et al., 2002). Again we will focus the analysis on the interior defined as the longitudinal band from 55°E to 110°E. This will exclude the transports in the east shallower than 2000 dbar and also the major part of the boundary transport of the *East Madagascar Current* (EMC) at the eastern flank of MAD.

As an introduction, results from the recent BEAGLE cruise are presented to describe the gyre strength in early 2004. In detail the results come from the 20SBEAGLE cruise realisation with the OI applied to the cruise data to map the properties to 20°S, smoothed by the decorrelation length scales 200 km west of MAD and 600 km east of MAD (Chapter 3.1.3). Note that the actual latitude is 20.5°S given by the 1° x 1° grid

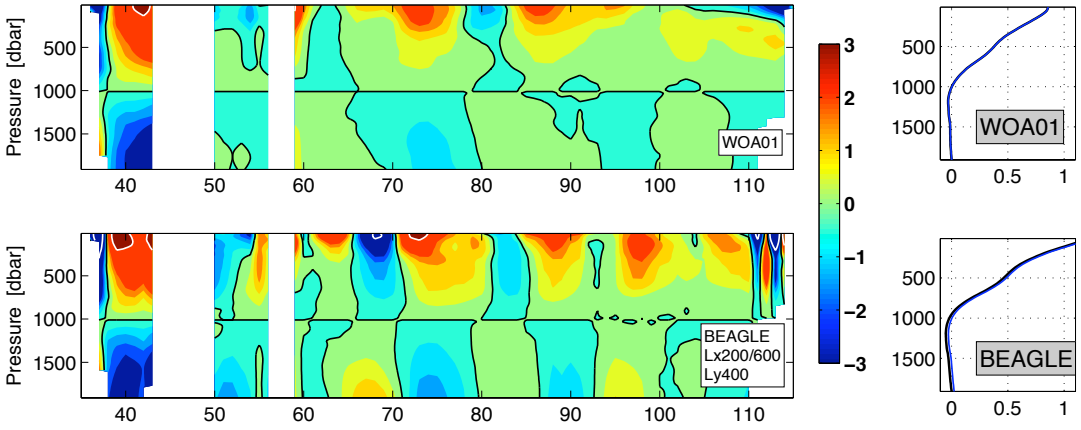

FIGURE 4.14: Left: Meridional geostrophic velocities [in $\mathrm{cm\,s^{-1}}$] referenced to and above 1000 dbar across 20°S, calculated from World Ocean Atlas 2001 climatology (top) and from 20SBEAGLE realisation (bottom). Black contours indicate zero velocity and white contours indicate $\pm 5\,\mathrm{cm\,s^{-1}}$. Right: Mean geostrophic velocity profiles [in $\mathrm{cm\,s^{-1}}$] referenced to 1900 dbar (black) and 1000 dbar (blue) averaged between 55°E and 110°E calculated from WOA01 climatology (top) and from 20SBEAGLE realisation (bottom).

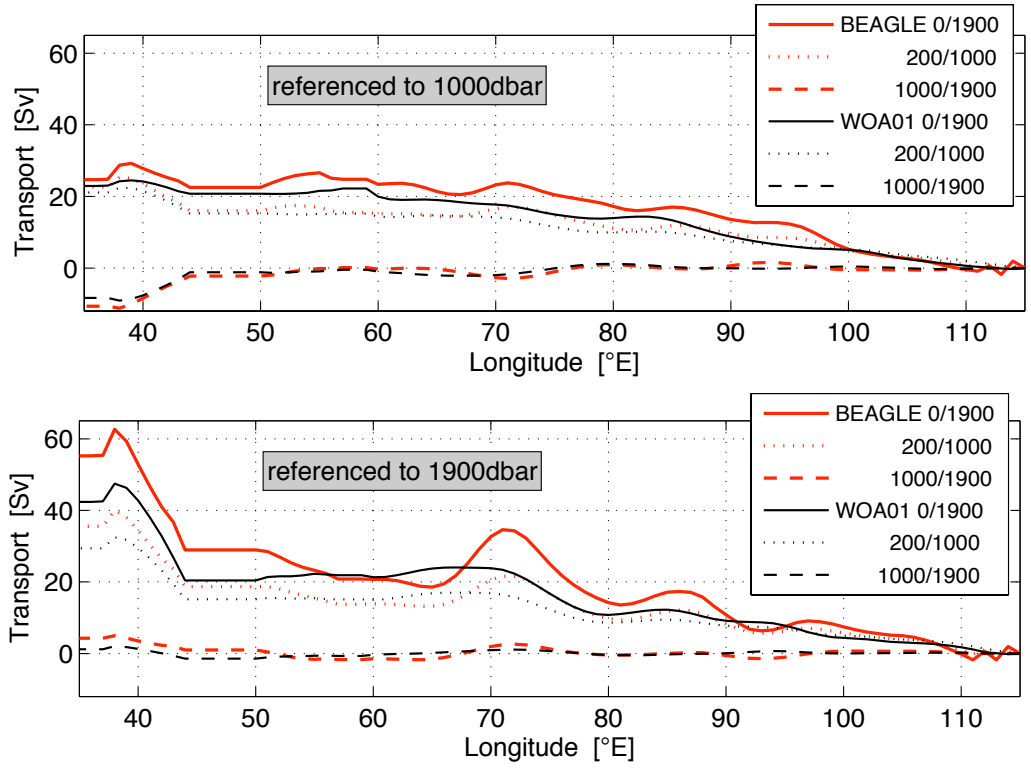

FIGURE 4.15: Meridional transport [Sv] across 20°S relative to and above 1900 dbar (top) and 1000 dbar (bottom), respectively for different depth levels cumulatve integrated from East to West from World Ocean Atlas 2001 climatology (black) and 20SBEAGLE (red).

of the background climatology but for the ease of reading we refer to it as 20°S as for the 32°S section. The cruise CTD stations between 48°E and 110°E have an average latitude of 20.1°S with a standard deviation of 0.19° latitude.

From the hydrographic measurements we calculated the geostrophic velocity and transport field referenced to either 1000 dbar or 1900 dbar. While Warren (1981) showed that the geostrophic transport estimates at 18°S, east of 60°E are not sensitive to the choice of the ZV level so long as it is chosen between 1000 dbar and 2000 dbar we find an area of large vertical shear of more than 1 cm s^{-1} in the geostrophic velocities between 1900 dbar and 1000 dbar between 65°E and 80°E (Fig. 4.14). This could result from a large mesoscale deep-reaching eddy or more likely from a meander of the southern most part of the SEC. In the WOA01 data the feature is less pronounced but we still find a shear in geostrophic velocities of 0.5 cm s^{-1} in that region. This indicates that care needs to be taken to estimate the gyre strength. Using the *MaxTrp* method we estimate either 34.8±3.5 Sv referenced to and above 1900 dbar, with the maximum transport in the interior at 71°E, or we estimate 27.1±4.1 Sv referenced to and above 1000 dbar with the maximum transport located at 55°E (Fig. 4.15). Using the *LinReg* method the estimates for the different ZV assumptions are 24.6± 2.8Sv and 27.0±2.3 Sv referenced to 1900 dbar and 1000 dbar, respectively.

From the general structure of the meridional geostrophic velocity section it seems likely that with a larger smoothing length scale this large signal at 71°E in the meridional transport (Fig. 4.15 bottom) would reduce or disappear from the cruise data, as it seems to represent an intense mesoscale eddy (Fig. 4.14). Additionally in the zonally averaged velocity profiles between 55°E and 110°E the change in the ZV level shows very little differences (Fig. 4.14). We will therefore use the 1000 dbar level for the ZV assumption in the following.

Both geostrophic velocity sections show large northward velocities in the eastern MOZC with only a small narrow band of southward velocities close to the continental slope (Fig. 4.14). Although a strong anticyclonic circulation was reported for 24°S at the southern exit of the MOZC using a global hydrographic inverse geostrophic box model, a net southward mass flux of 5 Sv (Stramma and Lutjeharms, 1997) to 14 Sv (Ganachaud and Wunsch, 2000) would be expected. That basically indicates that the uniform ZV assumption at the western boundary of either 1000 dbar or 1900 dbar is not valid and the derived velocities for either reference surfaces do not represent the circulation. In the following we start with the estimates of the seasonal gyre strength at 20°S which can then be included as a seasonal error contribution for the estimates of the annual gyre strength, described later.

As pointed out, the two methods to estimate the gyre strength, described previously (sec. 4.1.1.1 and 4.1.1.2) have different advantages. While for the $MaxTrp_{WOA}$ method measurements only at the end points are needed and therefore, it is more suited for long time records with moorings for example. In contrast, the *LinReg* method does take the interior into account making the method less dependent on the choice of end points but also in this case less sensitive to eddy signals in the transports, as seen for example in the CD139 cruise data near 104°E ((Palmer et al., 2004) their figure 3). The relatively early stage of the Argo project at the time of this study in the SIO indicates that the *LinReg* method may be the appropriate method, being less sensitive to the profile distribution. Therefore, in the following at 20°S we use solely the *LinReg* method to estimate the gyre strength.

4.2.1 Seasonal estimates of the gyre strength at 20°S

The seasonal coverage of profiles is very good, even in the western boundary region west of MAD. Only during the autumn season does a profile free area exist further south of 20°S between 85°E and 95°E with a latitudinal extent of 3° latitude, which does not affect the seasonal estimate because many profiles exist close to 20°S (Fig. 4.16). Additionally it is important to keep in mind that in this area many floats with a parking level of 1000 dbar or 1500 dbar have been deployed taking only every 3rd cycle (or less frequently) a profile down to 1900 dbar. For the seasonal float realisations this affects mainly the interior between MAD and 80°E, where for depths below 1000 dbar only 30% to 50% of the number of profiles are available compared to the upper 1000 dbar, while in the east the percentage of deep profiles ($\geq$1900 dbar) is generally more than 70% compared to the upper 1000 dbar.

Generally the seasonal geostrophic velocity sections (not shown) agree well with the geostrophic velocity section from WOA01 climatology with two large areas of northward velocities in the interior between 65°E and 80°E and between 85°E and 100°E, respectively. In summer the broad southward flow in the east of the section is reversed to a deep reaching northward flow with velocities up to $2\,\mathrm{cm\,s^{-1}}$ extending between 100°E and 110°E and a narrow southward boundary flow at 113°E. While during the other seasons the flow field east of 100°E is more like the one seen from climatology, with generally southward velocities and a northward boundary or under current (Fig. 4.14). In the west of the section, intense southward velocities exist directly off the African coast followed by strong northward velocities of more than $5\,\mathrm{cm\,s^{-1}}$ occupying the major part of the MOZC as seen in the climatology, indicating the weakness of the ZV assumption in that region (Chapter 4.2). Between MAD and MAU southward flow

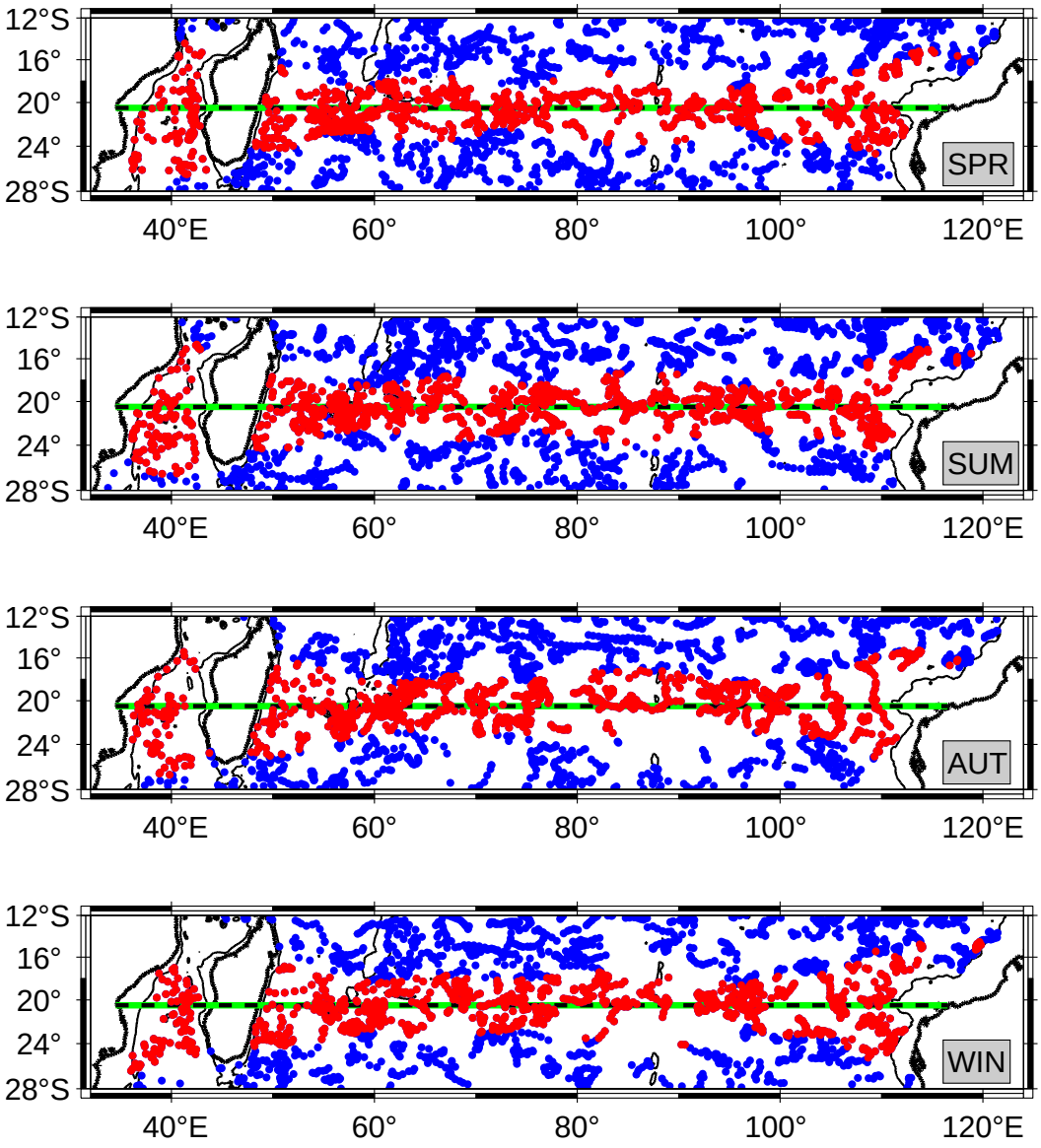

FIGURE 4.16: Maps showing seasonal distribution of all delayed-mode quality controlled Argo float profiles in the subtropical South Indian Ocean (blue dots) and those finally taken into account for the seasonal estimate of temperature and salinity from the optimal interpolation scheme (red dots) along 20°S (green and black dashed). Contours highlight 1900 m isobath (thin solid black) and coastline (bold).

is dominating with maxima of -3 cm s^{-1} existing in an intense and focused EMC during summer and winter. East of MAU northward velocities form a narrow but intense boundary current.

The cumulated seasonal transports from the float realisations for the upper 1900 dbar referenced to 1000 dbar indicate a very consitent interior flow between 100°E and 45°E. East of 100°E the summer period shows a northward transport of 6.3 Sv between 110°E and 100°E, while during spring and winter a small southward transport of -0.3 Sv exists

and during autumn a northward transport of 2.5 Sv exists. The estimate from the interpolated cruise data (20SBEAGLE) fits well in the seasonal transport estimates (Fig. 4.17).

The transport estimates for the layer between 200 dbar and 1000 dbar indicate a very similar structure to the total transport structure in the interior and at the eastern end of the section. While the deep layer between 1000 dbar and 1900 dbar indicates differences to the total transport over the upper 1900 dbar. In the deep layer the seasons spring and summer indicate a very similar structure and magnitude between 100°E and 55°E, with a southward transport of about 4 Sv between 80°E and 70°E which is in the order of the total meridional layer transport between 110°E and 55°E. During the autumn and winter season the cumulated meridional transport is positive in autumn and almost zero in winter. Additionally the deep layer gyre strength estimate of the interpolated

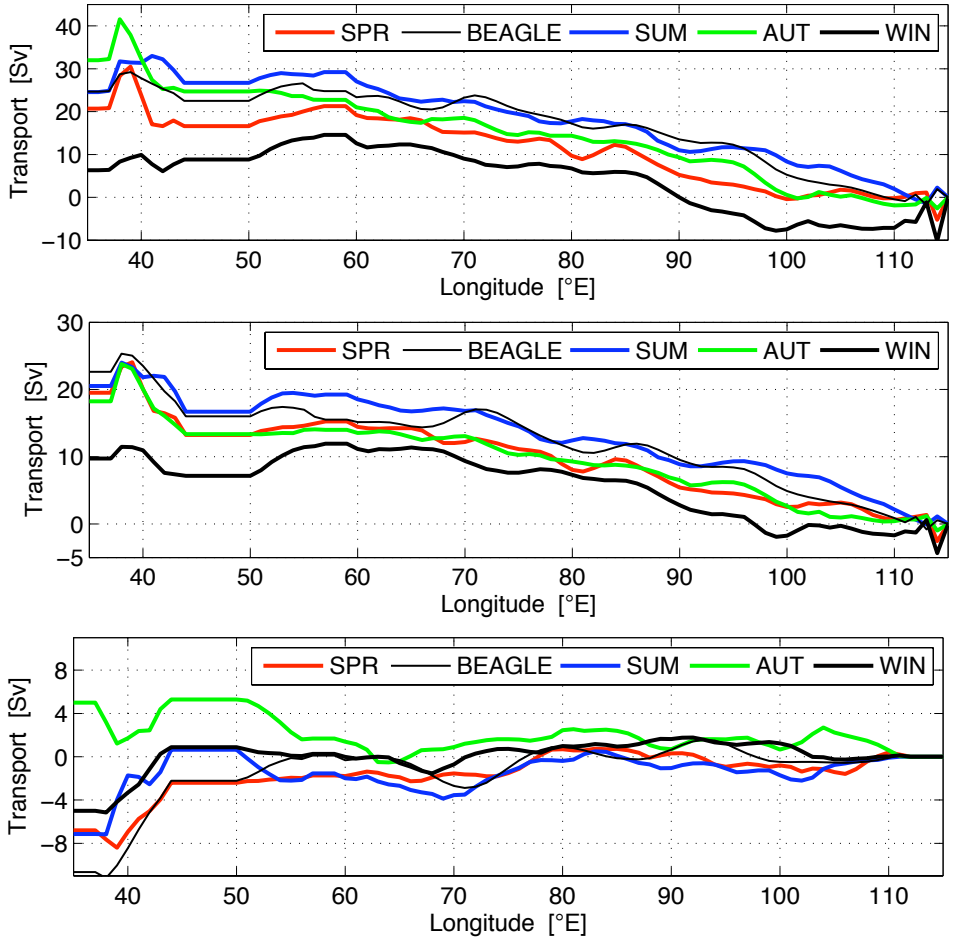

FIGURE 4.17: Cumulated geostrophic transports for the upper 1900 dbar (top), the thermocline layer between 200 dbar and 1000 dbar (middle) and the deeper layer between 1000 dbar and 1900 dbar, derived from seasonal float realisations along 20°S using a ZV level at 1000 dbar. Also shown is the transport derived from the 20SBEAGLE realisation (black thin).

cruise data (20SBEAGLE) does not fit well in the west to the appropriate summer season.

With the *LinReg* method applied we get a semi-annual variation of 4.2 Sv in the gyre strength between the surface and 1900 dbar and between 55°E and 110°E estimated as standard deviation of the seasonal estimates (Tab. 4.9). In the upper layer (200 dbar to 1000 dbar) we find a maximum gyre strength of 17.6±0.7 Sv during summer while for the other seasons it is smaller with 13.5 Sv, 13.1 Sv and 12.3 Sv in spring, autumn and winter, respectively. Also a seasonality can be found with the maximum gyre strength during summer with the minimum much less pronounced during winter (Tab. 4.9). In the deep layer (1000 dbar to 1900 dbar) the situation is different again, with spring and summer showing similar estimates for the gyre strength of -2.2±0.4 Sv while in autumn we estimate 2.2±0.4 Sv and in the winter period no net transport of 0±0.3 Sv (Tab. 4.9).

It is interesting that the magnitude of change in the gyre strength in the upper layer between spring and summer is of the same order as between summer and autumn. In contrast, the change of the gyre strength for the upper 1900 dbar between spring and summer is 3 times larger than between summer and autumn. This difference is balanced in the deeper layer with almost no change between spring and summer but an increase in the gyre strength of 4 Sv between summer and autumn, compensating almost completely the decrease in gyre strength in the upper layer (Tab. 4.9). Between autumn and winter and between winter and spring, respectively the change seems to take place mainly in the deep layer as well as in the surface layer, which we conservatively take to be the upper 200 dbar. The change from spring to summer is based

TABLE 4.9: Similar to table 4.7 but now along 20°S for interpolated BEAGLE cruise data (December and January) and for seasonal float realisations with the *LinReg* method applied to the vertical integrated geostrophic transport profiles referenced to 1000 dbar between 55°E and 110°E. Listed are the estimates for the full profile depth (0 dbar to 1900 dbar) and two separate layers, the thermocline layer mainly occupied by the MW and IW between 200 dbar and 1000 dbar and the deeper layer below 1000 dbar reaching to the maximum depth of 1900 dbar of the float realisations. Error contribution from meso-scale variability and from sampling given by the OI are included as square-root of the sum of the squares.

Season	LinReg $_{0/1900}$	LinReg $_{200/1000}$	LinReg $_{1000/1900}$
SPR (SON)	19.6 ±1.5	13.5 ±0.7	-2.1 ±0.3
BEAGLE (DJ)	27.0 ±2.3	16.5 ±1.3	-0.3 ±0.4
SUM (DJF)	27.5 ±1.4	17.6 ±0.7	-2.2 ±0.4
AUT (MAM)	25.0 ±1.5	13.1 ±0.7	2.2 ±0.4
WIN (JJA)	18.8 ±1.4	12.3 ±0.6	0 ±0.3

in the upper (200 dbar to 1000 dbar) and the surface layer (0 dbar to 200 dbar). This shift in the dominant role contributing to the seasonal changes in the gyre strength is represented in the seasonal or semi-annual variation of both layers, estimated as standard deviation of the seasonal estimates with 2.4 Sv in the upper layer and 2.1 Sv in the deeper layer. Such a shift was not found at the 32°S section (Tab. 4.7 and 4.5). It is worthwhile to note that the seasonal error estimates at 20°S are slightly smaller than those at 32°S. This might be due to a better spatial coverage of profiles possibly resulting in a smaller error contribution from sampling or meso-scale variability.

4.2.2 Annual estimates of the gyre strength at 20°S

The annual distribution of profiles in the vicinity of 20°S is sparse in the earlier two years (Fig. 4.18). In 2002 almost no profiles are available, with the largest number in the east of the section east of 100°E. Therefore year 2002 is excluded from the following analysis, because the density field is based almost entirely on the WOA01 climatology (Chapter 3). In year 2003 the situation is slightly better but still a large area exists between 75°E and 90°E with no profiles available (Fig. 4.18). In 2004 east of 108°E only profiles north of 16°S exist but with some profiles existing very close to 20°S at 105°E there should not be problems for the analysis. The number of profiles taken into account for levels deeper than 1000 dbar is less than 10% in the interior between 50°E and 95°E for 2003 compared to levels above 1000 dbar. In contrast for 2004 a good coverage exists with generally more than 70% of profiles taken into account compared to the level above 1000 dbar, which is due to the deployment of 13 floats during the BEAGLE cruise in early 2004. In 2005 and 2006 the coverage on deep levels is comparable to the seasonal float realisations with a better coverage east of 80°E.

The annual geostrophic velocity sections (not shown) agree well with the broad structure seen in the WOA01 climatology. Still the interior structure is relatively noisy making it difficult to see clear differences. In the west of the section, we find the southward flowing EMC very strongly represented in 2003 and 2006. In 2004 the flow field in the MOZC seems dominated by strong southward flow at the African coast and northward flow west of MAD. None of the years show a possible net southward flow in the geostrophic velocity section in the MOZC which indicates again the problem of the ZV assumption in the boundary current region as pointed out in the beginning of this section (Chapter 4.2 and 4.2.1). The geostrophic transports referenced to 1000 dbar cumulated from east to west are very focussed together within a range of 10 Sv from the eastern end of the section at 115°E to 55°E. The transport for the interpolated BEAGLE data (20SBEAGLE) fits very well between the 2003 and 2004 data with about 5 Sv larger transports around 95°E.

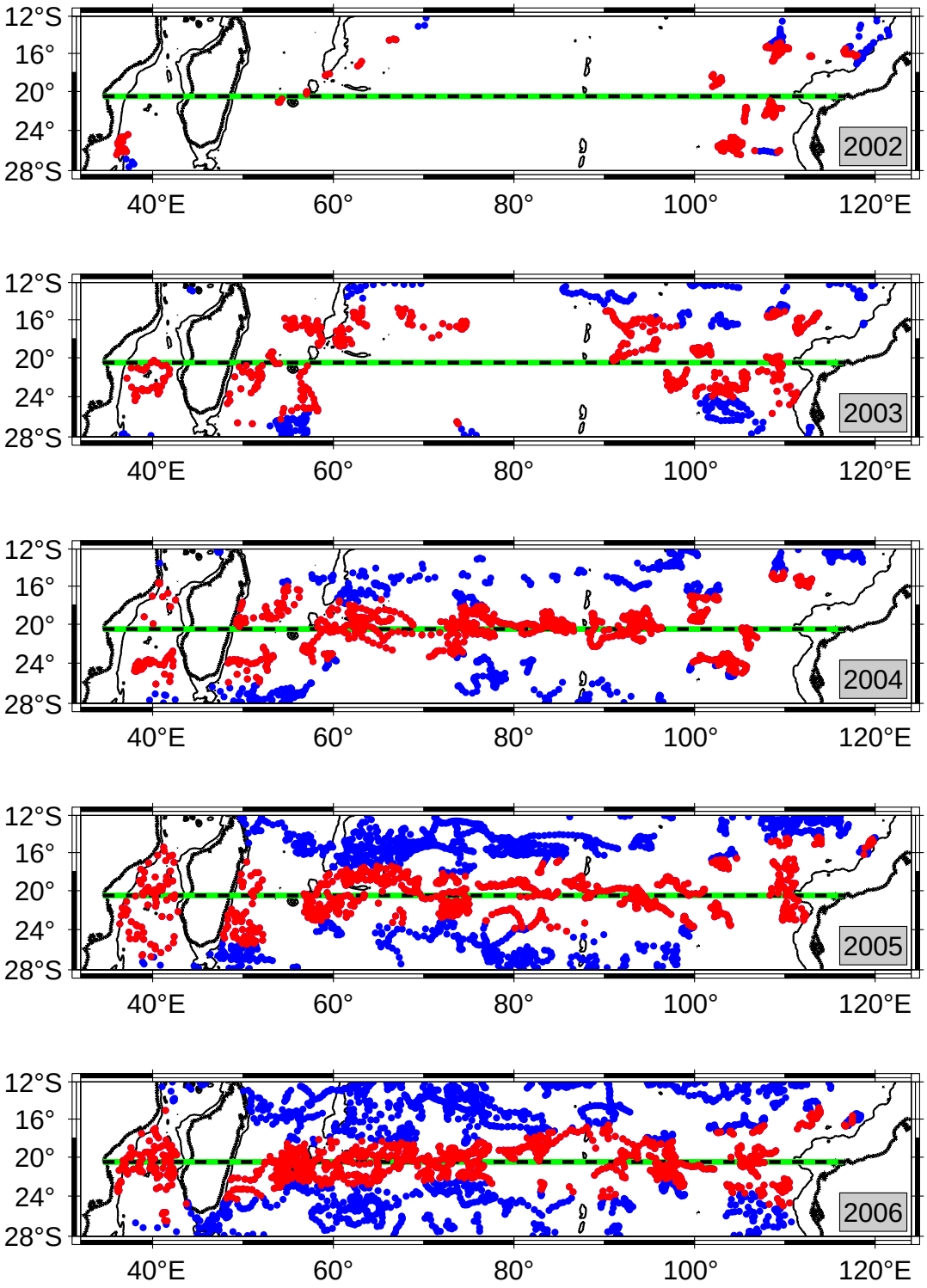

FIGURE 4.18: Maps showing annual distribution of all delayed-mode quality controlled Argo float profiles in the subtropical South Indian Ocean (blue dots) and those finally taken into account for the annual estimate of temperature and salinity from the optimal interpolation scheme (red dots) along 20°S (green and black dashed). Contours highlight 1900 m isobath (thin solid black) and coastline (bold).

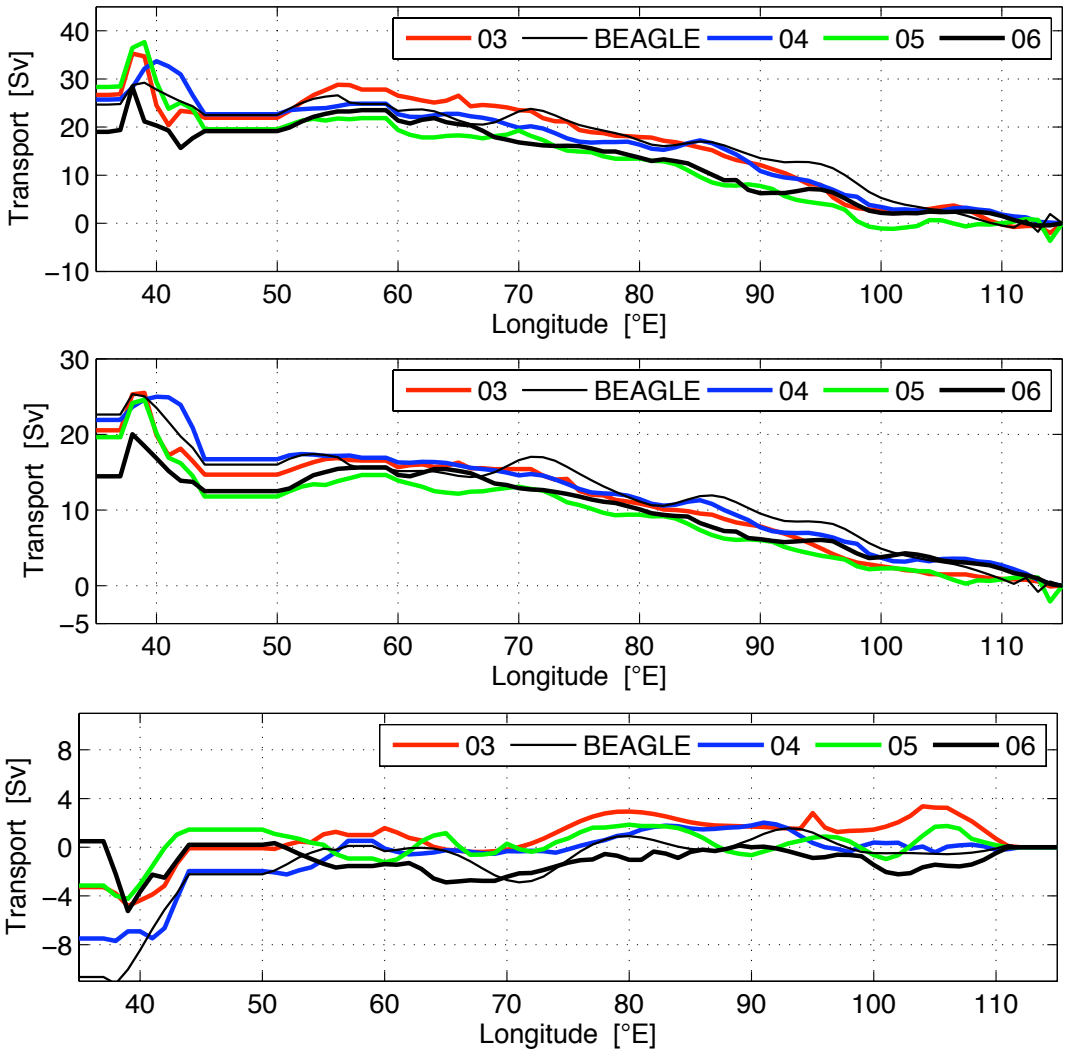

FIGURE 4.19: Cumulated geostrophic transports for the upper 1900 dbar (top), the thermocline layer between 200 dbar and 1000 dbar (middle) and the deep layer between 1000 dbar and 1900 dbar, derived from annual float realisations across 20°S using a ZV level at 1000 dbar. Also shown is the transport derived from 20SBEAGLE realisation (black thin).

From the cumulated geostrophic transports, referenced to and above 1000 dbar (Fig. 4.19), we derive the gyre strength estimates by applying the *LinReg* method between 55°E and 110°E as described previously (Chapter 4.1.1.2). The annual float realisation show a decrease in gyre strength from 29.0±4.8 Sv in 2003 to 21.0±2.4 Sv in 2005 followed by a small increase to 22.5±2.0 Sv in 2006, with a similar tendency given for the upper layer between 200 dbar and 1000 dbar. The deep layer between 1000 dbar and 1900 dbar exhibits an different change, from a negative gyre strength in 2003 to a positive one in 2005 and finally a negative one in 2006 again, but taking the errors into account, these changes might not give a robust signal in interannual

TABLE 4.10: Similar to table 4.9 but now for annual float realisations at 20°S. Including the estimate for the layer 0 dbar to 1000 dbar for later comparison with geostrophic Sverdrup transport. Given errors include contributions from meso-scale variability (ϵ_{EDDY}) and sample errors given by the OI (ϵ_{OI}). Additionally for the year 2003 a sub-annual error contribution (ϵ_{SUB}) is taken into account, due to the sparse data coverage.

Year	LinReg $_{0/1900}$	LinReg $_{200/1000}$	LinReg $_{1000/1900}$	LinReg $_{0/1000}$
2003	29.0 ±4.8	15.8 ±2.7	-1.0 ±0.7	28.1 ±4.5
BEAGLE	27.0 ±2.3	16.5 ±1.3	-0.3 ±0.4	26.1 ±2.2
2004	22.5 ±2.1	14.7 ±1.1	-0.9 ±0.4	23.4 ±2.0
2005	21.0 ±2.4	12.5 ±1.3	0.2 ±0.5	20.9 ±2.1
2006	22.5 ±2.0	13.5 ±1.0	-1.3 ±0.4	23.5 ±1.7

chnage (Tab. 4.10). This means that a small, but not significant, anticorrelation exists, between the upper and the deeper layer in the changes in gyre strength between 2003 and 2006. A compensation of the changes in the gyre strength in the upper layer (200 dbar to 1000 dbar) by the deeper layer (1000 dbar to 1900 dbar), as clearly seen in the seasonal estimates, is not identifiable.

The given errors include contributions from meso-scale variations (ϵ_{EDDY}) and from sampling which is given by the OI (ϵ_{OI}). Additionally for the year 2003 a sub-annual error contribution (ϵ_{SUB}) is taken into account, due to the sparse data coverage. This sub-annual error contribution is taken as the standard deviation of the seasonal estimates for the different layers (from top to bottom), 4.2 Sv, 2.4 Sv and 2.1 Sv, respectively (Sec. 4.2.2). Therefore, differences in the data coverage as seen between 2003 and 2006 for example are represented in the sub-annual error contribution, while the differences in sampling error estimates and meso-scale error contributions, respectively, play a minor role in the finally error estimate.

4.2.3 Variability of the gyre strength at 20°S

The estimated mean gyre strength at 20°S over the 4 year period 2003 to 2006 is 23.8±1.4 Sv. The interannual variability is 3.6 Sv and the seasonal variability is 4.2 Sv, estimated as standard deviation of the annual and seasonal gyre strength, respectively. The direction of interannual and seasonal changes are the same as those seen at 32°S (Chapter 4.1.3). Although we have fewer estimates at 20°S we calculate a trend for the period 2003 to 2006 with associated correlation coefficient as shown in section 4.1.3. We find a negative trend in the estimates of the gyre strength at 20°S but depending on the period and data selected this trend shows small or no significance especially including the associated error estimates (Fig. 4.20 and Tab. 4.11).

TABLE 4.11: Comparison of the time series of estimated gyre strength split into the period 2003 to 2006 including estimates from Argo and cruise data or solely from the Argo float data, and also for the period 2004 to 2006. The gyre strength was estimated using the *LinReg* method applied to the vertically integrated geostrophic transport profiles. Trends of the change in the gyre strength are given with associated correlation coefficient, the p-value and the significance level.

Period	Trend [Sv/year]	R	p-value	Significance level
2003 - 2006 Cruise & Argo	-2.4	-0.82	0.09	91%
2003 - 2006 Argo only	-2.2	-0.79	0.21	79%
2004 - 2006 Cruise & Argo	-1.7	-0.70	0.30	70%
2004 - 2006 Argo only	-0.2	-0.22	0.86	24%

The seasonal peak-to-peak variation in the gyre strength seen between summer and winter exceeds the associated errors for both seasons and indicates that they are significantly different. The seasonal estimates suggest an important role of the deep layer (1000 dbar to 1900 dbar) contributing to the seasonal gyre strength indicated by the large seasonal variations of 2.1 Sv which is about the same as the 2.4 Sv seasonal variability seen in the upper layer (200 dbar to 1000 dbar). The deep layer is acting as a buffer between summer and autumn and between winter and spring, respectively, compensating the decrease/increase in gyre strength in the upper layer. In contrast, between autumn and winter the deep layer indicates the largest changes of the two layers and between spring and summer the change takes place mainly in the upper layer (always excluding the near surface layer of the upper 200 dbar). The interannual variations indicate anticorrelated changes in the deep layer compared to the upper layer too, but less pronounced. The gyre strength estimated from BEAGLE cruise data is in good agreement with both the annual and seasonal estimates, repsectively.

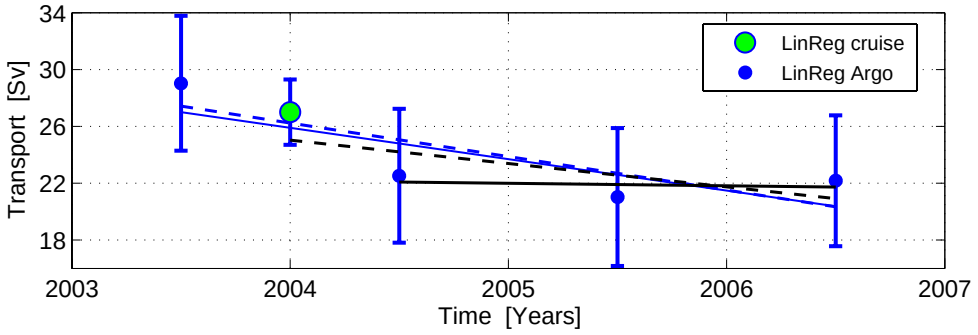

FIGURE 4.20: Time series of gyre strength estimated using the *LinReg* method with associated errors for the annual float realisations (blue dots) and the interpolated cruise data (green filled). Also shown is the trend estimated for the period between 2003 and 2006 including the interpolated BEAGLE data (blue dashed) or solely the Argo realisations (blue solid) and the same for 2004 to 2006 including the cruise data (black dashed) or solely the float realisations (black solid).

In the following sections we try to put the results into context with other observations such as Sverdrup transport derived from wind-stress curl or sea surface height anomaly measured from satellite.

4.3 Comparison to Sverdrup transport

Generally the structure of the cumulated transports with its linearity reflects the Sverdrup flow one would expect at the centre of the subtropical gyre (Tomczak and Godfrey, 1994). The Sverdrup theory relates the curl of the wind-stress to mass transport within the upper ocean assuming that the flow is stationary, that lateral friction and molecular viscosity are small, and that turbulence near the sea surface can be described using an eddy viscosity (Sverdrup, 1947). Furthermore, the theory assumes that the flow is baroclinic and that a uniform level of no motion exists for the wind-driven layer at some depth. With the horizontal momentum equations written as follows

$$-f\rho v = -\frac{\partial p}{\partial x} + \frac{\partial}{\partial z}\left(A_z \frac{\partial u}{\partial z}\right) , \tag{4.4}$$

$$f\rho u = -\frac{\partial p}{\partial y} + \frac{\partial}{\partial z}\left(A_z \frac{\partial v}{\partial z}\right) , \tag{4.5}$$

where f is the Coriolis parameter, ρ the density, u and v are the horizontal velocity components, $\partial p/\partial x$ and $\partial p/\partial y$ the horizontal pressure gradient, and the last term on the right hand is side the eddy viscosity. Sverdrup defined the mass transport in the wind driven layer $M_x \equiv \int \rho u(z)dz$ and $M_y \equiv \int \rho v(z)dz$ and set the wind-stress (τ_x, τ_y) as horizontal boundary conditions of the eddy viscosity while there is zero stress at the depth of the assumed level of no motion. Vertical integration of the horizontal momentum equations over the depth of the wind-driven layer with these definitions and boundary conditions applied and cross differentiation with respect to x and y as well as the combination with the similarly integrated continuity equation provides the fundamentals of Sverdrup's theory

$$\beta M_y = curl_z\ (\tau_\eta) , \tag{4.6}$$

where $curl_z\ (\tau_\eta)$ is the vertical component of the wind-stress curl, the only component which is non-zero for a horizontal wind. The symbol β refers to the rate of change of

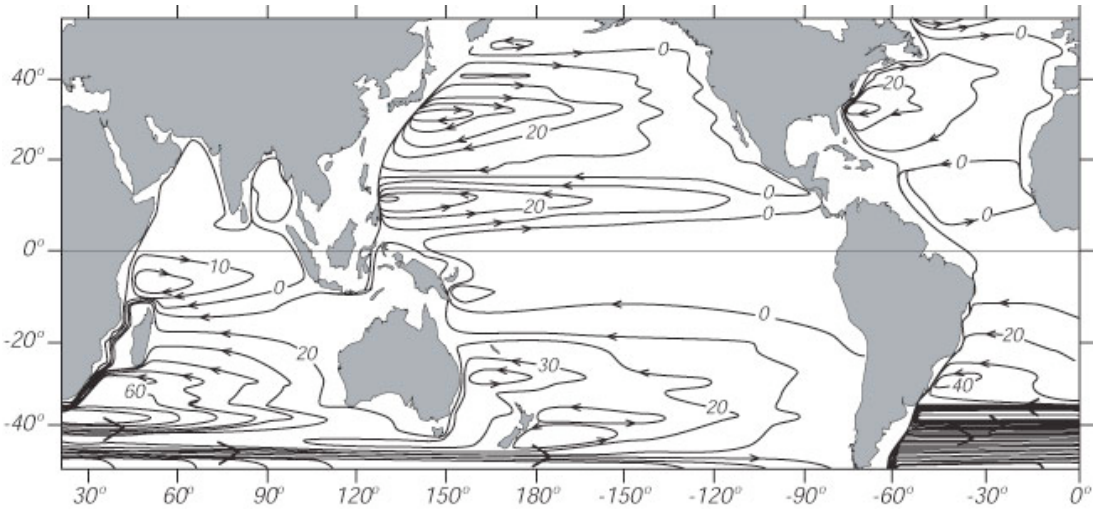

FIGURE 4.21: Depth-integrated Sverdrup transport applied globally using the wind-stress from HELLERMAN AND ROSENSTEIN (1983). Contour interval is 10 Sverdrups. Figure taken from TOMCZAK AND GODFREY (1994).

the coriolis parameter with latitude $\beta = \partial f / \partial y$. Finally, M_y is the total mass transport in the wind-driven layer extending down to an assumed level of no-motion

$$M_y = M_{yE} + M_{yg} \ , \tag{4.7}$$

including the Ekman wind-driven transport (M_{yE}) and the geostrophic transport (M_{gE}). A detailed description of Sverdrup's theory is given in many physical oceanography textbooks, as for example POND AND PICKARD (1983); PEDLOSKY (1987, 1996); TOMCZAK AND GODFREY (1994).

The Sverdrup solution has been used for describing the global system of upper ocean currents. While the solution is applied throughout each basin all the way to the western limit of the basin, conservation of mass is forced by including north-south currents confined to a narrow, horizontal western boundary layer (Fig. 4.21). The Sverdrup relation has been used widely to deduce the wind-driven interior circulation of the ocean (e. g. WELANDER (1959); HELLERMAN AND ROSENSTEIN (1983)) and it is well suited to the subtropical regions where it provides a good indication of the mean flow in the upper 1000 m of the ocean. This is due to the stratification in the main thermocline where the effect of topography is proportional to the vertical scale distance. In the subtropics for features with a horizontal scale of about 100 km the vertical scale will be less than 2.5 km (WEBB AND SUGINOHARA, 2001). In high latitude regions where bottom topography is important and the ZV assumption at the bottom may

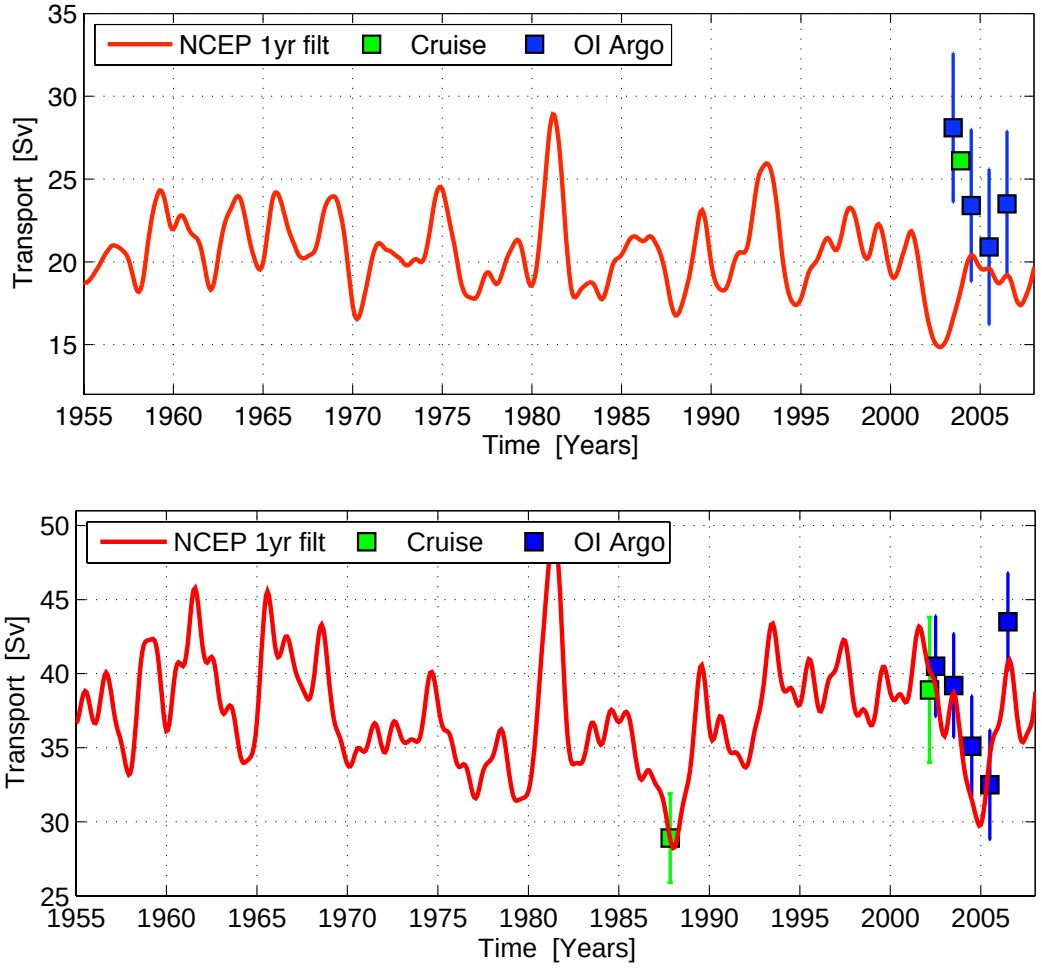

FIGURE 4.22: Comparison between time series of geostrophic Sverdrup transport across 20°S (top) and 32°S (bottom) derived from monthly NCEP wind-stress data and estimates for the gyre strength in the upper 1000 dbar from cruise data (green squares) and optimally interpolated Argo float data (blue squares) using the *LinReg* method (Sec. 4.1.1.2 and 4.1). The wind-stress data have been averaged over a 6° latitudinal band with a 1-year low-pass filter applied (solid red). The time lag in the estimates derived from wind-stress data shown here is 1 year at 20°S and at 32°S.

be invalid, the Sverdrup relation is not sufficient to describe upper ocean circulation (WEBB ET AL., 1991).

Here we apply the Sverdrup solution to the interior of the SIO, excluding the western boundary region, to compare the geostrophic component of the Sverdrup transport derived from the wind-stress curl with the previously estimated meridional transports. The estimates of the gyre strength using the *LinReg* method are used due to greater confidence in these results (Chapter 4.1). The wind-stress curl is taken from the monthly surface fields from the NCEP-NCAR Reanalysis Project CDAS-I[1] (KISTLER ET AL., 2001). Time series of Sverdrup transport across 20°S and 32°S were generated using

[1]Climate Data Assimilation System I from NCEP-NCAR Reanalysis Project

the vertical component of the wind-stress curl ($curl_z(\tau_\eta)$, see Equation 4.6) averaged over a 6° latitudinal band centred around 20°S and 32°S, respectively. With the decomposition of the total mass transport in the wind-driven layer into Ekman (M_{yE}) and geostrophic (M_{yg}) components (Eq. 4.7) we derive geostrophic Sverdrup transport across 20°S and 32°S, respectively. The data have been low-pass filtered with a 1-year second-order Butterworth filter (Butterworth, 1930) with different time lags of 1 year, 18 months, 2, 3 and 4 years applied (to accommodate different possible time scales of dominating processes such as Rossby Waves for example). At 20°S away from the centre of the subtropical gyre the geostrophic Sverdrup transport is smaller than further south while the Ekman component increases, therefore it might be easier to find an agreement at 32°S than at 20°S (Fig. 4.22). At 32°S a crude estimate for the transient baroclinic adjustment time to long baroclinic Rossby waves would be at least 5 years (Qiu and Chen, 2006), while at 20°S it would only take about half of that time (Chelton and Schlax, 1996; Qiu and Chen, 2006). In contrast, the annual estimates of the gyre strength between 45°E and 110°E show good agreement with a time lag of 1 year to 2 years at 32°S, while at 20°S no significant correlations are found (Fig. 4.22).

The estimated gyre strength derived from cruise data and annual float realisation agree well with the gyre strength derived from Sverdrup transport, if the later is lagged by one year. While it is to note, that the gyre strength estimate for 1995 would probably not fit very well, because it was assumed that the major changes in the gyre strength have taken place between 1995 and 2002 (Palmer et al., 2004). From their results it seems likely that in 1995 the gyre strength estimate from the cruise data would be much smaller than those derived from wind-stress curl. Between the 1 year filtered Sverdrup transport, lagged by 1 year, and the estimates from the cruise data and float realisations at 32°S we find a large correlationof $R^2 = 0.92$ with a 99% significance level (Tab. 4.12). We also see that the correlation is still large for a lag of 18 months or 2 years with a high level of confidence. These correlations are based on the estimates of the gyre strength derived from the interpolated cruise data and from the Argo float realisations (Tab. 4.5). The response to the wind field with a 1-year time lag agrees well with findings from De Ruijter et al. (2004); Palastanga et al. (2006) on the relation between the interannual variability in the EMC and large-scale climate variability in the IO. The westward propagation of the large-scale anomalies associated with ENSO/IOD-cycles is suggested to take one year (Murtugudde et al., 2000). According to Palastanga et al. (2006) an intensification of the subtropical gyre occurs after a positive ENSO/IOD event. Additionally, during a positive IOD event sea surface temperature anomalies off western Australia are positive and connected with positive SLA. The good correlation at 32°S

TABLE 4.12: Correlation of the gyre strength at 32°S (top) and 20°S (bottom) from geostrophic Sverdrup transport time series and the *LinReg* estimates using cruise data and float realisations. Different time lags have been applied to the Sverdrup transport time series, which have been additionally low-pass filtered with 1 year.

Time lag	R	p-value	Significance level
no lag	0.10	0.83	17%
1 year	0.92	0.002	99%
18 months	0.67	0.10	90%
2 years	0.48	0.28	72%
4 years	0.03	0.95	5%

Time lag	R	p-value	Significance level
no lag	0.59	0.30	70%
1 year	-0.75	0.14	86%
18 months	-0.98	0.003	99%
2 years	-0.87	0.05	95%
4 years	0.75	0.14	86%

for a time lag of 1 to 2 years, between Sverdrup transport time series and that from float realisations, does not agree with the typical assumption of perturbations being initiated in the east of the basin and travelling over the whole basin to affect the west. The adjustment time for such phenomena is longer than 1 to 2 years. But, if the perturbations are forced near the western boundary, then the adjustment time would reduce and a time lag of 1 or 2 years could be possible. Additionally, MATANO ET AL. (1998) showed that the MADR has a significant effect on westward propagating perturbations at 40°S probably leading to large baroclinic wave energy arising from the interaction of barotropic waves from the interior of the Indian Ocean and the ridge. At 20°S no significant correlation between the gyre strength estimated from the Argo and cruise data and the Sverdrup transport time series can be detected (Tab. 4.12).

Now the question is, how does the estimated gyre strength, derived from the float realisations, fits in detail to the time series of geostrophic Sverdrup transport. For this we look at the non-cumulated geostrophic Sverdrup transport at 32°S with a moving average of 5° longitude applied for the time period 1971 to 2007 to identify possible areas of importance (Figure not shown, but the discussed features can also be found in Figure 4.23). Generally, the structure shows alternating strong and weak northward geostrophic Sverdrup transports on an annual scale with local maxima in the east at 110°E but also with maxima between 50°E and 110°E varying over time. The stronger transports are associated with the winter season (defined by June, July and August), while the weaker transports occur during summer. Only in the years 1978, 1986, 1987

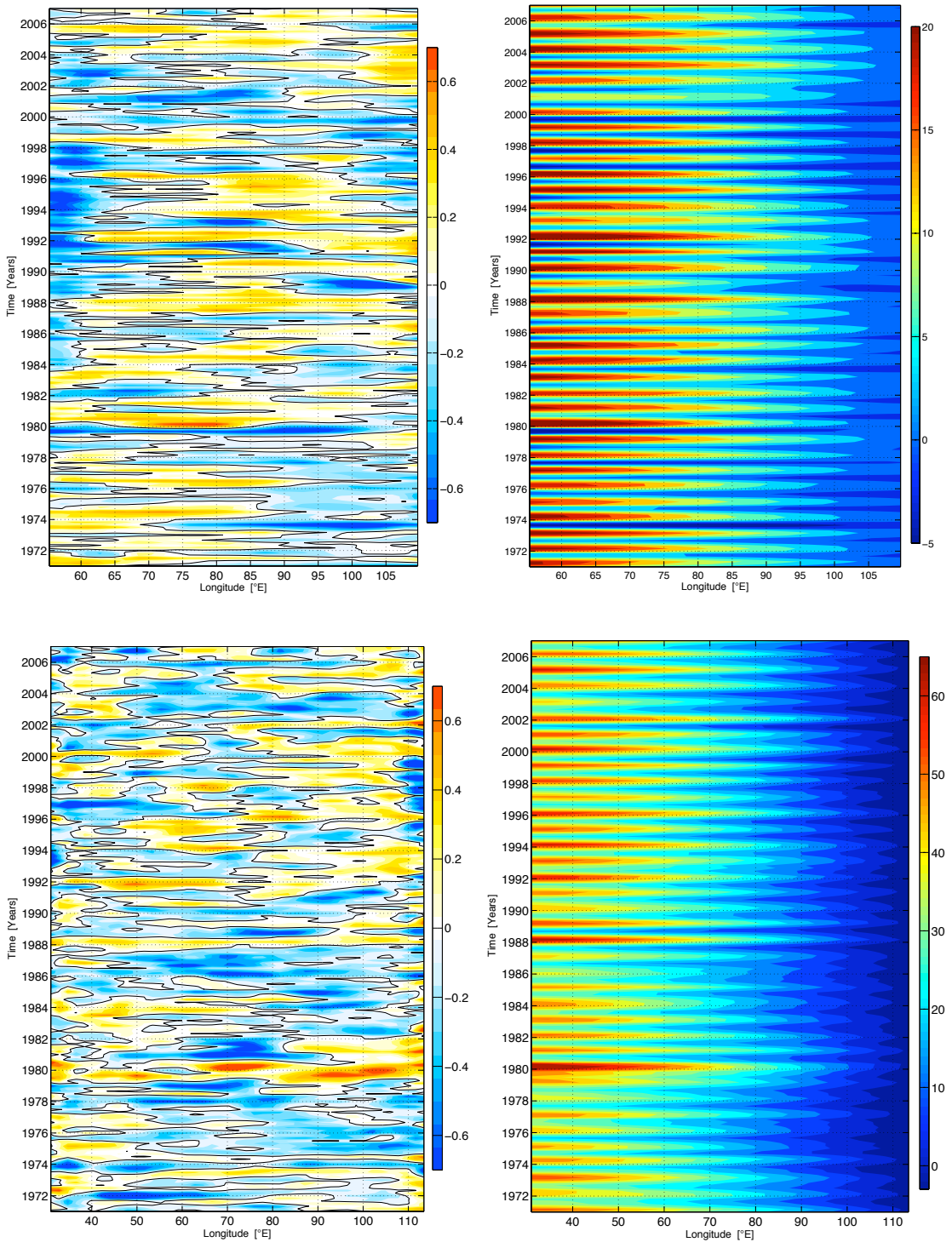

FIGURE 4.23: Left: Longitude time plot of geostrophic Sverdrup transport anomalies at 20°S (top) and 32°S (bottom) calculated between 110°E and 55°E and between 115°E and 30°E as described in the text, with a moving average of 3 months and of 5° longitude applied. Right: Longitude time plot of geostrophic Sverdrup transports at 20°S (top) and 32°S (bottom) integrated from east to west also with a 13 months and 5° longitude moving average applied. Note that the colour scales in the left column are identical for 20°S and 32°S, whereas in the right column the colour scale is different.

and 2003 do the winter seasons, show very little northward transport with early 1987 showing exceptionally weak transports between 60°E and 80°E, which is also apparent in the seasonal anomalies, generated using seasonal means from the time period 1949 to 2007 (Fig. 4.23). This could be an indicator for the change in the gyre transport structure reported in the 1987 data from CD29, where the point of maximum transport was shifted unusually far to the east to 55°E (Palmer et al., 2004). In 2003 the situation is similar but less pronounced, here the winter season is missing large ($\geq$1.5 Sv) northward transports (not shown) and additionally the winter in 2003 and 2004 does show negative anomalies in the geostrophic Sverdrup transport between 50°E and 65°E (Fig. 4.23), while in 2003 also there are negative anomalies across the whole interior basin. This could be the cause for the only moderate increase of cumulated geostrophic transport estimated from the 2004's float realisation west of 60°E. Additionally this could have affected the 2005 estimate too, resulting in weak northward transports in the interior between 70°E and 100°E (Fig. 4.4). At 20°S the maximum in the cumulated geostrophic Sverdrup transport is given in winter too, while the seasonal estimate of the gyre strength showed the maximum during summer (Fig. 4.4, Tab. 4.9). The comparison of the 20°S cumulated geostrophic Sverdrup transport with the one at 32°S shows extreme weak transports in 1989 and 2001 at 20°S with a time lag of 1 year and 2 years, respectively. This could be just a coincidence, since for the weak transport in 1978 at 32°S no connected signal can be found at 20°S.

In the context of changes in the gyre strength, at 32°S the time series from geostrophic Sverdrup transport (with the wind leading by one year) shows a clear minimum of 28 Sv in the gyre strength around 1987. From 1987 to 2002 the gyre strength increases, indicating a positive trend (3.6 Sv/decade; with a statistical significance of more than 85%), while for the period 1987 to 2006, no significant trend is detectable. Testing the trend's dependency on the selected period, with period length changed by up to 4 years, gives still robust positive trends with a confidence level of more than 85%, but with a smaller slope. From around 2002 on, a strong decrease exists until 2005 but with no significant trend detectable. It is interesting, that at 32°S, the minimum in gyre strength derived from Sverdrup transport, as well as the increase afterwards to larger values, occurs in the beginning of the period of reported increase in global mean surface temperatures (IPCC, 2007). Whereas, at 20°S, no such connection is apparent nor are any regimes with significant trends detectable.

4.4 Comparison to satellite altimetric height

We compare the results from the annual float realisations with merged data from satellite altimetric height collected over the 13 year period from 1993 to 2006 from various satellite missions (Dibarboure et al., 2008) available from the Aviso Data Product website[2], to gain knowledge about changes in the spatial structure of the subtropical South Indian Ocean gyre. A shift of the centre of the gyre, as found by Roemmich et al. (2007) in the subtropical South Pacific, leads to changes in the observed gyre strength, if the observations are locally fixed (i. e. to a specific latitude). To detect possible shifts, 2-dimensional maps of the dynamic height, computed from the annual float realisations, are examined and compared with maps of absolute dynamic topography (ADT), derived from satellite altimetry. The ADT dataset can provide essential space-time context for interpreting sparser in-situ datasets. Additionally, the high-resolution altimetric data can be used to identify signal propagation across the basin.

From the temperature and salinity fields from the annual float realisations we compute dynamic height differences (ΔDH) following the proposal of Bjerknes and Sandström (1910)

$$\Delta DH = \frac{\Delta\Phi}{g} \tag{4.8}$$

where g is the acceleration potential in $\mathrm{m\,s^{-2}}$ and $\Delta\Phi$ is the difference in geopotential distance in $\mathrm{m^2\,s^{-2}}$ as described in standard oceanographic textbooks (for example Pond and Pickard (1983); Tomczak and Godfrey (1994); Stewart (2007)).

$$\Delta\Phi = \Phi_2 - \Phi_1 = -\int_1^2 \delta \mathrm{d}p \tag{4.9}$$

with δ the specific volume anomaly in $\mathrm{m^3\,kg^{-1}}$ integrated between the pressure levels p_1 and p_2 in decibars (dbar). The slope of the sea surface is proportional to geostrophic flow at the sea surface that can also be expressed by the gradient of differences in dynamic height.

Here we compare Dynamic Height (DH) calculated from the float realisations at the surface, relative to 1900 dbar (DH0/1900) with maps of absolute dynamic topography (ADT) derived from satellite altimetry (Fig. 4.24). The structure of the DH maps agree very well with those from ADT, with little large scale variation over the 5 years. The maximum of the gyre reaches from the Southeast African coast to east of MAD.

[2] http://www.aviso.oceanobs.com/en/data/products/index.html

The northern part of the *Antarctic Circumpolar Current* (ACC) is well represented extending from the west at 40°S to the east at 45°S with a large meridional gradient in the isolines. In the ADT data the maximum is apparent east and south west of MAD with a tendency to expand eastward and southward from 2002 to 2006. A similar tendency is found in the map of DH0/1900 where the maximum east of MAD extends eastward and southward. In 2003 we also see a separation of the maximum in the ADT into two separate maxima, one in the MOZB and one east of MAD, this is also apparent in the map of DH at the surface, referenced to 1900 dbar. Additionally, in the east we see patches of low DH near the southern tip of Australia in all years but also extending west to BP at 95°E in 2003 and 2004. This is also partly apparent in the maps of ADT where we find patches of low ADT near the south western tip of Australia. The lows in ADT or DH are presumably connected to eddies generated in the LCS as observed for example in late 2003 (Feng et al., 2007). In 2003 there seems to be a pathway of eddy activity represented by low DH from the south western tip of Australia to BP in the north west. The lack of that feature in the maps of ADT might be explained by spatial and temporal sampling bias of the float data.

Remarkable is that in 2006 the area east of 95°E from 30°S to about 42°S, including the whole Perth Basin (PB) and parts of the connecting South Australia Basin (SAB) further south, indicates an ADT increase of 10 dyn cm. This signal is not represented in the field of DH although this area is very well sampled from float profiles. A possible explanation can be found by looking at annual differences in ADT with respect to 2001 (not shown), where only year 2006 indicates a positive difference for almost the complete SIO area.

The separation into a shallow layer (DH200/1000) between 200 dbar and 1000 dbar and a deeper layer (DH1000/1900) between 1000 dbar and 1900 dbar gives the following (Fig. 4.25). The centre of the gyre is indicated by two separated maxima in the upper layer, the southern one extends from the MOZB to southeast of the Southwest Indian Ridge (SWIR) at 60°E and 40°S, while the northern one occupies the region east of MAD to 70°E. This separation is induced by large eddy activity at the southern tip of MAD (Lutjeharms, 1988; Palastanga et al., 2006) and the east or north eastward flowing *South Indian Counter Current* (SICC) at about 25°S (Palastanga et al., 2007).

As reported previously, the maps of DH200/1000 also indicate a patch of low DH in 2003 north of BP and at the southern and northern tip of Australia. In 2005 and 2006 we find again patches of low DH west of Australia, while in 2005 the shape and orientation of the patch suggest a connection to the northeast, in 2006 the patch is located and oriented to the south east (Fig. 4.25). From the south western tip of

Australia a possible source of low DH are cyclonic eddies formed in the LCS between 30°S and 35°S. From the north western coast of Australia a possible source might be perturbations at the exit of the ITF in combination with the SEC. The deeper layer (DH1000/1900) indicates only one centre of the gyre located further east and south

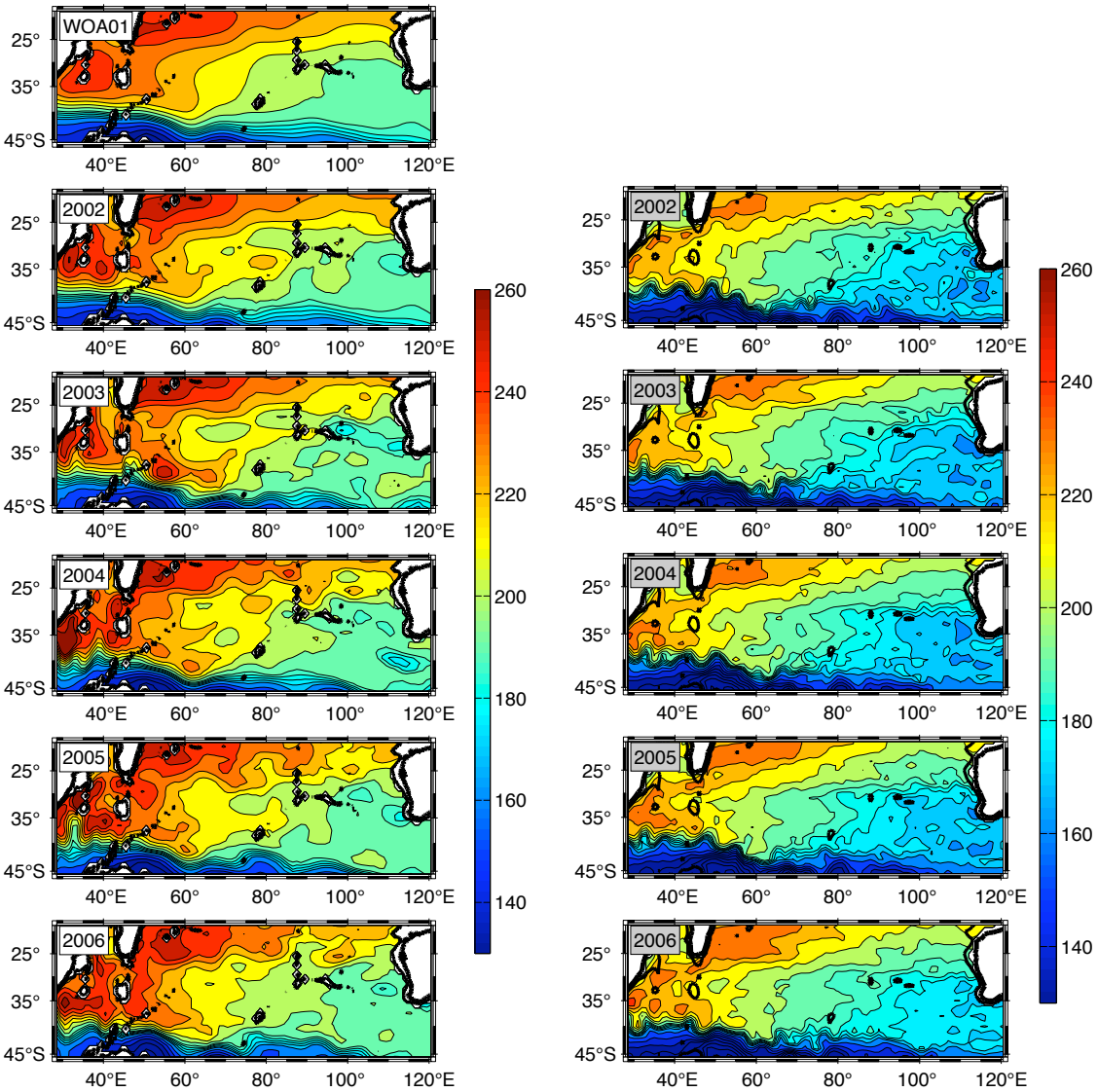

FIGURE 4.24: Left: Maps of dynamic height (0/1900 dbar) computed from the WOA01 climatology (top) and the annual float realisations (2nd to 6th panel). Colour contours generally indicate 10 dyn cm intervals but between 170 dyn cm and 190 dyn cm intervals are refined to 5 dyn cm. Bold black contours indicate coastline and the 1900 m isobath. Right: Maps of annual mean of satellite altimetric height using the merged Aviso MADT product with a Gaussian filter of 2° longitude and 1° latitude applied. Colour contours set accordingly to the dynamic height maps (generally 10 cm intervals but between 170 cm and 190 cm intervals are refined to 5 cm).

than in the upper layer, as is characteristic for subtropical gyres (Roemmich et al., 2007). The centre extends from east of the coast of South Africa to 70°E across the SWIR. Additionally the connection to the subtropical gyre of the South Pacific becomes apparent, indicated by the 60 dyn cm isoline (Ridgway and Dunn, 2007; Roemmich, 2007). The near-surface portion of the so-called supergyre controls a significant amount of the planetary heat balance. For ocean surface waters, the westward limb of the South Pacific gyre bifurcates at the coast of Australia, where part of the current turns northward across the Equator and feeds the Indonesian Throughflow. The connection south of Tasmania constitutes a second pathway for Pacific waters to reach the Indian Ocean.The large transport of warm water into the Indian Ocean, balanced by much colder eastward flow south of Australia, represents an immense heat exchange from the

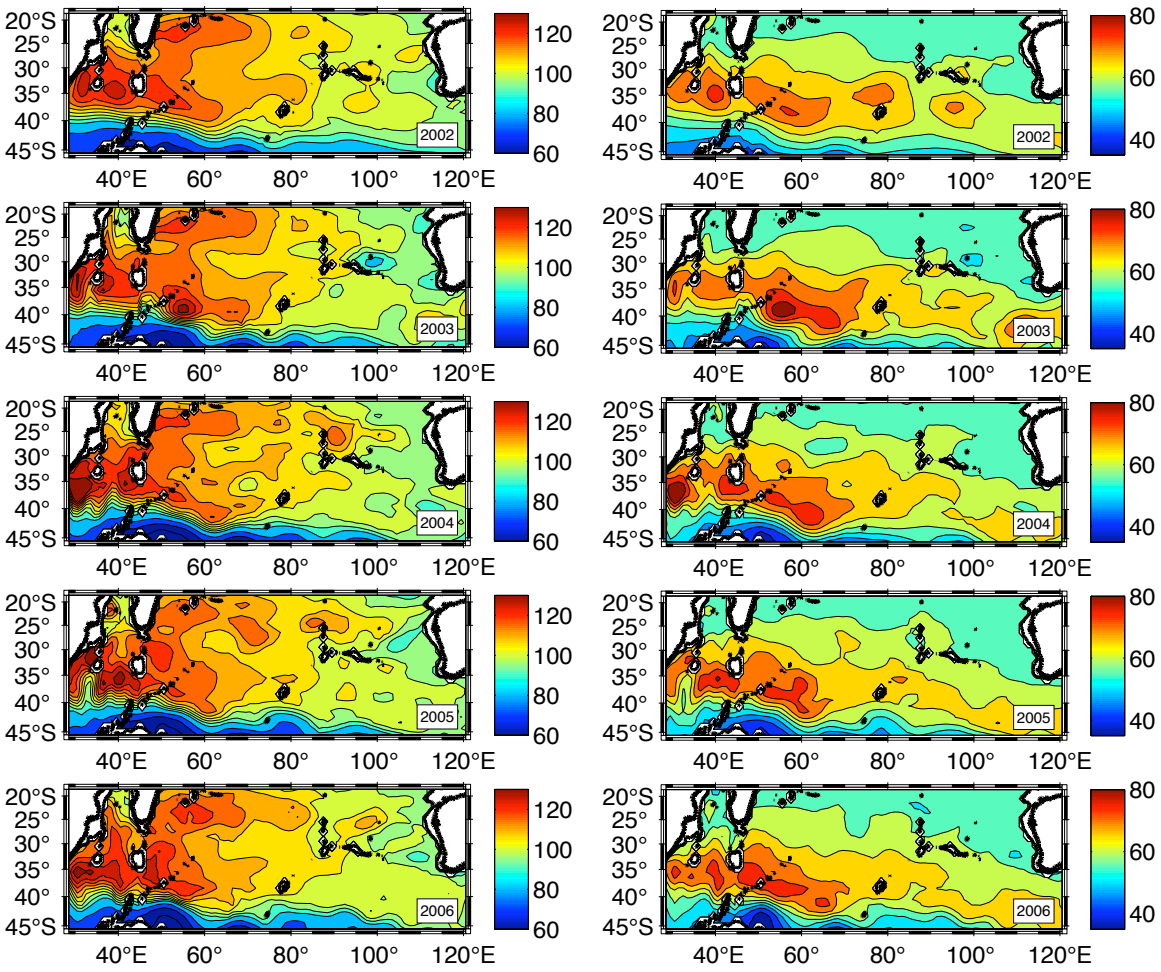

Figure 4.25: Maps of dynamic height [dyn cm] computed from the annual float realisations (left: dynh200/1000; right: dynh1000/1900). Colour contours generally indicate 10 dyn cm intervals but between 170 dyn cm and 190 dyn cm intervals are refined to 5 dyn cm. Bold black contours indicate coastline and the 1900 m isobath.

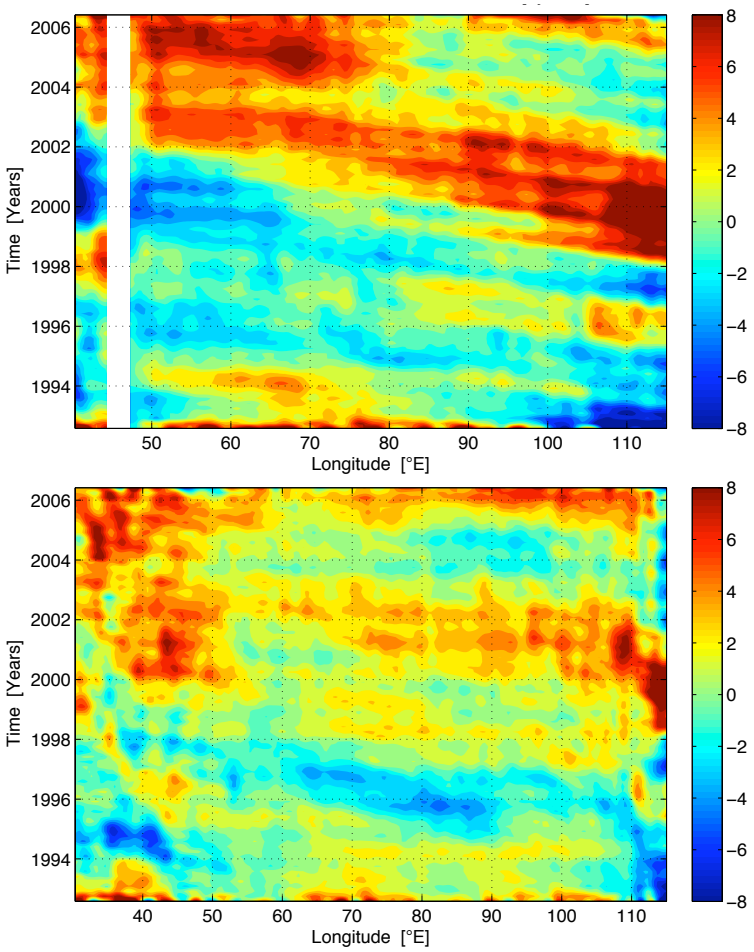

FIGURE 4.26: Longitude time plots of sea level anomaly derived from the merged Ssalto/Duacs MSLA product filtered with a 3 months and a 5° longitude moving average at 20°S (top) and 32°S (bottom).

Pacific (ROEMMICH, 2007). As shown by RIDGWAY AND DUNN (2007) it is possible to detect the supergyre using Argo float data by tracing the salinity minimum along its path, associated with the AAIW, in combination with the acceleration potential field.

Sea level anomalies show for both latitudes a positive signal propagating from the eastern boundary starting in 1998 (Fig. 4.26). At 20°S the signal has a maximum of more than 8 cm in SLA at 110°E and in late 2002 at 45°E it still shows anomalies of 5 cm. While at the southern section at 32°E the signal is much weaker and in the west it is superimposed by a anomaly appearing at 45°E between 2000 and 2002 with more than 5 cm. Additionally, it seems that the signal seen at 20°S needs about 2 to 3 years to reach MAD, while at 32°S the signal reaches the western part at 45°E within 1 year. That difference in the transit time could be explained by the fact, that at midlatitudes where the transient time is long, the wind-forced sea surface height signals tend to dissipate due to eddy mixing as they propagate westward (QIU AND CHEN,

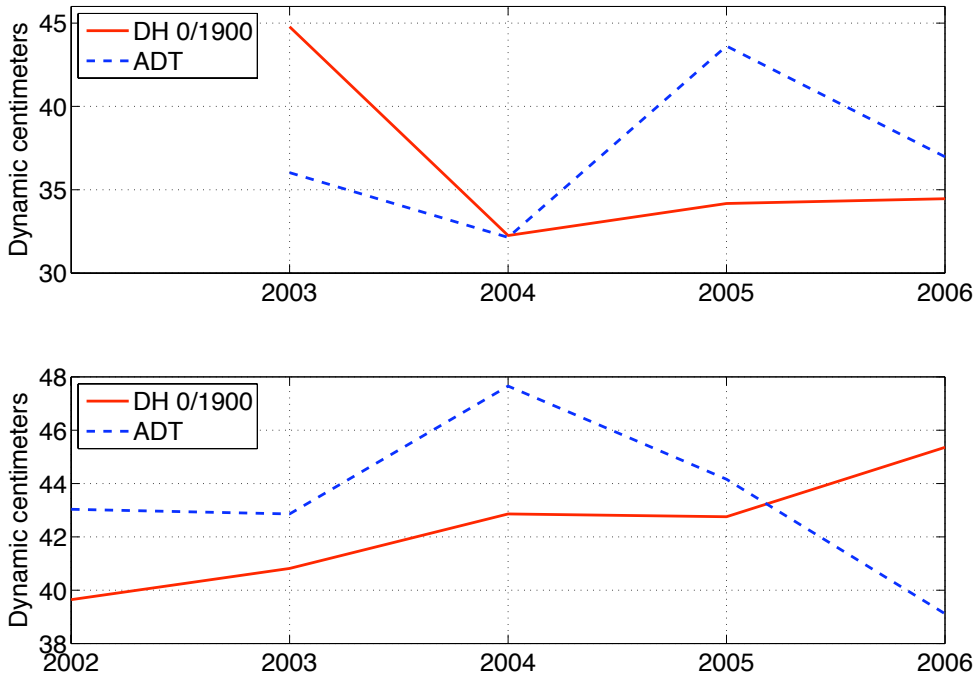

FIGURE 4.27: Annual estimates of differences in linearly regressed ADT or DH (0/1900 dbar) differences between 55°E and 110°E at 20°S (top) and between 45°E and 110°E at 32°S (bottom), at both latitudes averaged over a two degree latitudinal range. DH is calculated from annual float realisations.

2006). Additionally, it was shown that a possible connection exists between interannual changes in the EMC and ENSO/IOD-cycles. PALASTANGA ET AL. (2006) suggested that a positive ENSO/IOD event causes an intensification of the gyre. Additionally, sea surface temperature anomalies are positive off western Australia and associated with positive SLA. In the longitude time plots of SLA (Fig. 4.26) large anomalies are found in the east in 2000 at 32°S and 20°S, respectively. The signal is propagating westwards and reaches 55°E within one year at 32°S and within two years at 20°S.

ROEMMICH ET AL. (2007) found an excellent agreement between estimates of sea surface height from satellite altimeters and dynamic height calculated from the density field from Argo float data. For our comparison, we calculated annual differences of linearly regressed ADT and DH (0/1900 dbar) between 55°E and 110°E at 20°S, and between 45°E and 110°E at 32°S, at both latitudes averaged over a 2 degree latitudinal range (Fig. 4.27). The comparison does show an agreement between 2002 and 2005 between the different variables, while in 2006, differences in ADT show an ongoing decrease, especially at 32°S, whereas differences in DH (0/1900 dbar) show an increase. At 20°S, the gyre strength estimates is represented quite well from DH, while the ADT data show a large increase in the year 2005. At 20°S, the interannual variability, defined

as standard deviation of the annual estimates is 5.8 dyn cm in ADT and 4.5 dyn cm in DH. At 32°S, the differences in DH do not represent the change in the gyre strength estimated from geostrophic transports referenced to and above 1900 dbar. Here, a continuous increase is observed in DH differences, with no decrease in 2004 and 2005. The changes in the differences in ADT do not match with the changes in gyre strength either. At 32°S, the interannual variability, defined as standard deviation of the annual estimates is 3.1 dyn cm in ADT and 2.2 dyn cm in DH. A speculative explanation for the differences between changes in ADT and DH could be that signals of different time scales are included. Whereas it is not clear, why the differences exist in the results of interannual changes derived from DH and changes in the gyre strength estimates, using the *LinReg* method applied to geostrophic transports. Here, more work is needed on this to examine a possible reason for the differences.

4.5 Summary

In this chapter we analysed changes in the subtropical SIO gyre circulation using recent hydrographic cruise data from CD29 in 1987 and CD139 in 2002 along 32°S, from BEAGLE in 2003/2004 along 20°S and from Argo float profiles from the 5 year period 2002 to 2006, repsectively. The major focus was set to 32°S to investigate potential ongoing trends over the 5 year period 2002 to 2006 in changes of the gyre strength, based on reported changes for the 15 year period between 1987 and 2002 derived from two hydrographic cruise data (Palmer et al., 2004; McDonagh et al., 2005). Palmer et al. (2004) showed that most of the change happened between 1995 and 2002. Furthermore, they concluded that there has been a persistent change between the flow structure of the 1987 and 2002 sections, that can be seen by the westward shift of the maximum southward transport (in 1987 this maximum is located at 55°E, while in 1995 at 45°E and in 2002 at 40°E, respectively). Note, that the 1995 cruise data are not used in this study, due to the sparse coverage in the interior resulting from the different cruise tracks compared to 1987 and 2002. In the context of interannual changes in the gyre circulation, the seasonal variability was investigated too, to classify the reported decadel change between 1987 and 2002 in terms of possible seasonal bias of the results, because the CD29 cruise took place in October/November 1987 while the CD139 cruise took place in March/April 2002, namely the spring and autumn season, respectively.

We compared two methods ($MaxTrp_{WOA}$ and *LinReg*) to estimate the gyre strength at 32°S between 45°E and 110°E (at 20°S between 55°E and 110°E) derived from geostrophic velocity fields using a ZV level at 1900 dbar (at 20°S 1000 dbar is used).

At 32°S the ZV level was set as deep as the data coverage allowed to fulfil the need for a deep reference level, whereas at 20°S we followed the ZV assumption proposed by Warren (1981). The longitudinal band was selected to exclude major boundary currents but also because the varibility in the greater boundary current area in the west together with partly sparse coverage of profile data generates large errors in the final estimates. We found that using the *LinReg* method with the cumulated transport from WOA01 climatology at 110°E does change the gyre strength estimates by less than 3% compared to the gyre strength estimates based solely on cruise and float data, respectively. For the $MaxTrp_{WOA}$ method a change of up to 10% became apparent. While both methods showed broadly the same results in terms of interannual variability and the seasonal cycle, we prefer to use the *LinReg* method because it depends less on the choice of end points. Furthermore, the relatively early stage of the Argo project at the time of this study in the SIO indicates, that the *LinReg* method might be the appropriate method, being less sensitive to the profile distribution.

Gyre circulation at 32°S: We estimate a mean gyre strength of 44.4±1.2 Sv over the 5 year period 2002 to 2006. The interannual variability, defined as standard deviation, is 5.2 Sv with a maximum amplitude of interannual changes of 13 Sv between 2005 and 2006. We found no significant trend in the annual gyre strength between 2002 and 2006. The gyre strength estimate from the CD29 cruise section in 1987 is more than 10 Sv smaller than the mean gyre strength for the period 2002 to 2006, exceeding $2\,\sigma$ of the interannual variability estimated for the 5 year period. Whereas, the amplitude of the change in gyre strength between the 1987 and the 2002 estimate from cruise data is smaller than the maximum amplitude of the interannual changes (about 13 Sv between 2005 and 2006) derived from float realisations (Tab. 4.5). The estimate from CD139 cruise data in 2002 is in good agreement, within the given errors, with the 2002 annual estimate from float data.

The seasonal variability of the gyre strength is estimated to be 3.0 Sv with maxima in spring and autumn. This seasonal cycle exists only in the upper 1000 bar (Tab. 4.7). The gyre strength estimate from the CD29 cruise section in 1987 is more than 12 Sv smaller than the spring season estimate, exceeding the $3\,\sigma$ of the seasonal variability calculated for 2002 to 2006. Whereas the 2002 estimate from cruise data is in good agreement, within the given errors, with the autumn estimate.
The results obtained from section 4.1 show that the structure as well as the strength of the gyre circulation was significantly different to the mean state of the very early 21st century. But also they show that interannual changes can be larger than possible decadal changes. That might yield to problems estimating trends in the change of the gyre circulation when the temporal coverage is sparse.

Gyre circulation at 20°S: Depending on the method *MaxTrp or LinReg* we found differences in the estimated gyre strength and structure using either a ZV assumption at 1000 dbar (Warren, 1981) or at 1900 dbar. This difference is mainly caused by large northward velocities in the geostrophic velocity field between 70°E and 80°E. To avoid that problem we use the *LinReg* method with a proposed ZV level at 1000 dbar.

The estimated mean gyre strength at 20°S over the 4 year period 2003 to 2006 is 23.8±1.4 Sv. From the seasonal float realisations we get a semi-annual variation in the gyre strength with largest estimates in summer and autumn with 27.5±1.4 Sv and 25.0±1.5 Sv respectively, while the total variation is 4.2 Sv. Additionally, we found an important role attributed to the deep layer (1000 dbar to 1900 dbar) contributing to the seasonal changes in the gyre strength. The deep layer is acting as a buffer between summer and autumn and between winter and spring, respectively, compensating the deacrease/increase in gyre strength in the upper layer. Whereas between autumn and winter the deep layer indicates the largest changes of the two layers and between spring and summer the change takes place mainly in the upper layer. The interannual variations indicate a countermovement in the deep layer compared to the upper layer too, but less pronounced. The gyre strength estimated from BEAGLE cruise data is in good agreement with the annual and seasonal estimates, repsectively.

Comparison to Sverdrup transport: The comparison of the gyre strength estimates at 32°S with Sverdrup transports derived from National Centers for Environmental Prediction (NCEP) wind-stress data reveal a high correlation in the time series with lags between 1 year and 2 years. Changes in the wind-stress curl and therefore in the resulting geostrophic Sverdrup transport that take place within 10° longitude could be responsible for significant parts of the interannual changes in the gyre strength. The good correlation at 32°S for a time lag of 1 to 2 years, between Sverdrup transport time series and that from float realisations, does not agree with the typical assumption of perturbations being initiated in the east of the basin and travelling over the whole basin to affect the west. The adjustment time for such phenomena is longer than 1 to 2 years. If perturbations are forced near the western boundary, the adjustment time would reduce and a time lag of 1 or 2 years could be possible. Additionally, Matano et al. (1998) showed that the MADR has a significant effect on westward propagating perturbations at 40°S probably leading to large baroclinic wave energy arising from the interaction of barotropic waves from the interior of the Indian Ocean and the ridge. At 20°S the Sverdrup transport and its variability is generally smaller because that latitude is further away from the centre of the subtropical gyre and the maximum of wind-stress curl. In the context of changes in the gyre strength, at 32°S it is to note, that the time series from geostrophic Sverdrup transport indicates a robust positive

trend (3.6 Sv/decade; with a statistical significance of more than 85%) for the period 1987 to 2002. Testing the trend's dependency on the selected period, with period length changed by up to 4 years, gives still robust positive trends with a confidence level of more than 85%, but with a smaller slope. It is interesting, that at 32°S, the minimum in gyre strength derived from Sverdrup transport, as well as the increase afterwards to larger values, occurs in the beginning of the period of reported increase in global mean surface temperatures (IPCC, 2007). Whereas, at 20°S, no such connection is apparent nor are any regimes with significant trends detectable.

Comparison to satellite altimetric height: Time series of SLA indicate for both latitudes large positive anomalies in the east in early 2000 which seem to propagate westward. While the magnitude of the anomaly is $\geq$8 cm at 20°S between 105° and 115°E for about 2 years, it is much more confined at 32°S to 115°E. Additionally to the spatial differences, temporal differences exist in propagation times. At 32°S the anomaly seems to cross the basin interior within 1 year, while at 20°S it takes more than 2 years to reach MAD. This defies linear Rossby wave theory, where the transit time is shorter at lower latitudes. An explanation is that the MADR has an significant effect on westward propagating signals, leading to large baroclinic wave energy from the interaction of barotropic waves from the interior and the ridge.

Generally, the large scale structure of DH0/1900 calculated over the full profile depth agrees well with ADT data, with both showing local minima at the southern tip of west Australia extending into the PB indicating eddy activity in the LCS. But no significant change in the structure or position of the gyre can be detected, as seen on decadel time scales in the South Pacific Ocean (Roemmich et al., 2007). The different layers of DH show clearly different circulation patterns. The upper layer DH200/1000 maps show the two centres of the subtropical gyre divided at the southern tip of MAD by eddy activity and the north eastward orientated SICC dominating the upper 500 bar. The deeper layer DH1000/1900 maps indicate the recently described connection to the subtropical South Pacific Ocean as part of the supergyre of the Southern Ocean (Ridgway and Dunn, 2007; Roemmich, 2007) and reveal that this is a strong permanent circulation feature on annual and seasonal time scales.

Chapter 5

Subsurface reference velocities from float trajectories

As well as information about the density structure the floats provide further useful information, namely a mean subsurface drift velocity. In section 3.3 a simple method is described to derive subsurface velocities from each float's drift at parking level. At this stage the method includes errors from the drift during ascent and descent, from the drift at the surface before the float's position is recorded by a satellite, and from the uncertainties in positioning. A difficulty in interpreting the data is the relatively sparse temporal and spatial coverage of data, at least in the SIO up to 2006. There is the potential for single profiles to bias velocity estimates in the mapping procedure. The overall errors might be too large to use the float's subsurface velocities as reference velocities for geostrophic calculations (at least at this stage of the project). Nevertheless, useful information is provided about temporal and spatial scales of deep velocity features in the interior of the ocean.

First, meridional reference velocities along the CD139 cruise track are compared with reference velocities derived from an inverse calculation (McDonagh et al., 2008). Then seasonal and annual estimates of meridional reference velocities at different levels are presented for the 32°S and 20°S section, respectively. Finally, subsurface velocity maps for the SIO are shown to examine possible permanent circulation features at depth.

5.1 Comparison of reference velocities across CD139 cruise track: Float estimates vs. inverse calculation

McDonagh et al. (2008) used the geostrophic shear derived from the density field from the CD139 cruise and initialised their inverse method with reference velocities from the ADCP[1] data with an additional Ekman velocity imposed on the top 60 m of the section using the Hellerman and Rosenstein (1983) wind climatology. Furthermore, 11 constraints of volume and silicate flux of the major currents and basins are used to solve the system for reference velocities (for a detailed description of the inverse method see McDonagh et al. (2008)). Here we compare reference velocities from the inverse calculation (INV, OI_INV) with velocity estimates from float trajectories (OI±2mon, OI2002). The appropriate float realisations are estimated by applying the OI to the dataset of deep reference velocities (1900 dbar) derived from the floats subsurface drift (Tab. 3.5). Different temporal coverage is used, first extending the cruise period by ±2 months (OI±2mon) and second using the 2002 annual mean (OI2002). Additionally a smoothed inverse solution reference velocity field is used (OI_INV). This is generated by applying the OI to the reference velocities from the inverse calculation.

Beginning in the far west of the CD139 section west of MOZP at 35°E, we find large gradients in the reference velocities (Fig. 5.1). This is probably due to the sparse data coverage in that region. The inverse solution shows large northward velocities indicating the Agulhas Undercurrent. In the MOZB between 35°E and 45°E the velocities compare

[1] Acoustic Doppler Current Profiler

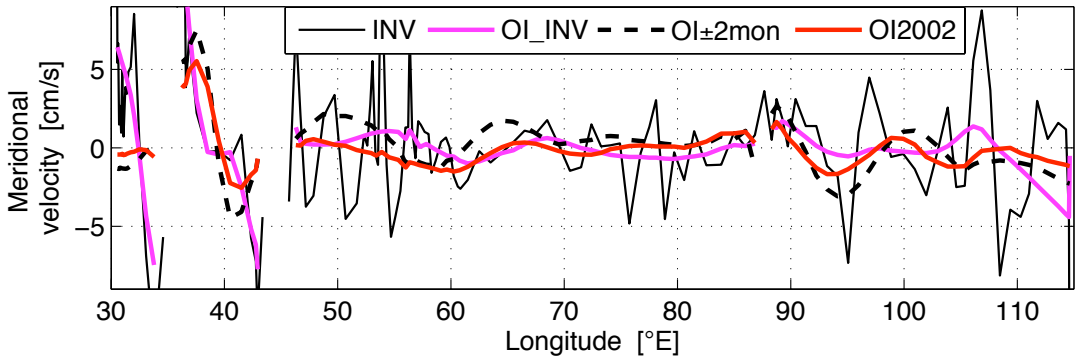

Figure 5.1: Meridional reference velocity section at 1900 dbar across CD139 cruise track. Shown are the velocities taken from the inverse calculation from McDonagh et al. (2008) with the ADCP solution (thin black), the filtered velocities after applying the Optimal Interpolation algorithm on the inverse solution (magenta), the velocities from the OI±2mon (thick dashed black) and OI_2002 (thick red) realisation using the Optimal Interpolation algorithm.

rather well, reproducing the deep front there. At 50°E the 4 month mean (OI±2mon) shows a deep northward current with velocities up to 2 cm s^{-1} but with even large errors. Between 60°E and 85°E the annual estimate (OI2002) agrees relatively well with the smoothed velocities from the inverse solution, here the associated errors are smallest with less than 0.7 cm s^{-1}. Especially the transition from southward velocities of -2 cm s^{-1} at about 60° to zero or northward velocities at 65°E is well represented in the inverse solution (unfiltered and filtered) and the annual float estimates. At 87°E where the topography is shallower than 1900 m no estimate exists from the float data. East of BP up to 95°E the tendency of decreasing velocities agrees well between the smoothed inverse solution (OI_INV) and the float realisations (OI±2mon, OI2002). Further east, especially near 105°E the velocities indicate opposite directions, although the unfiltered inverse solution shows negative velocities there as well. The comparison showed a good agreement in some parts of the section between the inverse solution velocities, especially the unfiltered ones, and the annual float realisations. From the permanent deep circulation feature suggested by McDonagh et al. (2008) the float data do confirm the southward velocities east of BP at 95°E as well as the southward velocities in the Crozet Basin (CB) at 60°E.

The zonally averaged (between 45°E and 110°E) meridional velocities for the different float realisations (OI±2mon and OI2002) give an indicator of the accurracy of the ZV assumption, which was applied when the gyre strength was estimated (Tab. 5.1). The averaged velocities are relatively small, while the associated errors given by the OI method are much larger. Assuming these mean velocities are uniformly applied over the water column down to 1900 dbar (only around BP this assumption is infringed) as well

Table 5.1: Zonally averaged (between 45°E and 110°E) meridional reference velocities at 1900 dbar across CD139 cruise track. Given are the velocities taken from the inverse calculation from McDonagh et al. (2008) with the ADCP solution (INV), the filtered velocities after applying the Optimal Interpolation algorithm on the inverse solution (OI_INV), the velocities from the OI±2mon and OI2002 realisation using the Optimal Interpolation algorithm. The second column gives the associated average errors (from OI), while the third column gives the standard deviation of the meridional velocities. The last column gives a crude estimate of the associated transport induced solely by these mean velocities applied uniformly over the water column down to 1900 dbar between 45°E and 110°.

	mean velocity	mean error (from OI)	standard deviation	approx. transport
INV	0.21 cm s^{-1}	-	±3.2 cm s^{-1}	30 Sv
OI_INV	0.14 cm s^{-1}	1.0 cm s^{-1}	±0.7 cm s^{-1}	20 Sv
OI ± 2mon	0.22 cm s^{-1}	0.8 cm s^{-1}	±1.3 cm s^{-1}	31 Sv
OI2002	-0.25 cm s^{-1}	0.7 cm s^{-1}	±0.7 cm s^{-1}	-36 Sv

as for the longitudinal range from 45°E to 110°E, large transports can result. These, together with the possible errors included (here the errors to estimate the subsurface drift velocities directly from the float profiles is not taken into account) highlight two things. Firstly, it is shown that very accurate measurements/methods are needed to derive subsurface reference velocities since even small velocities can produce large transport estimates (Tab. 5.1). If we assume for a moment, that the velocities are accurate enough, this method would show that the ZV assumption is not fulfilled in 2002 along the CD139 cruise track. Secondly, the missing background reference field during the OI algorithm is partly responsible for the large error contributions. The standard deviation is much larger than the mean value highlighting the large variability along the section.

5.2 Meridional reference velocities along 32°S

At 32°S the majority of floats are adjusted to drift on a deep parking level at either 1900 dbar or 2000 dbar, which is assumed to be a good choice of a ZV level(Toole and Warren, 1993; Palmer et al., 2004). McDonagh et al. (2008) showed that the 2000 dbar level is in the horizon where the northward flowing Circumpolar deep water and the southward flowing Indian deep water are separated, thus absolute velocities in that level should be small allowing a reasonable good ZV assumption.

Seasonal estimates of reference velocities at 32°S: The seasonal float realisations show a relatively good coverage for all seasons with zonally coherent error estimates between 75°E and 110°E (Fig. 5.2). The reference velocities highlight a deep current west of BP at 85°E with relatively large northward velocities in winter and spring of up to 2 cm s^{-1} and 3 cm s^{-1} respectively, while in autumn and summer the current is weaker or changes direction with small southward velocities of -1 cm s^{-1}. The errors in that region are smaller than 1 cm s^{-1} for all seasons. A detailed control of the contributing float data reveals that no bias to a specific year causes this seasonal variation.

In the east at 104°E a strong southward current is found during the summer period with velocities of -2 cm s^{-1}, whereas the other seasons do not show this deep southward current. The errors are smaller than 1 cm s^{-1} but the distribution of the data points does give reason to believe that the summer estimate is biased or erroneous in that region because the large southward velocities come from 3 data points collected close to the grid point from one float within 1 month.

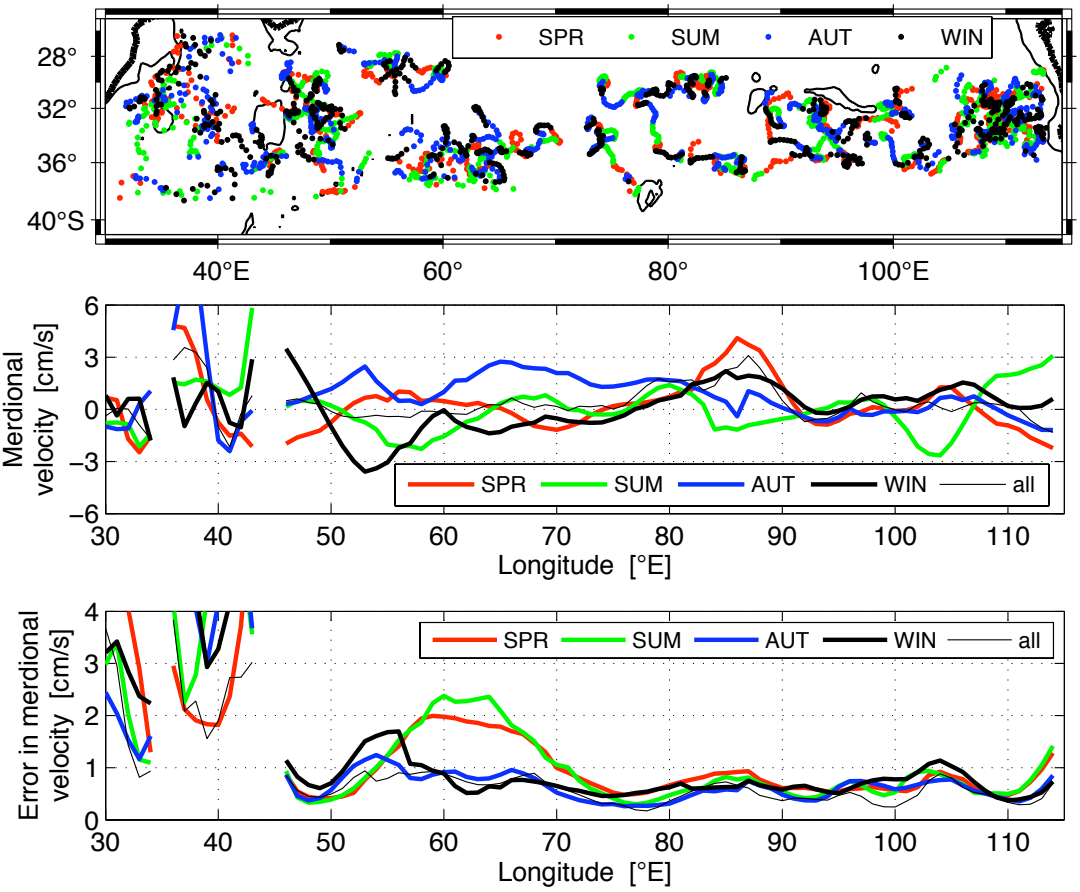

FIGURE 5.2: Top: Position of data points used for the seasonal realisations of subsurface velocities during the Optimal Interpolation algorithm to produce gridded velocities along 32°S. Bold black contours indicate coastline and the 1900 m bathymetry. Middle: Final seasonal estimates of meridional velocities [cm s^{-1}] across 32°S. Bottom: Associated errors of seasonal meridional velocities solely taken from Optimal Interpolation.

Between 60°E and 85°E the autumn estimate shows northward velocities of more than 1 cm s^{-1} with errors of the same order. Such a broad northward flow is not represented in the other seasons. In the east of the section at 113°E northward velocities exist of up to 3 cm s^{-1} in summer, while in spring and autumn the reference velocities are southward with -2 cm s^{-1} and -1 cm s^{-1} respectively. The winter estimate does not show any significant velocities there. The error estimate in that region increases slightly to about 1 cm s^{-1}. This area shows large eddy activity with different pathways of cyclonic and anticyclonic eddies (MORROW ET AL., 2004). It is thought that the general spreading of the eddies in specific directions could be responsible for the differences in the reference velocities. The seasonally varying LC shows largest mesoscale eddy production during it's maximum in winter (WAITE ET AL., 2007). Since the velocity estimates are for the 1900 dbar level it seems difficult to derive a general rule

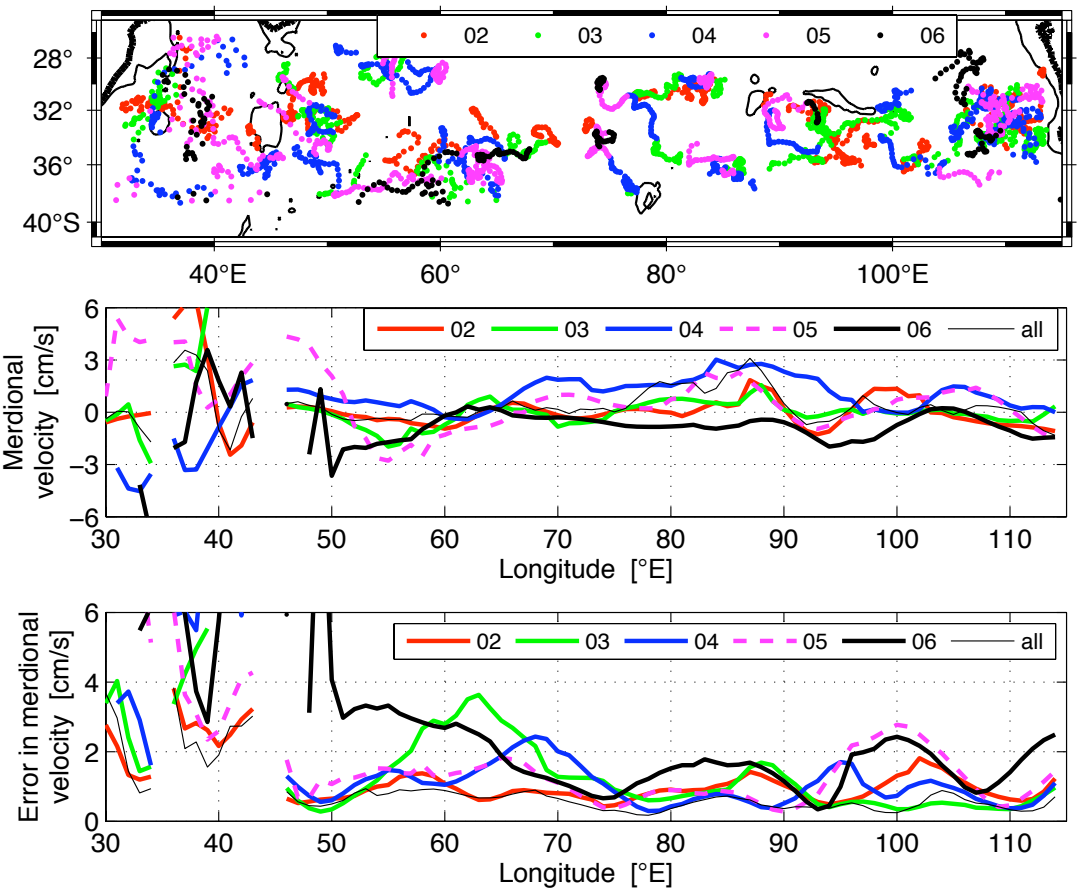

FIGURE 5.3: As figure 5.2 but for the annual realisations of meridional reference velocities across 32°S, showing the position of the data points (top), the estimated velocities (middle) and the associated error estimates given by the Optimal Interpolation algorithm (bottom).

for which eddies are generated during which season. Here, the velocity estimate for the 1000 dbar level would be helpful, because the majority of the eddies does not penetrate to 1900 dbar. Although generally the LC/LUC interactions result in the generation of eddy pairs where cyclonic eddies form in the LUC and anticyclonic eddies in the LC (RENNIE ET AL., 2007).

In the west of the section in the MOZB around 40°E, the velocities become larger due to deep reaching boundary currents or associated undercurrents. At the same time the error estimates increase, due to larger variability on shorter time scales than in the interior. Therefore, the reference velocities in the western boundary region are not discussed here. Although they clearly indicate that the ZV assumption comprises large uncertainties in that region.

Annual estimates of reference velocities at 32°S: The annual velocity estimates give less reliable information about deep currents across 32°S due to large errors of the order of the velocity estimates themselves, and due to an inferior data coverage especially in 2005 and 2006 (Fig. 5.3). Although the total number of profiles and floats stayed more or less the same along 32°S over the 5 year period (Chapter 3.1.1), the sparse coverage for the velocity estimates is due to the spreading of floats using a deep parking level away from the 32°S section while more and more floats adjusted to a shallower parking level enter that region in the last two years of the 5 year period.

At first glance, the summary of the zonally averaged meridional velocities suggest that for the winter and the 2002 realisation a ZV assumption would be acceptable. But, taking the standard deviation of the averaged velocities into account, it becomes clear that, even though the zonally averaged meridional velocity is small, large variations exist over the section that could affect the transport estimate dramatically (Tab. 5.2). Additionally, the zonally averaged errors, given by the OI algorithm, suggest a relatively equally distribution of the seasonal data, while for the different years the errors change largely.

TABLE 5.2: Zonally averaged (between 45°E and 110°E) meridional reference velocities at 1900 dbar across 32°S for the different seasonal and annual float realisations using the Optimal Interpolation algorithm. The second column gives the associated average errors (from OI), while the third column gives the standard deviation of the meridional velocities. The last column gives a crude estimate of the associated transport induced solely by these mean velocities applied uniformly over the water column down to 1900 dbar between 45°E and 110°.

	mean velocity	mean error (from OI)	standard deviation	approx. transport
SPR	0.32 $cm\,s^{-1}$	0.9 $cm\,s^{-1}$	$\pm$1.2 $cm\,s^{-1}$	46 Sv
SUM	-0.27 $cm\,s^{-1}$	0.9 $cm\,s^{-1}$	$\pm$1.1 $cm\,s^{-1}$	-38 Sv
AUT	0.92 $cm\,s^{-1}$	0.6 $cm\,s^{-1}$	$\pm$0.9 $cm\,s^{-1}$	131 Sv
WIN	0.03 $cm\,s^{-1}$	0.8 $cm\,s^{-1}$	$\pm$1.4 $cm\,s^{-1}$	4 Sv
2002	0.02 $cm\,s^{-1}$	0.9 $cm\,s^{-1}$	$\pm$0.7 $cm\,s^{-1}$	3 Sv
2003	-0.06 $cm\,s^{-1}$	1.2 $cm\,s^{-1}$	$\pm$0.7 $cm\,s^{-1}$	-9 Sv
2004	1.14 $cm\,s^{-1}$	1.1 $cm\,s^{-1}$	$\pm$0.9 $cm\,s^{-1}$	162 Sv
2005	0.40 $cm\,s^{-1}$	1.2 $cm\,s^{-1}$	$\pm$1.5 $cm\,s^{-1}$	57 Sv
2006	-0.78 $cm\,s^{-1}$	2.0 $cm\,s^{-1}$	$\pm$0.8 $cm\,s^{-1}$	-111 Sv

5.3 Meridional reference velocities along 20°S

At 20°S a large number of floats are adjusted to drift at 1000 dbar taking periodically deep profiles from 2000 dbar to the surface every 3rd cycle or less. Between 55°E and

85°E no data are available from floats adjusted to a deep parking level (≥1900 dbar), therefore it does not seem useful to examine and discuss estimates of subsurface velocities at a depth of 1900 dbar or 2000 dbar along the whole 20°S transect. Whereas it is possible to use data from floats adjusted to drift at 1000 dbar to estimate velocities across the 20°S section.

Annual estimates of reference velocities at 20°S: The reference velocity data points show a good coverage from 2004 to 2006, especially in the interior between 50°E and 85°E (Fig. 5.4). It was already noted (Chapter 4.2) that especially in 2002 only sparse data coverage exist. Although 13 floats have been deployed during the BEAGLE cruise along 20°S in 2003/2004, the annual coverage in 2003 is still insufficient, since the first float deployment on that cruise was on the 26th of December 2003 at 55°E. In the remaining annual estimates (2004, 2005 and 2006) the zonally focused band of data points between 23°S and 18°S in the interior between 55°E and 85°E is remarkable, possibly indicating the southern border of the SEC and the associated zonally orientated velocity field north of 18°S (Stramma and Lutjeharms, 1997).

A possible signal exists at 100°E in 2006 showing a northward velocity of 9 cm s^{-1}. Few data points are within 200 km distance and the associated error is 2 cm s^{-1} which is about average compared to the other years at this location. Further investigation showed that this signal results from one nearby profile from float 5900259 at the end of year 2006, therefore a similar signal can be found in the summer realisation discussed later. The float generally shows large velocities in the meridional and zonal direction mainly of the order of O(10 cm s^{-1}) while travelling north north-east for the whole year 2006. The direction of travel indicates strong eddy activity seen by the float at 1000 dbar.

At 65°E annual variations exist with northward velocities up to 2 cm s^{-1} in 2004 and southward velocities up to -2 cm s^{-1} in 2005 and 2006, while in 2003 no significant velocities exist also due to the large error estimates and insufficient coverage in that year. The errors for 2004 and 2006 are small in that region with less than 1 cm s^{-1} while in 2005 errors are slightly larger with 1.5 cm s^{-1}. For the rest of the section east of 45°E the estimated velocities at 1000 dbar are very small and do not show significant meridional flows within the error estimates (Fig. 5.4).

Seasonal estimates of reference velocities at 20°S: The seasonal estimates of the subsurface reference velocities at 20°S indicate a reasonable coverage for all seasons, especially between 50°E and 100°E. Hence, only a small (2° x 2°) data free area exists near 100°E. The coverage is comparable to the annual data point distribution discussed

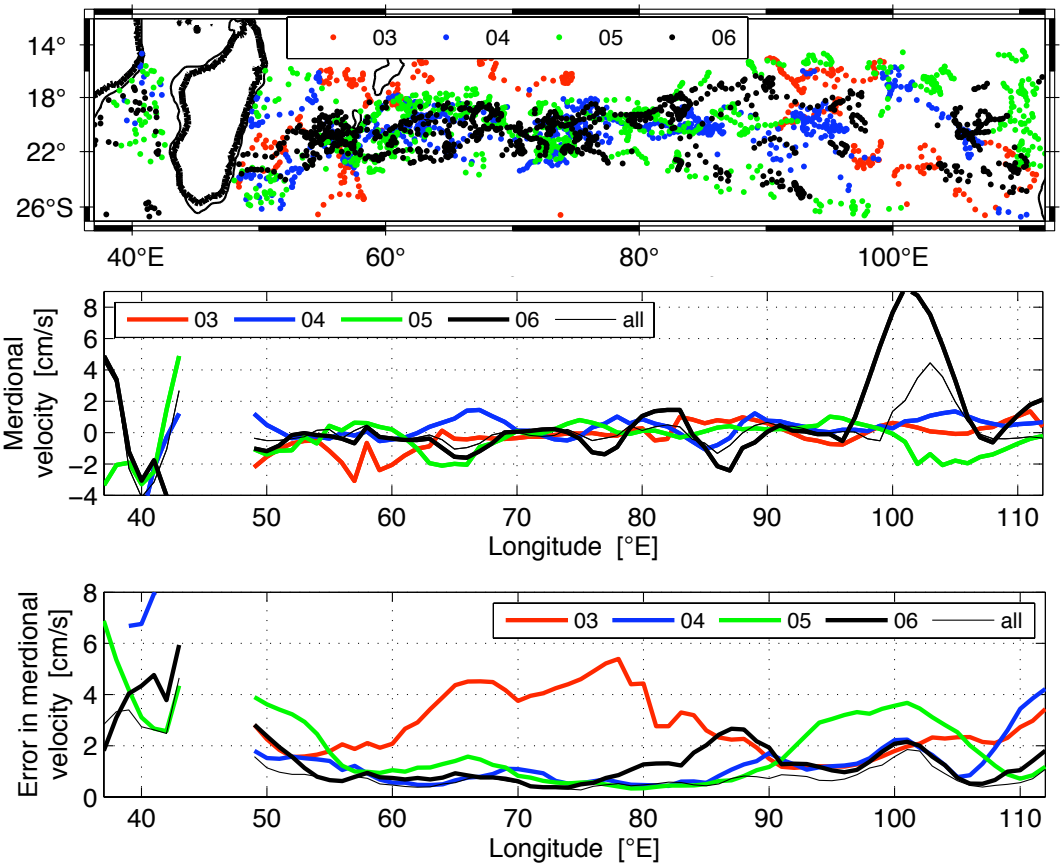

FIGURE 5.4: Top: Position of data points used for the annual realisations of subsurface velocities during the Optimal Interpolation to produce gridded velocities along 20°S. Bold black contours indicate coastline and the 1000 m bathymetry. Middle: Final annual estimates of meridional velocities [cm s^{-1}] across 20°S. Bottom: Associated errors of annual meridional velocities solely taken from OI.

previously including the zonally focused distribution in the interior between 55°E and 80°E (Fig. 5.5).

Here three features in the velocity section need to be mentioned. First, similar to the 2006 annual estimate a strong northward velocity signal at 100°E is found in summer time, with velocities up to 8 cm s^{-1}. Several data points are within 150 km distance and the associated error is 2 cm s^{-1}, that is on average compared to the other years. Nevertheless the closest profile comes again from float 5900259 from the end of December 2006. This bias of the mapping from one single profile indicates the care that needs to be taken concluding results from the analysis. This is because for the subsurface velocities no first guess background velocity field exist, unlike for the estimates of temperature and salinity (Sec. 3.1). That means the mapped velocities are completely controlled by the decorrelation length scales. It is known, that the results from the OI method depend ultimately on the decorrelation length scales

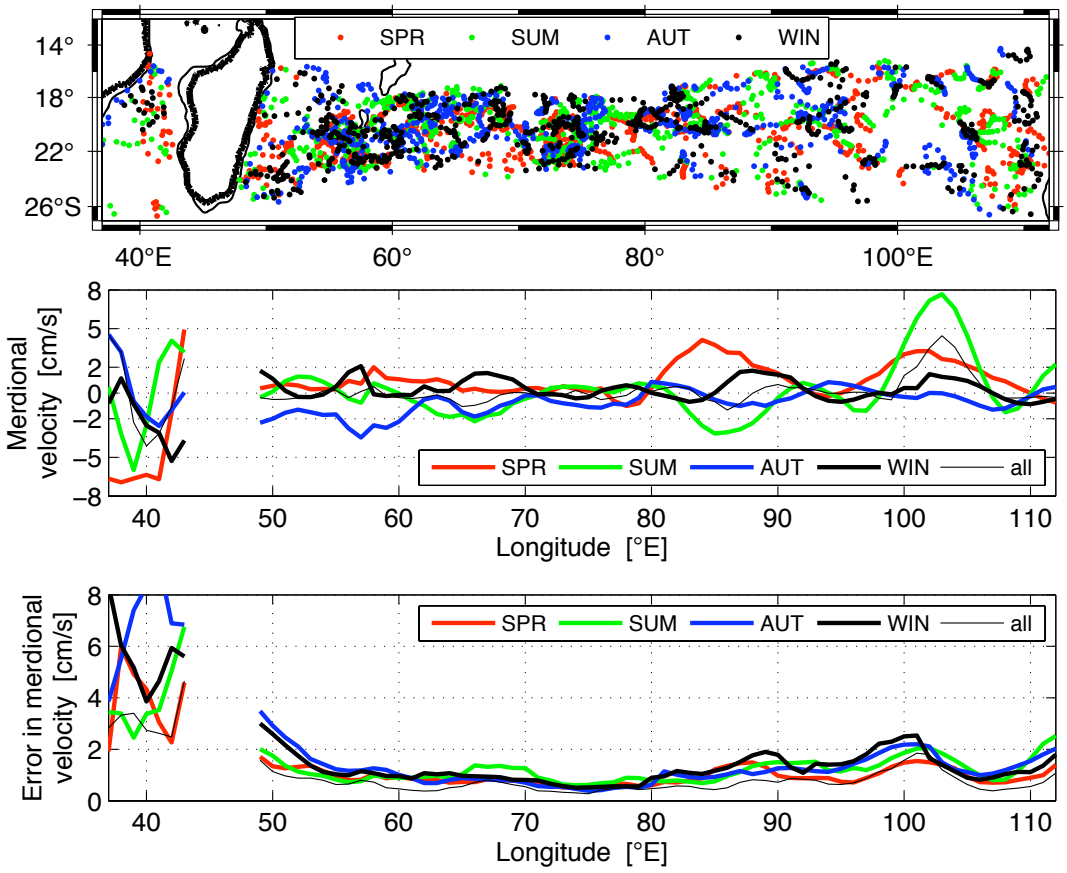

FIGURE 5.5: As figure 5.4 but for seasonal realisations of meridional reference velocities across 20°S.

(BÖHME AND SEND, 2005), especially where large gradient exist (HADFIELD ET AL., 2007). Additionally there exists a relatively broad area between 95°E and 110°E of northward velocities in spring but with smaller velocities, only up to 3 cm s^{-1} and a relatively large associated error of up to 2 cm s^{-1}.

The second feature in the seasonal estimates of reference velocities is at the western flank of the Ninetyeast Ridge (NER) at 85°E. A similar signal was found in the seasonal estimates of deep (at 1900 dbar) reference velocities at 32°S (Fig. 5.2). Northward velocities exist with a maximum of 3 cm s^{-1} in spring and southward velocities with a maximum of -3 cm s^{-1} in summer respectively. The data coverage is very good with several data points near by and the associated errors are smaller than 1 cm s^{-1}. A further investigation of contributing float data shows that no bias to a specific year exist. At 65°E seasonal variations exist comparable to the ones described for the annual velocity estimates. During winter time northward velocities exist up to 1.5 cm s^{-1}, and in summer and autumn southward velocities exist up to -1.5 cm s^{-1}, while in spring

no significant velocities are apparent. The errors for summer in that region is slightly larger than $1\,\mathrm{cm\,s^{-1}}$ while for the other seasons they are less than $1\,\mathrm{cm\,s^{-1}}$. A closer look at the floats involved shows that here no bias from single profiles seems possible, because the summer and autumn realisations show contributions from all years.

The zonally averaged (between 55°E and 110°E) meridional velocities are relative small and for the autumn season and the years 2003 and 2005 they are even negative (Tab. 5.3). This could have several reasons, first, the 1000 dbar level is not the appropriate ZV level. Secondly, as mentioned previously, the OI method uses no background velocity field, just the average of the subset of velocity measurements at each grid point, therefore the method heavily relies on the spatial decorrelation length scales as well as the data distribution. The impact of this can be found in the large averaged errors from the OI method and the standard deviation of the meridional velocities along the 20°S section.

TABLE 5.3: Zonally averaged (between 55°E and 110°E) meridional reference velocities at 1000 dbar across 20°S for the different seasonal and annual float realisations using the Optimal Interpolation algorithm. The second column gives the associated average errors (from OI), while the third column gives the standard deviation of the meridional velocities. The last column gives a crude estimate of the associated transport induced solely by these mean velocities applied uniformly over the water column down to 1000 dbar between 55°E and 110°.

	mean velocity	mean error (from OI)	standard deviation	approx. transport
SPR	1.2 $\mathrm{cm\,s^{-1}}$	0.9 $\mathrm{cm\,s^{-1}}$	±1.2 $\mathrm{cm\,s^{-1}}$	64 Sv
SUM	0.1 $\mathrm{cm\,s^{-1}}$	1.1 $\mathrm{cm\,s^{-1}}$	±2.4 $\mathrm{cm\,s^{-1}}$	7 Sv
AUT	-0.7 $\mathrm{cm\,s^{-1}}$	1.1 $\mathrm{cm\,s^{-1}}$	±0.9 $\mathrm{cm\,s^{-1}}$	-37 Sv
WIN	0.4 $\mathrm{cm\,s^{-1}}$	1.2 $\mathrm{cm\,s^{-1}}$	±0.8 $\mathrm{cm\,s^{-1}}$	20 Sv
2003	-0.2 $\mathrm{cm\,s^{-1}}$	2.8 $\mathrm{cm\,s^{-1}}$	±0.8 $\mathrm{cm\,s^{-1}}$	-11 Sv
2004	0.3 $\mathrm{cm\,s^{-1}}$	1.1 $\mathrm{cm\,s^{-1}}$	±0.6 $\mathrm{cm\,s^{-1}}$	17 Sv
2005	-0.3 $\mathrm{cm\,s^{-1}}$	1.5 $\mathrm{cm\,s^{-1}}$	±0.9 $\mathrm{cm\,s^{-1}}$	-17 Sv
2006	0.7 $\mathrm{cm\,s^{-1}}$	1.1 $\mathrm{cm\,s^{-1}}$	±2.6 $\mathrm{cm\,s^{-1}}$	39 Sv

5.4 Maps of subsurface velocities for the SIO

The estimated meridional and zonal velocity components are then used to generate maps of the SIO showing the estimated subsurface flow field at 1000 dbar and 1900 dbar (Fig. 5.6 and 5.7, respectively). The velocities in the boundary region are much larger than in the interior. Hence, velocities $\geq 5\,\mathrm{cm\,s^{-1}}$ ($\geq 10\,\mathrm{cm\,s^{-1}}$) are scaled

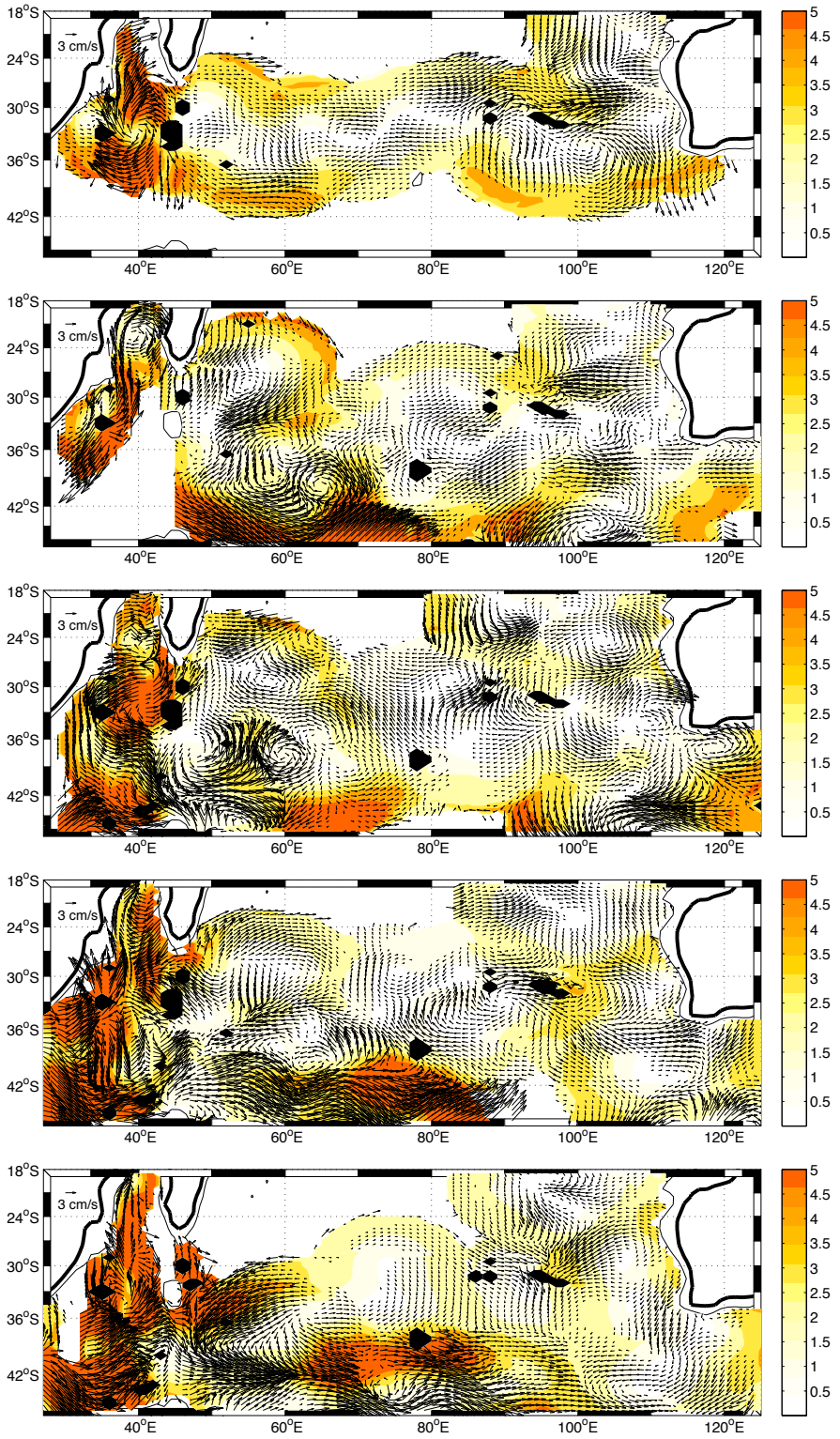

FIGURE 5.6: Annual vector fields of subsurface velocities at 1900 dbar from float trajectories from 2002 (top) to 2006 (bottom). Velocities smaller than 0.5 cm s^{-1} are not shown, additionally velocities larger 5 cm s^{-1} are scaled down to 5 cm s^{-1}. Coloured contours indicate error given by the Optimal Interpolation algorithm and black line contours indicate coast line (bold) and 1900 m bathymetry (thin).

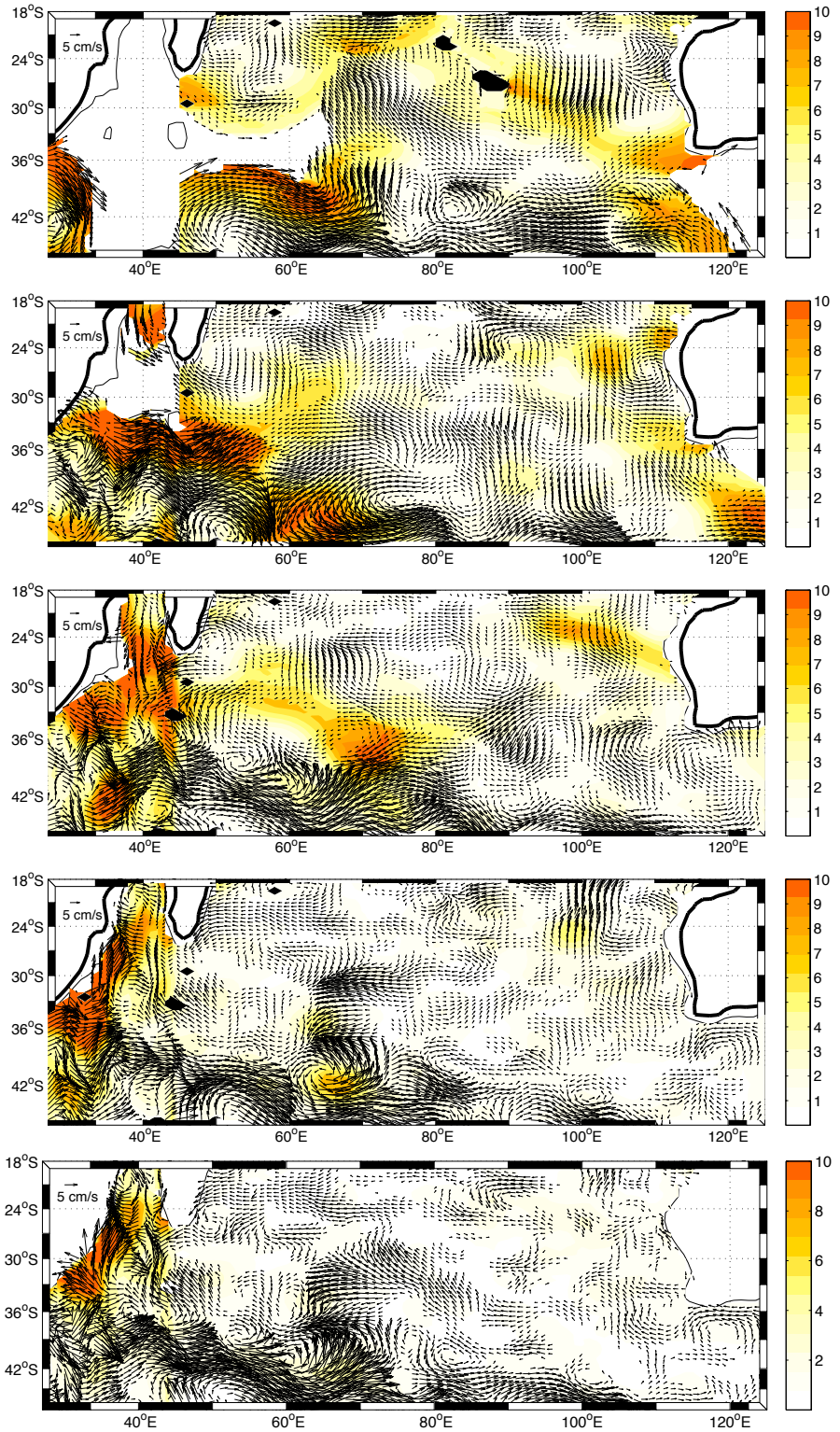

FIGURE 5.7: Annual vector fields of subsurface velocities at 1000 dbar from float trajectories from 2003 (1st panel) to 2006 (4th panel) as well as from the whole 5 year period (5th panel). Velocities smaller than 1 cm s^{-1} are not shown, additionally velocities larger 10 cm s^{-1} are scaled down to 10 cm s^{-1}. Coloured contours indicate error given by the Optimal Interpolation algorithm and black line contours indicate coast line (bold) and 1900 m bathymetry (thin).

down to 5 cm s^{-1} (10 cm s^{-1}) at the 1900 dbar (1000 dbar) level. Furthermore, velocities $\leq$0.5 cm s^{-1} ($\leq$1 cm s^{-1}) are not shown at the 1900 dbar (1000 dbar) level (Fig. 5.6 and 5.7).

The annual velocity estimates from float's subsurface drift at 1900 dbar show a cyclonic recirculation at the southern exit of the MOZC north of 25°S with different intensities (Fig. 5.6). The same circulation pattern is found in the seasonal estimates (Figure not shown). Further south at 32°S between 36°E and 45°E only in 2002 a strong cyclonic recirculation existed as suggested by McDonagh et al. (2008) while in 2004 an anticyclonic circulation of similar strength exists there (Fig. 5.6). The deep circulation features highlighted by McDonagh et al. (2008) as southward flow at 60°E and topography following eastward flow at 95°E are represented in the 2002 velocity estimates as well (Fig. 5.6). South of 40°S in the west both levels indicate strong eastward velocities, associated with the SIOC (Stramma and Lutjeharms, 1997) as a continuation of the Agulhas retroflection, in combination with the gyre return flow. While at 1000 dbar the flow in the south east is predominantly eastward (Fig. 5.7) a south-westward directed flow exists at 1900 dbar in that area south of *Australia* with different intensities (Fig. 5.6).

The mean velocity field for the 5 year period (Fig. 5.7 5th panel) shows only broadly agreement with results from Davis (2005), who derived the intermediate-depth circulation of the Indian and South Pacific Oceans at 900 m depth from autonomous floats. The SIOC is well represented in magnitude and location, with velocities of $5 - 10$ cm s^{-1} flowing eastward to south-west corner of the study area at 45°S, 110°E. The SEC is represented too, with westward velocities of $2 - 5$ cm s^{-1}, but it can not be traced over the whole basin. Additionally, the mainly north-westward return flow in the ocean interior is only partly given with velocities of $1 - 3$ cm s^{-1}, while Davis (2005) estimate slightly large velocities of about 3 cm s^{-1}. The maps show clearly the missing background reference velocity field. A compensation for this could be a two step mapping with large decorrelation length scales of the order of 1000 km or more in the first step and the now used scales in the second step. On the one hand this would possibly highlight more clearly the large scale circulation features, such as the SEC around 20°S, the SIOC around 42°S, the WAC in the east of the basin and the AC in the west. On the other hand, the errors would increase largely with such a second mapping step (Wong et al., 2001).

5.5 Summary

Mean reference velocities are estimated from the float's subsurface drift as described in section 3.3. With the appropriate modified OI annual and seasonal averages are derived for meridional velocities across 20°S and 32°S, respectively. The aim was to reveal robust circulation features in mid-depth at 1000 m and deeper at 1900 m.

The results of reference velocities from different float realisations along CD139 are compared with the solution from an inverse calculation performed along the CD139 cruise track (McDonagh et al., 2008). It is shown that some deep circulation features agree very well in both studies such as the southward flow around 60°E and at 95°E. Nevertheless, it was shown that the reference velocities derived from float's subsurface drift are not accurate enough to provide useful reference velocities for the geostrophic transport calculations, since the variability and the error from the method are much larger than the velocities. Additionally, it was shown, that the ZV assumption could lead to large errors of O(10 Sv) and even larger in the final transport estimate.

The relatively sparse data coverage showed that seasonal and annual estimates are easily biased by single data points from one single float. Nevertheless, the results revealed seasonally varying currents west of BP and NER at 85°E across 32°S at 1900 dbar and across 20°S at 1000 dbar. Additionally, from the 1900 dbar velocity maps a recirculation north of 27°S in the MOZC became apparent, with northward inflow in the west and southward outflow in the east, showing varying intensity over the 5 year period. The strong cyclonic recirculation between MOZP and MADR at 32°S (McDonagh et al., 2008) was confirmed in the 1900 dbar data but it was shown that this is not a permanent feature since in 2004 an anticyclonic circulation existed there of similar intensity.

In conclusion the number and distribution of observations available for the 5 year period 2002 to 2006 does not seem sufficient to provide robust estimates of annual or seasonal subsurface velocity fields for the SIO. This is concluded from the examples of biased velocity estimates as seen at 20°S and 103°E. Additionally, the sparse annual data coverage cannot mask out the eddy activity, at least with the confiuration of the analysis used in this study. The OI procedure does not use a reference background field (because no such field was available). Therefore, the large-scale circulation field is rather poorly represented, since the velocities themselves are mapped rather than the anomalies to the reference field. This could be compensated with a two step mapping procedure, with large decorrelation length scales of the order of 1000 km or more in the first step and the now used scales in the second step. Comparing the 5 year mean velocity field at 1000 dbar with results from Davis (2005) or Sallee et al. (2006)

shows that only some of the large-scale circulation features are fully represented in magnitude and location. For the deep level around 2000 dbar no such mean velocity fields have been estimated yet.

Chapter 6

Property changes in the subtropical South Indian Ocean between 2002 and 2006

Many authors have reported a warming trend over the past decade for both the world ocean (Levitus et al., 2000) and in individual basins at mid-depths associated with MW and IW (Parilla et al., 1994; Wong et al., 2001; Gille, 2002; Curry et al., 2003; Bryden et al., 2003b; McDonagh et al., 2005). In addition, coincident changes of increasing ocean salinity and its distribution are reported, for example in the deep waters of the Mediterranean (Roether et al., 1996), the IW in the Pacific (Wong et al., 1999) and in the SIO (Bryden et al., 2003b; McDonagh et al., 2005). The global importance of these changes and their broader implications are more and more taken into the focus of present studies on global climate change. Recent studies have highlighted the role of SAMW in the climate system via observed changes in temperature, salinity and CO_2 in MW properties (Sabine and Feely, 2001) or indirectly by the control on CO_2 fluxes (Caldera and Duffy, 2000; Sarmiento et al., 2004).

In chapter 4 changes in the gyre strength are analysed in the first 5 years of the Argo project in the SIO in the context of decadal changes reported by Palmer et al. (2004); McDonagh et al. (2005). Here, in this chapter, we investigate the link between changes in the gyre strength and changes in the water mass properties with a focus on the MW and IW because of the restriction in profile depth of the Argo floats to 2000 dbar. Again, the analysis is focused on 32°S. That latitude is close to the centre of the gyre and therefore may provide the clearest signal of possible property changes, compared to the section at 20°S.

6.1 Water mass property field at 32°S

This section gives a brief overview of the characteristic water mass properties at 32°S derived from the WOA01 climatology (Fig. 6.1). Although the WOA01 climatology does not necessarily represent the best dataset to identify water mass signals, it does show the typical water masses that can be found along 32°S. For a more detailed description of the water masses at this latitude, the reader is referred to Toole and Warren (1993).

At the surface, the subtropical SIO is characterised by Surface Water showing the highest salinity (S > 35.4 psu) and temperature (T > 14°C) along the section (Fig. 6.1 a, b). Additionally, it can be identified by minima in silicate, phosphate and nitrate concentrations (McDonagh et al., 2008). Generally this layer moves northward but at the western and astern boundaries the Agulhas and Leeuwin current move this layer south. The layer of Surface Water includes the Subtropical Mode Water (STMW), that can be found in the southwest Indian subgyre (Gordon et al., 1987; Stramma and Lutjeharms, 1997), although not identifiable in the WOA01 climatology. Indian Ocean STMW properties are 17 - 18°C and 35.6 psu. It was noted in the 1987 section along 32°S (Toole and Warren, 1993) and also in the 2002 section (McDonagh et al., 2005), but it was not observed in the 1995 section along 32°S (Donohue and Toole, 2003).

Below the Surface water, the SAMW exists, it can be identified by its minimum in large-scale PV ($PV = |f|/\rho \cdot d\rho/dz$, where f is the Coriolis parameter, ρ the density and z is the depth) as well as a maximum in oxygen (Fig. 6.1 c, d). The derived parameter PV plays an important role in large-scale oceanography, acting both passively as a tracer and dynamically to direct flow. Since the float data used in this study contain only temperature and salinity, PV is used to identify SAMW. The SAMW, a major contributor to the MW, is formed south of the subtropical gyre along the Subantarctic Front primarily as a result of air-sea interaction (Speer et al., 1995) and is advected equatorwards in each ocean basin of the Southern Hemisphere (McCartney, 1977, 1982). While it is difficult to directly measure changes in the air-sea fluxes generating the MW characteristics at the formation site, the northward spreading of this vertically and horizontally nearly homogeneous water mass enables direct measurements further north in the subtropical gyres. In the Indian Ocean, a special type of SAMW needs to be mentioned, the Southeast Indian Subantarctic Mode Water that is the densest subducting water formed in the southeastern Indian Ocean, south of Australia (S ≈ 34.55 psu and T ≈ 8°C; Hanawa and Talley (2001)). While generally moving north, at the western boundary, the SAMW layer moves southward.

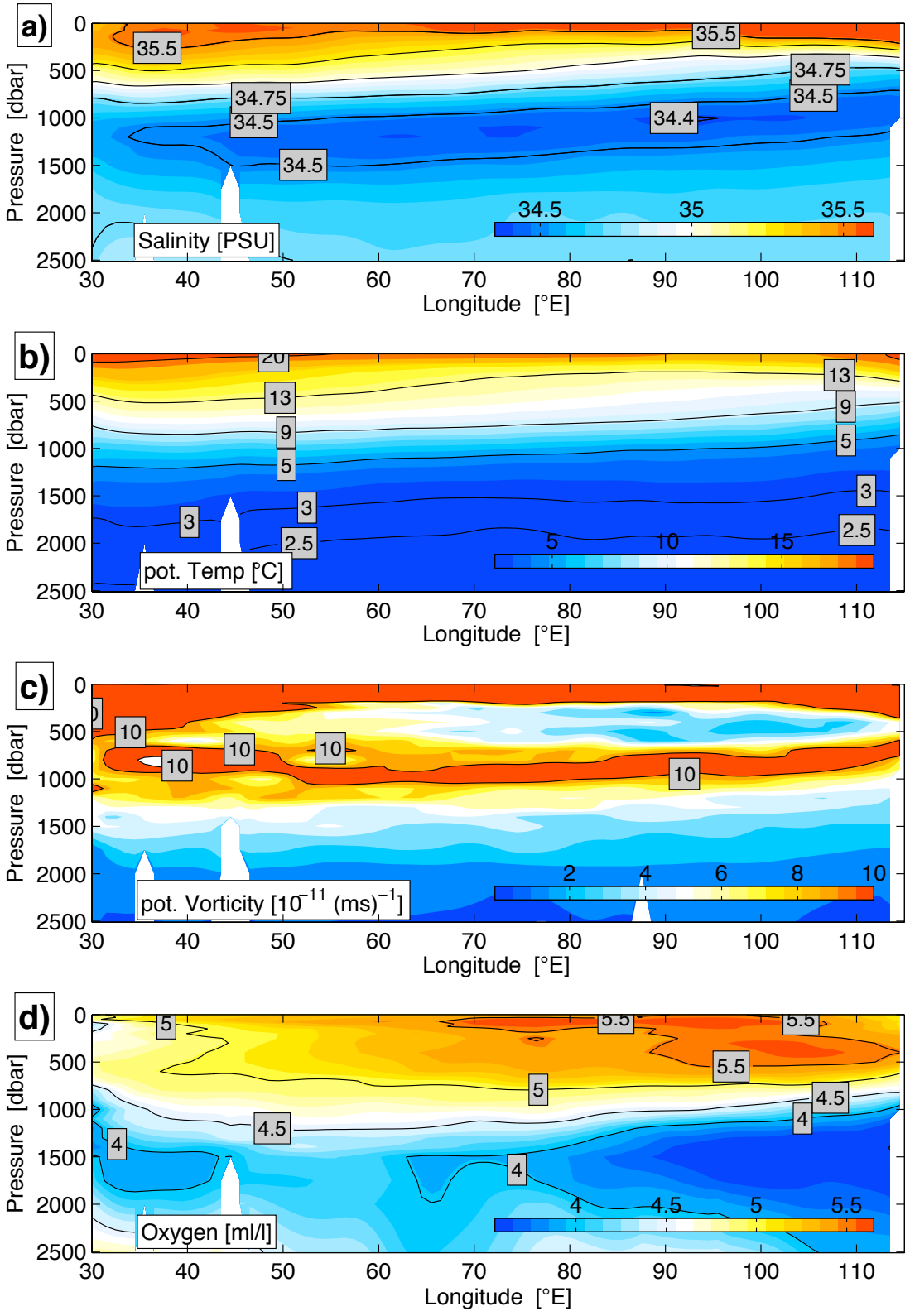

FIGURE 6.1: Property sections (from top to bottom: salinity [psu], potential temperature [°C], potential vorticity [10^{-11} ms^{-1}] and oxygen [ml/l]) along 32°S derived from WOA01 climatology.

Further below, the AAIW, a major contributor of IW, exists. AAIW is formed by a combination of deep winter mixing and circumpolar cross-frontal exchange of Antarctic Surface Water and SAMW (McCartney, 1977; Sloyan and Rintoul, 2001). The AAIW is distributed in each ocean basin and can be identified by it's minimum in salinity (Fig. 6.1 a; $S < 34.5$ psu). At 32°S, this low salinity layer is invaded at the western end of the section by southward flowing warm, high salinity Red Sea Water, that was formed in the evaporative regime at the surface of the Red Sea (Bower et al., 2000). In the WOA01 climatology this water mass is not well represented at 32°S, but it generally can be identified by a salinity maximum and oxygen minimum, compared to other South Indian Ocean intermediate water masses (Beal et al., 2000; Donohue and Toole, 2003). The AAIW generally moves north but with southward flow in the western boundary current.

The last water mass to mention for this study is the Upper Deep Water, identifiable by a minimum in oxygen concentration (Fig. 6.1 d) and relative high phosphate and nitrate concentrations (McDonagh et al., 2008). The Upper Deep Water flows south and is part of the upper limb of the deep overturning of the Indian Ocean.

6.2 Characteristics of thermocline water mass properties at 32°S

The subtropical SIO is characterised in the upper 2000 dbar by its MW and IW. Here, the annual float realisations (Tab. 3.2) along 32°S are used to compare characteristics of MW properties with the cruise data from CD139 in 2002 and CD29 in 1987. In the main thermocline PV is a good indicator for the location of the mode waters, here the SAMW, identifiable by it's minimum in potential vorticity.

The properties of the potential vorticity minimum of the annual float realisations along 32°S show very coherent structures for the different years. While McDonagh et al. (2005) reported a system of two modes between 40°E and 115°E with a transition in between, however here, three separate modes are identified (Fig. 6.2). These modes are identified most clearly in salinity but also in potential temperature from the annual float realisations and the cruise data, but only tentative in the WOA01 climatological data (Fig. 6.2). The reason for the poor representation of the thermocline properties in the climatology is given by the interpolation on pressure surfaces during generation (Stephens et al., 2002; Boyer et al., 2002), the relatively sparse data coverage in that region as well as the coarse vertical resolution. For comparison, the properties of the potential vorticity minimum are directly calculated from the Argo

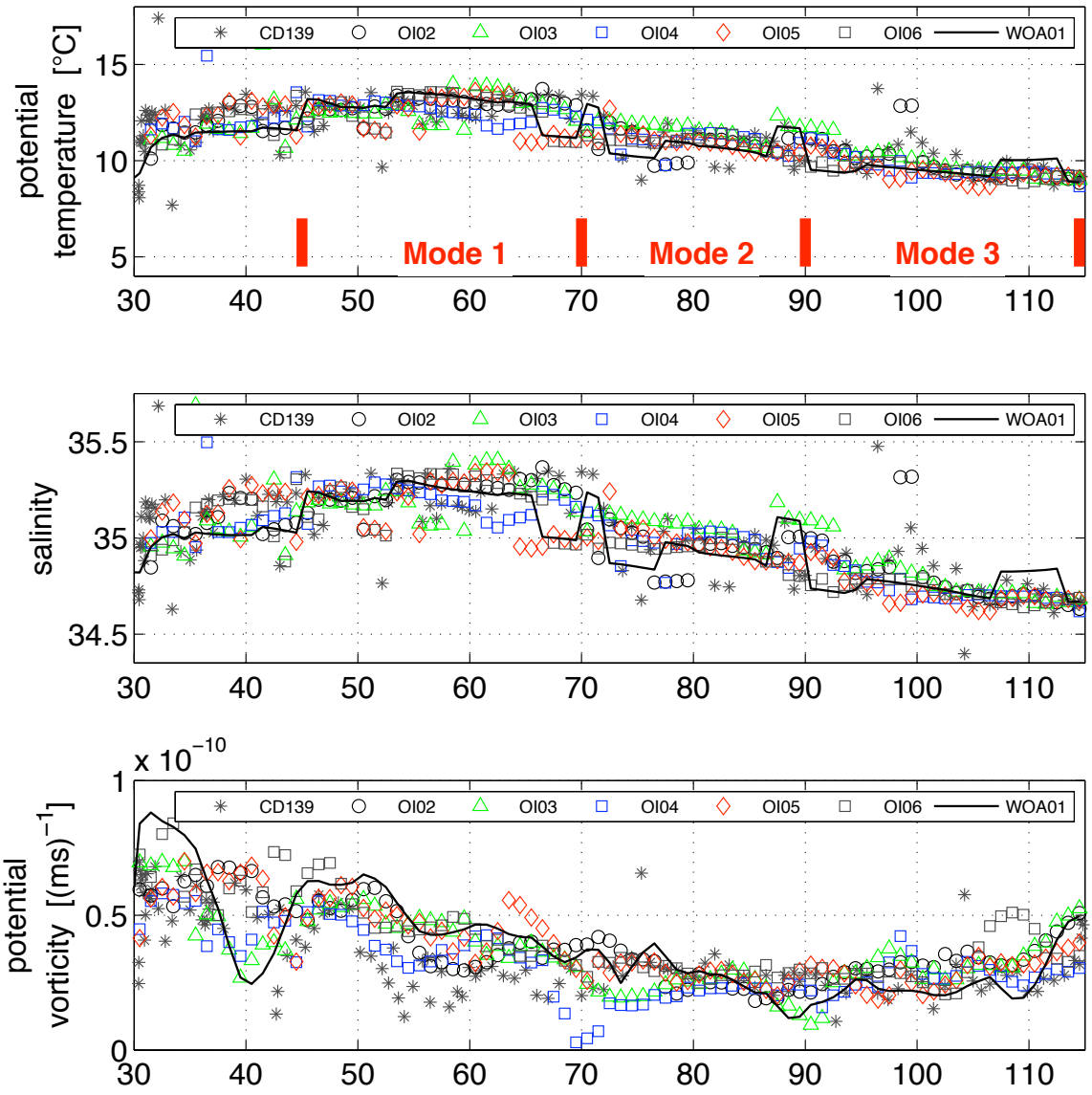

FIGURE 6.2: Properties at the minimum of potential vorticity at 32°S (from top to bottom: potential temperature [°C], salinity [psu], potential vorticity [ms^{-1}]) analysed between 200 dbar and 800 dbar, from the annual float realisations. For comparison the properties derived from the CD139 cruise data in 2002 (grey star), as well as from WOA01 climatology (black line) are shown.

float profiles within each year within the latitude range 30°S to 34°S, with a linear interpolation onto the one-degree spacing grid at 32°S applied. Here, the properties show more variations, but it seems that broadly these three modes are represented as well (Fig. 6.3). Additionally, larger gaps in the annual distribution of the profiles can be identified in the property plots, indicated by the linearly characteristics, for example in 2004 between 35°E and 48°E and in 2005 between 55°E and 67°E (Fig. 4.1) . For consistency, the results from the annual float realisations, using the OI algorithm, are

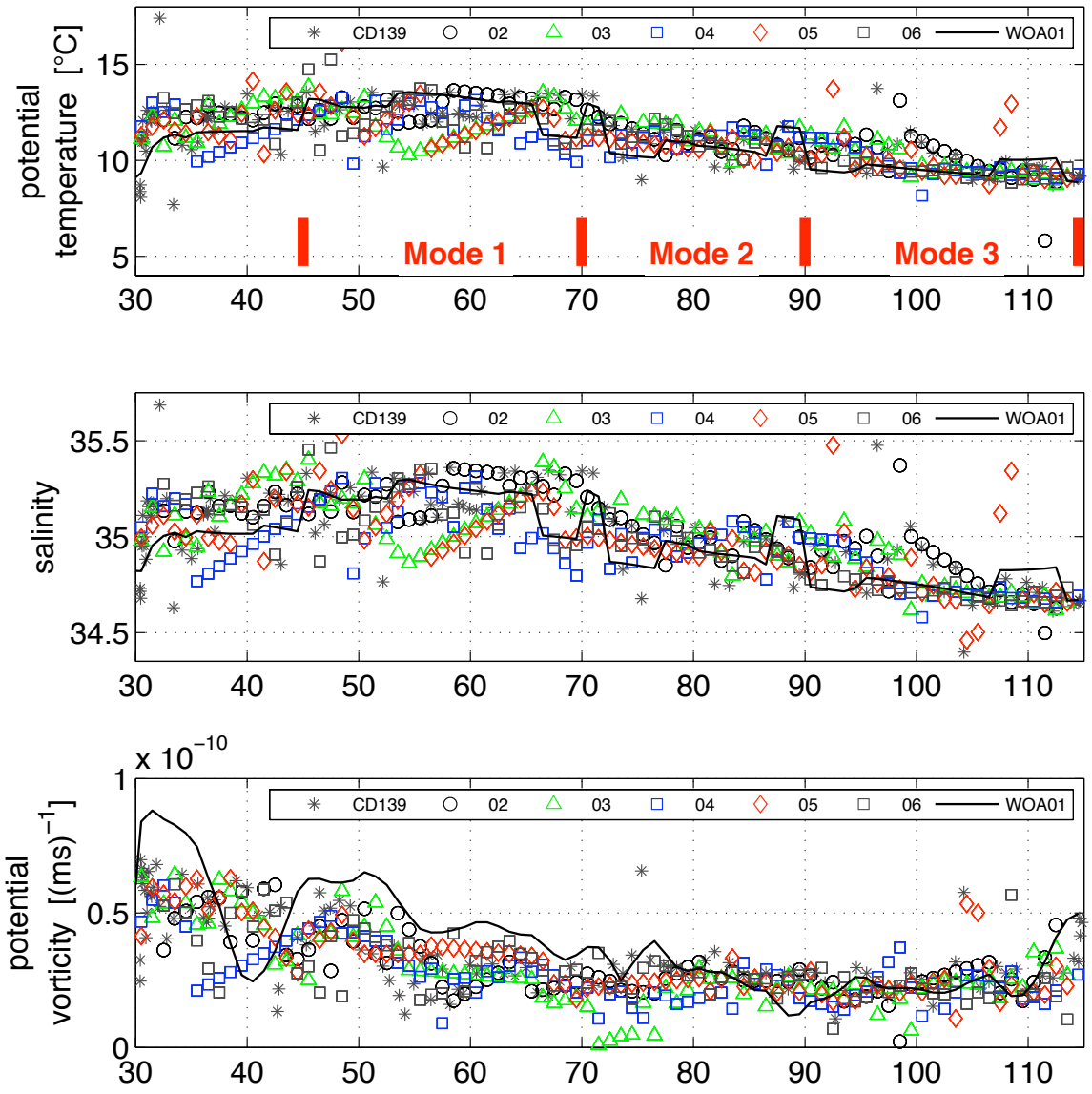

FIGURE 6.3: Properties at the minimum of potential vorticity at 32°S (from top to bottom: potential temperature [°C], salinity [psu], potential vorticity [ms^{-1}]) analysed between 200 dbar and 800 dbar, directly Argo profiles within the latitudinal range between 30°S and 34°S. For comparison the properties derived from the CD139 cruise data in 2002 (grey star), as well as from WOA01 climatology (black line) are shown.

used to investigate a possible link between changes in the gyre strength and changes in the water mass properties.

Returning now to the property characteristics of the potential vorticity minimum derived from the annual float realisations using the optimal interpolation method (Fig. 6.2). Interannual variations are largest in the MOZB west of 45°E, in the CB between 55°E and 70°E, and near BP at 90°E. In the west only in 2003 a 17°C mode water at 35°E is also identified by a PV minimum, while in 2004 a variant with 16°C

and less saline, with 35.5, is found at 36°E. It is suggested that this STMW is the result of winter mixing in the Agulhas retroflection zone forming that relatively weak 17°C mode, which is not permanent over the last decade. Furthermore, the mode water west of 40°E is a mix of recirculated waters containing several variants carried south by the AC (Gordon et al., 1987; McDonagh et al., 2005). The first mode along the section broadly extends from 45°E to 70°E with temperatures between 12°C and 13°C, and salinities between 35.2 and 35.4 (Fig. 6.2 top and middle). We define the start of the first mode at 45°E due to the shallow barrier of MADR reaching to 850 dbar. Additionally, there is more variability apparent west of 45°E this, on the one hand, because of variations in the recirculation in the MOZB, and on the other hand, due to sparser float data coverage. The second mode covers 70°E to 90°E with temperatures around 11°C and salinities between 34.9 and 35.1. The third mode extends from 90°E to 115°E with temperatures between 9°C and 10°C and salinities between 34.65 and 34.85. Both transitions between the modes are rather short and steep.

The exact position of the second mode (Fig. 6.2 top and middle) varies by year over several degrees longitude and by strength of transition. It seems that the boundary of the inner regime can also be identified from the annual relative geostrophic velocities (Fig. 4.3). In 2002 the second mode extends from 70°E to 90°E where we find a large patch of southward velocities in the west and a patch of large northward velocities in the east. In 2003 the second mode covers 70°E to 93°E, and while the same gross structure in the velocity field is found, there are more variations in the east at 90°E. Additionally, the most western mode shows large variations. In 2004 the separation between the first two modes is difficult due to large variations around 60°E. For 2004 the second mode is set from 74°E to 92°E. Note this covers only a large patch of northward velocities with some additional variations in the flow field in the east at 90°E. In 2005 a clearer separation exists again, with the second mode reaching from 64°E to 92°E showing patches of alternating directions in the velocities. Finally in 2006 the second mode could be identified from 66°E to 85°E, coinciding again with patches of alternating but relatively weak geostrophic velocities. With the relatively small variations in properties within the second mode it seems likely that this part of the section represents recirculations from the SIOC over the Crozet Basin (CB), with the alternating directions in the velocities indicating the meandering of the flow field (Stramma and Lutjeharms, 1997).

The eastern mode (Fig. 6.2 top and middle) shows variations between 90°E and 100°E, while east of 100°E the properties remain very constant, with temperatures around 9.5°C and salinities of 34.65. This is close to the original SEISAMW characteristics (Hanawa and Talley, 2001).

The properties of the PV minimum estimated from the float realisations show little variations, compared to the CD139 data in 2002. This confirms the stable characteristics of the SAMW. Next the change in salinity at 32°S is compared, where the gyre strength was estimated previously. It is possible that the strong increase in gyre strength between 2005 and 2006 can be associated with in property changes in the thermocline waters, as was found for the 15 year period between 1987 and 2002 (Bryden et al., 2003b; McDonagh et al., 2005).

6.3 Interannual variations in thermocline properties at 32°S

The analysis of the zonal structure of the water property changes between the CD29 data from 1987 and the CD139 data taken in 2002, showed a zonally coherent increase in upper thermocline salinity on potential temperature levels between 13°C and 11°C to 9°C. However this was not necessarily connected with the PV minimum (McDonagh et al., 2005). For completeness this comparison is shown again but including the differences to the annual float realisations (Fig. 6.4). The salinity differences of annual float realisations to the CD29 data do all show the zonally coherent increase in salinity in the upper thermocline centred between 11°C in the east and 13°C in the west. Only in 2006 (Fig. 6.4, 6th panel) the increase in salinity occures mainly on the potential temperature levels between 9°C and 15°C.

When the differences are directly compared between the CD139 and the float realisations along 32°S no zonally coherent change is found instead the changes vary substantially in strength and location (Fig. 6.5). In 2002 a freshening signal exists around 80°E penetrating from the surface into the MW and IW down to 1900 dbar (Fig. 6.5, 1st panel). This partly agrees with results from direct comparison of SAMW properties of the cruises in 1987 and 2002 and the first year of float data at 32°S reported by King and McDonagh (2005). However, they see the freshening of the 2002 float data extending further east up to 110°E. It seems likely that the float profiles had to be corrected in the salinity during the DMQC, as shown in the example of the CORIOLIS[1] 1900136 float and the BODC 5900184 float (Fig. 6.6). The two floats shown have been active from January 2003 to August 2004 (CORIOLIS 1900136) and from April 2002 to December 2004 (BODC 5900184), respectively. The period of interest for the comparison made by King and McDonagh (2005) is from early 2002 up to May 2003. This is the sampling period of the first 42 profiles from float 5900184. King and McDonagh (2005) assumed a drift in the salinity sensor of float BODC 5900184 and

[1]The Coriolis data center was initiated as a French contribution to operational oceanography

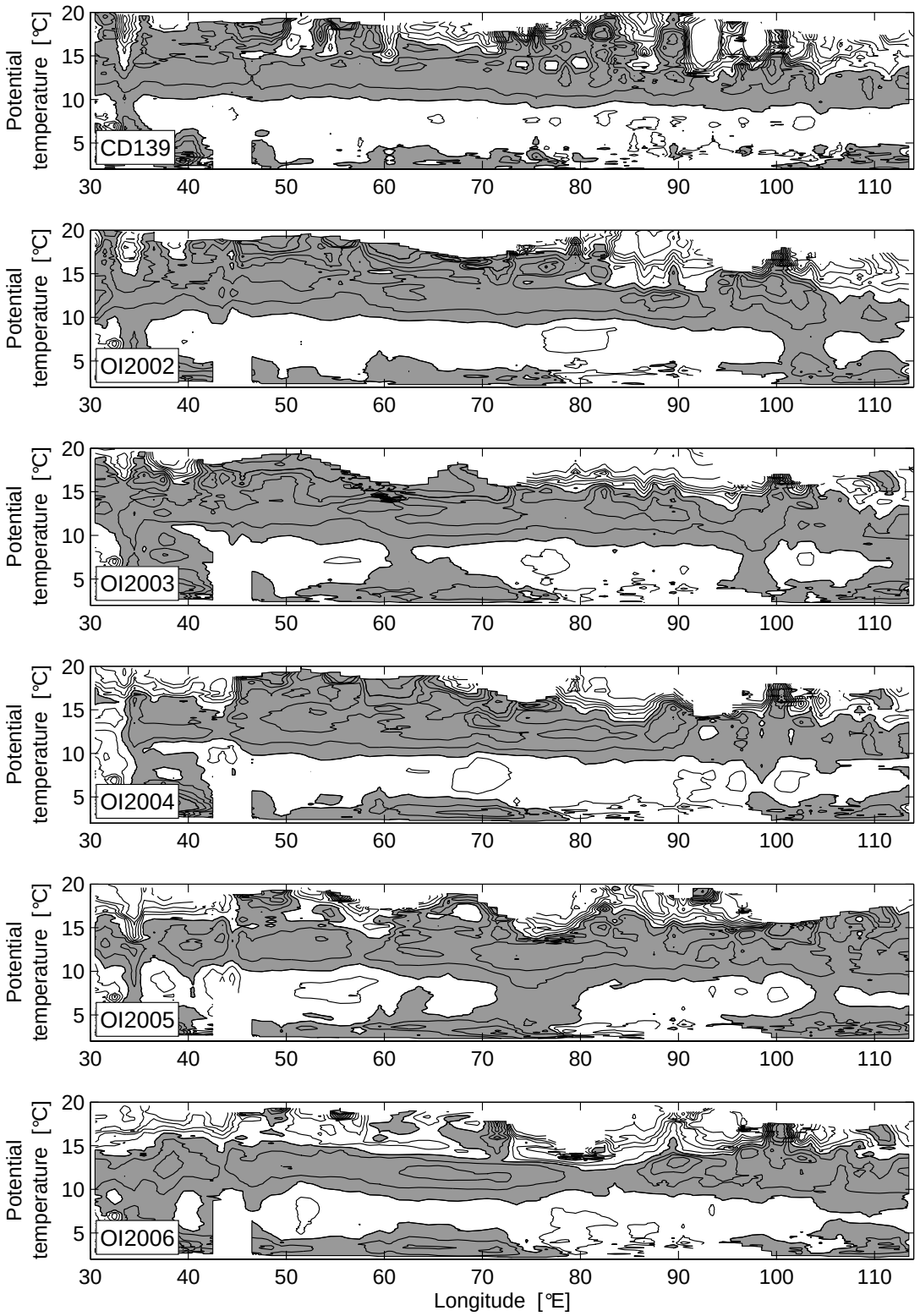

FIGURE 6.4: Salinity changes with respect to CD29 data in 1987, for CD139 data in 2002 and annual float estimates. Salinity has been interpolated onto 0.1°C Θ-levels and then horizontally onto a 0.5°-longitude grid. Grey shading denotes increase (positive changes) in salinity on Θ-levels and contour intervals are 0.2.

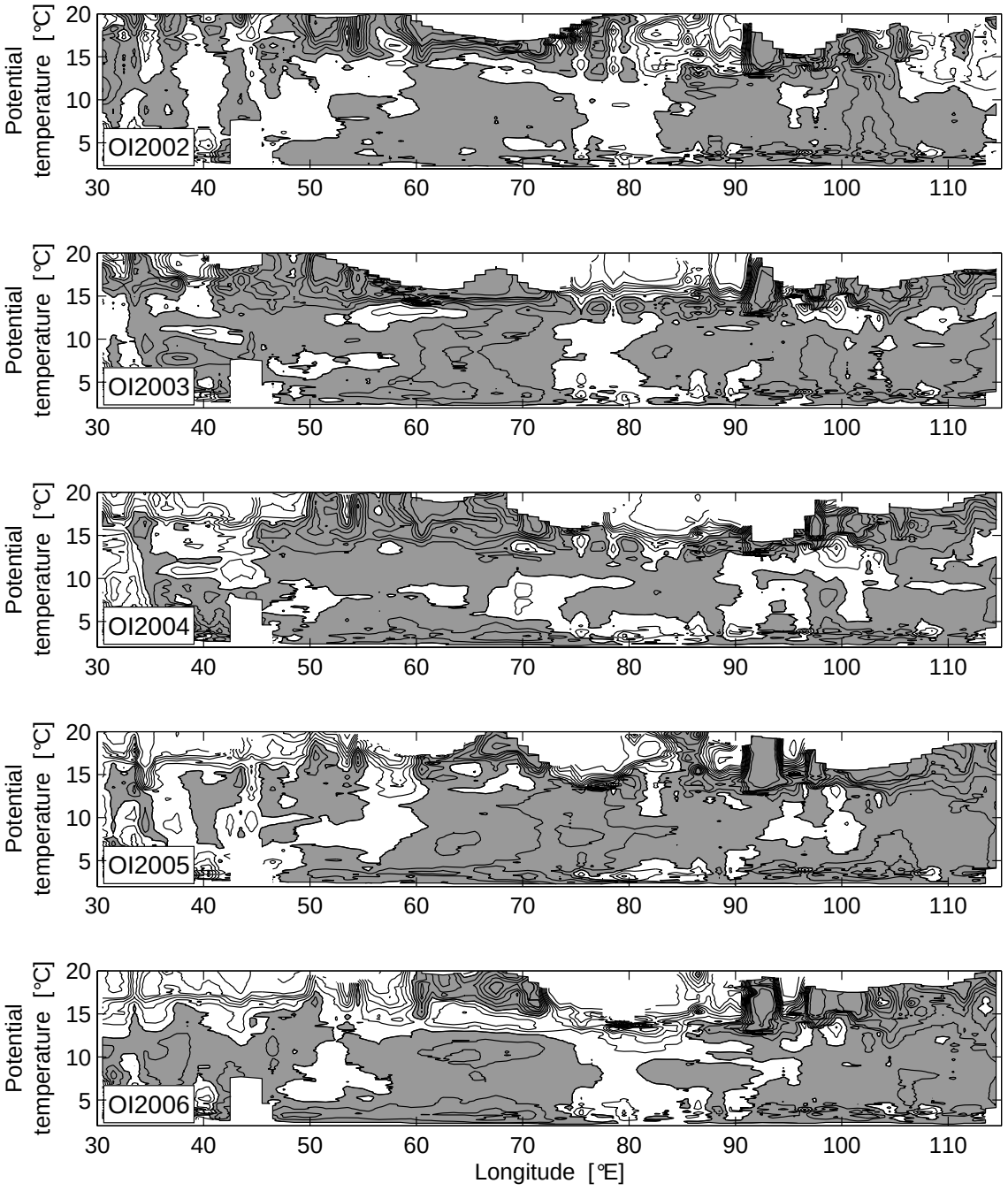

FIGURE 6.5: Salinity changes between the annual float realisations and the CD139 cruise data. Salinity has been interpolated onto 0.1°C Θ-levels and then horizontally onto a 1°-longitude grid. Grey shading denotes increase (positive changes) in salinity on Θ-levels with respect to CD139, contour lines give 0.02 intervals.

included only the first ten profiles in their analysis, while from float 1900136 the first 13 profiles have been used. During the DMQC procedure, described in section 2.1.1, an offset to fresher salinity values was found almost for the whole profile depth indicating a drift in the salinity sensor. From the DMQC software a vertically averaged salinity

additive correction of about 0.06, for float number 1900136, and of about 0.03, for float number 5900184, is suggested. These measurements clearly give reason to believe that at least part of the freshening seen in the analysis of King and McDonagh (2005) east of 80°E, is due to salinity sensor drift or malfunction. In 2003 (Fig. 6.5, 2nd panel) the patch of fresher waters at 80°E seen in 2002 is still present but less pronounced. A more uniform increase in salinity is seen over most of this section, with local maxima

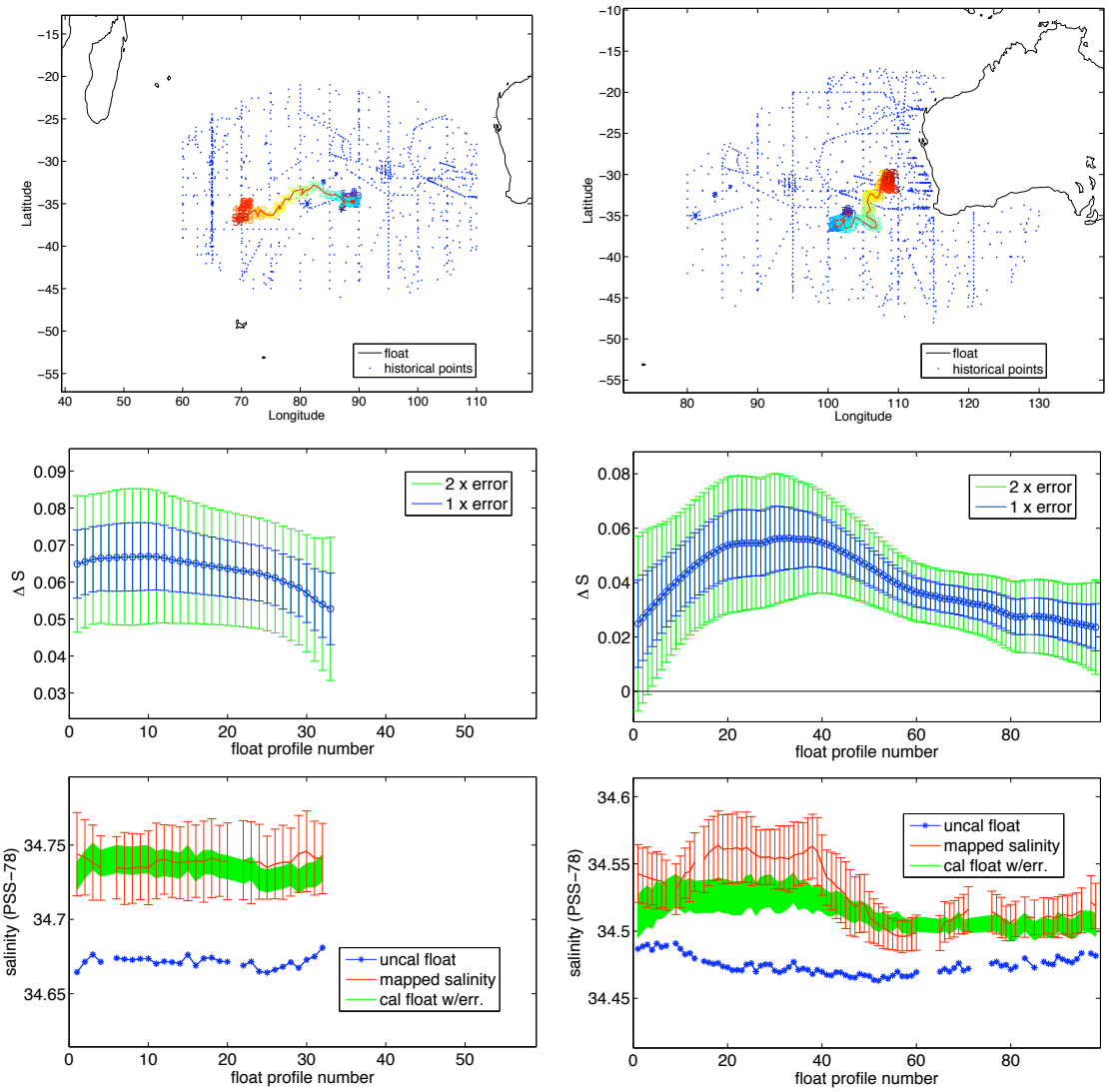

FIGURE 6.6: Different plots generated with the DMQC software (Wong et al., 2003) for float number 1900136 (CORIOLIS operated) active from January 2003 to August 2004 (left panels) and float number 5900184 (BODC operated) from September 2002 to December 2004 (right panels). For both floats a map of float profile locations with surrounding historical data points taken into account for delayed-mode quality control is shown (top) as well as the proposed vertically averaged salinity additive correction with errors (middle) and the salinities on isotherm with smallest salinity variance (bottom), which is Θ=9.5°C for float 1900136 and Θ=7.5°C for float 5900184, respectively.

of 0.02 over the full profile depth around 60°E. In 2004 (Fig. 6.5, 3rd panel) again less uniform changes are found, while in 2005 (Fig. 6.5, 4th panel) around 75°E a patch exists showing a salinity increase larger than 0.02 up to 1900 dbar. Additionally, west of 60°E large areas exist showing freshening mainly near the surface but also deep reaching. In 2006 (Fig. 6.5, 5th panel) this freshening aggregates to more than 0.02 and forms a pool of fresher water at the surface from the western boundary to 60°E reaching down to the 13°C isotherm. From 60°E to 90°E this signal continues while at 80° it penetrates down to 1900 dbar. Around 65°E a relatively large signal of increased salinity ($\Delta S \geq 0.02$) exists in the lower SAMW.

Θ-S property differences on isopycnals According to previously identified three modes (Fig. 6.2) changes between Θ-S properties on isopycnals are examined in the following. The profiles have been vertically interpolated onto $2 \times 10^{-3}\,\mathrm{kg\,m^{-3}}$ spaced σ-levels. Then they have been horizontally averaged within the longitude band of the western (45°E to 70°E), inner (70°E to 90°E) and eastern (90°E to 115°E) segments, representing the different modes seen in the properties of the potential vorticity minimum, at 32°S (Fig. 6.7). The changes on Θ-levels have been computed with respect to the 2002 estimate from the annual float realisations. The 2002 float realisation showed small differences to the CD139 cruise estimate of less than 0.1°C in temperature of the MW and IW in the eastern and inner segment and a change in salinity off about 0.02 occured (not shown).

In the western mode (averaged between 45° and 70°E; Fig. 6.7 left column) the interannual changes of water mass properties are smallest compared to the other modes. The vertical structure of the changes for the different years is quite similar below the 13°C isotherm, showing generally an increase in temperature up to 0.1°C and in salinity up to 0.02, respectively. Additionally, a local maximum in warming and salinification exist near the 3°C isotherm. The increase in salinity and temperature between the 2°C and 13°C isotherm is largest in 2004 and 2006 with an increase of 0.02 in salinty and 0.12°C in temperature. Above 13°C the 2003 estimate shows a large warming of 0.2°C around 15°C with a parallel increase in salinity of 0.06. Further up in the water column most of the years (2004, 2005 and 2006) show a cooling and freshening of the near surface waters compared to the 2002 estimate above the 15°C isotherm.

In the inner region (averaged between 70° and 90°E; Fig. 6.7 middle column) the interannual changes below the 9°C isotherm are relatively small with 0.01 in salinity and 0.05°C in temperature below the 9°C isotherm. Only in 2005 larger changes exist with an increase in salinity of 0.02 and in temperature of 0.1°C, respectively. On the 11°C isotherm, defining the level of the minimum in PV, interannual variations are

about 0.03 in salinity and 0.15°C in temperature. The salinity and temperature around 11°C increase from 2003 to 2004 and further to 2005, while to 2006 the properties decrease again. This counter movement in the property changes to the gyre strength changes appears to exist for the levels below the 12°C isotherm (Fig. 6.7 middle column, 1st and 2nd row). Only 2003 does not fit in that scheme because the gyre strength decreased from 2002 to 2003, while the water mass properties do the same. At 14°C

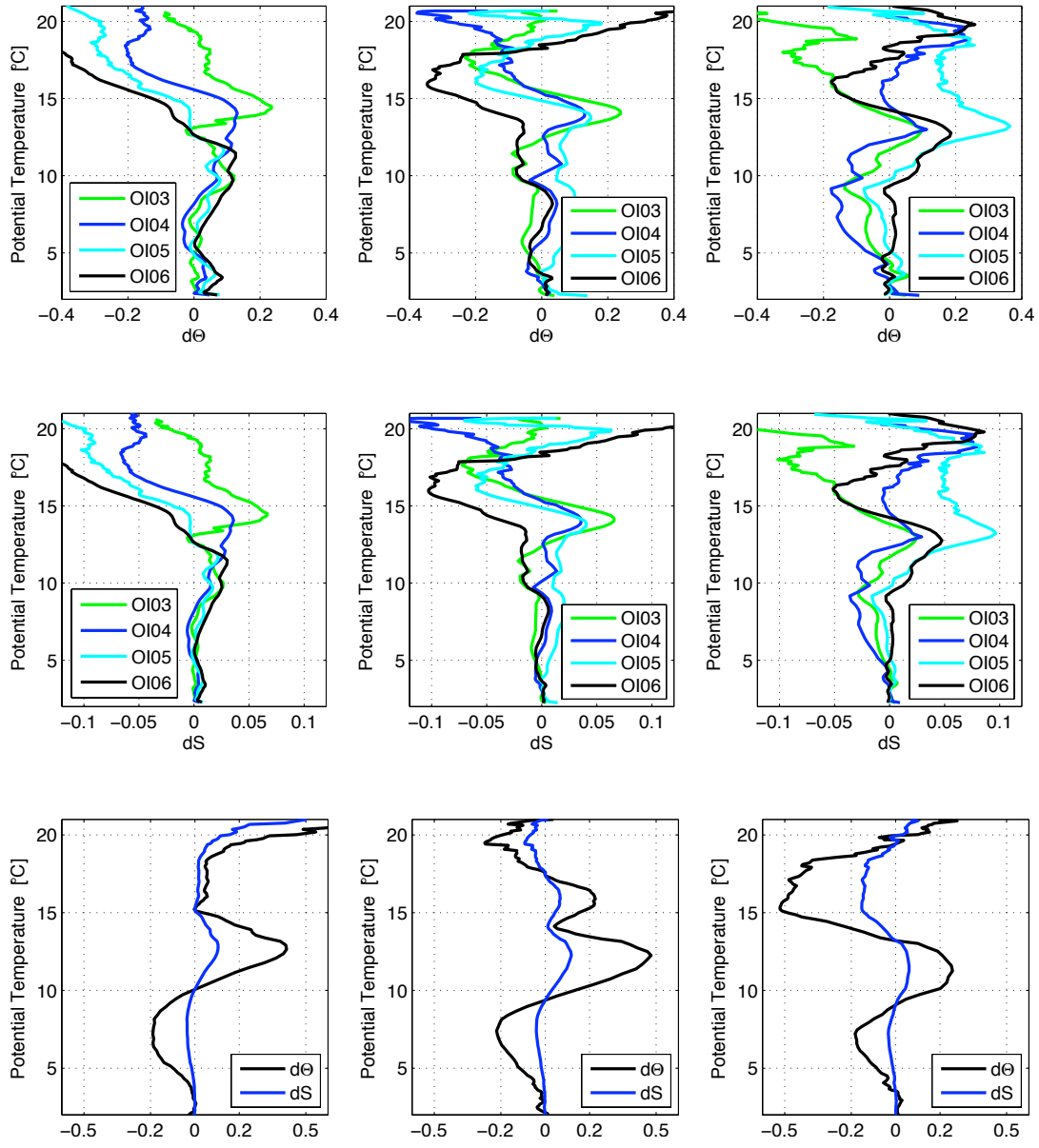

FIGURE 6.7: Changes in potential temperature (top) and salinity (middle) on σ_Θ-levels between annual float estimates and the 2002 estimate from the annual float realisations. Also shown for comparison the changes in potential temperature (black) and salinity (blue) between CD139 and CD29 cruise data on σ_Θ-levels (bottom). Divided into western part (45°E to 70°E), inner part (70°E to 90°E) and eastern part (90°E to 115°E). Please note that for clarity different scales have been used.

a local maximum exists for 2003, 2004 and 2005 with an increase of more than 0.1°C in temperature and 0.04 in salinity. The properties in 2006 are cooler by 0.2°C and fresher by 0.05 then in the other years between the 13°C and 17°C isotherm. On the 17°C isotherm all years show a local minimum in temperature and salinity compared to 2002.

In the east (averaged between 90° and 115°E; Fig. 6.7 right column) the largest interannual changes exist, especially in the SAMW level and below. Except for 2006, a cooling of up to 0.2°C and a freshening of up to 0.03 in salinity is shown below the 9°C isotherm, which we relate to the core of SAMW, above the AAIW. The largest changes occur here in 2004, with the other years showing a continuous decrease (2002 to 2004) and increase again (2004 to 2006). Above, we find a local maximum of increased temperature and salinity around the 13°C isotherm for all years. 2005 shows by far the largest change (about twice the size compared to the other years). In 2003 a constant freshening and cooling is found, while the other years show a salinification and warming up to close to the surface.

In conclusion the variations seen in the changes on σ_Θ levels are smallest in the western segment on levels below the 9°C isotherm. The second mode exhibits large year-to-year variations in the properties below 13°C in the order of O(0.1°C) in temperature and O(0.02) in salinity. Closer to the surface the changes become even larger. The eastern mode shows the largest interannual variations, especially between 2005 and 2006 above 10°C. A clear signal connecting the water mass property changes with the changes in gyre strength was not detected with our analysis. The large increase in the strength between 2005 and 2006 may be connected with the large cooling and freshening of the water masses above the 12°C isotherm in the eastern mode and over the whole profile depth in the interior mode. In the eastern mode these changes are largest with a cooling between 0.2°C and 0.35°C between 13°C and 16°C and a freshening between 0.05 psu and 0.1 psu in the same range. Such a signal is also found in the property changes between the 1987 and the 2002 cruise data. But the interannual variability did not show such zonally coherent change of temperature and salinity below the 14°C isotherm. In contrast the increase in gyre strength between 1987 and 2002 was thought to be at least partly connected to the warming and increase in salinity (McDonagh et al., 2005) seen in the 2002 thermocline properties (Fig. 6.7, lower panel). Possibly a different mechanism is responsible to alter the water mass properties on short time scales such as years. As a mode water, SAMW takes the temperature and salinity properties of its formation layer into the ocean interior. A freshening (increase in salinity) of SAMW on isopycnals can be the result of either warming (cooling) or freshening (increase in salinity) on pressure surfaces of the winter mixed layer where

the water mass outcrops (Bindoff and McDougall, 2000). Generally, the formation of the cold dense eastern 10°C mode is at 45°S, 110°E or further east, while the warmer western 13°C mode is formed around 40°S, 70°E (Belkin and Gordon, 1996; McDonagh et al., 2005; Stark et al., 2006). These mode waters are then subducted and moved northwards in the subtropical gyre, while the anticyclonic subgyre (Stramma and Lutjeharms, 1997) in the southwest Indian Ocean enhances the separation into the western and eastern mode. From the analysis of the properties of the PV minimum it seems that the fronts in the geostrophic velocities (Fig. 4.2) are directly linked to the annual variation of boundaries of the modes, especially at the transition between the 1st and the 2nd mode at 70°E (Fig. 6.2 , 6.3). Therefore, changes in the location or extension of the southwest Indian Ocean subgyre could alter the mode water properties. At the formation site, direct surface forcing or Ekman processes can change the winter mixed layers in the SAMW formation outcrop regions (England et al., 1993; Rintoul and England, 2002; Ribbe, 1999). Rintoul and England (2002) showed, that a density-compensating change in properties of the mode water is unlikely to be caused by air-sea fluxes, but rather by the advection of water with different $\Theta - S$ properties but similar density into the formation site. The thickness of the mode water layers and the short time available in winter to modify their properties means that large surface flux anomalies are needed to change mode water properties (Warren, 1972; Rintoul and England, 2002). Using a coupled climate model, Rintoul and England (2002) showed, that the model changes in SAMW properties are correlated significantly with changes in the wind stress and northward Ekman transport of cool low-salinity water. This was also suggested by Sallee et al. (2006), who analysed the formation of the SAMW in the southeastern Indian Ocean using Argo float data, surface drifter and surface forcing and wind fields from NCEP reanalyis.

Additionally, the OI method could be partly responsible for a poor connection of changes in water mass properties and changes in the gyre strength, since mapping temperature and salinity on pressure levels could dilute the water mass signals, especially when using WOA01 as a background climatology. Here, it becomes clear that longer monitoring is necessary, preferably with a better temporal resolution, to define the interannual variability in the water mass properties. On the one hand, these results agree with the findings of Stark et al. (2006), who explored the consistency between observed changes in SAMW properties at 32°S in the SIO and model simulations. They concluded that the observed changes between 1987 and 2002 in SAMW properties are due to interannual oscillations. On the other hand, the structure of the change and therefore of the water masses is significantly different in the period 2002 to 2006 compared to the changes from 1987 to 2002.

6.4 Summary

Three separate modes in upper thermocline properties are identified along the 32°S section, the western mode between 45°E and 70°E, the inner mode between 70°E and 90°E and the eastern mode between 90°E and 115°E, with the boundaries of the inner mode varying by several degree longitude from year to year. This is different to the results shown by McDonagh et al. (2005) who identified two separate modes. This difference could be caused by the deviation of the cruise tracks in 1987 and 2002 from the 32°S latitude.

The analysis of thermocline properties showed that the large freshening in the eastern part of the CD139 section, reported from Argo float data collected near 32°S in 2002 and 2003 (King and McDonagh, 2005) is at least partly caused by salinity sensor malfunction of individual floats.

Finally, the analysis of differences in Θ-S properties at 32°S averaged over each segment on isopycnals does not give a complete explanation for the large variation in the gyre strength between 2005 and 2006, although large variations exist in the east in the upper thermocline water between 2005 and 2006, comparable to those reported by McDonagh et al. (2005). Hence, it is suggested that the variations seen between 2002 and 2006 do show year-to-year variability because the changes did not show a coherent signal between the three modes. The changes observed are most likely due to changes in the equatorward Ekman transport of cool, low salinity water across the subantarctic front because the magnitude and density-compensating nature of the temperature and salinity changes cannot be explained by variations in air-sea exchange of heat and freshwater in the subantarctic zone where SAMW is formed (Rintoul and England, 2002). Additionally, Sallee et al. (2006) found a rapid transition to thicker of mode water layers in the central SIO, at about 70°S, associated with a reversal of the horizontal eddy heat diffusion in the surface layer and the meridional expansion of the ACC near the Kerguelen Plateau. These effects are ultimately related to the bathymetry of the region, leading to the seat of formation in the region southwest of Australia. While upstream of this region, the dominant terms in the heat budget are the air-sea flux, eddy diffusion, and Ekman heat transport, all having approximately equal importance, within the formation area, the Ekman contribution dominates and leads to a downstream evolution of mode water properties.

Chapter 7

Discussion and conclusion

This study has provided a quantitative description of the temporal evolution of the strength and zonal structure of the subtropical SIO gyre circulation derived from Argo float data. The Argo project, as a follow-up of the WOCE program, is part of a global observing system providing high resolution measurements of the upper ocean in space and time. In the SIO the Argo program started with the deployment of a small number of floats in late 1999, south of MAD and northwest of Australia in the ITF region. The number of profiles taken in the SIO until the end of 2001 was only about 650 in total. Whereas, in early 2002 a major step towards a continuous realtime monitoring of the ocean basins was taken in the SIO, marked by the deployment of 25 floats along 32°S during the R/V *Charles Darwin* cruise 139 (Bryden et al., 2003a).

The subtropical SIO connects the equatorial Indian Ocean to its major export path in the south west, the AC. This connection is largely accomplished by narrow currents or eddies propagating in the MOZC and the east of MAD, respectively (De Ruijter et al., 2004; Schouten et al., 2002; Quartly and Srokosz, 2004). While the low-frequency variability in the boundary regions has been the focus of recent studies (Schouten et al., 2002; Palastanga et al., 2006; Matano et al., 2008; Birol and Morrow, 2001, 2003), the present study focusses on seasonal to interannual variations in the interior gyre circulation, away from the direct influence of the boundary currents in the west and east.

The study is motivated by recent analyses reporting decadal changes in the gyre circulation in the SIO at 32°S over the past 50 years (Bindoff and McDougall, 2000; Palmer et al., 2004; McDonagh et al., 2005) and an increasing gyre strength in the South Pacific (Roemmich et al., 2007). Palmer et al. (2004) reported an increase in the gyre strength of up to 40% estimated from three hydrographic transects along 32°S in the SIO taken in 1987, 1995 and 2002. Their findings together with the

start of the Argo project in the SIO area are the foundations of this work. The following questions have been addressed in detail:

- What is the interannual and seasonal variability in the interior gyre circulation at 32°S over the 5 year period between 2002 and 2006?
- Does the gyre strength exhibits a trend between 2002 and 2006?
- How well do the results derived at 32°S compare with those derived at 20°S?

7.1 Summary and discussion

Answering the above questions using Argo float data a careful preparation of the data was required. This is due to the early stage of the Argo project in the SIO area. Only a small fraction of the Argo data was already DMQC processed by the DAC in the beginning of 2005, while now about 30% to 40% are processed. Nevertheless, the years 2005 and 2006 still contain large numbers of profiles from the SIO without appropriate DMQC applied. Therefore, the data have been quality controlled using a DMQC procedure as proposed and supplied by Wong et al. (2003). The recommended reference climatology (King and Sudheer, 2006) was updated and accomplished with recent hydrographic cruise data in the subtropical SIO. During the DMQC process a selection criterion was used, to identify possible salinity sensor malfunctions. According to this criterion vertically averaged salinity that differ by more than 0.05 from the climatology are carefully inspected for malfunctions of the sensor. The final accuracy of the DMQC profiles was then within the $\Delta S = 2\sigma$ criterion selected by Wong (2005b). The finally selected DMQC profiles were linearly interpolated onto 20 dbar levels.

The accuracy of the DMQC salinity measurements is then estimated at 32°S following broadly the approach used by Wong (2005b) in their study on averaged SAMW and AAIW proprties. They estimated the uncertainties in salinity to be 0.01, based on minimum noise variance on 4 predefined isotherms (Θ=11.7°C, 10°C, 9.5°C and 9°C) from profiles averaged on isotherms over 10° x 5° boxes. The 4 isotherms were selected because they are within the range of the tightest part of the Θ-S relationship in the SIO (Wong, 2005b). In contrast, in the present study the profile data are mapped on pressure levels using an OI algorithm. Therefore, the nearest pressure levels to the 4 preselected isotherms are used. The time series of 12 month averages generally indicate a noise level of about 0.04 in salinity. The test with a larger averaging period of 24 months gives smaller noise levels of order of O(0.02). The larger noise level compared to Wong (2005b) results from the interpolation on pressure levels and the

shorter averaging period of 12 months. The final accuracy of the salinity measurements, presented here is estimated to be 0.04.

The DMQC float dataset was then mapped onto a regular grid (either 1° x 1° grid from the WOA01 or repetitive cruise tracks from CD139 and BEAGLE) using an OI, which was successfully applied in the DMQC procedure (Wong et al., 2003; Böhme and Send, 2005; Owens and Wong, 2008) but also in recent studies using Argo float data (e. g. Guinehut et al. (2002); Wong (2005b); Hadfield et al. (2007); Roemmich et al. (2007)). For the mapping procedure important decorrelation length scales are estimated from variance analysis of temperature and salinity residuals of float and cruise data, relative to the WOA01 climatology. For the SIO area anisotropic decorrelation length scales are selected for the full profile depth of 2000 m of the Argo floats. The final choice of decorrelation length scales was somewhat subjective trying to balance the weight given to cruise and float data. The zonal length scale (Lx_W) for the western boundary region, between Africa and 45°E was set to 200 km, while for the rest of the basin (Lx_E) 600 km was selected. The meridional decorrelation length scale (Ly) was set to 400 km. Compared to other studies in subtropical oceans White (1995); Hadfield et al. (2007); Roemmich et al. (2007) the scales are of similar size.

The accuracy of the OI method was evaluated by means of resampled cruise tracks (CD139 in March/April 2002 along 32°S and BEAGLE in December/January 2003/2004 along 20°S) using optimally interpolated float data within ±1 month and ±2 months of the cruise date compared to 5° box averaged smoothed cruise data. It was shown that the section wide averaged root-mean-squares of differences is 0.05 for salinity and 0.5°C for temperature, which is smaller than estimated from the climatology. This is consistent with the results of Hadfield et al. (2007) who included a temporal separation in their mapping procedure used for studying the accurracy of Argo heat storage fields

The quality controlled Argo data are then used to calculate geostrophic velocity and transport sections at 32°S and 20°S. The ZV level is set at 1900 dbar and 1000 dbar for 32°S and 20°S, respectively. The ZV assumption at 32°S is used in order to fulfil the need for a deep reference level and to allow the inclusion of as many data as possible. Although the float profiles sampled generally to the 2000 dbar pressure level, the number of valid data points on pressure levels below 1900 dbar decreased rapidly with depth. Additionally, according to Palmer et al. (2004), who analysed changes in the gyre circulation from three hydrographic transects along 32°S using ZV level at 2230 dbar, their transport estimates were affected by less than 3% if the ZV level was varied by up to 800 dbar. The decision to use a shallow ZV level at 1000 dbar at

20°S is based on the study by Warren (1981) and on the fact that at 20°S, there are generally less data points available below 1000 dbar due to differences in the predefined setting of floats deployed in that region.

Two methods for the calculation of the gyre strength are compared at 32°S, the *MaxTrp* and the *LinReg* method. The gyre strength is defined as the transport over the ocean interior, between 45°E and 110°E. The *MaxTrp* method, which simply takes the maximum difference over the defined longitude referenced to 110°E, was used in the study by Palmer et al. (2004). They used this method to compare the hydrographic transects between 1987 and 2002. Additionally, it was shown in the present study that the method's sensitivity to the choice of end points is due to eddy activity in the east around 110°E which are connected to the LCS (Fang and Morrow, 2003; Rennie et al., 2007; Waite et al., 2007). Referencing the eastern end point to the WOA01 climatology largely solved that problem and showed good agreement between changes in the estimated gyre strength and changes at 110°E, which was selected to be the eastern end point. The region around the western end point at 45°E contained large error estimates, increasing further to the west, due to sparse data coverage and the large eddy activity in the MOZB south of MAD as seen in the RMS of weekly SLA data analysed for the period 1992 to 2004 (Palastanga et al., 2007). The *LinReg* method avoids the necessary referencing to the climatology, because it depends only marginally on the eastern end point (the gyre strength changed less than 3% by referencing to the WOA01 data). The method uses a zero-order linear fit to the vertically integrated transport profiles at each grid point of the ocean interior defined between 45°E and 110°. The gyre strength is then taken to be the difference at the end points of the fitted transport data integrated from the east. This method is less sensitive to the end points and the residuals provide a useful error estimate, especially in the present case where property estimates can be biased by the float data distribution. Furthermore, the *LinReg* method is less biased by large eddy signals in the transport compared to a simple regression of the zonally integrated gyre transports. Additionally, the error estimates from the *MaxTrp* method are slightly larger than for the *LinReg* method. Therefore, for this study the *LinReg* method seemed to be the better suited method.

The mean gyre strength between 2002 and 2006 at 32°S was estimated to be 44.4±1.2 Sv, i. e. northward flow. The interannual variability, defined as standard deviation, is 5.2 Sv. The seasonal variability, defined as standard deviation, was estimated to 3.0 Sv, with maxima in spring and autumn. The interannual peak to peak changes are large, up to 13 Sv, indicating the dominant role of the interannual variability at 32°S. The comparison with the gyre strength estimated from CD29 cruise in 1987 and CD139 cruise in 2002 showed clearly the significant difference between the 1987

estimate and the state of the gyre circulation during the 5 year period 2002 to 2006, as reported by Palmer et al. (2004); McDonagh et al. (2005). Palmer et al. (2004) showed that most of the change happened between 1995 and 2002. Furthermore, they concluded that there has been a persistent change between the flow structure of the 1987 and 2002 sections, that can be seen by the westward shift of the maximum southward transport (in 1987 this maximum is located at 55°E, while in 1995 at 45°E and in 2002 at 40°E, respectively). Note, that the 1995 cruise data are not used in this study, due to the sparse coverage in the interior resulting from the different cruise tracks compared to 1987 and 2002. However, no significant trend in gyre strength was found over the 5 year period. The 1987 estimate is more than 10 Sv lower than the mean gyre strength estimate, exceeding 2 standard deviations of the interannual variability estimated for the 2002 to 2006 period. The amplitude of the change between 1987 and 2002 is smaller than the largest interannual peak-to-peak variations which are observed between 2005 and 2006. The estimate from CD139 cruise in 2002 is well within the given errors with the 2002 estimate using optimally interpolated float data.

The analysis showed that a possible bias of the large increase in the gyre strength between 1987 and 2002 due to the sampling season can be excluded. The gyre strength estimate in 1987 is more than 12 Sv smaller than the appropriate spring estimate, exceeding 3 standard deviations of the seasonal variability calculated for the period 2002 to 2006. The 2002 estimate from CD139 cruise data is in good agreement, within the given errors, with the autumn estimate. This indicates that the gyre strength may be estimated from single hydrographic cruise data but this estimate is restricted to a period of one year or so. The large interannual variability indicates that care needs to be taken to interpret changes in gyre strength from just two or three transects as decadal trends.

The comparison of the geostrophic Sverdrup transport time series with the gyre strength time series constructed from cruise and float data estimates, respectively, indicates a large correlation of $R^2 = 0.92$, with a time lag of one year. Here annual averages and cruise data are used, providing 6 independent estimates. Additionally, the comparison shows surprisingly good agreement in the magnitude of the gyre strength estimates, at least for the interior gyre circulation of the upper 1000 dbar, which is different to the findings showed by Bryden et al. (2005). They reported a difference of about 25 Sv between AC transport and Sverdrup transport at 31°S, from analyses of a year-long moored array of current meters and synoptic hydrographic sections. The geostrophic Sverdrup transport time series was calculated from NCEP wind-stress data averaged over a 6° latitudinal band centred at 32°S, with a Gaussian low-pass filter of one year applied. Anomalies of geostrophic Sverdrup transport show small

positive anomalies over the interior in most of 2005 while in 2003 and 2004 relatively large negative anomalies exist. Additonally, the extremely small gyre strength in 1987 can be at least partly attributed to the persistent large negative zonal wind-stress anomalies over the longitudinal band between 50°E and 100°E existing between 1985 and 1988. The time lag of 1 to 2 years at 32°S, between Sverdrup transport time series and that from float realisations, does not agree with the typical assumption of perturbations being initiated in the east of the basin and travelling over the whole basin to affect the west. The adjustment time for such phenomena is longer than 1 to 2 years. However, if perturbations are forced near the western boundary, then the adjustment time is reduced and a time lag of 1 or 2 years could be possible. Additionally, Matano et al. (1998) showed that the MADR has a significant effect on westward propagating perturbations at 40°S probably leading to large baroclinic wave energy arising from the interaction of barotropic waves from the interior of the Indian Ocean and the ridge. The good correlation of the 32°S gyre strength time series with 1-year time lag supports the findings by De Ruijter et al. (2004); Palastanga et al. (2006). They reported a connection between interannual variability in the strength of the EMC related to equatorial climate modes such as ENSO/IOD. The westward propagation of the large-scale anomalies takes about one year (Murtugudde et al., 2000).

However, it seems that changes in the wind-stress in the SIO area cannot be the main driving force for seasonal changes in the gyre strength between 45°E and 110°E. The seasonal cycle of the wind-stress curl shows its maximum in July around 50°E, 40°S and its minimum in January over the whole SIO (Schott and McCreary, 2001). In comparison, the seasonal cycle of the gyre strength at 32°S estimated from float data shows a higher frequency with two maxima of similar amplitude during spring and autumn and two minima of similar size during summer and winter. This suggests that a sub-annual modulation of the wind induced signal may exist as for example the observed semi-annual (Morrow and Birol, 1998) and 4 - 5 time/year (Schouten et al., 2002) westward propagating Rossby waves in the latitudinal band 20°S - 30°S. Additionally, Palastanga et al. (2007) reported seasonal variations in the SICC, being stronger (weaker) in summer (winter) while the SEC weakens (strengthens) due to large-scale wind variability (Tchernia, 1980). At 32°S the time series from geostrophic Sverdrup transport indicates a robust positive trend (3.6 Sv/decade; with a statistical significance of more than 85%). It is interesting, that at 32°S, the minimum in gyre strength derived from Sverdrup transport, as well as the increase afterwards to larger values, occurs in the beginning of the period of reported increase in global mean surface temperatures (IPCC, 2007). Whereas, at 20°S, no such connection is apparent nor are any regimes with significant trends detectable.

Additionally, altimetry data are used to evaluate the temporal evolution and propagation of signals apparent in SLA. At 32°S a large positive anomaly exists in the east at 110°E between 1999 and 2002. This positive anomaly could be associated with the persistent La Niña state in the equatorial Pacific between 1998 and 2001 (Palastanga et al., 2006). The positive SLA propagates westward with a pronounced westward decrease of the amplitude, reaching 50°E within less than 12 months. This coincides with a large positive SLA signal developing at 45°E in the vicinity of MADR. In 2004 and 2005 the SLA shows negative anomalies in the east, while in 2006 the SLA is back to the 2002 state or even increased, especially in the eastern and western boundary regions.

The reported decadal change in gyre strength between 1987 and 2002 (Palmer et al., 2004) was associated with a large increase in salinity in the upper thermocline Θ-S properties as well as with an increase of the dissolved oxygen concentration (McDonagh et al., 2005). The large interannual changes in gyre strength between 2005 and 2006 estimated from the annual float data are associated with the largest year to year variability in Θ-S properties, especially in the east. However, the decreases in salinity of about -0.08 and in temperature of about -0.3°C, are limited to levels between the near surface layer and the upper portion of the SAMW, which is between 13°C and 17°C. Although the magnitude of the change in properties is similar between 2005 to 2006 and 1987 to 2002 in the 5 year period the change is less coherent over the whole section but focused on the eastern end between 90°E and 115°E. At the moment it is not quite clear if the large increase in salinity and temperature between 1987 and 2002 could be attributed solely to interannual variability, as reported by Stark et al. (2006).

Applying the *LinReg* method at 20°S shows the same tendency in the interannual changes in the gyre strength, though less pronounced and with smaller interannual peak to peak changes (maximum interannual change is 6.5 Sv between 2003 and 2004). The estimated mean gyre strength at 20°S over the 4 years period 2003 to 2006 is 23.8±1.4 Sv, with an interannual variability, defined as standard deviation, of 3.6 Sv. The largest gyre strength estimates exist during summer with 27.5±1.4 Sv and the smallest estimates exist during winter with 18.8±1.4 Sv, while the total seasonal variation estimated as standard deviation of the four seasons is 4.2 Sv. This is again, contrary to the seasonal cycle in the geostrophic Sverdrup transport derived from wind-stress curl (Schott and McCreary, 2001). Compared with the 32°S section the role of the deep layer, defined between 1000 dbar to 1900 dbar is different. The deep layer is acting as a buffer between summer and autumn and between winter and spring, respectively

compensating the decrease/increase in gyre strength in the upper layer (defined between 200 dbar and 1000 dbar). Between autumn and winter the deep layer undergoes the larger changes of the two layers, and between spring and summer the change takes place mainly in the upper layer. The estimated gyre strength using the BEAGLE cruise data (27±2.3 Sv) is in good agreement with the 2003 and 2004 estimates of 29±4.8 Sv and 22.5±2.1 Sv, respectively. An even better agreement exists with the appropriate summer estimate, for all 4 years, which is 27.5±1.4 Sv.

Anomalies of geostrophic Sverdrup transport at 20°S do not give explanations for the decrease in the gyre strength from 2003 to 2005 and the following increase in 2006. Nevertheless, the influence from the persistent La Niña event between 1998 and 2001 becomes apparent in the negative wind-stress anomalies that can be identified in the east in 1999 and 2000, and in the interior between 1999 and 2002, which is in agreement with the results reported by (Palastanga et al., 2007). This negative anomaly results in a pronounced reduction of the zonally integrated geostrophic Sverdrup transport between 2000 and 2002. Assuming that the Sverdrup balance is valid, the negative feedback on the gyre strength would result in an increased southward Ekman transport of at least the order of the change in the geostrophic component.

Sea level anomaly time series at 20°S do show large positive anomalies in the east at 110°E, between 1999 and 2001. These anomalies are propagating westward and reach 55°E within 3 years, which corresponds to the transit time for long baroclinic Rossby waves at 20°S (Chelton and Schlax, 1996; Qiu and Chen, 2006). In 2004 an intensification of the anomaly is found around 70°E. This additional positive signal could be forced either by anomalies from the equatorial region (Jochum and Murtugudde, 2005) or by intensification in the MADB at topographic features. The comparison of gyre strength changes, derived from float realisations, with annual changes in the ADT did show only few agreement.

From the results presented here the exact link between the observed features in the wind-field, the SLA and the upper ocean's density field is not fully clear. At 32°S, the influence from changes in the wind-stress seems to be the important contribution to interannual changes in the gyre strength, with modulations of the signal possibly by eddy variability in the west, southwest of MAD (Palastanga et al., 2006). In contrast, at 20°S, the situation is more complex, due to the proximity to the tropical regime, the ITF and the SEC. Palastanga et al. (2006) showed that positive SLA east of MAD can be associated with a positive IOD inducing a weakening of the SEC and its branches along east MAD. In combination with the decrease in the geostrophic Sverdrup transport this could be a possible explanation for the observed decrease in gyre strength at 20°S between 2003 and 2005.

Annual maps of DH have been produced for the SIO, confirming recent observation features like the SICC (Palastanga et al., 2006) and the connection between the subtropical gyres of the SIO and the South Pacific Ocean, described as a super-gyre (Ridgway and Dunn, 2007; Roemmich, 2007). The observed interannual variability in the gyre strength was not associated with a shift/change in the centre/structure of the gyre as observed on decadal scales in the South Pacific Ocean (Roemmich et al., 2007).

Additionally, subsurface velocities were estimated applying the OI to individual subsurface velocities estimated from the float's trajectory data. Interpolated velocities at 1900 dbar derived from float data within ±2 months of the CD139 cruise or from all data within 2002 were compared to reference velocities derived from an inverse calculation using the CD139 geostrophic velocities (McDonagh et al., 2008). It was shown that some deep velocity features are represented in all realisations. Around 60°E and 95°E southward velocities of about -1.5 $cm\,s^{-1}$ and -2 $cm\,s^{-1}$ exist. Other features, for example the large northward velocities at 105°E, are not represented in the float data. Additionally, it was shown, that the ZV assumption could lead to large errors of O(10 Sv) and even larger in the final transport estimate. In the past subsurface velocities estimated from float trajectories have already been used to create mean subsurface velocity fields (Sallee et al., 2006; Davis, 2005). The comparison of the mean velocity field for the period 2002 - 2006 shows only broadly agreement with results from Davis (2005), who derived the intermediate-depth circulation of the Indian and South Pacific Oceans at 900 m depth from autonomous floats. Only a few of the major currents and circulation features are represented while the large scale-circulation is missing, which is due to the missing background reference velocity field used in the OI method. With the focus in this study on low-frequency variability, annual and seasonal estimates of mean subsurface velocities were generated to gain knowledge about possible permanent currents at depth (1000 dbar and 1900 dbar). The results reveal seasonally varying currents west of BP and NER at 85°E across 32°S at 1900 dbar and across 20°S at 1000 dbar indicating possible topographic control of the deep current. Additionally, from the 1900 dbar velocity maps a recirculation north of 27°S in the MOZC becomes apparent, with northward inflow in the west and southward outflow in the east, showing varying intensity over the 5 year period. The strong cyclonic recirculation between MOZP and MADR at 32°S (McDonagh et al., 2008) is confirmed in the 1900 dbar data but it is shown that this is not a permanent feature over the 5 year period, since in 2004 it is replaced by an anticyclonic circulation of similar intensity. The relatively sparse data coverage, due to the early state of the Argo project in the SIO showed that seasonal and annual estimates are easily biased by single data points from one single float. Additional it is to say, that the OI method uses no background

velocity field, just the average of the subset of velocity measurements at each grid point, therefore the method heavily relies on the spatial decorrelation length scales as well as the data distribution.

7.2 Conclusion

This work highlights the important contribution provided by the Argo project. Firstly, it was shown that a large portion of the real-time float data provide accurate measurements and that in addition, with DMQC procedures, a high confidence in the quality of the data can be achieved. This is an important point in an area which showed sparse data coverage in the previous decades. Therefore, a continuous global monitoring network such as Argo, will become more and more important in the future.

Secondly, the results presented for the ocean interior at 32°S and 20°S show important relations, such as the good agreement between interannual gyre strength estimated from float data for the upper 1000 dbar and the geostrophic Sverdrup transport at 32°S. In contrast, the missing agreement in the seasonal gyre strength and the geostrophic Sverdrup transport indicates the importance of other dominating processes. At 20°S the equatorial influence together with climate phenomena such as IOD and ENSO is felt, while at 32°S in the interior, the change in wind-stress seems to dominate interannual changes. Meredith et al. (2008) showed the strong correlation of the Southern Annular Mode (SAM) index with southern hemisphere zonal winds. That means the decrease in gyre circulation between 2002 and 2005 is well matched by the previous decrease in the SAM index. However, the 5 year period of annual and seasonal averages allows only tentatively to suggest relationships to climate phenomena such as ENSO and SAM, because the present results include relatively large error bars. The continuing of Argo will allow longer time series in the future allowing better temporal resolution. That will provide the possibility to define the seasonal and annual signals in the gyre circulation, as well as possible trends over half a decade or longer, even more clearly.

Nevertheless, the 5 year period of float data already provided useful and robust information on the different states of the gyre circulation in the late 1980s and the period 2002 to 2006. The significant difference in the gyre strength and structure in 1987 needs to be taken into account for future numerical simulations, if findings on the present state of the circulation are to be achieved. Palmer (2005) suggested that both the size and the zonal structure of the deep inflow across 32°S may have changed between 1987 and 2002, if forced with the different flow fields at the southern boundary

at 32°S. These results were based on simulations using a general circulation model in the configuration described by Ferron and Marotzke (2003).

In conclusion, the present work achieved an important task by defining, for the first time, the low-frequency seasonal to interannual variability in the SIO gyre circulation from hydrographic observations. With the here shown methods it will be possible to monitor the low-frequency variability of the gyre circulation in most parts of the world's ocean assuming a similar data coverage with Argo floats as in this study. Especially at higher latitudes, where the gyre circulation accounts for a large fraction of the meridional heat transport (Cabanes et al., 2008), for example in the North Atlantic at 45°N. Results derived from observations of the oceans interior are needed to evaluate output from numerical general circulation models and from altimetry observations.

Bibliography

Beal, L. M., A. Ffield and A. L. Gordon, 2000: Spreading of the Red Sea Overflow Waters in the Indian Ocean. *J. Geophys. Res.*, **105**, pp. 8549–8564.

Belkin, I. M. and A. L. Gordon, 1996: Southern Ocean fronts from the Greenwich meridian to Tasmania. *J. Geophys. Res.*, **101**, pp. 3675–3696.

Bindoff, N. and T. J. McDougall, 2000: Decadal changes along an Indian Ocean section at 32°S and their interpretation. *J. Phys. Oceanogr.*, **30**, pp. 3162–3186.

Birol, F. and R. Morrow, 2001: Source of the baroclinic waves in the southeast Indian Ocean. *J. Geophys. Res.*, **106**, pp. 9145 – 9160.

Birol, F. and R. Morrow, 2003: Separation of the quasi-semiannual Rossby waves from the eastern boundary of the Indian Ocean. *J. Mar. Res.*, **61**, pp. 707 – 723.

Bjerknes, V. and J. W. Sandström, 1910: Dynamic meteorology and hydrography. In: *Pt.I, Statics*, Carnegie Inst. Washington, pp. 146 + tables.

Böhme, L. and U. Send, 2005: Objective analyses of hydrographic data for referencing profiling float salinities in highly variable environments. *Deep–Sea Res. II*, **52**, pp. 651 – 664.

Bower, A. S., H. D. Hunt and J. F. Price, 2000: Character and dynamics of the Red Sea and Persian Gulf. *J. Geophys. Res.*, **105**, pp. 6387–6414.

Boyer, T. P., C. Stephens, J. I. Antonov, M. E. Conkright, R. A. Locarnini, T. D. OBrien and H. E. Garcia, 2002: *World Ocean Atlas 2001, Volume 1: Salinity.* NOAA Atlas NESDIS 50, U.S. Government Printing Office, Washington, D. C., 167 pp.

Bretherton, F. P., R. E. Davis and C. B. Fandry, 1976: A technique for objective analysis and design of oceanographic experiments applied to MODE-73. *Deep–Sea Res.*, **23**, pp. 559–582.

Broecker, W. S., 1991: The Great Ocean Conveyor. *Oceanogr.*, **4**, pp. 79–89.

Bryden, H. and S. Imawaki, 2001: Ocean Heat Transport. In: *Ocean Circulation and Climate*, G. Siedler, J. Church and J. Gould, ed., Academic Press, Volume 77 of *International Geophysics Series*, Chapter 6, pp. 455–545.

Bryden, H. L. and L. M. Beal, 2001: Role of the Agulhas Current in Indian Ocean circulation and associated heat and freshwater fluxes. *Deep–Sea Res.*, **48**, pp. 1821–1845.

Bryden, H. L., L. M. Beal and L. M. Duncan, 2005: Structure and transport of the Agulhas Current and its temporal variability. *J. Phys. Oceanogr.*, **61** (3), pp. 479 – 492.

Bryden, H. L., L. M. Beal, B. A. King, R. Sanders, S. Cunningham, M. Palmer, V. Latham, M. Witt, M. Bridger, L. Duncan, D. P. Wisegarver, K. McHugh, M. Alvarez, A. F. Rios, J. Wynar and J. Benson, 2003a: RRS Charles Darwin Cruise 139, 01 Mar-15 Apr 2002. Trans-Indian Hydrographic Section across 32°S. Cruise report, no. 45, 122pp., National Oceanography Centre.

Bryden, H. L., E. L. McDonagh and B. King, 2003b: Changes in Ocean Water Mass Properties: Oscillations or Trends ? *Science*, **300**, pp. 2086–2088.

Butterworth, S., 1930: On the Theory of Filter Amplifiers. *Experimental Wireless and the Wireless Engenieer*, **7**, pp. 536–541.

Cabanes, C., T. Lee and L.-L. Fu, 2008: Mechanisms of interannual variations of the meridional overturning circulation of the North Atlantic Ocean. *J. Phys. Oceanogr.*, **38**, pp. 467 – 480.

Caldera, K. and P. B. Duffy, 2000: The Role of the Southern Ocean in Uptake and Storage of Anthopogenic Carbon Dioxide. *Nature*, **287**, pp. 620–622.

Carval, T., B. Keeley, Y. Takatsuki, T. Yoshida, S. Loch, C. Schmid, R. Goldsmith, A. Wong, R. McCreadie, A. Thresher and A. Thran, 2006: Argo data management: User's manual. Technical Report 2.1, IFREMER.

Chelton, D. B. and M. G. Schlax, 1996: Global Observations of oceanic Rossby waves. *Science*, **272**, pp. 234 – 238.

Cresswell, C. R. and T. J. Golding, 1980: Observations of a south-flowing current in the southeastern Indian Ocean. *Deep–Sea Res. A*, **27**, pp. 449 – 466.

Cunningham, S. A., T. Kanzow, D. Rayner, M. O. Baringer, W. E. Johns, J. Marotzke, H. R. Longworth, E. M. Grant, J. J.-M. Hirschi, C. S. Beal, L. M. Meinen and H. L. Bryden, 2007: Temporal Variability of the Atlantic Meridional Overturning Circulation at 26.5°N. *Science*, **317**, pp. 935 – 938.

Curry, R. G., B. Dickson and I. Yashayaev, 2003: A change in the freshwater balance of the Atlantic Ocean over the past four decades. *Nature*, **426**, pp. 826 – 829.

Davis, R. E., 1998: Preliminary results from directly measuring middepth circulation in the tropical and South Pacific. *J. Geophys. Res.*, **103**, pp. 24,619 – 24,639.

Davis, R. E., 2005: Intermediate-Depth Circulation of the Indian and South Pacific Oceans Measured by Autonomous Floats. *J. Phys. Oceanogr.*, **35**, pp. 683 – 707.

De Ruijter, W. P. M., A. Biastoch, S. S. Drijfhout, J. R. E. Lutjeharms, R. Matano, T. Pichevin, P. J. van Leeuwen and W. Weijer, 1999: Indian-Atlantic Inter-Ocean Exchange: Dynamics, Estimation and Impact. *J. Geophys. Res.*, **104**, pp. 20,885 – 20,910.

De Ruijter, W. P. M., H. M. van Aken, E. J. Beier, J. R. E. Lutjeharms, R. Matano and M. W. Schouten, 2004: Eddies and dipoles around South Madagascar: formation, pathways and large-scale impact. *Deep–Sea Res. I*, **51**, pp. 383 – 400.

Dibarboure, G., O. Lauret, F. Mertz and V. Rosmorduc, 2008: SSALTO/DUCAS User Handbook: (M)SLA and (M)ADT Near-Real Time and Delayed Time Products. User handbook, issue: 1 rev 9, CLS: Aviso Altimetry, Ramonville St Agne, France.

Domingues, C. M., M. E. Maltrud, S. E. Wijffels, J. A. Church and M. Tomczak, 2007: Simulated Lagrangian pathways between the Leeuwin Current System and the upper-ocean circulation of the southeast Indian Ocean. *Deep–Sea Res. II*, **54**, pp. 797 – 817.

Donohue, K. A. and J. M. Toole, 2003: A near-synoptic survey of the Southwest Indian Ocean. *Deep–Sea Res. II*, **50**, pp. 1893–1931.

England, H., M., J. S. Godfrey, A. C. Hirst and M. Tomczak, 1993: The Mechanism for Antarctic Intermediate Water Renewal in a World Ocean Model. *J. Phys. Oceanogr.*, **23**, pp. 1553 – 1560.

Fang, M. and R. Morrow, 2003: Evolution, movement and decay of warm-core Leeuwin current eddies. *Deep–Sea Res. II*, **50**, pp. 2245 – 2261.

Feng, M., L. J. Majewski, C. B. Fandry and A. M. Waite, 2007: Characteristics of two counter-rotating eddies in the Leeuwin Current system off the Western Australian coast. *Deep–Sea Res. II*, **54**, pp. 961 – 980.

Feng, M., G. Meyers, A. Pearce and S. Wijffels, 2003: Annual and interannual variations of the Leeuwin current at 32∘S. *J. Geophys. Res.*, **108** (C11), pp. doi:10.1029/2002JC001763,2003.

Feng, M., S. Wijffels, J. S. Godfrey and G. Meyers, 2005: Do eddies play a role in the momentum balance of the Leeuwin current? *J. Phys. Oceanogr.*, **35**, pp. 964 – 975.

Ferron, B. and J. Marotzke, 2003: Impact of 4D-variational assimilation of WOCE hydrography on the meridional circulation of the Indian Ocean. *Deep–Sea Res. II*, **50**, pp. 2005 – 2021.

Fu, L.-L., 1986: Mass, heat and freshwater fluxes in the South Indian Ocean. *J. Phys. Oceanogr.*, **16**, pp. 1683 – 1693.

Fukumori, I. and C. Wunsch, 1991: Efficient representation of the North Atlantic hydrographic and chemical distributions. *Progress in Oceanography*, **27**, pp. 111 – 195.

Ganachaud, A. and C. Wunsch, 2000: Improved estimates of global ocean circulation, heat transport and mixing from hydrographic data. *Nature*, **408**, pp. 453 – 457.

Gandin, L. S., 1963: *Objective Analysis of Meteorological Fields*. Leningrad, Gidrometizdat, (English translation No. 1373 by Israel Program for Scientific Translations (1965), Jerusalem, 242 pp.).

Getzlaff, K., C. W. Böning and J. Dengg, 2006: Lagrangian perspectives of deep water export from the subpolar North Atlantic. *Geophys. Res. Letters*, **33**, DOI: 10.1029/2006GL026470.

Gille, S. T., 2002: Warming of the Southern Ocean since the 1950s. *Science*, **295**, pp. 1275 – 1277.

Gille, S. T., 2003: Float observations of the Southern Ocean: part 1. Estimating mean fields, bottom velocities, and topographic steering. *J. Phys. Oceanogr.*, **33**, pp. 1167 – 1181.

Gordon, A. L., 1986: Interocean exchange of thermocline water. *J. Geophys. Res.*, **91**, pp. 5037 – 5046.

Gordon, A. L., 1997: World Ocean Circulation Experiment Indian Ocean I09N 1995. Technical Report, Lamont-Doherty Earth Observatory.

Gordon, A. L. and R. A. Fine, 1996: Pathways of water between the Pacific and Indian oceans in the Indonesian seas. *Nature*, **379**, pp. 146 – 149.

Gordon, A. L., J. R. E. Lutjeharms and M. L. Gründlingh, 1987: Stratification and Circulation at the Agulhas Retroflection. *Deep–Sea Res.*, **34**, pp. 565 – 599.

Grassl, H., 2001: Climate and Oceans. In: *Ocean Circulation and Climate*, G. Siedler, J. Church and J. Gould, ed., Academic Press, Volume 77 of *International Geophysics Series*, Chapter 1.1, pp. 3–9.

Griffiths, R. W. and A. F. Pearce, 1985: Satellite images of an unstable warm eddy derived from the Leeuwin. *Deep–Sea Res. A*, **32**, pp. 1371 – 1380.

Guinehut, S., G. Larnicol and P. Y. Le Traon, 2002: Design of an array of profiling floats in the North Atlantic from model simulations. *J. Mar. Syst.*, **35** (1-2), pp. 1 – 9.

Hadfield, R. E., N. C. Wells, S. A. Josey and J. J.-M. Hirschi, 2007: On the accuracy of North Atlantic temperature and heat storage fields from Argo. *J. Geophys. Res.*, **112**, C01009, doi:10.1029/2006JC003825.

Haines, K., J. D. Blower, J.-P. Drecourt, C. Liu, A. Vidard, I. Astin and X. Zhou, 2006: Salinity Assimilation Using $S(T)$: Covariance Relationships. *Mon. Wea. Rev.*, **134**, pp. 759 – 771.

Hanawa, K. and L. D. Talley, 2001: Mode Waters. In: *Ocean Circulation and Climate*, G. Siedler and J. Church, ed., Academic Press, Marine Series, pp. 373 – 386.

Hellerman, S. and M. Rosenstein, 1983: Normal Monthly Wind Stress Over the World Ocean with Error Estimates. *J. Phys. Oceanogr.*, **13**, pp. 1093 – 1104.

Hirschi, J., J. Baehr, J. Marotzke, J. Stark, S. Cunningham and J.-O. Beismann, 2003: A monitoring design for the Atlantic meridional overturning circulation. *Geophys. Res. Letters*, **30 (7)**.

IPCC, 2007: *Climate Change 2007: Synthesis Report. Contribution of Working Groups I, II and III to the Fourth Assessment Report of the Intergovernmental Panel on Climate Change [Core Writing Team, Pachauri, R. K. and Reisinger, A. (eds)].* IPCC, Geneva, Switzerland.

Jochum, M. and R. Murtugudde, 2005: Internal Variability of the Indian Ocean. *J. Climate*, **18**, pp. 3726 – 3738.

Johnson, D. R., T. P. Boyer, H. E. Garcia, R. A. Locarnini, M. T. Mishonov, A. V. Pitcher, O. K. Baranova, J. I. Antonov and I. V. Smolyar, 2006: World Ocean Database 2005 Documentation. NODC Internal Report 18.

Kalnay, E., M. Kanamitsu, R. Kistler, W. Collins, D. Deaven, L. Gandin, M. Iredell, S. Saha, G. White, J. Woollen, Y. Zhu, M. Chelliah, W. Ebiszusaki, W. Higgins, J. Janowiak, K. Mo, C. Ropelewski, J. Wang, A. Leetma, R. Reynolds, R. Jenne and D. Joseph, 1996: The NCEP/NCAR 40-year Reanalysis Project. *Bull. Amer. Meteor. Soc.*, **77**, pp. 437 – 471.

King, B. and J. Sudheer, 2006: REPROT ON SECOND ARGO DELAYED MODE QC WORKSHOP. Technical Report 1.0, NOC, Southampton.

King, B. A. and E. L. McDonagh, 2005: Decadal Changes in Ocean properties revealed by Argo floats. *Geophys. Res. Letters*, **32**, L15601, doi:10.1029/2005GL023145.

Kistler, R., E. Kalnay, W. Collins, S. Saha, G. White, J. Woollen, M. Chelliah, W. Ebiszusaki, M. Kanamitsu, V. Kousky, H. van den Dool, R. Jenne and M. Fiorino, 2001: The NCEP/NCAR 50-yearreanalysis: Monthly means CD-ROM and documentation. *Bull. Amer. Meteor. Soc.*, **82**, pp. 247 – 267.

Kobayashi, T. and T. Suga, 2006: The Indian Ocean HydroBase: A high-quality climatological dataset for the Indian Ocean. *Progress in Oceanography*, **68**, pp. 75 – 114.

Lebedev, K. V., H. Yoshinari, N. A. Maximenko and P. W. Hacker, 2007: YoMaHa'07: Velocity data assessed from trajectories of Argo floats at parking level and at the sea surface. Technical Note No.4(2), International Pacific Research Center.

Lee, T. N. and J. Marotzke, 1998: Seasonal cycles of meridional overturning and heat transport of the Indian Ocean. *J. Phys. Oceanogr.*, **28**, pp. 923 – 943.

Levitus, S., J. Antonov, T. Boyer and C. Stephens, 2000: Warming of the World Ocean. *Science*, **287**, pp. 2225 – 2229.

Levitus, S., T. Boyer, M. Conkright, T. O'Brien, J. Antonov, C. Stephens, L. Stathoplos, D. Johnson and R. Gelfeld, 1998: *World Ocean Database 1998 Volume 1: Introduction.* NOAA Atlas NESDIS 18, U.S. Gov. Printing Office, Wash., D.C.

Locarnini, R. A., A. V. Mishonov, J. I. Antonov, T. P. Boyer and H. E. Garcia, 2006: *World Ocean Atlas 2005, Volume 1: Temperature.* NOAA Atlas NESDIS 61, U.S. Government Printing Office, Washington, D. C., 182 pp.

Lutjeharms, J. R. E., 1988: Remote sensing corroboration of retroflection of the East Madagascar Current. *Deep–Sea Res.*, **35**, pp. 2045 – 2050.

Lutjeharms, J. R. E. and I. J. Ansorge, 1997: The Agulhas Return Current. *J. Mar. Syst.*, **30**, pp. 115 – 138.

Matano, R. P., E. J. Beier and P. T. Strub, 2008: The seasonal variability of the circulation in the South Indian Ocean: Model and observations. *J. Mar. Syst.*, doi:10.1016/j.jmarsys.2008.01.007.

Matano, R. P., C. G. Simionato, W. P. de Ruijter, P. J. van Leeuwen, P. T. Strub, D. B. Chelton and M. G. Schlax, 1998: Seasonal Variability in the Agulhas Retroflection region. *Geophys. Res. Letters*, **25**, pp. 4361 – 4364.

McCartney, M., 1998: World Ocean Circulation Experiment Indian Ocean I08S/I09S 1994/1995. Technical Report, Woods Hole Oceanographic Institute.

McCartney, M. S., 1977: Subantarctic Mode Water, in: *A voyage of discovery. Deep–Sea Res.*, **24 (Suppl.)**, pp. 103 – 119.

McCartney, M. S., 1982: The subtropical recirculation of Mode Waters. *J. Mar. Res.*, **40**, pp. 427 – 464.

McDonagh, E. L., H. L. Bryden and B. A. King, 2005: Decadal Changes in the South Indian Ocean thermocline. *J. Climate*, **18**, pp. 1575 – 1590.

McDonagh, E. L., H. L. Bryden, B. A. King and R. J. Sanders, 2008: The Circulation of the Indian Ocean at 32°S. *Progress in Oceanography*, doi:10.1016/j.pocean.2008.07.001.

McIntosh, P., 1990: Oceanographic data interpolation: Objective analysis and splines. *J. Geophys. Res.*, **95** (C8), pp. 13529 – 13541.

Meredith, M. P., E. J. Murphy, E. J. Hawker, J. C. King and M. I. Wallace, 2008: On the interannual variability of ocean temperatures around South Georgia, Southern Ocean: Forcing by El Nino/Southern Oscillation and the Southern Annular Mode. *Deep–Sea Res. II*, doi:10.1016/j.dsr2.2008.05.020.

Metz, N., 2008: Sea Surface and Atmospheric fCO2 data in the South Indian and Southern Oceans during OISO cruises onboard the R/V Marion Dufresne. Website, http://cdiac.ornl.gov/ftp/oceans/OISO_line/.

Miyama, T., J. P. McCreary, T. G. Jensen, J. Loschnigg and A. Ishida, 2003: Structure and dynamics of the Indian-Ocean Cross-Equatorial Cell. *Deep–Sea Res. II*, **50**, pp. 2023 – 2047.

Morrow, R. and F. Birol, 1998: Variability in the southeast Indian Ocean from altimetry: forcing mechanisms for the Leeuwin Current. *J. Geophys. Res.*, **103**, pp. 18529 – 18544.

Morrow, R., F. Birol, D. Griffin and J. Sudre, 2004: Divergent pathways of cyclonic and anti-cyclonic ocean eddies. *Geophys. Res. Letters*, **31**, Art. No. L24311.

Morrow, R., F. Fang, M. Fieux and R. Molcard, 2003: Anatomy of three warm-core Leeuwin Current eddies. *Deep–Sea Res. II*, **50**, pp. 2229 – 2243.

Murtugudde, R., J. P. McCreary and A. J. Busalacchi, 2000: Oceanic processes associated with anomalous events in the Indian Ocean with relevance to 19971998. *J. Geophys. Res.*, **105**, pp. 3295 3306.

Owens, W. B. and A. P. S. Wong, 2008: An improved calibration method for the drift of the conductivity sensor on autonomous CTD profiling floats by theta-s climatology. *Deep-Sea Research*, accepted.

Palastanga, V., P. J. van Leeuveen and W. P. M. de Ruijter, 2006: A link between low-frequency mesoscale eddy variability around Madagascar and the large-scale Indian Ocean variability. *J. Geophys. Res.*, **111**, C09029, doi:10.1029/2005JC003081.

Palastanga, V., P. J. van Leeuveen, M. W. Schouten and W. P. M. de Ruijter, 2007: Flow structure and variability in the subtropical Indian Ocean: Instability of the South Indian Ocean Countercurrent. *J. Geophys. Res.*, **112**, C01001, doi:10.1029/2005JC003395.

Palmer, M. D., 2005: Decadal variability of the subtropical gyre and deep meridional overturning circulation of the Indian Ocean. Dissertation, University of Southampton, UK.

Palmer, M. D., H. L. Bryden, J. Hirschi and J. Marotzke, 2004: Observed changes in the South Indian Ocean gyre circulation, 1987-2002. *Geophys. Res. Letters*, **31**, L15303, doi:10.1029/2004GL020506.

Parilla, G., A. Lavin, H. L. Bryden, M. Garcia and R. Millard, 1994: Rising temperatures in the subtropical North Atlantic Ocean over the past 35 years. *Nature*, **369**, pp. 48 – 51.

Park, J. J., K. Kim, B. A. King and S. C. Riser, 2005: An Advanced Method to Estimate Deep Currents from Profiling Floats. *J. Atmos. Oceanic Technol.*, **22**, pp. 1294 – 1304.

Pedlosky, J., 1987: *Geophysical Fluid Dynamics*. Springer Verlag, New York, 2. Edition.

Pedlosky, J., 1996: *Physics of the Ocean*. Springer Verlag, New York, 2. Edition.

Pond, S. and G. L. Pickard, 1983: *Introductory Dynamical Oceanography*. Pergamon Press, Oxford, 2. Edition.

Potemra, J. T., 2001: Contribution of equatorial pacific winds to southern tropical Indian Ocean Rossby waves. *J. Geophys. Res.*, **106 C2**, pp. 2407 – 2422.

Qiu, B. and S. Chen, 2006: Decadal Variability in the Large-Scale Sea Surface Height Field of the South Pacific Ocean: Observations and Causes. *J. Phys. Oceanogr.*, **36**, pp. 1751 – 1762.

Quartly, G. D. and M. A. Srokosz, 2004: Eddies in the Southern Mozambique Channel. *Deep–Sea Res. I*, **51**, pp. 69 – 83.

Reid, J. R., 2003: On the total geostrophic circulation of the Indian Ocean: flow patterns, tracers, and transports. *Progress in Oceanography*, **56**, pp. 137–186.

Rennie, S. J., C. P. Pattiaratchi and R. D. McCauley, 2007: Eddy formation through the interaction between Leeuwin Current, Leeuwin Undercurrent and topography. *Deep–Sea Res. II*, **54**, doi:10.1016/j.dsr2.2007.02.005.

Ribbe, J., 1999: On wind driven mid-latitude convection in ocean general circulation models. *Tellus*, **51A**, pp. 505–516.

Ridgway, K. R. and J. R. Dunn, 2007: Observational evidence for a Southern Hemisphere oceanic supergyre. *Geophys. Res. Letters*, **34**, doi:10.1029/2007GL030392.

Rintoul, S. R. and M. H. England, 2002: Ekman Transport dominates local Air-Sea-fluxes in driving variability of Subantarctic Mode Water. *J. Phys. Oceanogr.*, **32**, pp. 1308 – 1321.

Rio, M.-H. and F. Hernandez, 2005: A mean dynamic topography computed over the world ocean from altimetry, in-situ measurements and a geoid model. *J. Geophys. Res.*, **109**, C12032.

Rio, M.-H., P. Schaeffer, J.-M. Lemoine and F. Hernandez, 2005: Estimation of the ocean Mean Dynamic Topography through the combination of altimetric data, in-situ measurements and GRACE geoid: From global to regional studies. *Proceedings of the GOCINA international workshop, Luxembour*.

Roemmich, D., 2007: Super spin in the southern seas. *Nature*, **449**, pp. 34 – 35.

Roemmich, D., J. Gilson, R. Davis, P. Sutton, S. Wijffels and S. Riser, 2007: Decadal Spinup of the South Pacific Subtropical Gyre. *J. Phys. Oceanogr.*, **37**, pp. 162 – 173, DOI:10.1175/JPO3004.1.

Roether, W., B. B. Manca, B. Klein, D. Bregant, D. Georgopoulos, V. Beitzel, V. Kovaevi and A. Luchetta, 1996: Recent Changes in the Eastern Mediterranean Deep Waters. *Science*, **271**, pp. 333 – 335.

Sabine, C. L. and R. A. Feely, 2001: Comparison of recent Indian Ocean anthropogenic CO_2 estimates with a historical approach. *Global Biogeochem. Cycles*, **15**, pp. 31 – 42.

Sallee, J.-B., N. Wienders and K. Speer, 2006: Formation of subantarctic mode water in the southeastern Indian Ocean. *Ocean Dynamics*, **56**, DOI:10.1007/s10236-005-0054-x.

Sarmiento, J. L., N. Gruber, M. A. Brezinski and J. P. Dunne, 2004: Highlatitude controls of thermocline nutrients and lowlatitude biological productivity. *Nature*, **427**, pp. 56 – 60.

Schiller, A., S. E. Wijffels and G. A. Meyers, 2004: Design Requirements for an Argo Float Array in the Indian Ocean Inferred from Observing System Simulation Experiments. *J. Atmos. Oceanic Technol.*, **21**, pp. 1598 – 1620.

Schoenefeldt, R. and F. A. Schott, 2006: Decadel variability of the Indian Ocean cross-equatorial exchange in SODA. *Geophys. Res. Letters*, **33**, L08602, doi:10.1029/2006GL025891.

Schott, F. and J. P. McCreary, 2001: The monsoon circulation of the Indian Ocean. *Progress in Oceanography*, **51**, pp. 1 – 123.

Schott, F. A., J. P. McCreary and G. C. Johnson, 2004: Shallow overturning circulation of the tropical subtropical oceans. In: *AGU Geophysical Monography "Ocean-atmosphere interaction and climate variability"*, C. Wang, J. Carton and S.-P. Xie, ed., AGU, Washington, pp. 261 – 304.

Schouten, M. W., W. P. M. de Ruijter and P. J. van Leeuwen, 2002: Upstream control of the Agulhas Ring shedding. *J. Geophys. Res.*, **107**, doi:10.1029/2001JC00804.

Schouten, M. W., W. P. M. de Ruijter, P. J. van Leeuwen and H. Dijkstra, 2003: Eddies and variability in the Mozambique Chanel. *Deep–Sea Res. II*, **50**, pp. 43 – 55.

Shamsundar, N., 1970: Implementation of Akima's univariate interpolation method. *Journal of the ACM*, **17** (4), pp. 589 – 602.

Sloyan, M., B. and R. Rintoul, S., 2001: Circulation, renewal, and modification of Antarctic Mode and Intermediate Water. *J. Phys. Oceanogr.*, **31**, pp. 1005 – 1030.

Smith, R. L., A. Huyer, J. S. Godfrey and J. A. Church, 1991: The Leeuwin current off Western Australia 1986-1987. *J. Phys. Oceanogr.*, **21**, pp. 323 – 345.

Speer, K. G., H.-J. Isemer and A. Biastoch, 1995: Water mass formation from revised COADS data. *J. Phys. Oceanogr.*, **25**, pp. 2444 – 2457.

Sprintall, J. S., S. Wijffels, T. Chereskin and N. Bray, 2002: The JADE and WOCE I10/IR6 Throughflow sections in the southeast Indian Ocean. Part 2: velocity and transports. *Deep–Sea Res. II*, **49**, pp. 1363 – 1389.

Stark, S., R. A. Wood and H. T. Banks, 2006: Reevaluating the Causes of Observed Changes in Indian Ocean Water Masses. *J. Climate*, **19**, pp. 4075 – 4086.

Stephens, C., J. I. Antonov, T. P. Boyer, M. E. Conkright, R. A. Locarnini, T. D. OBrien and H. E. Garcia, 2002: *World Ocean Atlas 2001, Volume 1: Temperature*. NOAA Atlas NESDIS 49, U.S. Government Printing Office, Washington, D. C., 167 pp.

Stewart, R. H., 2007: *Introduction To Physical Oceanography*. Web published by Stewart, R. H., Department of Oceanography, Texas A & M University.

Stramma, L. and J. R. E. Lutjeharms, 1997: The flow field of the subtropical gyre of the South Indian Ocean. *J. Geophys. Res.*, **102**, pp. 5513 – 5530.

Sverdrup, H. U., 1947: Wind-driven currents in a baroclinic ocean; with application to the equatorial currents of the eastern Pacific. *Proc. Natl. Acad. Sci.*, **33**, pp. 318 – 326.

Tchernia, P., 1980: *Descriptive Regional Oceanography*. Marine Series, Pergamon Press, Oxford.

Thacker, W. C., 2008: Estimating Salinity between 25◦ and 45◦S in the Atlantic Ocean Using Local Regression. *J. Atmos. Oceanic Technol.*, **25**, pp. 114 – 130.

Tomczak, M. and J. S. Godfrey, 1994: *Regional Oceanography: An Introduction*. Pergamon Press, London.

TOOLE, J. M. and B. A. WARREN, 1993: A hydrographic section across the subtropical South Indian Ocean. *Deep–Sea Res.*, **40**, pp. 1973 – 2019.

UCHIDA, H. and M. FUKASAWA, 2005: WHP P6, A10, I3/I4 REVISIT DATA BOOK: Blue Earth Global Expedition 2003 (BEAGLE2003). Technical Report, JAMSTEC.

UNESCO, 1985: The international system of units (SI) in oceanography. Unesco technical papers no. 45, iapso pub. sci. no. 32, UNESCO, Paris, France.

WAITE, A. M., P. A. THOMPSON, S. PESANT, M. FENG, L. E. BECKLEY, C. M. DOMINGUES, D. GAUGHAN, C. E. HANSON, C. M. HOLL, T. KOSLOW, M. MEULENERS, J. P. MONTOYA, T. MOORE, B. A. MUHLING, H. PATERSON, S. RENNIE, J. STRZELECKI and L. TWOMEY, 2007: The Leeuwin Current and its eddies: An introductory overview. *Deep–Sea Res. II*, **54**, pp. 789 – 796.

WARREN, B. A., 1972: Insensitivity of subtropical mode water characteristics to meteorological fluctuations. *Deep–Sea Res.*, **19**, pp. 1 – 19.

WARREN, B. A., 1981: Transindian hydrographic section at Lat. 18°S: Property distribution and circulation in the South Indian Ocean. *Deep–Sea Res.*, **28**, pp. 759 – 788.

WEBB, D. J., P. D. KILLWORTH, A. C. COWARD and S. R. THOMPSON, 1991: *The FRAM Atlas of the Southern Ocean*. National Environmental Research Council, Swindon, UK.

WEBB, D. J. and N. SUGINOHARA, 2001: The Interior Circulation of the Ocean. In: *Ocean Circulation and Climate*, G. Siedler, J. Church and J. Gould, ed., Academic Press, Volume 77 of *International Geophysics Series*, Chapter 4, pp. 205–214.

WEIJER, W., W. P. M. DE RUIJTER, A. STERL and S. S. DRIJHOUT, 2002: Response of the Atlantic overturning circulation to South Atlantic sources of buoyancy. *Glob. and Planet. Change*, **34**, pp. 293 – 311.

WELANDER, P., 1959: On the Vertically Integrated Mass Transport in the Oceans. In: *The Atmosphere and the Sea in Motion*, Bolin, ed., Rockefeller Inst. Press in association with Oxford Univ. Press, New York, pp. 95 – 101, Rossby memorial vol. Edition.

WHITE, W. B., 1995: Design of a global observing system for gyre-scale upper ocean temperature and salinity. *Progress in Oceanography*, **36**, pp. 169 – 217.

WONG, A. P. S., 2005a: How to use Matlab to include additional data in the reference database in WJO. Technical Report, University of Washington, http://prelude.ocean.washington.edu/references.html.

WONG, A. P. S., 2005b: Subantarctic Mode Water and Antarctic Intermediate Water in the South Indian Ocean based on profiling float data 2000-2004. *J. Mar. Res.*, **63**, pp. 789–812.

WONG, A. P. S., N. L. BINDOFF and J. A. CHURCH, 1999: Large-scale freshening of intermediate waters in the Pacific and Indian oceans. *Nature*, **400**, pp. 440–443.

WONG, A. P. S., G. C. JOHNSON and W. B. OWENS, 2001: Freshwater and heat changes in the North and South Pacific Oceans between the 1960s and 1985-94. *J. Climate*, **14**, pp. 1613–1633.

WONG, A. P. S., G. C. JOHNSON and W. B. OWENS, 2003: Delayed-Mode calibration of autonomous CTD profiling float salinity data by θ-S Climatology. *J. Atmos. Oceanic Technol.*, **20**, pp. 308–318.

WYRTKI, K., 1973: Physical Oceanography of the Indian Ocean. In: *The Biology of the Indian Ocean*, B. Zeitschel, ed., Springer, Berlin, pp. 18 – 36.

YOU, Y. and M. TOMCZAK, 1993: Thermocline circulation and ventilation in the Indian Ocean derived from water mass analysis. *Deep–Sea Res. I*, **40**, pp. 13 – 56.